Yu-Fei Song *Editor*

Polyoxometalate-Based Assemblies and Functional Materials

Springer

176
Structure and Bonding

Series Editor:

D.M.P. Mingos, Oxford, United Kingdom

Aims and Scope

Structure and Bonding is a publication which uniquely bridges the journal and book format. Organized into topical volumes, the series publishes in depth and critical reviews on all topics concerning structure and bonding. With over 50 years of history, the series has developed from covering theoretical methods for simple molecules to more complex systems.

Topics addressed in the series now include the design and engineering of molecular solids such as molecular machines, surfaces, two dimensional materials, metal clusters and supramolecular species based either on complementary hydrogen bonding networks or metal coordination centers in metal-organic framework materials (MOFs). Also of interest is the study of reaction coordinates of organometallic transformations and catalytic processes, and the electronic properties of metal ions involved in important biochemical enzymatic reactions.

Volumes on physical and spectroscopic techniques used to provide insights into structural and bonding problems, as well as experimental studies associated with the development of bonding models, reactivity pathways and rates of chemical processes are also relevant for the series.

Structure and Bonding is able to contribute to the challenges of communicating the enormous amount of data now produced in contemporary research by producing volumes which summarize important developments in selected areas of current interest and provide the conceptual framework necessary to use and interpret mega-databases.

We welcome proposals for volumes in the series within the scope mentioned above. Structure and Bonding offers our authors and readers:

- OnlineFirst publication. Each chapter is published online as it is finished, ahead of the print volume
- Wide dissemination. The chapters and the volume will be available on our platform SpringerLink, one of the largest collections of scholarly content in the world. SpringerLink attracts more than 50 million users at 15.000 institutions worldwide.
- Easy manuscript preparation. Authors do not have to spend their valuable time on the layout of their contribution. Springer will take care of all the layout related issues and will provide support throughout the complete process.

More information about this series at http://www.springer.com/series/430

Yu-Fei Song

Editor

Polyoxometalate-Based Assemblies and Functional Materials

With contributions by

W. Chen · R. J. Errington ·T. Izuagie · B. Kandasamy ·
Y.-Q. Lan · D. Lebbie · C.-G. Lin · W. Liu · J. McAllister ·
H. N. Miras · Y.-F. Song · C. Streb · R. Tsunashima ·
S. Uchida · X.-L. Wang

🕊 Springer

Editor
Yu-Fei Song
Beijing University of Chemical Technology
Beijing, China

Preface

Metal oxides have attracted wide attention due to their unique structures, and recent focus has shifted from accidental discovery of intriguing molecular structures to rational design of sophisticated complex assemblies and the development of various functionalities. Polyoxometalates (POMs), as a large group of anionic metal oxides, have experienced a similar process during the past two centuries. POMs have expanded the research area to include a new range of multifunctional materials, aiming to find practical application in both academics and industries. Thanks to the rapid progress of crystallography and spectroscopic techniques, the advances in structural controllability and the elaboration of structure-property relationship have endowed POMs-based materials with outstanding performances in catalysis, photo-sensing, energy conversion, storage etc. In this volume of *Structure and Bonding*, we invite a few young and vibrant chemists in this field to contribute a comprehensive discussion on the recent development of novel polyoxometalate syntheses and functionality.

In the chapter 'Building Block Libraries and Structural Considerations in the Self-assembly of Polyoxometalate and Polyoxothiometalate Systems', Miras and coworkers give an overview of the development of polyoxometalates with a particular focus on the synthetic methodologies and reactivity. Even though a complete understanding of the self-assembly process during polyoxometalate cluster formation is a challenge, the template synthetic approach proposed by the authors' group might throw light on the design and discovery of novel complex clusters. In the chapter 'Structure and Bonding in Molecular Vanadium Oxides: From Templates via Host–Guest Chemistry to Applications', the historic development and current trends in polyoxovanadate synthesis and applications in catalysis and magnetism are discussed by Streb et al., with specific considerations on the formation mechanisms of linking isolated vanadates into supramolecular architectures. In the chapter 'Polyoxometalate-Based Photo-Sensitive Functional Hybrid Materials', Song and colleagues concentrate on the photo-sensitive properties of polyoxometalate hybrids. The synthetic methods of covalently grafting organic functional molecules onto polyoxometalate clusters have been presented, and the

photo-responsive properties of such hybrids in both solid states and solutions have been investigated in detail. In the chapter 'Porous Ionic Crystals Based on Polyoxometalates', Uchida et al. summarizes the recent work of her group on polyoxometalate-containing porous ionic crystals, and the potential applications in heterogeneous catalysis, gas adsorption/separation, and ion-uptake/conduction are also featured. The kinetic control of the self-assembly process provides a great insight into the relation of ionic crystal structure and the relevant properties. In the chapter 'Polyoxometalates Assemblies and Their Electrochemical Applications', Lan and coworkers explore the redox activity of polyoxometalates and their applications for clean and renewable energy. Various strategies to prepare polyoxometalate-assisted composite materials are discussed and the reactivity towards hydrogen evolution reaction, oxygen evolution reaction, and water splitting are highlighted. In the chapter 'Gel-Electrophoretic Chromatography of Polyoxometalate Clusters in Aqueous Solution', a study of gel electrophoresis on the discovery and separation of polyoxometalate clusters is investigated by Tsunashima et al. The cluster size, charge density, and countercation are suggested to be correlated to the mobility and separation mechanism of unknown cluster systems in solution. In the chapter 'Alkoxido-Derivatised Lindqvistand Keggin-Type Polyoxometalates', Errington describes the latest research achievements on the protolytic behaviors of Lindqvist- and Keggin-type polyoxometalates in organic solvents. The syntheses and subsequent reactivity of such clusters are explored and monitored by the powerful technique of NMR in non-aqueous solution.

   As a volume editor, I would like to express my sincere appreciation to all the authors who have contributed to this book. Without their hard and excellent work this book might have not been completed. Such a collection of important research works in the field of polyoxometalate surely will be an essential reference to chemists, material scientists, and industrial researchers. We wish this book will be of great interest to young researchers who wish to get involved in this area, and inspire them to explore the beauty of polyoxometalates.

Beijing, China   Yu-Fei Song
November 2017

Contents

Building Block Libraries and Structural Considerations in the Self-assembly of Polyoxometalate and Polyoxothiometalate Systems

James McAllister and Haralampos N. Miras

Abstract Inorganic metal-oxide clusters form a class of compounds that are unique in their topological and electronic versatility and are becoming increasingly more important in a variety of applications. Namely, Polyoxometalates (POMs) have shown an unmatched range of physical properties and the ability to form structures that can bridge several length scales. The formation of these molecular clusters is often ambiguous and is governed by self-assembly processes that limit our ability to rationally design such molecules. However, recent years have shown that by considering new building block principles the design and discovery of novel complex clusters is aiding our understanding of this process. Now with current progress in thiometalate chemistry, specifically polyoxothiometalates (POTM), the field of inorganic molecular clusters has further diversified allowing for the targeted development of molecules with specific functionality. This chapter discusses the main differences between POM and POTM systems and how this affects synthetic methodologies and reactivities. We will illustrate how careful structural considerations can lead to the generation of novel building blocks and further deepen our understanding of complex systems.

Contents

J. McAllister and H.N. Miras (✉)
School of Chemistry, The University of Glasgow, Glasgow G12 8QQ, UK
e-mail: charalampos.moiras@glasgow.ac.uk

1 Introduction

Today, Polyoxometalates (POMs) [1] are a key emerging area that promises to allow the development of sophisticated designer based materials and devices that exploit developments in instrumentation, nanoscale science and material fabrication methods. POMs are constructed by combinations of early transition metaloxide units (e.g. M = Mo, W, V and Nb) at their high oxidation states. POMs are large frameworks, where the transition-metal oxyanions are linked together by the sharing of oxygen atoms to form structures with the general formula $\{MO_x\}_n$ [2] They may contain tens to hundreds of metal atoms that reach nuclearities as high as 368 metal atoms in one single cluster molecule forming nanosized architectures approaching the sizes of small protein molecules [3]. Over the last decade, a number of reviews have addressed different aspects of POM science; including new structures, biomedical applications, catalysis, theoretical calculations and perspectives for new materials [4, 5].

POMs have a rich history and have been known for more than two centuries, but due to a lack of appropriate analytical methods, the field remained for long one of the most underdeveloped disciplines in inorganic chemistry. Their discovery dates back to 1826, when the first synthesized POM system was reported. The compound isolated was ammonium phosphomolybdate and contained the $[PMo_{12}O_{40}]^{3-}$ anion. However, it was not until almost a century later, when in 1933, Keggin determined the structure of $H_3[PW_{12}O_{40}]$ by powder X-ray diffraction [6]. Since then, the ongoing development of synthetic methodologies and spectroscopic techniques has led to an eruption of structurally characterized POM compounds, see Fig. 1 [7]. In terms of technique development, fast and high-resolution single crystal data collection has allowed the area to blossom in an unimaginable way. The observed explosion of POM chemistry attracted the attention of various research groups who demonstrated the desire to develop the field further by focusing their efforts on understanding the underlying chemical processes masked by the self-assembly which govern these chemical systems. These efforts were mainly associated with fine manipulation of a long list of experimental variables which affect the self-assembly process to different extents (Fig. 1), in marked contrast to the oxochalcogenide chemistry, which is the key factor for the observed diversity in architectures and functionalities of POM-based species. Consequently, the rational utilization of this set of variables introduces an element of design in complex chemical processes which facilitates a degree of control during the self-assembly process.

Fig. 1 Representations of the structures of some polyoxometalate (POM) clusters, all synthesized under 'one-pot' – 'one-step' reaction conditions (space filling: Mo *large grey spheres*, and O *smaller grey spheres*) from the well-known and studied {M$_{12}$}/ {M$_{18}$} Keggin/Dawson ions to the {Mo$_{154}$}/{Mo$_{132}$} and {Mo$_{256}$}/{Mo$_{368}$} clusters. These clusters are compared (to scale) with the protein Human Carbonic Anhydrase II (a medium-sized protein with 260 residues, MW 29.6 kD) to demonstrate their macro dimensions
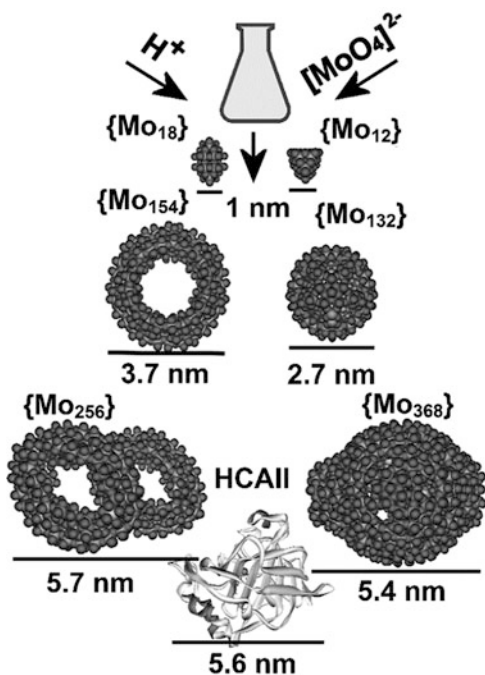
The development of novel synthetic approaches over the last decades has helped synthetic chemists realize the correlation between experimental variables and complexity of the generated building block libraries. This observation is the driving force which renders POM chemistry a key emerging area that promises to allow the development of highly complex modular molecule-based materials and molecular devices with predefined functionality. Moreover, advances in other spectroscopic techniques such as electrospray-ionization mass spectrometry (ESI-MS) and heteronuclear NMR have allowed researchers to bridge the gap between solution and solid state complex self-assembled chemical systems and reveal mechanistic aspects of the underlying chemistry [8]. However, despite all the efforts, the increase in the number of reported species and the investigation of their physical properties, it is frustratingly difficult to reveal crucial information regarding the selection rules that trigger the organization of the generated building blocks in a controlled fashion and even more difficult to design specific routes leading to predefined functionality or emergence of new properties and phenomena. There-fore, given the enormous challenge in understanding and controlling the self-assembly processes for a range of self-assembled cluster-based architectures, numerous research groups have focused their efforts on the development and/or discovery of new selection rules. These efforts trigger the formation of highly diverse and complex building block libraries which will allow to shine light upon the underlying processes of high nuclearity POMs as well as the construction of new architectures [9].

Interestingly, Polyoxothiometalates (POTMs), a closely related family of compounds similar to POMs, have attracted the attention of researchers due to their seemingly similar chemical behaviour. Recent interest surrounding POTMs has proved fruitful. The insertion of soft donating centres such as sulphur atoms in molecular structures has provided access to various unique properties. The properties of this new class of molecular clusters can be attributed directly to the addition of sulphur, as in addition to its own properties of softness and polarization, it presents intense redox activity different from that of oxygen. This provides access to a plethora of interesting building blocks and molecular clusters with chemistries differing to that of POMs.

2 Classification of Polyoxometalates

POMs exhibit a diverse array of structural types exhibiting an abundance of structural features, compositions and sizes ranging from 1 to 5.6 nm [3]. In this way, many thousands of POMs are known to exist, which may be functionalized and exploited to suit particular design criteria. Thus, attempting to understand the relationships between different cluster types can often seem daunting and on occasions perplexing. In order to aid the researchers' understanding of different cluster types, a very general approach has been adopted to make the connections between different building block types, archetypes and physical properties. This has been done by dividing the family of POMs into three domains:

1. The first general subset consists of *Heteropolyanionic* species which are metal-oxide species that are formed by incorporation of an oxoanion of another element, notable p- and d-block oxoanions such as PO_4^{3-}, SO_4^{2-}, SiO_4^{2-}, etc. As a result of the huge amount of structural variety possible from the various combinations of POM moieties with other fragments, this subgroup is by far the most explored subset of POM clusters. Archetypical examples of this category include Keggin $[XM_{12}O_{40}]^{n-}$, Dawson $[X_2M_{18}O_{62}]^{n-}$ and Anderson $[XM_6O_{24}]^{n-}$, see Fig. 2.
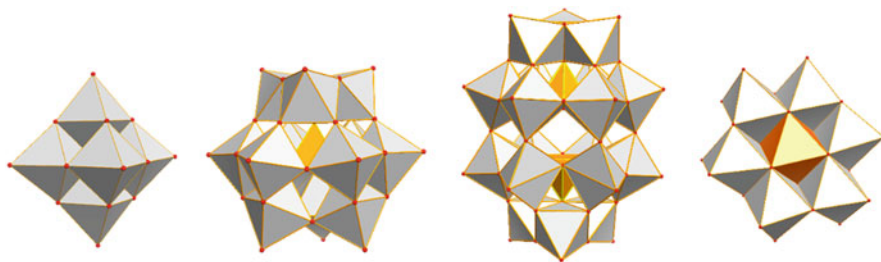

Fig. 2 Archetypical POM structures: left to right, Lindqvist, Keggin, Dawson and Anderson

2. *Isopolyanions* are metal-oxide frameworks lacking the addition of a heteroanion/heteroatom. For example, Lindqvist anions $[M_6O_{19}]^{n-}$ are part of this subset, as only one metal type is present in the framework. Subsequently, these clusters are often structurally less robust than their heteropolyanion counterparts [10]. However, they also exhibit interesting physical properties, such as high charges and strongly basic oxygen surfaces, which means that they are attractive units for use as building blocks [11].

3. *Molybdenum-blue* and *Molybdenum-brown* reduced Mo-based POM clusters are related to molybdenum blue type species, which was first reported by Scheele in 1783 [12]. Their composition was largely unknown until Müller et al. reported, in 1995, the synthesis and structural characterization of a very high nuclearity cluster $\{Mo_{154}\}$ crystallized from a solution of Mo-blue, which has a ring topology [13]. The interest generated by this result is partly due to its high nuclearity and partly because of the size of this cluster; with an outer diameter of ca. 34 Å, an inner diameter of 25 Å and with a thickness of 14 Å, it is a truly nanoscopic molecule. Using reaction conditions of pH ~1, with a concentration of Na_2MoO_4 of ca. 0.5 M and a degree of reduction of between 1 and 20%, the solution yields the 'Giant-Wheel' $[Mo_{154}O_{462}H_{14}(H_2O)_{70}]^{14-}$ in over 80% yield in 24 h [14]. The building up principle does not stop there, a series of mixed-valence Mo-blue (containing delocalized Mo^V-Mo^{VI}) clusters (e.g. $[Mo_{256}Eu_8O_{776}H_{20}(H_2O)_{162}]^{20-} \equiv \{Mo_{256}\}$) [15] have been reported as well as a class of spherical Mo-brown (containing localized Mo^V-Mo^V units) clusters (e.g. $[Mo^{VI}_{72}Mo^V_{60}O_{372}(MeCO_2)_{30}(H_2O)_{72}]^{42-} \equiv \{Mo_{132}\}$) [16] and the highest nuclearity cluster reported to date, a 'lemon'-shaped cluster $([H_xMo_{368}O_{1032}(H_2O)_{240}(SO_4)_{48}]^{48-} \equiv \{Mo_{368}\})$ [3], see Fig. 3.
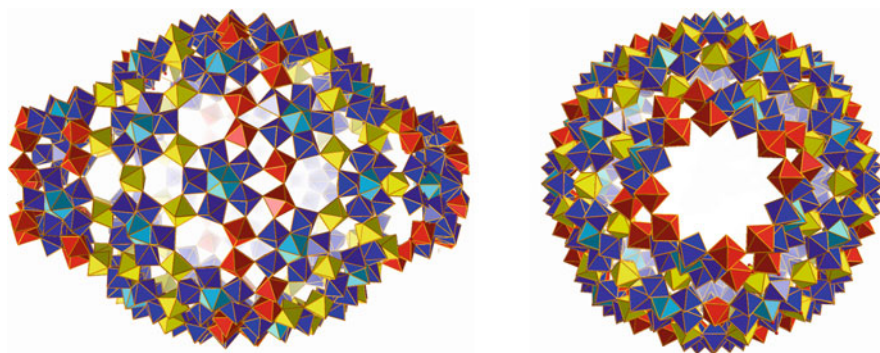

Fig. 3 Structure of the $\{Mo_{368}\} \equiv [H_xMo_{368}O_{1032}(H_2O)_{240}(SO_4)_{48}]^{48-}$ cluster shown with polyhedral plots. The transferable building blocks are highlighted in different colours according to the scheme: $\{Mo_1\}$ *yellow*, $\{Mo_2\}$ *red*, $\{(Mo)Mo_5\}$-pentagon *blue/cyan*

3 The Building Block Approach

At first sight, the synthesis of POMs species can often appear to be trivial, as reported POM-based studies frequently use ill-defined and vague terms such as 'one-pot' or self-assembly synthesis. The use of such terms evades discussing the complex nature and sequence of events that occur along the reaction pathway. Instead, it is common only to focus on the outcome, providing a false sense of simplicity and serendipitous nature of the underlying chemical events. Generally, the approach used in the synthesis of POMs requires in most cases just one step. This usually involves the acidification of a solution of molybdates, tungstates or vanadates leading to an initial condensation process forming low nuclearity metal-oxide species (primary BBs) which react to form larger architectures. This sequence of events is influenced by a variety of experimentally controlled variables, such as: (a) concentration/type of metal-oxide anion, (b) pH, (c) ionic strength, (d) heteroatom type/concentration, (e) presence of additional ligands, (f) reducing environment, (g) temperature and pressure of reaction (e.g. microwave, hydrothermal and refluxing), (h) counter-ion and metal-ion effect and (i) processing methodology (one-pot, non-equilibrium conditions). Careful consideration of the above experimental variables in combination with experimentally observed outcomes has not only led to the discoveries of new clusters and emergence of new functionalities but also to understanding the relationship between the starting materials (metallic salts of tungsten, molybdenum, etc.), the generated library of building blocks, the architecture of the isolable POM-based compounds and finally the potential functionality of the POM-based material. The realization and understanding of the first steps of building block formation is crucial for the further development of POM chemistry; the primary constituents of the reaction mixture as well as the isolated species could act as a set of transferable building blocks that can be reliably utilized in the formation of larger architectures and potentially give rise to new properties and finally new functional materials. The first key point at this stage is the use of reliable synthetic routes for the regeneration of previously observed synthons at sufficient concentration and utilize them for the construction of new architectures.

Considering the inherent difficulties in terms of understanding and controlling the assembly processes, researchers have based most of the work on known structural archetypes of this family of clusters. Members from each of the structural archetypes discussed above can then be further modified and functionalized to form derivative structures. For instance, removal of at least one metal centre from the above (*plenary*) structures forms *lacunary* anions. More specifically, lacunary species of the Keggin structure are obtained when one or more addenda atoms are removed along with their oxo ligands unshared with other addenda. In this manner, mono- [17], di- [18] or trilacunary [19] clusters have been isolated. These polyanions are fairly reactive and tend to fill these vacant positions with other addenda metals or a wide range of electrophiles capable of octahedral coordination.

The lacunary Keggin clusters can be prepared by two different routes. Firstly, they can be formed in solution by controlled hydrolysis of the parent Keggin

cluster. In monolacunary Keggin derivatives, an $[MO]^{4+}$ unit is removed by careful addition of base. This method was employed to isolate the first lacunary species. However, they can also be prepared more efficiently from solutions of simple addenda metal and heteroanion salts under strict pH control. More specifically, monolacunary clusters such as $[SiW_{11}O_{39}]^{8-}$ and trilacunary species such as $[SiW_9O_{34}]^{10-}$ are prepared in this manner whilst di-lacunary $[SiW_{10}O_{36}]^{8-}$ is obtained from the monolacunary precursor [20]. For example, the clusters $\{Ln_2As_3W_{29}\}$ and $\{(UO_2)_3As_3W_{29}\}$ result from the reaction of $\{XW_9\}$ lacunary anions where lanthanide anions are used as linkers. In another example, the anion $[Ln_2(H_2O)_7As_3W_{29}O_{103}]^{17-}$ (Ln^{III} = La, Ce) [21] contains three $\{AsW_9\}$ fragments bridged by two additional tungsten atoms and two Ln^{III} cations [22]. Clusters based on four linked $\{XW_9\}$ have also been identified. The cluster $[As_4W_{40}O_{140}]^{28-}$ [22] is a cyclic anion, being composed of four $\{\alpha-AsW_9\}$ units linked by additional tungsten atoms; the structure shown in Fig. 4 is a dicobalt derivative [19]. Derivatives of $[As_4W_{40}O_{140}]^{28-}$ have also been produced with lanthanide cations [22].

Following the same approach, Pope et al. have synthesized a massive heteropolytungstate anion which is a dodecamer of the $\{XW_9\}$ units, $[Ln_{16}As_{12}W_{148}O_{524}(H_2O)_{36}]^{76-}$ [23]. The 12 $\{XW_9\}$ units are linked by Ln^{III} cations (Ln = La, Ce, Nd, Sm) and additional tungsten atoms to produce a folded cyclic cluster with a D_{2d} idealized symmetry. The anion is completed by the four $\{W_5O_{18}\}$ lacunary fragments and the structure is shown in Fig. 5. This anion is extremely interesting and exhibits interesting topology and high nuclearity of metal ions.

In a similar manner, stable lacunary derivatives can be generated by Dawson or Lindqvist structures which can be used further as building blocks to construct larger

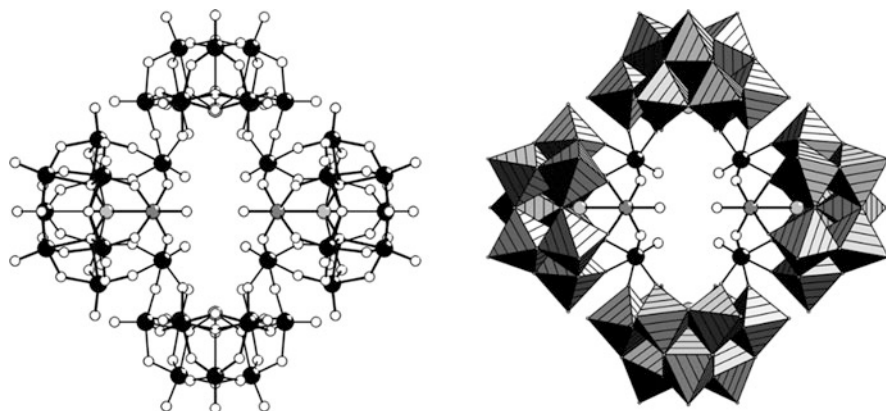**Fig. 4** The structure of the cyclic anion $[As_4W_{40}O_{140}]^{28-}$. A ball-and-stick representation is shown on the LHS and a polyhedral representation is shown on the RHS with the linking units shown in *ball* and *stick*. The W atoms are shown as *black spheres*, the As atoms as *grey spheres* and the O atoms as *white spheres*
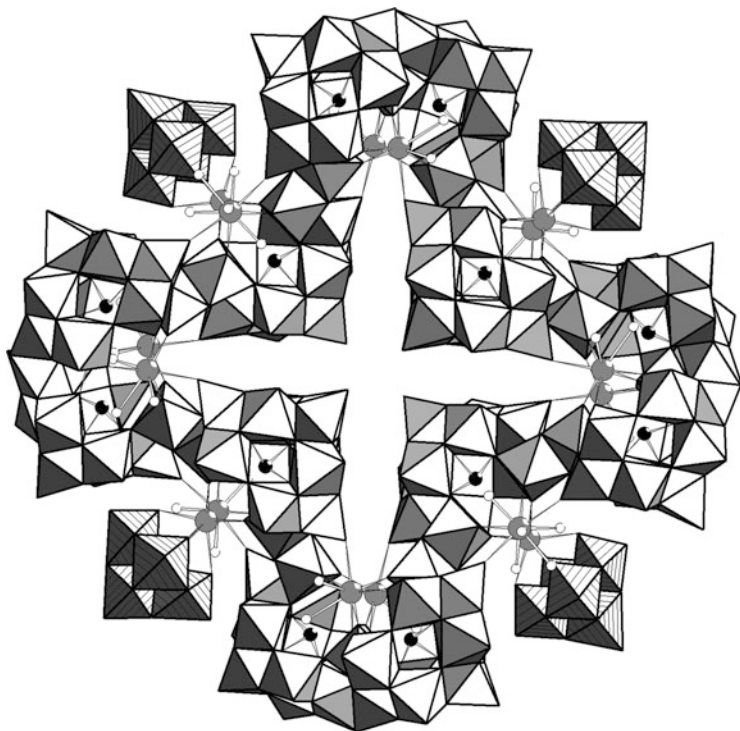
Fig. 5 Structure of the anion $[Ln_{16}As_{12}W_{148}O_{524}(H_2O)_{36}]^{76-}$ as a folded cyclic assembly of 12 {B-α-AsW$_9$} groups linked by additional W centres, all shown as polyhedral representations and four {LnW$_5$} groups. Ce(La) centres as *large grey spheres* and As centres as *small black spheres*. Finally, the water ligands are shown as *white spheres*

structures. The formation of lacunary Dawson clusters is driven by a controlled increase of the pH in solutions of the plenary cluster. Unlike the lacunary Keggins, the Dawson equivalents cannot be directly obtained from the condensation of the [MO$_6$] units and templating heteroanions. Mono-, di-, tri- and hexalacunary species have been isolated [24].

Many new compounds have been constructed recently using lacunary building units, which have been increasingly used as rigid inorganic ligands to stabilize multinuclear metallic cores that could significantly alter the overall functionality of the isolated material [25]. For example, Cronin et al. demonstrated successfully the stabilization of a multinuclear {Fe$_{12}$(OH)$_{18}$} core, utilizing the trivacant polyanion {α-P$_2$W$_{15}$O$_{56}$} and form an inorganic tetramer cluster [KFe$_{12}$(OH)$_{18}$(α-1,2,3-P$_2$W$_{15}$O$_{56}$)$_4$]$^{29-}$ [26]. Recently, a novel planar {Mn$_{19}$} magnetic cluster [Mn$_{19}$(OH)$_{12}$(SiW$_{10}$O$_{37}$)$_6$]$^{34-}$ have been isolated by Kortz et al. adopting a similar approach and utilization of the Keggin tungstosilicate lacunary fragment instead [27]. The planar {Mn$_{19}$(OH)$_{12}$}$^{26+}$ core is incorporated in the centre of six {SiW$_{10}$} fragments. Lately, our group developed this field further by combining the

stabilization effect offered from the lacunary fragments and redox process of the manganese centres (Mn^{II} to Mn^{III}) and reported an unprecedented Mn-mixed-valence architecture with the formula: $[Mn^{III}_2Mn^{II}_4(\mu_3\text{-O})_2(H_2O)_4(B\text{-}\beta\text{-}SiW_8O_{31})$ $(B\text{-}\beta\text{-}SiW_9O_{34})(\gamma\text{-}SiW_{10}O_{36})]^{18-}$ [28]. The in situ isomerization and partial reorganization of the starting lacunary $\{\gamma\text{-}SiW_{10}O_{36}\}$ species to $\{B\text{-}\beta\text{-}SiW_8O_{31}\}$ and $\{B\text{-}\beta\text{-}SiW_9O_{34}\}$ units led to the entrapment of a mixed-valence $\{Mn_5O_6\}$ cubane core, which is structurally relevant to the oxygen evolving centre of the biological photosystem II (PSII) (Fig. 6) [29]. These results demonstrate the vast possibilities and potential for the preparation of the many known multinuclear magnetic cores embedded within a POM framework where they can be finely tuned and magnetically isolated by altering their overall functionality. Furthermore, it is also possible following relatively simple synthetic procedures to prepare nanosized redox active assemblies using simple metal salts.

Many lacunary derivatives of the $\{P_2W_{18}\}$ cluster have been isolated. The two isomers of the monolacunary $\{\alpha\text{-}P_2W_{17}\}$ differ in the position of the vacancy. They are labelled as α_1 and α_2 for clusters where the vacancy is in a 'polar' position or in a 'belt' position, respectively [30]. The existence of $\{P_2W_{16}\}$ is still much debated yet the As analogue has been isolated [31]. Both α and β isomers have been isolated of the trilacunary derivative $\{P_2W_{15}\}$ [32]. In both cases, an entire polar triad is
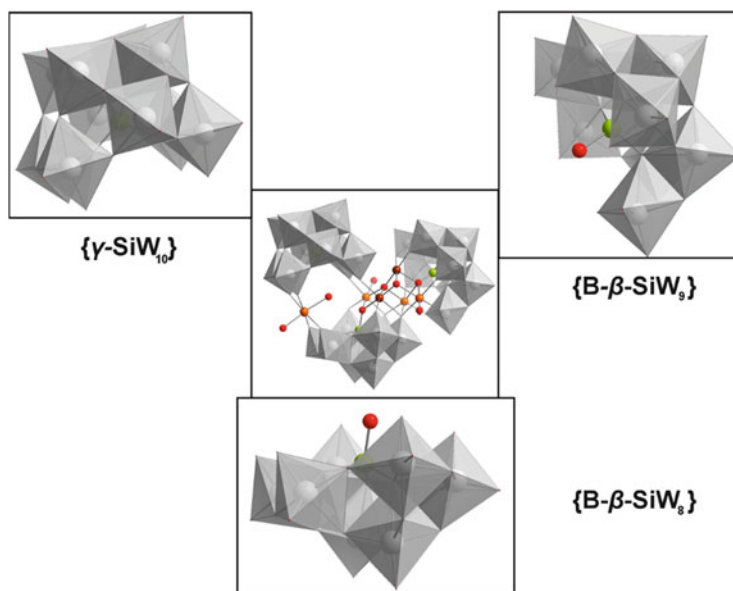
Fig. 6 Polyhedral/ball-and-stick representation of the $[Mn^{III}_2Mn^{II}_4(\mu_3\text{-O})_2(H_2O)_4(B\text{-}\beta\text{-}SiW_8O_{31})$ $(B\text{-}\beta\text{-}SiW_9O_{34})\text{-}(\gamma\text{-}SiW_{10}O_{36})]^{18-}$ anion, showing the three inequivalent silicotungstate Keggin fragments $\{SiW_8\}$, $\{SiW_9\}$ and $\{SiW_{10}\}$ and the $\{Mn_4O_4\}$ cubane core with an appended 'pendant' Mn ion very similar to that found in the structure of photosystem II (PSII). Colour code: WO_6, *grey polyhedral*; Mn^{III}, *red-brown spheres*; Mn^{II}, *orange spheres*; Si, *green spheres* and O, *red spheres*. Counter ions and solvent molecules have been omitted for clarity

removed to form a reactive heptadentate inorganic ligand. In the hexalacunary derivative, $\{\alpha\text{-}P_2W_{12}\}$, six adjacent addenda centres are removed from one side of the plenary cluster (see Fig. 7). Another highly relevant lacunary fragment based on the Wells–Dawson structure is the hexavacant $\{P_2W_{12}\}$. The structure of this cluster has been indirectly elucidated from elemental analysis and NMR spectroscopy. The occupation of the vacant positions by six Mo centres and the spectroscopic characterization of these heterometals have provided additional support for a 'boat-like' structure in $\{P_2W_{12}\}$. This lacunary fragment has proven to be an exceptional building block for the assembly of dimeric, trimeric and tetrameric structures. A cyclic tetrameric assembly of this hexalacunary fragment, $\{P_8W_{48}\}$, is also known [26].

The largest polyanion cluster isolated so far constructed using Dawson lacunary synthons, $[Mn^{III}_{40}P_{32}W^{VI}_{224}O_{888}]^{144-}$ ($\{Mn_{40}W_{224}\}$), is linked by Mn^{III} precursors and the hexavacant phosphotungstate $[a\text{-}H_2P_2W_{12}O_{48}]^{12-}$ ($\{P_2W_{12}\}$) [33]. The structure of $\{Mn_{40}W_{224}\}$ shows how different archetypal building blocks can be assembled via a network of Mn-O = W bridges (Fig. 8) into an unprecedented architecture. The core of the architecture is based on the $\{P_8W_{48}\}$ unit, which acts as scaffold for the organization of the remaining building blocks giving rise to the final structure. It is worth noting that the discussed synthetic approach is transferrable and can be extrapolated to a wide range of other POM architectures in principle, which demonstrates the exciting potential using a cluster-built-on-cluster design approach to expand the size of the POM clusters way beyond the current state of the art.

The obtained knowledge has prompted researchers to go a step further and adopt a synthetic approach which utilizes preformed POM clusters as a set of transferable building blocks that can be reliably used in the formation of new materials under controlled experimental conditions [11, 34]. A representative example of this effort is the utilization of the $[P_8W_{48}O_{184}]^{40-}$ ring-shaped macrocyclic POM cluster as building unit, with an integrated 1-nm pore as an 'aperture synthon', with manganese linkers yielding a vast three-dimensional extended framework architecture
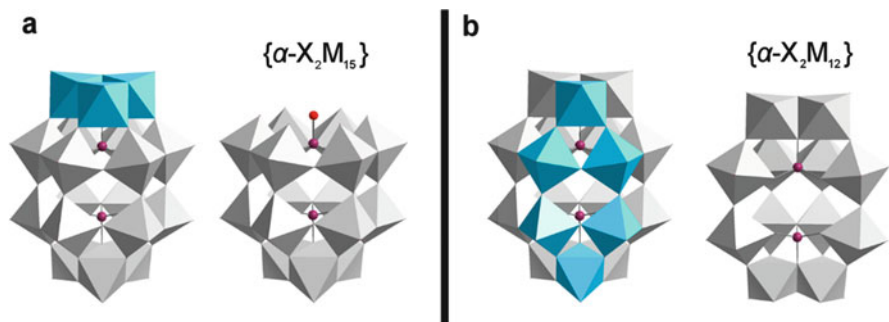

Fig. 7 Representation of the $\{\alpha\text{-}X_2M_{15}\}$ (**a**) and $\{\alpha\text{-}X_2M_{12}\}$ (**b**) lacunary isomers of the Wells–Dawson structure. Two representations of the plenary $\{\alpha\text{-}X_2M_{18}\}$ structures, which highlight the removed $[MO_6]$ octahedra, are included to the left of each lacunary fragment

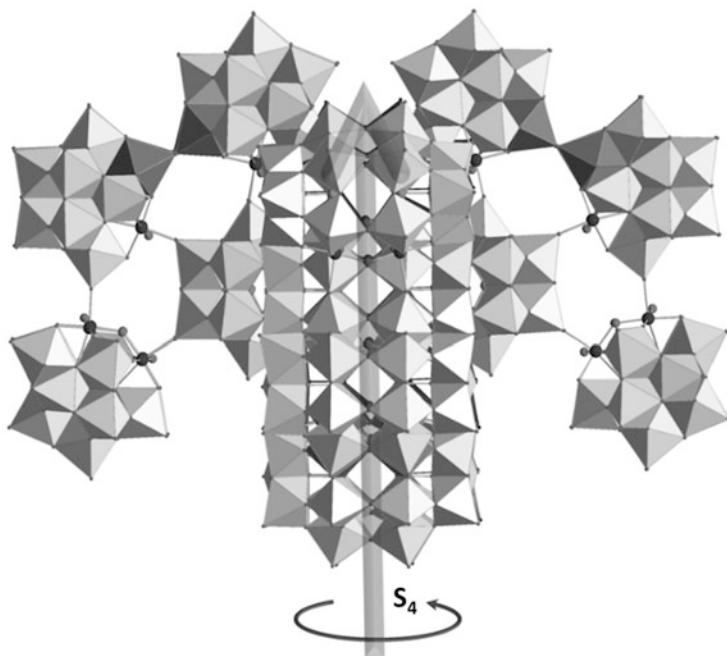**Fig. 8** Polyhedral representation of $[Mn^{III}_{40}P_{32}W^{VI}_{224}O_{888}]^{144-}$ shows that all the fragments are joined together through Mn^{III}-O = W bridges. The entire cluster adopts an idealized S_4 symmetry, with the principal axis coinciding with the fourfold axis of the central $\{P_8W_{48}\}$ wheel. The WO_6 units are shown in *light grey polyhedra* and the W/Mn disordered positions are in *dark grey polyhedra*. Counter ions and solvent molecules have been omitted for clarity

based on a truncated cuboctahedron (Fig. 13) [35]. The 1-nm-diameter entrance pores of the $\{P_8W_{48}\}$ structural building unit lead to approximately spherical 7.24 nm^3 cavities containing exchangeable alkali-metal cations that can be replaced by transition-metal ions through a cation exchange process (Fig. 9). The whole process can be controlled either via electrochemical switching of the overall framework charge by manipulating the oxidation state of the manganese linker ions or by physically gating the pores with large organic cations, thus demonstrating how metal–organic framework-like structures with integrated pores and new physical properties can be designed. In this way, cluster-based building blocks are assembled either through M-O-M′ oxo bridges or by the use of metal–organic complexes as linkers. However, the quest for deeper understanding of the assembly of POM-based chemical systems should not be confined by the predictability of a 'fully controlled' assembly process which could limit our horizons and minimize the chances of ground-breaking discoveries. The field of POMs is still expanding exponentially due to the obtained information in regard to the complex underlying chemistry which now can be better understood and controlled to an extent. The following sections will be devoted to discussing the similarities and differences observed in the closely related family of POTM clusters and the various synthetic
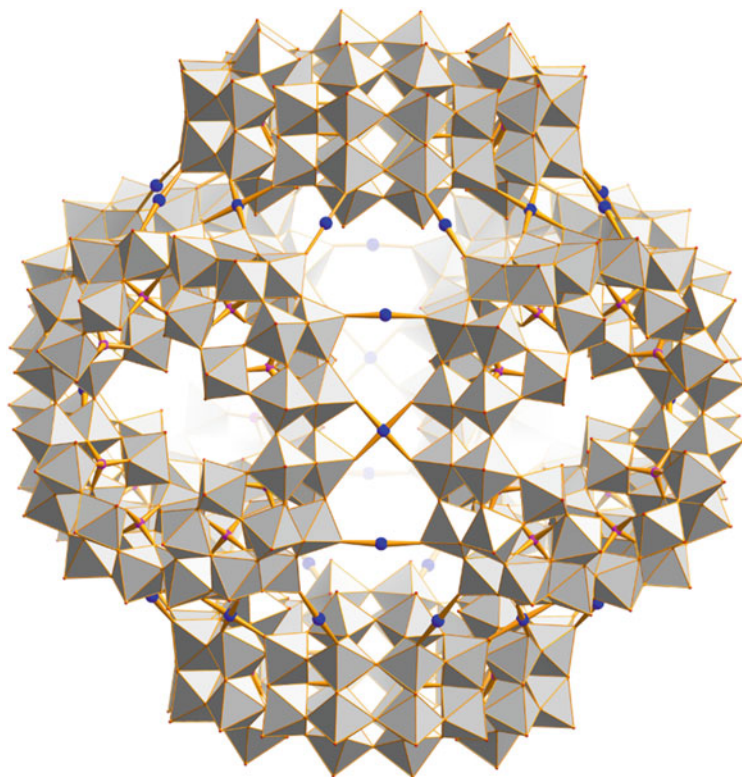
Fig. 9 Polyhedral representation of the face-directed assembly of the $[P_8W_{48}O_{184}]^{40-}$ molecular building unit, combined with electrophilic manganese linkers; colour code: WO_6, *grey polyhedra*, O, *red spheres*, Mn, *blue spheres* and P, *pink spheres*. Counterions and solvent molecules are omitted for clarity

methodologies which have been adopted in this case in order to improve our understanding and trigger a structural and information explosion similar to the one observed in POM chemistry.

4   Polyoxothiometalates

The transition-metal thioions of early transition metals have long been of interest due to their broad range of colours. In their highest oxidation state, V, Nb, Ta, Mo, W and Re form tetrahedral species that exhibit a plethora of interesting properties [36]. Initial investigation into thiometalates dates to the beginning of the nineteenth century where Berzelius noted their formation by passing H_2S gas into an aqueous solution for Mo_4^{2-} and WO_4^{2-}. However, it was not until the turn of the twentieth century that the true composition of these compounds was established. In contrast

to POMs, the chemistry of thiometalates remained a somewhat underexplored domain and only in the past 20 years has the field attracted the interest of researchers and shown signs of development [38]. Today, interest in thiometalates is due predominately to their implications in catalysis and bioinorganic chemistry because of the vital role of MoS_2 and WS_2 as catalysts for the hydrosulfurization, deoxygenation and denitrogenation of oil fractions [37]. In bioinorganic chemistry, their interest is directly related to their key role in molybdoenzymes [38]. Thus, the efforts to prepare appropriate synthetic models for the proper investigation of the active sites of molybdoenzymes led to the development of various sulfido and disulfido complexes; this group of clusters remains the most widely developed family of thiometalate compounds.

The introduction of sulphur in POM frameworks is expected to significantly modify the structural and electronic properties of POMs in an effort to develop complementary properties at the molecular level; such as the electrocatalytic function of the {M-S} core combined with the electron storage capacity of POMs. The study of the acidification of the basic thioanions $[MS_4]^{2-}$ (M = Mo, W) revealed that the condensation process of thiometalates is much more complex than oxometalates since it is systematically accompanied with intramolecular redox processes [39–43].

Different attempts to functionalize POMs by direct addition of sulphide by hydrogen sulphide failed because of facile and rapid reduction of the metallic framework and subsequent degradation into metal thio-species. However, the replacement of oxygen by sulphur has proved possible in less reducible POMs. Klemperer et al. reported the first example of a mixed Nb(Ta)-W Lindqvist $[W_5MO_{19}]^{3-}$ (M = Nb^v or Ta^v) succeeding to incorporate an M = S group and form the first thio-POM $[W_5MSO_{18}]^{3-}$. The methodology has successfully been transposed to the Keggin $\{PW_{11}MO_{40}\}^{4-}$ species allowing to isolate and characterize the first sulphur-containing Keggin derivative $[PW_{11}MSO_{39}]^{4-}$ [44]. In 1978, Müller et al. reported the novel $[(S_2)_2Mo(S_2)_2Mo(S_2)_2]^{2-}$ anionic complex and explicitly stated that S_2^{2-} anions can reduce Mo^{VI} to Mo^V and further form Mo–Mo bonds which may possibly lead to interesting magnetic properties [45]. Later, Müller and Sécheresse developed synthetic routes for the preparation of $[Mo_3S_4]^{4+}$ and $[Mo_2O_2S_2]^{2+}$ precursors, respectively. Similarly, Cohen and his co-workers reported the synthesis of $[W_2S_6]^{2-}$ based compounds in DMF instead of aqueous solution [46], whilst Sécheresse and co-workers adopted the preparation of the $[Mo_2O_2S_2]^{2+}$ building block from DMF and transferred it successfully to aqueous media (see Fig. 10) [47]. The $[Mo_3S_4]^{4+}$ cluster core belongs to the family of the general formula $\{M_3(\mu_3$-Q)$(\mu_2$-Q)$_3\}$ (Q = S, Se, Te) which contains a triangular metal cluster M_3 and four chalcogenide ligands (one μ_3-Q and three μ_2-Q). The previously reported pseudo-cuboidal fragment $[Mo_3S_4]^{4+}$ tends to form low nuclearity clusters. It can react with transition metals or noble metal ions to form dimeric structures [48, 49]. On the contrary, $[Mo_2O_2S_2]^{2+}$ proved to be a lot more versatile and chemically suitable to interact constructively with a variety of organic and inorganic ligands including POM-based species [50]. Thus, Sécheresse and Cadot set about the challenge to develop a synthesis for POTMs in water.
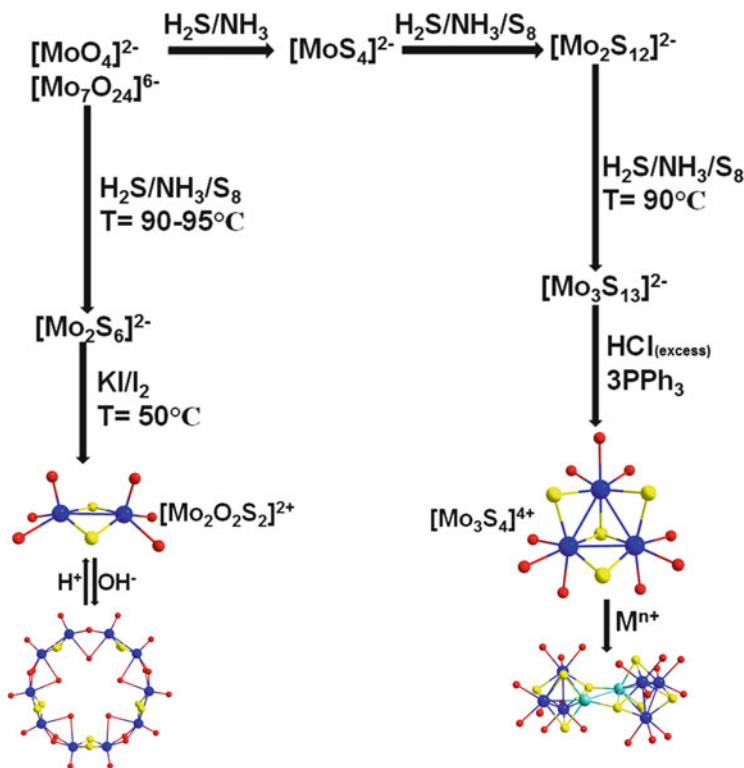
Fig. 10 Reaction pathways for the formation of the two archetypical electrophilic building blocks $[Mo_2O_2S_2]^{2+}$ and $[Mo_3S_4]^{4+}$

4.1 Fundamental Oxothiometalate Building Blocks

The choice of precursor for the core design of POTMs remains somewhat limited. For a precursor to be suitable, it should ideally display a reasonable degree of thermodynamic stability along the condensation process, an adapted electronic structure and its initial geometry should be suitable with respect to the target molecule. At present, there exist only two primary building block units for the synthesis of POTMs; these are the dimeric dication species $[M_2O_2S_2(H_2O)_6]^{2+}$, where M = Mo or W. The molybdenum (M = Mo) analogue of the dication has been most widely explored due to its ability to remain stable in aqueous medium. The $[Mo_2O_2S_2]^{2+}$ unit has acido-basic properties and polycondensation ability. The two Mo^V centres are equivalent and linked by a double sulfido bridge (Mo-S = 2.3 Å) with a metal–metal bond ($d(Mo^V \cdots Mo^V) = 2.8$ Å) improving the cohesion of the unit and leading to its excellent stability. The double sulfido bridges and the metal–metal bond confer to these building block specific coordination properties producing a unique class of compounds which are not observed with the full oxo analogue [51]. The coordination requirements are mainly restricted to the equatorial and axial

sites of the two equivalent Mo^V atoms leading to the highly predictable assembly. A common feature of this family of compounds is the ring-shaped topology, but the symmetry associated with the obtained structure is dependent on the geometry of the template, which gives rise to host–guest properties such as anion recognition and anion-templated synthesis. Additionally, the specific coordination ability and excellent stability of $[Mo_2O_2S_2]^{2+}$ make it superior to other oxothioanions.

The self-condensation of POTMs follows an opposite general trend to that observed in POM synthesis in terms of the pH range. Generally, the formation of POM species results from the acidification of a solution containing monomeric oxoanions $[MO_4]^{2-}$ (M = Mo, W). Conversely, the assembly of POTM species is triggered by addition of base which generates oleosis and oxoleosis products which can be spontaneously assembled further to larger architectures. It is worth noting that the self-condensation process is susceptible to the presence of structure directing agents (e.g. counter ions and metal ions) in a similar fashion to POM chemistry [51, 52].

Following these general reactivity and chemical behaviour trends, Cadot and co-workers have made great efforts to investigate the self-condensation process with and without templates (see Fig. 11). The first series of cyclic compounds, $[Mo^V_8S_8O_8(OH)_8(HMo^{VI}O_5(H_2O))]^{3-}$ = {Mo$_9$}, [53] $[I_2Mo_{10}S_{10}O_{10}(OH)_{10}(H_2O)_5]^{2-}$ = {Mo$_{10}$} [47] and $[Mo_{12}S_{12}O_{12}(OH)_{12}(H_2O)_6]$ = {Mo$_{12}$} [51], were obtained in the absence of templates at different pH values ranging from 5.0 to 2–3 and 1.5, respectively. Additionally, a gradual molecular growth has been indicated by a rational inter-conversion between {Mo$_{10}$} and {Mo$_{12}$} rings via self-rearrangement processes. The {Mo$_9$} ring is the first example of mixed valent POTMs where a monomeric oxoanion $[MO_4]^{2-}$ templates the formation of the ring [53]. The isolation of this cluster highlighted the potential of using organic templates of various lengths, flexibility and coordination ability to influence the self-condensation process of $[Mo_2O_2S_2]^{2+}$ units. Indeed, Cadot and co-workers using a templated synthesis approach have reported the constructive utilization of organic carboxylate ligands to template the self-condensation of $[Mo_2O_2S_2]^{2+}$ [54]. More specifically, a family of ring-shaped POTM clusters exhibiting a variety of nuclearities, shapes and symmetries have been synthesized and characterized as host–guest assemblies (see Fig. 12). The host–guest covalent and H-bond interactions [52, 55] between the fundamental building blocks $[Mo_2O_2S_2]^{2+}$ and polycarboxylate and (poly) phosphate ligands proved to be crucial for directing the self-condensation as well as defining the overall nuclearity of the obtained cluster. Another interesting feature of some members of this family is their ability to act as either anionic or cationic receptors depending on the pH value of the reaction mixture. For example, the addition of a strong base to the neutral inorganic ring $[Mo_{10}O_{10}S_{10}(OH)_{10}(H_2O)_5]$ in aqueous medium leads to partial deprotonation of the inner H_2O molecules and/or Mo-OH-Mo bridges. In the presence of Cs^+ cations, a reorganization occurs and a dianionic eight-membered ring capped by two Cs^+ cations with the formula $[Cs_2Mo_8O_8S_8(OH)_{10}(H_2O)] \cdot 33H_2O$ forms [56]. This class of compounds is mainly orchestrated by mutual adaptability between the host and guest components. To
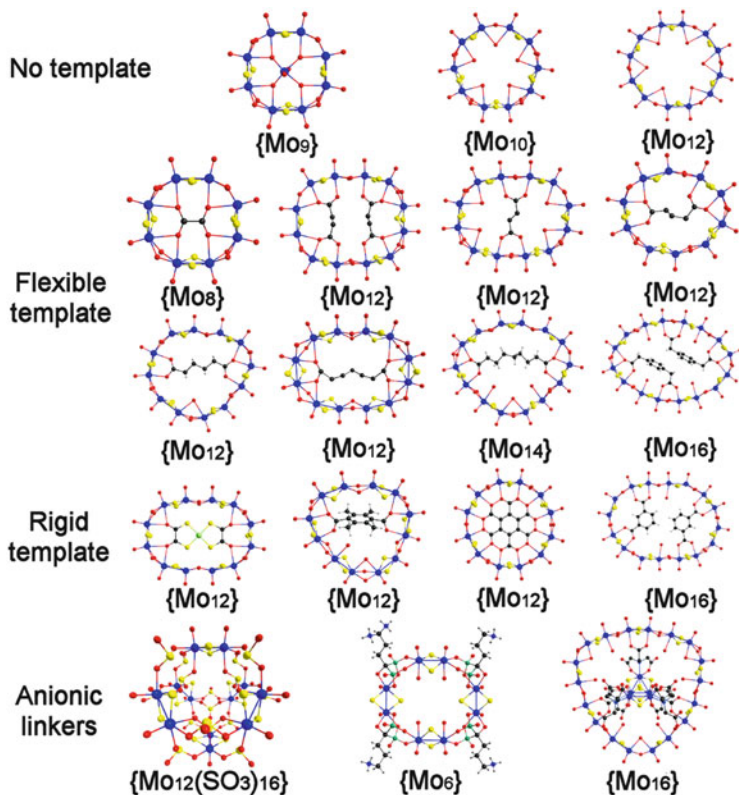
Fig. 11 Ball-and-stick representation of polyoxothiometalate (POTM) ring-shaped clusters templated by ligands or small clusters
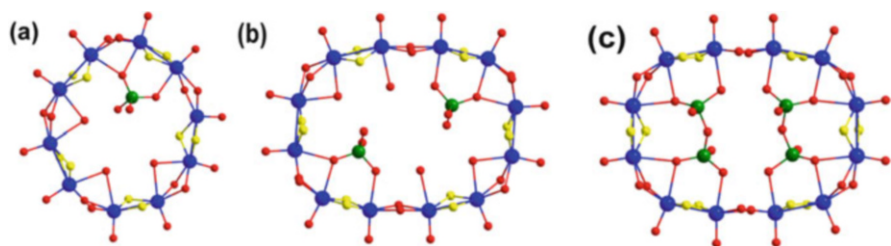
Fig. 12 Ball and stick representation of phosphate templated POTM rings: (**a**) [(H$_2$PO$_4$) Mo$_{10}$S$_{10}$O$_{10}$(OH)$_{11}$(H$_2$O)$_2$]2−; (**b**) [(H$_2$PO$_4$)$_2$Mo$_{12}$S$_{12}$O$_{12}$(OH)$_{12}$(H$_2$O)$_2$]4− and (**c**) [(P$_2$O$_7$)$_2$Mo$_{12}$S$_{12}$O$_{12}$(OH)$_{12}$]6−

date, the largest organic ligand templated macrocycle is an {Mo$_{18}$} cluster [57]. The fluxional behavior of the organic ligand templated rings has been investigated by NMR and identified the presence of conformational isomers in solution [58]. An interesting observation is that flexible organic ligands direct the assembly of

macrocycles with high flexibility, whilst rigid templates favour the formation of rings that have limited conformational transformations. Additionally, heteroanions can act as templates or linkers in a similar fashion. For example, phosphate anions can act as templates in the case of PO_3^{2-}, mono- and di-phosphato rings (see Fig. 12). When a single mono-protonated phosphate $[HPO_4]^{2-}$ anion was used, a decanuclear ring $\{Mo_{10}O_{10}S_{10}(OH)_{10}(HPO_4)\}$ was obtained. A dodecanuclear ring can also be formed containing two $[HPO_4]^{2-}$ or two $[P_2O_7]^{4-}$ anions [59].

An interesting deviation from the ring-shaped structural archetype was reported recently by Cadot and co-workers when they isolated two nanosized $\{Mo_{84}\}$ and Keplerate-type $\{Mo_{132}\}$ clusters, in concentrated acetate buffer (pH 3.6) solution (see Fig. 13) [60]. Müller et al. also employed the $[Mo_2O_2S_2]^{2+}$ fragment to combine $\{W_6O_{21}\}$ pentagonal building block in an effort to form the 'soft' analogue of a tungsten based Keplerate $\{W^{VI}_{72}Mo^V_{60}\}$ cluster [61]. The $\{Mo_{84}\}$ structure is quite interesting due to the fact that it incorporates a new triangular POTM building block $\{Mo_6S_6O_6(OH)\}^{5+}$. The $\{Mo_{84}\}$ molecular cube exhibits six open faces with the diameter ca. 9 Å. Interestingly, the cluster incorporates 24 outward-oriented acetate ligands which can be substituted by specific organic moieties, which paves the way for post-functionalization and design tailored for specific applications.
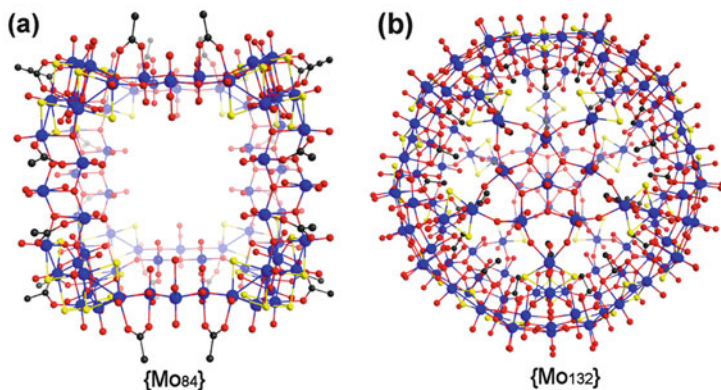
Fig. 13 (**a**) Representations of $[H_{32}Mo_{84}S_{48}O_{200}(AcO)_{24}]^{32-}$ which comprise two kinds of building blocks: $\{Mo^{VI}_3O_{11}\}^{4-}$ units forming the edges and $\{Mo_6S_6O_6(OH)\}^{5+}$ units located at the corners of the molecular cube; (**b**) representation of the sulphurated Keplerate-type anion $\{Mo_{132}\}$

4.2 Design of New Building Block Libraries

4.2.1 The Squarate Anion as Template

According to previously reported examples, hydrolytic condensation of the $\{Mo_2O_2S_2(H_2O)_6\}^{2+}$ cation produced a rich class of cyclic host–guest compounds, with the shape and size of the host cyclic rings being dependent on the size of flexible organic carboxylates [54]. However, this approach led to limited structural diversity due to the lack of a building block library of sufficient complexity. The only exception was the isolation of the nanosized $\{Mo_{84}\}$ molecular cube Fig. 13a, due to the generation of additional constituents, $\{Mo_6S_6O_6(OH)\}^{5+}$, that could be used for the construction of a larger structure. Intrigued by this observation, our group focused on the potential of generating a new and more diverse library of building blocks using a template of appropriate rigidity and symmetry. The choice of template candidate was the squarate anion which offers sufficient coordination sites whilst its planarity would introduce the appropriate rigidity necessary to stabilize the formation of new building blocks. Indeed, the first effort led to the generation of new building block which gave us the opportunity to isolate chiral clusters following a 'symmetry-breaking' strategy (Fig. 14).

More specifically, we showed how this symmetry breaking is manifested in a stepwise manner from $(NMe_4)_4[(Mo_2S_2O_2)_7(OH)_{14}(C_4O_4)_2(H_2O)_2]\cdot13H_2O$ $\{Mo_{14}\}$, **1** a planar molecule, to $K_8[(Mo_2S_2O_2)_6(OH)_8(C_4O_4)_2(Mo_2O_8)_2(H_2O)_4]\cdot$ $15H_2O$ $\{Mo_{16}\}$, **2** a non-planar molecule formed by the addition of $\{Mo_2O_8\}$ anions into the system and finally to $KH[NMe_4]_2[(Mo_2S_2O_2)_4(OH)_6(Mo_2O_8)(C_4O_4)]\cdot$ $10H_2O$ $\{Mo_{10}\}$, a chiral ring-shaped structure. Furthermore, it is possible to isolate the non-chiral version of the **3a** ring, **3b**, which contains a mirror plane within the ring (see Figs. 15 and 16) [62].

4.2.2 The Role of the Lindqvist-Based Building Unit $[Mo_5O_{18}]^{6-}$

Following on from the identification of the above compounds, the building blocks A and B have been utilized to synthesize an array of new compounds with unprecedented architectures and in doing so, the additional building block C ($[Mo_5O_{18}]^{6-}$, Fig. 17, centre) has been identified [63]. C is an isomer of the lacunary Lindqvist
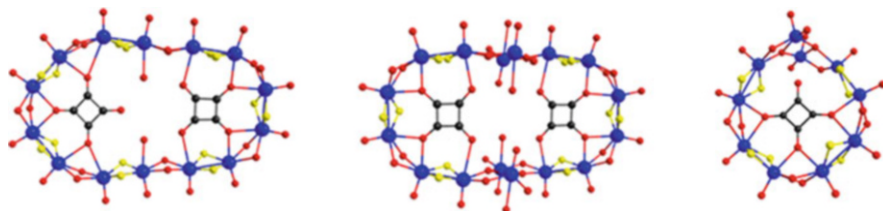
Fig. 14 *Left* – $\{Mo_{14}\}$; *middle* – $\{Mo_{16}\}$ and *right* – $\{Mo_{10}\}$ chiral
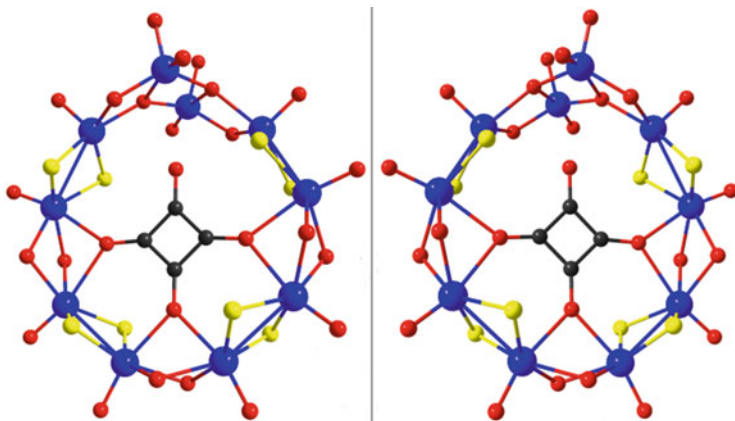
Fig. 15 The absolute configurations of the left- and right-handed {Mo_{10}} clusters. This is a very interesting observation because even though the structural features of this series of clusters did not deviate from the ring-shaped topology, it was possible to generate new building blocks with increased complexity, leading to the manifestation of spontaneous chiral resolution and control of the interaction of the available constituents
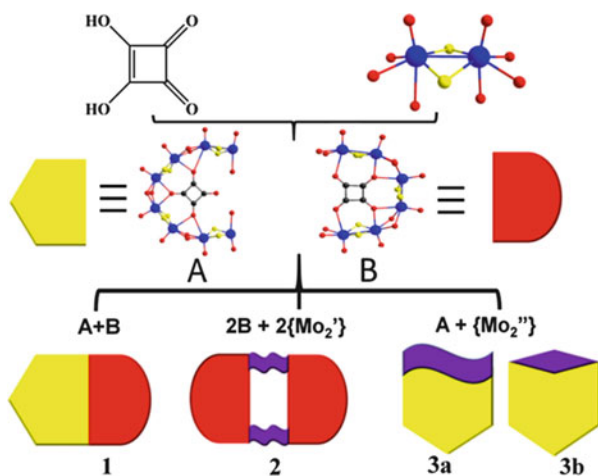
Fig. 16 Schematic representation of the new virtual building blocks A and B, and the constructive interaction for the construction of new species

anion which acts as a linking unit in these structures. Compared with the configuration of the traditional [Mo_5O_{18}]$^{6-}$, the coordination environment of the Mo^{VI} atom is greatly distorted which directly influences coordination mode considering the structural deviation from the traditional lacunary anion. The distortion leads to the active oxygen coordination atoms of the [Mo_5O_{18}]$^{6-}$ anion pointing further outwards, decreasing the steric hindrance, and allowing the subunit
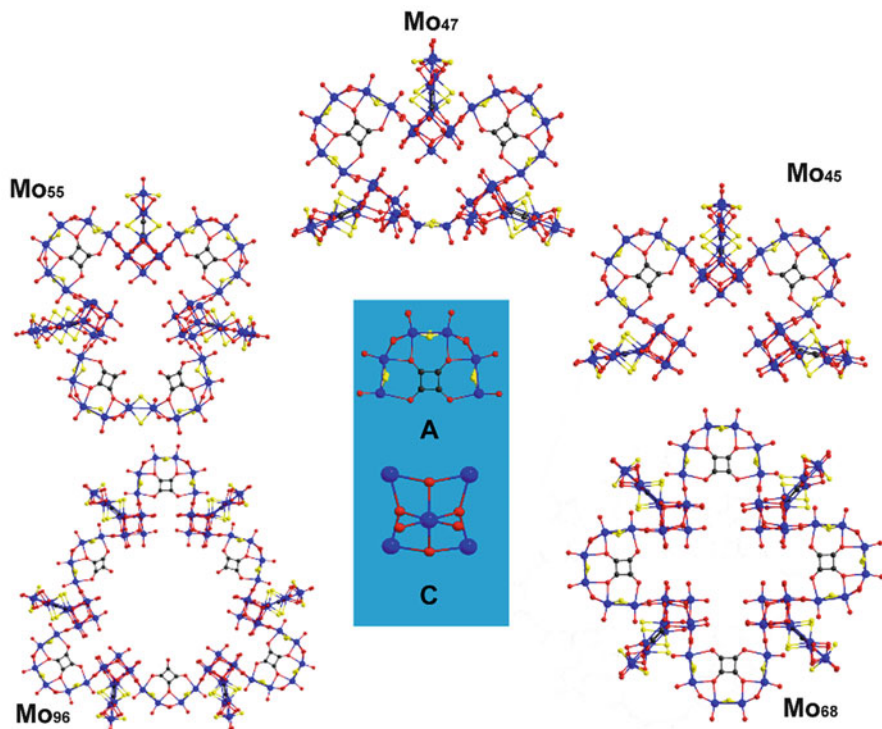
Fig. 17 Ball-and-stick representation of the new family of nanosized clusters and representation of the pentagonal common building blocks (Mo: *blue*, S: *yellow* and O: *red*)

$[(Mo_2O_2S_2)_3(OH)_4(C_4O_4)]$ to coordinate to the $[Mo_5O_{18}]^{6-}$ anion via Mo–O bonds (2.05(6)–2.49(5) Å). More specifically, the unit has three distinct sites to which A and B can bind: two of which are coplanar and are located on the exterior of the molecules, whilst the third, which is perpendicular to the others, resides on the inner surface. A, B and C can interact in several ways, with sequentially increasing size as more building blocks are incorporated, as shown in Fig. 17. The key points from the synthetic chemists point of view are that self-assembly can be directed by specifying the parameters such as pH, ratio of starting material and counter cation, and that molecular growth is facilitated by both fast self-condensation and subsequent increase in reactivity at certain regions of the clusters' periphery.

It is worth noting that the {Mo$_{96}$} cluster is the largest POTM reported to date that possesses a D_{3h} symmetry and incorporates three building blocks: $[Mo_5O_{18}]^{6-}$, $[(Mo_2O_2S_2)_3(OH)_4(C_4O_4)]$ and $[(Mo_2O_2S_2)_2(OH)_2(C_4O_4)]$, which assemble in an alternating orthogonal arrangement. Additionally, the molecule exhibits a 1.7-nm cavity; Fig. 18 shows the packing structure of {Mo$_{96}$}-wheel viewed along the *a*-axis, where the {Mo$_{96}$}-wheels are overlapped with respect to each other, forming an interdigitated molecular arrangement within the crystallographic *ab*-plane.
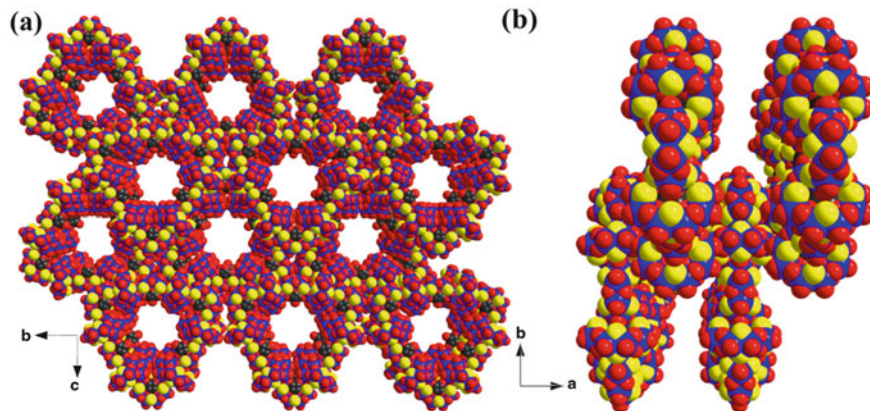
Fig. 18 (**a**) View along crystallograhic α-axis of the nanosized {Mo_{96}} cluster's packing structure; (**b**) Interdigitated molecular arrangement within crystallographic *ab*-plane

4.2.3 The Role of the Elusive Pentagonal Building Unit {Mo(Mo$_5$)}

It has been widely reported that lacunary POMs can be linked by transition metals into extended giant clusters and even high dimensional frameworks. However, such self-assembly systems are, to some extent, out of control because of the versatile coordination modes and configurations available to transition metals. For complex systems, using well-defined precursors to induce self-condensation into giant clusters has indubitable advantages for the study of self-assembly mechanisms. Interestingly, Müller and co-workers developed synthetic approaches based on libraries of virtual building blocks that allow target-driven self-assembly via the expression of the appropriate/necessary constituents for all possible components, resulting in high yield syntheses of inorganic superfullerenes and giant ring-shaped, electron-rich, mixed-valence polyoxomolybdates under appropriate conditions [64–66].

To date, there are only a few examples of lacunary POMs that have been used constructively in POTM chemistry for the construction of new topologies. Recently our group reported the first system that combines successfully the newly discovered POTM building block {$(Mo_2O_2S_2)_3(OH)_4(C_4O_4)$} with the elusive virtual lacunary POM fragment – pentagonal {$Mo^{VI}(Mo^{VI}_5)$} which has been described, as the fundamental component for the generation of a family of nanosized POTM–POM clusters (see Fig. 19). The {$(Mo_2O_2S_2)_3(OH)_4(C_4O_4)$} building block has unsaturated Mo^V centres resulting in a positively charged unit, which is susceptible to nucleophilic attack by the negatively charged pentagonal unit to generate a novel intriguing family of thiometalate 'butterfly-shaped' clusters, $(N(CH_3)_4)_3K_{11.5}Na_{0.5}[(Mo_2O_2S_2)_3(C_4O_4)$ $(OH)_4]_6(OH)_2[Mo^{VI}_6O_{21}(H_2O)]_2I\cdot19H_2O$ {**Mo$_{48}$**}. $[N(CH_3)_4]_3K_{11}[(Mo_2S_2O_2)_3(C_4O_4)$ $(OH)_4]_6(OH)_2[Mo^{VI}_6O_{21}(DMF)]_2\cdot2DMF\cdot33H_2O$ {**Mo$_{48}$**}, $[N(CH_3)_4]_4K_{18}[(Mo_2O_2S_2)_3(C_4O_4)(OH)_4]_6(OH)_2(Mo^{VI}_6O_{21}(H_2O))_2[Mo^{VI}_{12}O_{36}(C_4O_4)_4]\cdot$ $79H_2O$ {**Mo$_{60}$**} and $K_{16}[(Mo_2O_2S_2)_3(C_4O_4)(OH)_4]_4(Mo^{VI}_5O_{19}(H_2O)_2)_2\cdot42H_2O$, {**Mo$_{34}$**} (see Fig. 20).
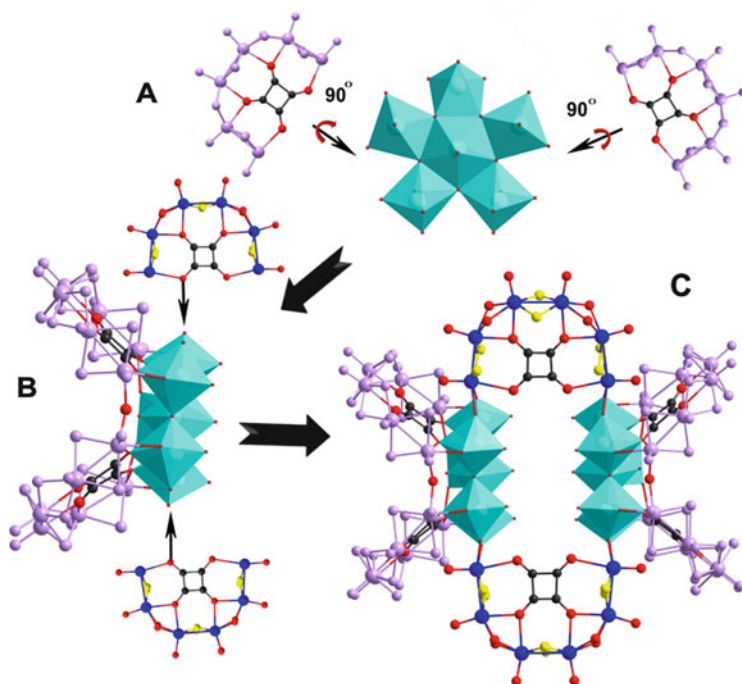
Fig. 19 Representation of the stepwise trapping of pentagonal {Mo$_6$} assemblies in POTM systems: Two building blocks [(Mo$_2$O$_2$S$_2$)$_3$(OH)$_4$(C$_4$O$_4$)] (*light violet*) rotate 90° to coordinate to the pentagonal unit via Mo–O bonds to form unit B and then two more [(Mo$_2$O$_2$S$_2$)$_3$(OH)$_4$(C$_4$O$_4$)] link two B units to construct the {Mo$_{48}$} (C) (pentagonal unit {Mo (Mo$_5$)}: *cyan polyhedra*; ball-and-stick representation for C: *black*; Mo^V: *blue*; S: *yellow* and O: *red*)

4.2.4 The Role of the SeO$_3^{2-}$ as Template and Linker

The family of small and flexible XO$_3^{2-}$ (X = S or Se) anions with pyramidal geometry was envisaged as very promising template candidates and assembly directing agents due to the numerous coordination modes and their lone pair of electrons which can potentially induce interesting electronic properties. The combination of structurally diverse POM synthons and tuneable chalcogen-based ones could give rise to unprecedented architectures and the emergence of unique properties. Indeed, our group investigated recently the potential variation induced by the generation of novel synthons (POM and POTM building block libraries) and demonstrated the effect of non-conventional heteroanions on the self-assembly processes and final structural motifs in thiometalate chemistry. The selenite anion template revealed a variety of coordination modes leading to the generation of different building blocks. Additionally, the SeO$_3^{2-}$ anion proved to be a highly diverse unit since it can act as template as well as a linker. The SeO$_3^{2-}$ anion
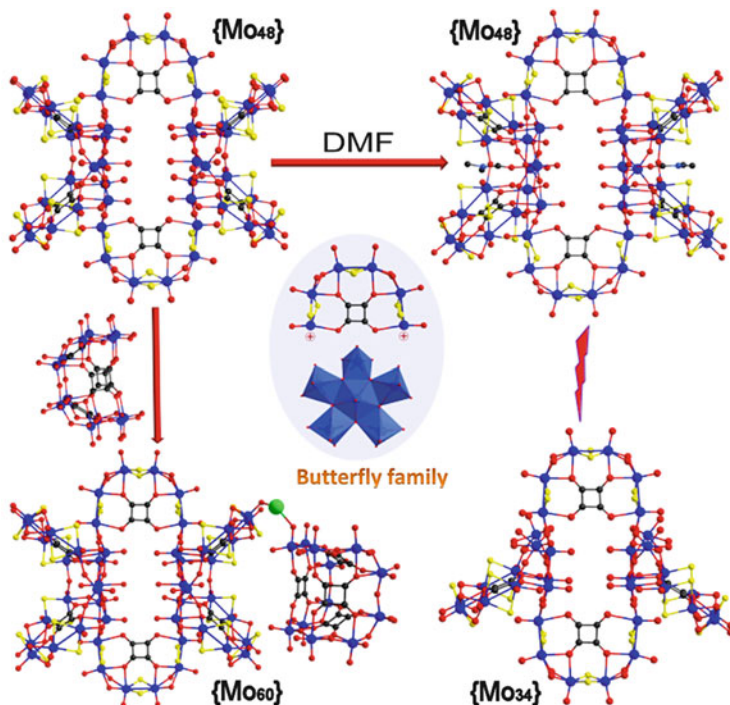
Fig. 20 Ball-and-stick representation of the 'butterfly' family; all the family members are based on the same building block library
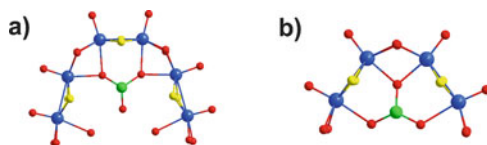
Fig. 21 SeO_3^{2-} templated POTM subunits (**a**) $[(Mo_2O_2S_2)_3(OH)_4(SeO_3)]$ and (**b**) $[(Mo_2O_2S_2)_2(OH)_2(SeO_3)]$

templates the self-condensation of $[Mo_2O_2S_2]^{2+}$ units giving two types of subunits $[(Mo_2O_2S_2)_3(OH)_4(SeO_3)]$ and $[(Mo_2O_2S_2)_2(OH)(SeO_3)]^+$, depending on the coordination mode of selenite anions (Fig. 21).

Investigation of the parameter space of the $\{Mo_2O_2S_2\}/XO_3^{2-}$ system and constructive use of the new building blocks led to the formation of new family of nanosized clusters with high nuclearities ranging from $\{Mo_8\}$ to $\{Mo_{36}\}$ and diverse architectures Fig. 22 [67, 68].
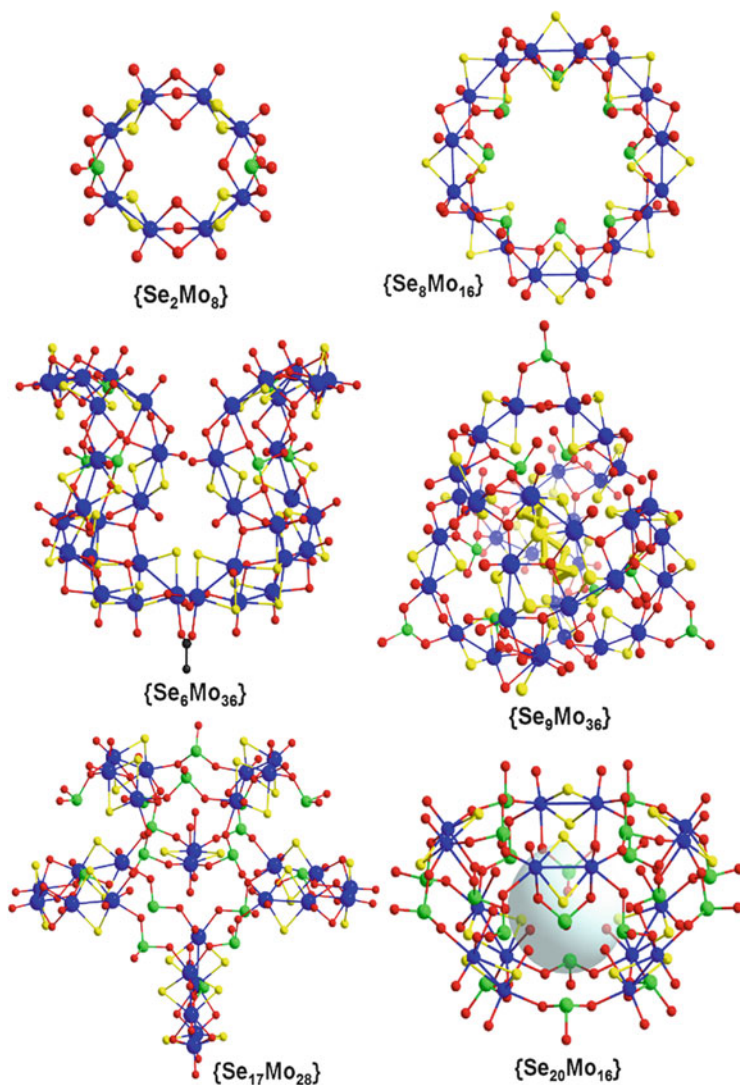
Fig. 22 Ball-and-stick representation of the SeO_3^{2-} templated POTMs family of six clusters with varying Mo: chalcogen ratios

5 Conclusions and Perspectives

The vast development in the field of POTM chemistry is in part due to recent synthetic approaches adopted by researchers. More specifically, the assembly of the fundamental $[Mo_2O_2S_2]^{2+}$ building block using templates of different rigidity and coordination ability led to the generation of new and more complex building block

libraries. The use of squarate anions as the template led to the formation of building blocks, e.g. $[(Mo_2O_2S_2)_3(OH)_4(C_4O_4)]$, able to retain their structural integrity over a wide range of pH values and used constructively for the construction of nanosized clusters with architectures which deviate from the archetypical ring-shaped topology. Also, it was shown that the building block libraries can be further diversified by the in situ generation of virtual building blocks observed in POM chemistry such as $[Mo_5O_{18}]^{6-}$ and the pentagonal $[Mo_6O_{21}]^{12-}$ observed mainly in Mo-Blue chemistry but have never been identified and regenerated in POTM systems. In a similar manner, the assembly of $[Mo_2O_2S_2]^{2+}$ units was influenced by the presence of the SeO_3^{2-} anion in a different way due to the flexibility, geometry and multiple coordination modes of the selenite anions. The coordination ability differs to organic carboxylate ligands, as the small size of the selenite anion acts as template as well as linker. This led to the formation of a fundamentally new building block library which was used for the construction of species with unprecedented topologies.

The POTM family is proved to be governed by similar selection rules which drive the assembly of the available constituents, with the only exception being the range of pH values where this condensation takes place. However, the field did not expand as rapidly as their POMs relatives. We showed that this bottleneck was mainly due to the fact that there was no available building block library of high enough diversity which will allow the system to 'evolve' from the ring-shaped topology and limited range of nuclearities to unprecedented architectures of increased complexity and nuclearities ranging from 16 to 96 metal centres. The above realization reveals an opportunity for further development of the oxothiometalate chemistry based upon the building block ideas discussed above; using these ideas, it should be possible to work towards designer nanomolecules of ever increasing size and complexity. Such clusters, for instance, are being proposed for the design of catalysts and molecule-based devices that could be used in molecular electronics. Potentially such systems could be used to probe the behaviour and even discover new physics in relation to the 2D metal chalcogenides or understand better the molecular growth processes. We are confident that the observed structural explosion in the area of POMs and recently in oxothiometalates will pave the way for the design and engineering of supramolecular systems with unprecedented properties and functionalities.

References

1. Pope MT, Müller A (1991) Polyoxometalate chemistry: an old field with new dimensions in several disciplines. Angew Chem Int Ed Engl 30:34–48
2. Long D-L, Tsunashima R, Cronin L (2010) Polyoxometalates building blocks for functional nanoscale systems. Angew Chem Int Ed Engl 49:1736–1758
3. Müller A, Beckmann E, Bögge H, Schmidtmann M, Dress A (2002) Inorganic chemistry goes protein size: a Mo_{368} nano-hedgehog initiating nanochemistry by symmetry breaking. Angew Chem Int Ed 41:1162–1167

4. Long D-L, Burkholder E, Cronin L (2006) Polyoxometalate clusters, nanostructures and materials: from self assembly to designer materials and devices. Chem Soc Rev 36:105–121

5. Hasenknopf B (2005) Polyoxometalates: introduction to a class of inorganic compounds and their biomedical applications. Front Biosci J Virtual Libr 10:275–287

6. Keggin JF (1934) The structure and formula of 12-phosphotungstic acid. Proc R Soc Lond Ser A 144:75–100

7. Hill CL (1998) Introduction: polyoxometalates multicomponent molecular vehicles to probe fundamental issues and practical problems. Chem Rev 98:1–2

8. Rosnes MH, Yvon C, Long D-L, Cronin L (2012) Mapping the synthesis of low nuclearity polyoxometalates from octamolybdates to Mn-Anderson clusters. Dalton Trans 41:10071–10079

9. Miras HN, Yan J, Long D-L, Cronin L (2012) Engineering polyoxometalates with emergent properties. Chem Soc Rev 41:7403–7430

10. Long D-L, Kögerler P, Farrugia LJ, Cronin L (2003) Restraining symmetry in the formation of small polyoxomolybdates: building blocks of unprecedented topology resulting from "shrink-wrapping" $[H_2Mo_{16}O_{52}]^{10-}$-type clusters. Angew Chem Int Ed 42:4180–4183

11. Long D-L, Cronin L (2006) Towards polyoxometalate-integrated nanosystems. Chem Eur J 12:3698–3706

12. Scheele CW (1971) In: Werke DSF, Hermbstädt M (eds) Sämtliche physische und chemische, vol 1. Sändig oHG, Niederwalluf/Wiesbaden, pp 185–200

13. Müller A, Krickemeyer E, Meyer J, Bögge H, Peters F, Plass W, Diemann E, Dillinger S, Nonnenbruch F, Randerath M, Menke C (1995) $[Mo_{154}(NO)_{14}O_{420}(OH)_{28}(H_2O)_{70}]^{(25\pm5)-}$: a water-soluble big wheel with more than 700 atoms and a relative molecular mass of about 24000. Angew Chem Int Ed Engl 34:2122–2124

14. Cronin L, Diemann E, Müller A (2003) Polyoxomolybdate clusters: nanoscopic wheels and balls. In: Woollins JD (ed) Inorganic experiments. Wiley-VCH, Weinheim, pp 340–346

15. Cronin L, Beugholt C, Krickemeyer E, Schmidtmann M, Bögge H, Kögerler P, Luong TKK, Müller A (2002) "Molecular symmetry breakers" generating metal-oxide-based nanoobject fragments as synthons for complex structures: $[\{Mo_{128}Eu_4O_{388}H_{10}(H_2O)_{81}\}_2]^{20-}$, a giant-cluster dimer. Angew Chem Int Ed 41:2805–2808

16. Müller A, Das SK, Talismanov S, Roy S, Beckmann E, Bögge H, Schmidtmann M, Merca A, Berkle A, Allouche L, Zhou Y, Zhang L (2003) Trapping cations in specific positions in tuneable "artificial cell" channels: new nanochemistry perspectives. Angew Chem Int Ed 42:5039–5044

17. Radkov E, Beer RH (1995) High yield synthesis of mixed-metal keggin polyoxoanions in non-aqueous solvents: preparation of (n-Bu$_4$N)$_4$[PMW$_{11}$O$_{40}$] (M = V, Nb, Ta). Polyhedron 14:2139–2143

18. Canny J, Teze A, Thouvenot R, Herve G (1986) Disubstituted tungstosilicates. 1. Synthesis, stability, and structure of the lacunary precursor polyanion of a tungstosilicate γ-SiW$_{10}$O$_{36}^{8-}$. Inorg Chem 25:2114–2119

19. Herve G, Teze A (1977) Study of α- and β-enneatungstosilicates and -germanates. Inorg Chem 16:2115–2117

20. Tézé A, Hervé G (1990) Inorganic syntheses. Wiley, New York

21. Wassermann K, Pope MT (2001) Large cluster formation through multiple substitution with lanthanide cations (La, Ce, Nd, Sm, Eu, and Gd) of the polyoxoanion $[(B-\alpha-AsO_3W_9O_{30})_4(WO_2)_4]^{28-}$. Synthesis and structural characterization. Inorg Chem 40:2763–2768

22. Müller A, Peters F, Pope MT, Gatteschi D (1998) Polyoxometalates: very large clustersnanoscale magnets. Chem Rev 98:239–272

23. Wassermann K, Dickman MH, Pope MT (1997) Self-assembly of supramolecular polyoxometalates: the compact, water-soluble heteropolytungstate anion $[As_{12}^{III}Ce_{16}^{III}(H_2O)_{36}W_{148}O_{524}]^{76-}$. Angew Chem Int Ed Engl 36:1445–1448

24. Contant R (1990) Inorganic syntheses. Wiley, New York

25. Ibrahim M, Lan Y, Bassil BS, Xiang Y, Suchopar A, Powell AK, Kortz U (2011) Hexadecacobalt(II)-containing polyoxometalate-based single-molecule magnet. Angew Chem Int Ed 50:4708–4711

26. Pradeep CP, Long D-L, Kögerler P, Cronin L (2007) Controlled assembly and solution observation of a 2.6 nm polyoxometalate "super" tetrahedron cluster: $[KFe_{12}(OH)_{18}(\alpha-1,2,3-P_2W_{15}O_{56})_4]^{29-}$. Chem Commun 2007:4254–4256

27. Bassil BS, Ibrahim M, Al-Oweini R, Asano M, Wang Z, van Tol J, Dalal NS, Choi K-Y, Ngo Biboum R, Keita B, Nadjo L, Kortz U (2011) A planar $\{Mn_{19}(OH)_{12}\}^{26+}$ unit incorporated in a 60-tungsto-6-silicate polyanion. Angew Chem Int Ed 50:5961–5964

28. Mitchell SG, Molina PI, Khanra S, Miras HN, Prescimone A, Cooper GJT, Winter RS, Brechin EK, Long D-L, Cogdell RJ, Cronin L (2011) A mixed-valence manganese cubane trapped by inequivalent trilacunary polyoxometalate ligands. Angew Chem Int Ed Engl 50:9154–9157

29. Brudvig GW (2008) Preface. Coord Chem Rev 252:231

30. Jorris TL, Kozik M, Casan-Pastor N, Domaille PJ, Finke RG, Miller WK, Baker LCW (1987) Effects of paramagnetic and diamagnetic transition-metal monosubstitutions on tungsten-183 and phosphorus-31 NMR spectra for Keggin and Wells-Dawson heteropolytungstate derivatives. Correlations and corrections. Tungsten-183 NMR two-dimensional INADEQUATE studies of $\alpha-[(D_2O)ZnO_4X^{n+}W_{11}O_{34}]^{(10-n)-}$ wherein $X^{n+} = Si^{4+}$ and P^{5+}. J Am Chem Soc 109:7402–7408

31. Contant R, Thouvenot R (1991) Hétéropolyanions de type Dawson. 2. Synthèses de polyoxotungstoarsénates lacunaires dérivant de l'octadécatungstodiarsénate. Étude structurale par RMN du tungstène-183 des octadéca(molybdotungstovanado)diarsénates apparentés. Can J Chem 69:1498–1506

32. Finke RG, Droege MW, Domaille PJ (1987) Trivacant heteropolytungstate derivatives. 3. Rational syntheses, characterization, two-dimensional tungsten-183 NMR, and properties of tungstometallophosphates $P_2W_{18}M_4(H_2O)_2O_{68}^{10-}$ and $P_4W_{30}M_4(H_2O)_2O_{112}^{16-}$ (M = cobalt, copper, zinc). Inorg Chem 26:3886–3896

33. Fang X, Kögerler P, Furukawa Y, Speldrich M, Luban M (2011) Molecular growth of a core-shell polyoxometalate. Angew Chem Int Ed Engl 50:5212–5216

34. Kögerler P, Cronin L (2005) Polyoxometalate nanostructures, superclusters, and colloids: from functional clusters to chemical aesthetics. Angew Chem Int Ed 44:844–846

35. Mitchell SG, Streb C, Miras HN, Boyd T, Long D-L, Cronin L (2010) Face-directed self-assembly of an electronically active Archimedean polyoxometalate architecture. Nat Chem 2:308–312

36. Müller A, Diemann E, Jostes R, Bögge H (1981) Transition metal thiometalates: properties and significance in complex and bioinorganic chemistry. Angew Chem Int Ed Engl 20:934–955

37. Ripperger W (1974) Sulphide catalysts, their properties and applications. Von O. Weisser U. S. Landa. Friedr. Vieweg & Sohn, Braunschweig, und Pergamon Press, Oxford – New York 1973. 1. Aufl., 506 S., 105 Abb., 93 Tab. geb. DM 74. Chem Ing Tech 46:222

38. Garner CD (1994) The chemical nature of the molybdenum centres in enzymes. Stud Inorg Chem 19:403–418

39. Diemann E, Müller A (1973) Thio and seleno compounds of the transition metals with the do configuration. Coord Chem Rev 10:79–122

40. Müller A, Rittner W, Neumann A, Königer-Ahlborn E, Bhattacharyya RG (1980) Polychalkogenoanionen der übergangsmetalle. III. $W_3S_9^{2-}$ und $W_3OS_8^{2-}$, das erste polyoxothiometallation. Z Für Anorg Allg Chem 461:91–95

41. Müller A, Rittner W, Neumann A, Sharma RC (1981) Polychalkogenoanionen der übergangsmetalle. IV. Neuartige redoxkondensationsreaktionen von $MoO_2S_2^{2-}$ in H_2O und zur darstellung von di-µ-sulfido-komplexen von mov. Z Für Anorg Allg Chem 472:69–74

42. Müller A, Bhattacharyya RG, Königerahlborn E, Sharma RC, Rittner W, Neumann A (1979) The formation of trinuclear W_3S_{2-9}-type species from WS_{2-4} by condensation redox processes. Inorg Chim Acta 37:L493

43. Secheresse F, Lefebvre J, Daran JC, Jeannin Y (1982) Synthesis and structure of the first tungsten complex having the $W_2S_4^{2+}$ core: $[P(C_6H_5)_4]_2W_4S_{12}$. Inorg Chem 21:1311–1314

44. Cadot E, Béreau V, Sécheresse F (1995) Synthesis and characterization of the polyoxothioanion α-$[PW_{11}NbSO_{39}]^{4-}$ derived from the Keggin structure. Inorg Chim Acta 239:39–42

45. Müller A, Sarkar S, Bhattacharyya RG, Pohl S, Dartmann M (1978) Directed synthesis of $[Mo_3S_{13}]^{2-}$, an isolated cluster containing sulfur atoms in three different states of bonding. Angew Chem Int Ed Engl 17:535–535

46. Rittner W, Müller A, Neumann A, Bäther W, Sharma RC (1979) Generation of the triangulo-group MOV-η-S_2 in the "condensation" of $[Mo^{VI}O_2S_2]_2$ to $[Mo_2^VO_2S_2(S_2)_2]_2$. Angew Chem Int Ed Engl 18:530–531

47. Cadot E, Salignac B, Marrot J, Dolbecq A, Sécheresse F (2000) $[Mo_{10}S_{10}O_{10}(OH)_{10}(H_2O)_5]$: a novel decameric molecular ring showing supramolecular properties. Chem Commun 2000:261–262

48. Richens DT, Pittet P-A, Merbach AE, Humanes M, Lamprecht GJ, Ooi B-L, Sykes AG (1993) Mechanism of substitution on trinuclear incomplete cuboidal $[M_3X_4(OH_2)_9]^{4+}$ ions: kinetic studies of water exchange and substitution by Cl^- on $[Mo_3S_4(OH_2)_9]^{4+}$. J Chem Soc Dalton Trans 1993:2305–2311

49. Hernandez-Molina R, Sokolov MN, Sykes AG (2001) Behavioral patterns of heterometallic cuboidal derivatives of $[M_3Q_4(H_2O)_9]^{4+}$ (M = Mo, W; Q = S, Se). Acc Chem Res 34:223–230

50. Cadot E, Sécheresse F (2002) Cyclic molecular materials based on $[M_2O_2S_2]^{2+}$ cores (M = Mo or W). Chem Commun 2002:2189–2197

51. Cadot E, Salignac B, Halut S, Sécheresse F (1998) $[Mo_{12}S_{12}O_{12}(OH)_{12}(H_2O)_6]$: a cyclic molecular cluster based on the $[Mo_2S_2O_2]^{2+}$ building block. Angew Chem Int Ed 37:611–613

52. Sécheresse F, Cadot E, Dolbecq A (2000) How solids can be obtained from the molecular $[Mo_2S_2O_2]^{2+}$ building block. J Solid State Chem 152:78–86

53. Dolbecq A, Cadot E, Sécheresse F (1998) $[Mo_9S_8O_{12}(OH)_8(H_2O)_2]^{2-}$: a novel polyoxothiomolybdate with a MoVI octahedron encapsulated in a reduced MoV cyclic octanuclear core. Chem Commun 1998:2293–2294

54. Salignac B, Riedel S, Dolbecq A, Sécheresse F, Cadot E (2000) "Wheeling templates" in molecular oxothiomolybdate rings: syntheses, structures, and dynamics. J Am Chem Soc 122:10381–10389

55. Lemonnier J-F, Floquet S, Marrot J, Cadot E (2009) Polyoxothiomolybdenum wheels as anionic receptors for recognition of sulfate and sulfonate anions. Eur J Inorg Chem 2009:5233–5239

56. Lemonnier J-F, Floquet S, Marrot J, Kachmar A, Bénard M, Rohmer M-M, Haouas M, Taulelle F, Henry M, Cadot E (2007) Changing the oxothiomolybdate ring from an anionic to a cationic receptor. Inorg Chem 46:9516–9518

57. Duval S, Floquet S, Simonnet-Jégat C, Marrot J, Biboum RN, Keita B, Nadjo L, Haouas M, Taulelle F, Cadot E (2010) Capture of the $[Mo_3S_4]^{4+}$ cluster within a {Mo_{18}} macrocycle yielding a supramolecular assembly stabilized by a dynamic H-bond network. J Am Chem Soc 132:2069–2077

58. Cadot E, Marrot J, Sécheresse F (2001) $[W_{16}S_{16}O_{16}(OH)_{16}(H_2O)_4(C_5H_6O_4)_2]^{4-}$: a flexible, pillared oxothiotungstate wheel. Angew Chem Int Ed 40:774–777

59. Cadot E, Salignac B, Loiseau T, Dolbecq A, Sécheresse F (1999) Syntheses and 31P NMR studies of cyclic oxothiomolybdate(V) molecular rings: exchange properties and crystal structures of the monophosphate Decamer $[(H_2PO_4)Mo_{10}S_{10}O_{10}(OH)_{11}(H_2O)_2]^{2-}$ and the diphosphate dodecamer $[(HPO_4)_2Mo_{12}S_{12}O_{12}(OH)_{12}(H_2O)_2]^{4-}$. Chem Eur J 5:3390–3398

60. Bannani F, Floquet S, Leclerc-Laronze N, Haouas M, Taulelle F, Marrot J, Kögerler P, Cadot E (2012) Cubic box versus spheroidal capsule built from defect and intact pentagonal units. J Am Chem Soc 134:19342–19345

61. Schäffer C, Todea AM, Bögge H, Cadot E, Gouzerh P, Kopilevich S, Weinstock IA, Müller A (2011) Softening of pore and interior properties of a metal-oxide-based capsule: substituting 60 oxide by 60 sulfide ligands. Angew Chem Int Ed 50:12326–12329

62. Zang H-Y, Miras HN, Yan J, Long D-L, Cronin L (2012) Assembly and autochirogenesis of a chiral inorganic polythioanion möbius strip via symmetry breaking. J Am Chem Soc 134:11376–11379

63. Zang H-Y, Miras HN, Long D-L, Rausch B, Cronin L (2013) Template-directed assembly of polyoxothiometalate scaffolds into nanomolecular architectures. Angew Chem Int Ed 52:6903–6906

64. Müller A, Das SK, Kögerler P, Bögge H, Schmidtmann M, Trautwein AX, Schünemann V, Krickemeyer E, Preetz W (2000) A new type of supramolecular compound: molybdenum-oxide-based composites consisting of magnetic nanocapsules with encapsulated Keggin-ion electron reservoirs cross-linked to a two-dimensional network. Angew Chem Int Ed 39:3413–3417

65. Müller A, Shah SQN, Bögge H, Schmidtmann M (1999) Molecular growth from a Mo_{176} to a Mo_{248} cluster. Nature 397:48–50

66. Miras HN, Cooper GJT, Long D-L, Bögge H, Müller A, Streb C, Cronin L (2010) Unveiling the transient template in the self-assembly of a molecular oxide nanowheel. Science 327:72–74

67. Zang H-Y, Chen J-J, Long D-L, Cronin L, Miras HN (2013) Assembly of thiometalate-based $\{Mo_{16}\}$ and $\{Mo_{36}\}$ composite clusters combining $[Mo_2S_2O_2]^{2+}$ cations and selenite anions. Adv Mater 25:6245–6249

68. Zang H-Y, Chen J-J, Long D-L, Cronin L, Miras HN (2016) Assembly of inorganic $[Mo_2S_2O_2]^{2+}$ panels connected by selenite anions to nanoscale chalcogenide–polyoxometalate clusters. Chem Sci 7:3798–3804

Structure and Bonding in Molecular Vanadium Oxides: From Templates via Host–Guest Chemistry to Applications

Carsten Streb

Abstract Molecular vanadium oxides are a structurally and chemically versatile sub-class of polyoxometalates. Fundamental concepts of their formation, templating mechanism and aggregation under aqueous and non-aqueous conditions are presented. Details about different template classes and their consequences on the vanadate reactivity are discussed together with concepts of linking vanadates into supramolecular architectures using various linkages. The final section briefly describes major applications of vanadium oxide clusters in (photo)catalysis, magnetism and molecular nanostructure design.

Keywords Catalysis • Magnetism • Polyoxometalate • Polyoxovanadate • Self-assembly • Vanadium oxide

Contents

C. Streb (✉)
Institute of Inorganic Chemistry I, Ulm University, Albert-Einstein-Allee 11, Ulm 89081, Germany
e-mail: carsten.streb@uni-ulm.de

1   Introduction

1.1   *Polyoxometalates: Fundamentals of Molecular Metal Oxides*

Polyoxometalates (POMs) are molecular metal oxide cluster anions of early, high valent transition metals (typically based on molybdenum, tungsten or vanadium). POMs are typically formed in aqueous solution by the self-assembly of small and reactive oxometalate precursors. Amongst metal oxides, the formation of molecular species rather than solid-state materials by early transition metals is unique and is based on the presence of high valent metal centres (V^V, Mo^{VI}, W^{VI}) capable of forming M=O multiple bonds. This significantly reduces the electron density on the terminal oxo ligands while forming a kinetically inert M–O bond ($t_{1/2}$ for exchange of the terminal oxygen is typically several weeks to months) [1, 2]. Therefore, an effective growth termination mechanism is established, which prevents the formation of infinite solid-state compounds. The self-assembly of POMs is probably best exemplified by the archetypal cluster known as the Keggin anion, $[PM_{12}O_{40}]^{3-}$ (M = Mo, W) [3–5]. This cluster has been known (although not structurally characterized) since the eighteenth century and is obtained by the reaction of phosphoric acid with oxomolybdates or oxotungstates, giving rise to this cluster anion [4]. Over the next century, chemists including *Berzelius, Pauling, Werner* and others provided varying structural descriptions of the cluster shell. Final evidence of the cluster architecture was provided in 1933 when *J.F. Keggin* solved the structure of the cluster using the emerging tool of powder-X-ray diffraction [3]. Briefly, the Keggin cluster is a phosphate-templated anion featuring four trigonal $\{M_3O_{13}\}$ building units known as triads, see Fig. 1. Depending on the connectivity of these triads, a range of geometric isomers can be formed by rotation of one to four triads by 60°. As a result, neighbouring triads are linked either by corner-sharing or edge-sharing modes. The archetypal (and most stable) isomer known as the α-Keggin structure is assembled based only on corner-sharing connections, see Fig. 1.

The self-assembly mechanism in polyoxometalates is still poorly understood, however, it is well known that the initial steps involve protonation of terminal M=O metal oxygen bonds, resulting in an elongation of the M–O distances and thereby in a destabilization of the bond. In addition, protonation results in a transition from metal oxo to metal hydroxo and finally to metal aquo ligands which are labile and can easily be replaced in condensation reactions according to Fig. 2.
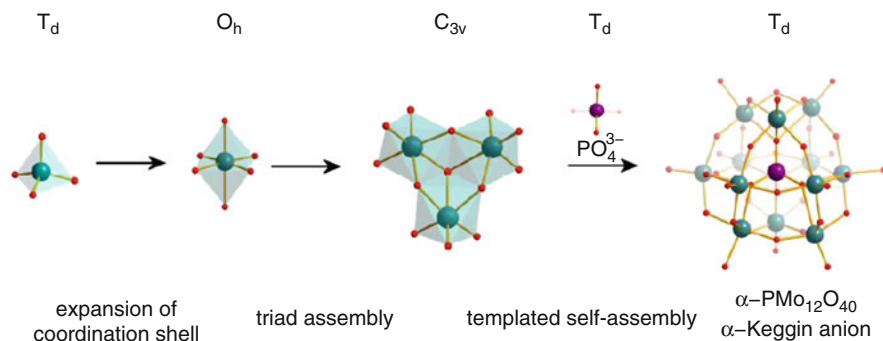
Fig. 1 Self-assembly of the α-Keggin anion α-$[PMo_{12}O_{40}]^{3-}$ starting from a tetrahedral molybdate MoO_4^{2-} anion. Protonation of the terminal oxo ligands and extension of the coordination shell result in a highly reactive, octahedral $H_x[MoO_6]^{(6-x)-}$ species. This moiety undergoes further condensation reactions, formally resulting in the formation of {Mo_3O_{13}} triads. Formally, four of these triads can be assembled around a central phosphate template, resulting in the formation of the stable α-Keggin anion. N.B.: The cluster shape is predetermined by the template anion structure
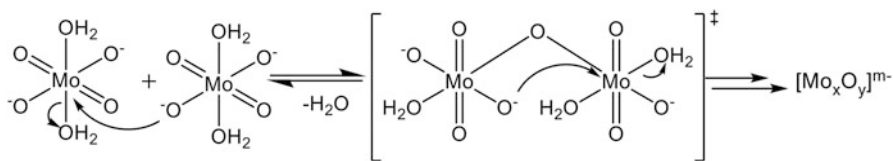
Fig. 2 Protonation on an oxometalate species $[MoO_4(H_2O)]^{2-}$ leads to the formation of a labile water ligand. Reaction with a second oxometalate results in a condensation reaction, giving a dinuclear complex, which can undergo further oligo-condensations, giving rise to the assembly of a polynuclear metal oxide cluster

1.2 Structural Principles in Vanadate Chemistry

While the chemistry of tungstates and molybdates is based on their octahedral building blocks $[MO_6]$ (M = Mo, W), vanadium oxide cluster chemistry is more diverse and often vanadium centres are found in tetrahedral $[VO_4]$, square pyramidal $[VO_5]$ or octahedral $[VO_6]$ coordination environments. This leads to a significantly increased structural flexibility so that arguably, vanadate chemistry is the structurally most diverse of POM chemistries. However, this flexibility comes as a price as often, vanadates are chemically less robust compared to their heavier molybdate and tungstate "siblings". A main difference in terms of structural changes is best exemplified using the Keggin anion above. Consider the change from a molybdate to a vanadate α-Keggin: $[PMo_{12}O_{40}]^{3-}$ vs $[PV_{12}O_{40}]^{15-}$. It is obvious that the proposed vanadate Keggin anion is too highly charged and thus unstable. However, due to the structural versatility of vanadium, a stabilization mechanism is observed where two additional vanadium oxide $[VO]^{3+}$ cations are

embedded within the oxide cluster shell of the vanadate Keggin anion, giving square pyramidal $[VO_5]$ units. Further, protonation of the cluster shell is possible even at moderately acidic pH, so that in consequence, both structural modifications reduce the negative cluster charge significantly and lead to the stable Keggin derivatives such as $[H_6PV_{14}O_{42}]^{5-}$ [6]. Thus the electrostatic stabilization of vanadates is often due to the use of vanadate building units with a lower number of oxygen ligands so that the overall negative charge introduced by oxo groups O^{2-} can be compensated by the vanadium centres.

1.3   Aqueous vs Non-aqueous Chemistry of Polyoxovanadates

The synthesis of new vanadium oxide clusters using the aqueous chemistry traditionally used for POMs is problematic, as over a wide range of pH, the decavanadate cluster $[H_xV_{10}O_{28}]^{(6-x)-}$ is formed as the thermodynamically most stable species (Fig. 3). This is in large due to the condensed structure of the decavanadate, where ten octahedral $[VO_6]$ units are linked in edge-sharing mode. Thus, the development of different vanadate structures (based on fully oxidized V^V) under aqueous acidic to neutral conditions is difficult. Under basic aqueous conditions, cluster hydrolysis makes polyoxovanadate assembly virtually impossible and leads to orthovanadate $[VO_4]^{3-}$ or metavandate (formally $[VO_3]^-_n$) species. The
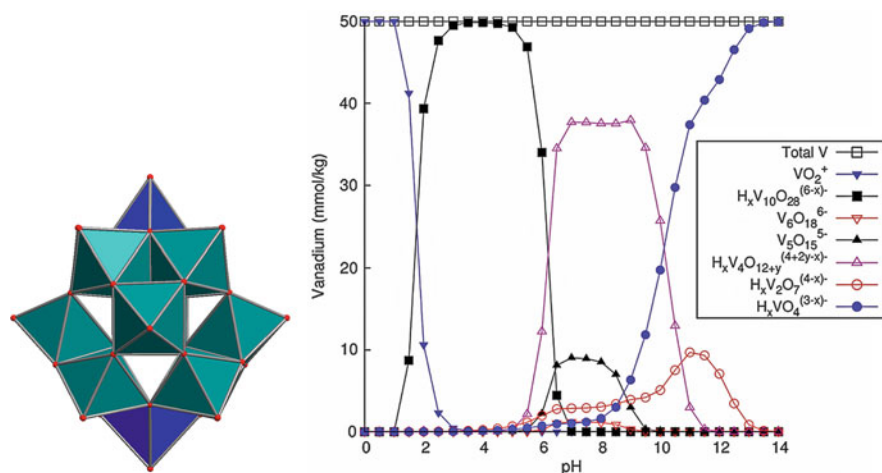
Fig. 3 *Left*: Polyhedral representation of the vanadate Keggin derivative $[PV_{14}O_{42}]^{9-}$. Note that the original α-Keggin structure (*teal*) is stabilized by two $[VO_5]$ square pyramids (*blue*) [6]. *Right*: Speciation diagram showing the occurrence of different vanadium oxide clusters in aqueous solution depending on the solution pH. With permission from RSC publishers [7]. Colour scheme: V: *teal*, *blue*, O: *red*

distribution of vanadate ions in aqueous solution as a function of pH is illustrated in Fig. 3 [7].

To overcome these synthetic challenges, non-aqueous assembly routes for polyoxovanadates have been explored and have led to a diverse family of vanadium oxide clusters obtained from organic coordinating solvents such as acetonitrile (ACN), dimethyl sulfoxide (DMSO) or dimethyl formamide (DMF). Typically an organo-soluble, labile precursor such as $(^nBu_4N)_4[V_4O_{12}]$ is deliberately fragmented using thermal, chemical or photochemical means, and the resulting fragments self-assemble under the given reaction conditions. The key difference between aqueous and non-aqueous synthesis is that under non-aqueous conditions, different reaction intermediates stabilized by the respective solvent are formed, such as the species $[V(O)(dmso)_5]^{2+}$ which was isolated and identified as an intermediate in the assembly of complex transition-metal functionalized vanadates [8]. Notably, the use of a V(IV) precursor not only allows the use of the "standard" reaction control parameters (solvent, temperature, pressure, acidity) but enables the assembly of new vanadates driven by redox-transitions (typically between V (IV) and V(V)) which leads to novel cluster architectures. This is best exemplified by comparing the self-assembly of "simple" aqueous vanadate solutions under oxidizing (leading to V(V)) or reducing (leading to V(IV)) conditions. While under oxidizing conditions and acidic pH, the decavanadate $[H_xV_{10}O_{28}]^{(6-x)-}$ is the dominating species [7], under reducing conditions, a structurally very different octadecanuclear cluster, $[V_{18}O_{42}]^{12-}$ is formed which is composed of V(IV) centres (although mixed V(IV)-V(V) species [9, 10] have also been reported). The most striking difference between {V$_{10}$} and {V$_{18}$} is that in {V$_{10}$}, only octahedral [VO$_6$] units are present while {V$_{18}$} is based on [VO$_5$] square pyramids. In addition, the vanadate octahedra in {V$_{10}$} are purely linked in edge-sharing mode while the square pyramids in {V$_{18}$} are linked by a combination of edge- and corner-sharing. Thus, it can be seen that both features result in a decrease of the O:V ratio for {V$_{18}$} (2.3) compared with {V$_{10}$} (2.8), leading to the electrostatic stabilization of the V (IV)-based {V$_{18}$}. We will return to the {V$_{18}$} architecture later in this chapter, see Fig. 4.

2 Building Principles in Vanadate Cluster Chemistry

2.1 Templates

Polyoxovanadates are structurally the most versatile sub-class amongst poly-oxometalates. This is partly caused by their diverse coordination geometry (vide supra), but is further due to the large variety of internal anionic templates which can be found in vanadium oxide clusters, particularly when compared with molybdate and tungstate chemistry: except for few examples, tungstates and molybdates are templated by tetrahedral or octahedral oxo-anions, e.g. XO_4^{n-} (X = B, Si, Ge, P,
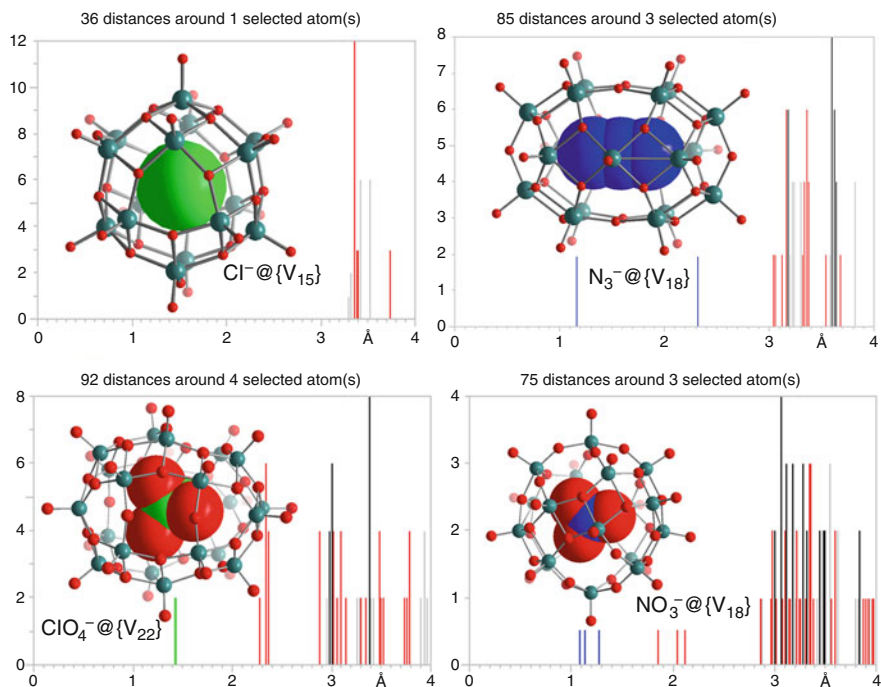
Fig. 4 Illustration of anion-templated vanadate clusters showing the ball-and-stick-representation of the vanadate shell, anions are shown as space-filling model. In the background distance histograms are given which show the atomic distances around the central template (oxygen distances: *red*, vanadium distances: *black/gray*). Colour scheme: V: *teal*, O: *red*, P: *magenta*, C: *gray*

etc.) [4] or XO_6^{m-} (X = Fe [11], Mn [11], I [12], Te [13]), thereby restricting the template-dependent architectures accessible. In contrast, vanadates can feature a wider range of anionic templates including oxo-anions, halides, pseudo-halides and others (vide infra). Pioneering work exploring the template-dependent formation of polyoxovanadates was carried out in the late twentieth century by the groups of Klemperer, Müller, Pope and others. When comparing templates in polyoxovanadate chemistry, three general cases can be distinguished, these will be discussed in detail in the following section:

1. *Strongly interacting anionic templates*: the first class of templates are oxo-anions which typically act as tetrahedral or octahedral templates $[XO_x]^{n-}$ in the formation of vanadates. This template class is characterized by the formation of strong X–O–V coordination bonds (V–O bond distance ca. 2.5–2.7 Å), thereby contributing significantly to the overall stability of the vanadate cluster framework. We have already encountered one example previously, namely the phosphate-templated Keggin derivative {PV_{14}}, see above. In this prototype, the phosphate anion template features four oxygen atoms, each oxygen bridges the central P atom to three V^V atoms with an average bond

length d(V–O) ca. 2.35–2.40 Å [6]. This corresponds to the "classical" oxoanion template binding mode as it is also observed in the archetypal Mo- and W-Keggin anions described above [5] and results in thermally and chemically stable cluster units. Note that these "classical" oxoanion templates can also be oxometalate anions themselves, as observed for oxomanganate- [14, 15] or oxocobaltate [15]-templated vanadates, e.g. $[Mn^{IV}V_{13}O_{38}]^{7-}$ [14] where formally a $[Mn^{IV}O_6]$ octahedron acts as internal template. More recently, a range of other transition metal oxoanions have been observed as internal templates in vanadates, e.g. Pd, Cu and Ni [16]. Furthermore, lanthanides have also been observed embedded in cyclic vanadates [17, 18]. However, here, it seems that lanthanides act as central "nucleation points" by coordinating to reactive vanadate fragments and linking them into the cyclic structures observed. To date, the chemistry and reactivity of these oxometalate-templated species have not been explored intensely. As a result, the application range of these materials is currently not well understood.

2. *Weakly interacting anionic templates:* In contrast to the classical oxoanions described above, many non-oxoanions such as halides, pseudohalides and even weakly coordinating oxoanions such as nitrate or perchlorate can be incorporated into vanadate shells where they formally act as structure-directing anions [19, 20]. The structural concept is exemplified using the chloride-templated anion $[ClV^V_7V^{IV}_8O_{36}]^{5-}$ [21]. In the mixed-valent cluster, a central chloride template is surrounded by 15 square pyramidal $[VO_5]$ centres which are linked in corner- or edge-sharing modes (Fig. 4). Note that the Cl···V distances in the compound are between ca. 3.3 and 3.5 Å. This is considerably longer than classical V–Cl coordination bonds (typically ca. 2.2–2.6 Å, depending on the V oxidation state and exact bonding situation). The significant increase in interaction distance between vanadium and chloride is attributed to repulsive electrostatic interactions between the chloride and oxo anions within the cluster which prevent the formation of strong V–Cl coordinating bonds. Theoretical computations have therefore shown that attractive (Cl···V) and repulsive (Cl···O) interactions are virtually equal so that the chloride does not significantly contribute to the overall stability of the cluster [22]. However, its presence per se indicates that the chloride is required for the initial cluster formation, possibly by organizing reactive vanadate precursors into a near-spherical shape which triggers cluster formation by introducing convexity into the assembly process.

Interestingly, chloride templating does not necessarily lead to the $\{V_{15}\}$ cluster discussed here [21], but has been observed in clusters ranging from $\{V_{12}\}$ [22, 23] to $\{V_{14}\}$ [24], $\{V_{15}\}$ [21, 25], and $\{V_{16}\}$ [26], so that a whole family of chloride-templated vanadates (many of them in mixed $V^{IV/V}$ oxidation state) are known [25]. Importantly, the overall cluster architecture is controlled to a large degree by the shape of the template anion, so that the spherical chloride introduces also spherical overall cluster shapes. In consequence, modification of the anion shape is a facile tool to control the overall cluster shape. As shown in Fig. 4, this has been used to access clusters templated by N_3^- with ellipsoidal

shape, NO_3^-, with flattened shape or ClO_4^- with a tetrahedral shape. Also shown in the figure are the distance histograms around the central ions where distinct distance ranges are observed for the interactions of the template with the surrounding vanadium oxide shell.

In a ground-breaking study, Schmitt et al. showed that multiple halide anion templates can be used to trigger the assembly of large phenylarsonate-stabilized vanadates containing up to 24 V and 8 As centres [27]. In one of the most spectacular assemblies, $\{Cl_6As_8V_{24}\}$, the authors report a vanadium oxide cluster shell stabilized by eight phenylarsonate substituents. Intriguingly, the capsule is templated by six internal chloride anions arranged in an octahedral fashion with Cl··Cl-distances of 3.9 Å, which is significantly longer than the sum of the van der Waals radii of chlorine ($r_{vdW,Cl} = 1.75$ Å). Each chloride template forms long-range interactions ($d(V··Cl)$ 2.9–3.0 Å) with four V centres which form a square "cap" on the cluster surface, see Fig. 5. These square caps are linked and stabilized by eight phenylarsonate ligands (which themselves form a cubic arrangement), thus resulting in the final cluster architecture. When the metal-only arrangement is considered, it can be seen that the V atoms in $\{Cl_6As_8V_{24}\}$ form a truncated octahedron where each of the eight hexagonal faces is capped by an As centre (Fig. 5). The enormous potential of this approach is obvious when considering that larger, multiatomic anions such as pseudohalides or oxoanions could be used in a similar approach to assemble even larger vanadate shells with even more diverse structures.

3. *Non-ionic templates and host–guest chemistry:* In 1989, Klemperer, Day and Yaghi reported the synthesis of an open, bowl-shaped dodecavanadate where an
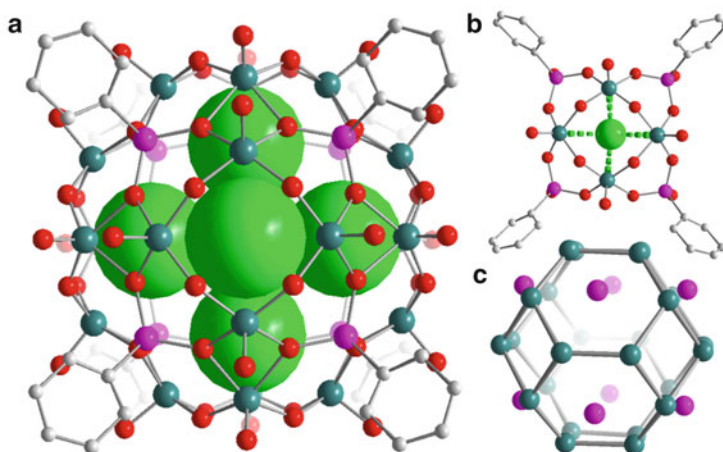
Fig. 5 (**a**) Illustration of the $\{Cl_6As_8V_{24}\}$ cluster reported by Schmitt et al., highlighting the six central chloride templates arranged in an octahedral fashion. (**b**) Each chloride anion templates a tetranuclear $\{V_4\}$ ring. (**c**) metal-only framework showing that the six $\{V_4\}$ rings are linked by eight phenylarsonate groups (each capping a six-membered vanadium ring) so that in sum, the $\{Cl_6V_8V_{24}\}$ cluster is obtained. Colour scheme: V: *teal*, O: *red*, As: *magenta*, C: *gray*

acetonitrile ligand seems to act as a template. The complex, $[(MeCN)V_{12}O_{32}]^{4-}$ is composed of a hemispherical vanadate bowl featuring twelve $[VO_5]$ square pyramidal units linked in corner- or edge-sharing mode. The acetonitrile template interacts with the twelve V centres with long-range V$\cdots$N interactions (ca. 3.3–3.5 Å) while the methyl group protrudes from the vanadate hemisphere. Later studies showed that other organonitriles, e.g. benzonitrile could also serve as template and bind in a similar mode albeit with slightly longer V$\cdots$N distances of ca. 3.5–3.8 Å. This pioneering study thus illustrates that vanadium oxide clusters can bring together aspects of classical structural templating with supramolecular host–guest chemistry and could in principle be used to build larger, complex architectures from suitable open-framework vanadates and multitopic organic linkages.

3 Supramolecular Vanadate Architectures

Pioneering studies into the linkage of open vanadate shells with organic ditopic ligands have been undertaken by Schmitt et al. [28]. The group investigated the self-assembly of supramolecular organic–inorganic capsules by linking two pentanuclear vanadate "caps" with aromatic di-phosphonate linkages. The authors placed the phosphonate groups in opposite positions so that linear linkages are formed between the vanadate caps. Variation of the linker size enables the modular tuning of the capsule size in the nanometer region (Fig. 6). The authors showed that the capsules are stable in solution and can also be deposited on suitable substrates, forming regular 2D arrays which could, for example, be relevant for guest uptake or pollutant removal from solution.

4 Supramolecular Vanadate Chemistry for Transition Metal Functionalization

When considering the chemistry of the "traditional" POM addenda metals V, Mo and W, it is noticeable that the transition-metal functionalization of vanadates has been lagging behind the corresponding research in molybdate and tungstate chemistry. The reasons for this are not absolutely clear but might be a combination of a perceived "lack of stability" of vanadates together with a lack of control and predictability of vanadate assembly, particularly when compared with the controlled assembly and functionalization of lacunary Keggin and Dawson tungstates and, to a lesser degree, lacunary molybdates. While early studies on transition metal functionalization of vanadates used classical one-pot self-assembly routes (c.f. Co- and Mn-functionalized vanadates, above), recently a supramolecular "placeholder"
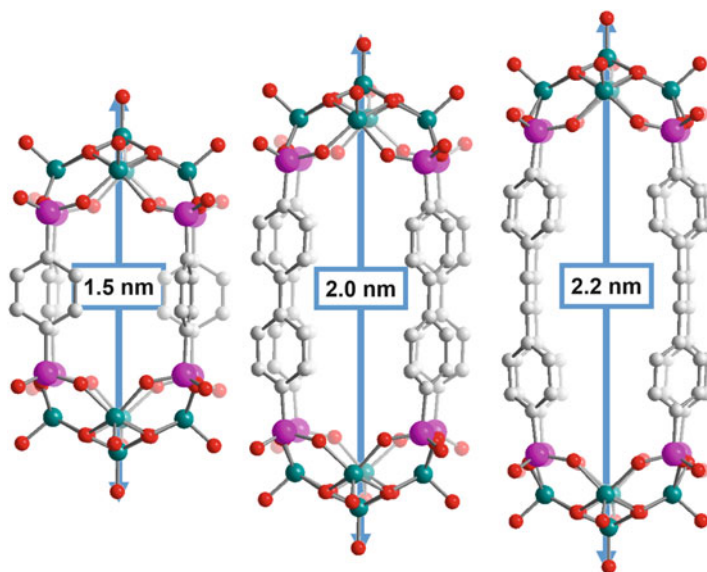
Fig. 6 Illustration of the supramolecular organic–inorganic vanadate capsules obtained by linking two vanadate caps (*top, bottom*) with ditopic diphosphonate linkages [28]. Each cap consists of a pentanuclear vanadate unit and is linked to the capsule by V–O–P coordination bonds. Tuning of the linker size allows the tuning of the capsule length in the low nanometer range. Colour scheme: V: *teal*, O: *red*, P: *magenta*, C: *gray*

approach was reported which enables the controlled and predictable transition metal incorporation into a family of dodecanuclear cluster [22, 23]. In the study, the authors assembled the vanadate cluster $(DMA)_2[ClV_{12}O_{32}]^{3-}$ in the presence of dimethyl ammonium (DMA) "placeholder" cations which led to the formation of a belt-shaped cluster featuring two hexagonal metal binding sites, each binding site blocked by a hydrogen-bonded DMA cation (Fig. 7). In a series of studies, it was shown that one or both DMA placeholders can be selectively (and stepwise) replaced with various transition metals (Fe^{3+}, Mn^{2+}, Cu^{2+}, Zn^{2+}) [22, 23] leading to transition metal functionalized species with applications, e.g. in selective C-H-activation and organosubstrate oxidation [23]. Structural analysis of the DMA-bound and metal-bound cluster shells reveals that significant geometric distortions (V–O bond length and O–V–O bond angle changes) are noted upon metal binding, resembling a "grabbing" motion of the cluster onto the metal ion (Fig. 7). Therefore, this cluster family can be likened to classical lacunary cluster species as it gives predictable access to transition metal functionalized vanadates.
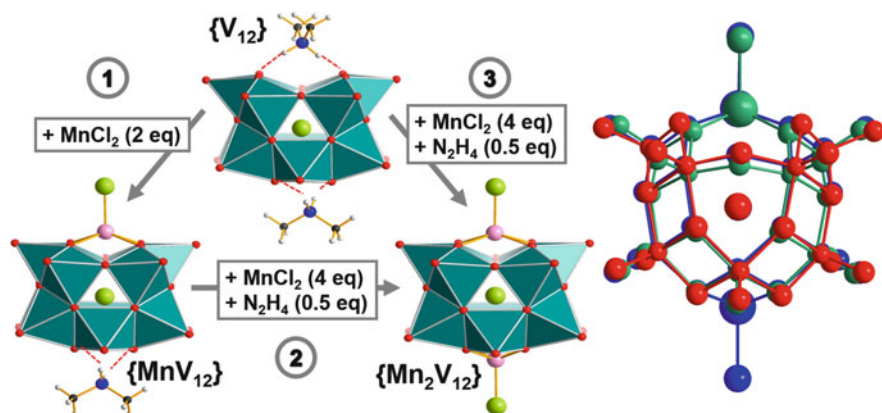
Fig. 7 *Left*: Illustration of the DMA-blocked {V$_{12}$} cluster where two dimethyl ammonium (DMA) placeholder cations block the metal binding sites on *top* and *bottom*. Reaction with a suitable transition metal under stoichiometric control allows the stepwise replacement of one or two DMA cations by the respective metal cation. *Right*: overlay of the metal oxide framework of the DMA-blocked {V$_{12}$} (*red*, DMA not shown for clarity), the mono-functionalized {MV$_{12}$} (*green*) and the di-functionalized {M$_2$V$_{12}$}, highlighting the significant framework distortions upon metal coordination [22, 23]. Colour scheme: V: *teal*, O: *red*, P: *magenta*, C: *gray*

5 The Importance of Internal Templates

Often, the internal template is perceived as a "passive" building block or at best a structural stabilizer for the vanadium oxide framework. However, recent studies have shown that the internal template can be a key component which controls the overall cluster reactivity. In a recent study on the photoredox-activity of halide-templated bismuth vanadates {XBi$_2$V$_{12}$} (X = Cl−, Br−) [29], it was shown that isostructural [V$_{12}$O$_{33}$]$^{6-}$ units can be templated by both chloride and bromide. As both clusters show virtually identical V–O bonding distances, the only major difference is the lightly longer V$\cdots$X distances observed for the smaller chloride template compared with the slightly larger bromide (ionic radii: Cl$^-$: 1.81 Å; Br$^-$: 1.96 Å). In contrast, attempts to incorporate the significantly larger iodide anion (ionic radius: 2.2 Å) were not successful. Based on earlier photochemical studies with bismuth vanadate clusters [30, 31], the {XBi$_2$V$_{12}$} anions were employed as visible light-driven photooxidation catalysts. In organosubstrate oxidation tests [32], significantly higher photoreactivity was observed for the bromide-templated cluster compared with the chloride species. Time-resolved spectroscopic and DFT theoretical studies showed that this reactivity difference is due to a more efficient singlet-triplet transition for the bromide-templated species as the central bromide template enables a higher spin-orbit coupling (the so-called heavy atom-effect)

42																																																																																																																																																																																																																																																																																																																																																																																																																																																																																																																																																																																																																																																																																																																																																																																																																																																																																																																																																																																																																																																																																																																																																																																																																																																																																																																																																																																																																																																																																																																																																																																																																																																																																																																																																																																																																																																																																																																																																																																																																																																																																																																																																																																																																																																																																																																																																																																																																																																																																																																																																																																																																																																																																																																																																																																																																																																																																																																																																																																																																																																																																																																																																																																																																																																																																																																																																																																																																																																																																																																																																																																																																																																																																																																																																																																																																																																																																																																																																																																																																																																																																																																																																																																																																																																																																																																																																																																																																																																																																																																																																																																																																																																																																																																																																																																																																																																																																																																																																																																																																																																																																																																																																																																																																																																																																																																																																																																																																																																																																																																																																																																																																																																																																																																																																																																																																																																																																																																																																																																																																																																																																																																																																																																																																																																																																																																																																																																																																																																																																																																																																																																																																																																																																																																																																																																																																																																																																																																																																																																																																																																																																																																																																																																																																																																																																																																																																																																																																																																																																																																																																																																																																																																																																																																																																																																																																																																																																																																																																																																																																																																																																															C. Streb

[32]. Thus, the central templates are not only structural features of the vanadate clusters but in addition can directly influence the reactivity of the clusters [29].

6 Applications of Polyoxovanadates

6.1 Catalysis

Applications of POMs in oxidation catalysis have mainly been the domain of tungstates [33] and, to a lesser degree, of molybdates [34]. This is also true for the recent explosion of research in molecular water oxidation catalysts where metal-functionalized tungstates were primarily used as key prototypes [35, 36]. However, over recent years researchers realized that vanadates are a promising alternative group of catalysts, particularly for oxidation catalysis [23], photoredox-catalysis [30, 37–39] and water oxidation [40]. Recent studies highlight that catalytic activity can be optimized by incorporation of reactive metal centres into vanadate cluster shells. A prototype example in the field of water oxidation catalysis was recently reported where the incorporation of a bio-inspired manganese oxo core into a vanadate cluster led to a unique homogeneous water oxidation catalyst. The compound $[Mn_4V_4O_{17}(AcO)_3]^{3-}$ ($=\{Mn_4V_4\}$) is based on a $[Mn_4O_4]$ manganese oxo cubane core with a mixed $Mn_2^{III}Mn_2^{IV}$ oxidation state (Fig. 8). The manganese cubane is stabilized by a tripodal $\{V_4\}$ and three acetate ligands. Electrochemical studies show that the system features several reversible redox waves so that an all-Mn^{IV} state can be accessed. When oxidation is performed in the presence of water (under electrochemical or photochemical conditions), the evolution of molecular oxygen is observed, indicating the water oxidation activity of $\{Mn_4V_4\}$. Under visible light-driven conditions using $[Ru(bpy)_3]^{2+}$ as photosensitizer and persulfate as electron acceptor, turnover numbers of ca. 1,150 and turnover frequencies of ca. 1.75 s^{-1} are reported. This example illustrates that the design of highly active metal-functionalized vanadate catalysts can be developed
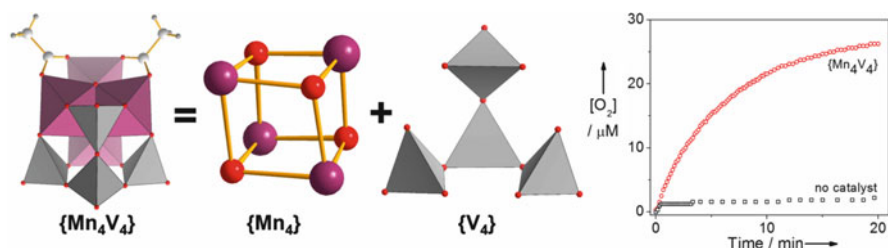

Fig. 8 *Left*: Illustration of the manganese vanadate $\{Mn_4V_4\}$ and the manganese and vanadate components. *Right*: electrochemical water oxidation performance by $\{Mn_4V_4\}$

for challenging homogeneous oxidation reaction involving proton-coupled multiple electron transfers.

6.2 Photocatalysis

Over the last decade, significant progress has been achieved in the development of visible light-driven polyoxovanadate oxidation catalysts [32]. A main focus of several studies was the development of systems where the photoactive ligand-to-metal charge transfer band (LMCT) which is typically in the UV region is shifted to longer wavelengths, i.e. towards the visible spectral region. In a pioneering study, it was shown that the structural flexibility of vanadium oxide clusters can be used to this effect [37]. A labile, ring-shaped vanadium oxide cluster, $[V_4O_{12}]^{4-}$ was heated in solution to trigger an in situ rearrangement to a pentanuclear unit, $[V_5O_{14}]^{3-}$. The structural change was accompanied by a significant shift of the absorption onset from the UV to the visible region. Subsequent photocatalytic oxidation studies (using the selective methanol-to-formadehyde oxidation as model reaction) showed that $[V_5O_{14}]^{3-}$ is capable of using visible light whereas $[V_4O_{12}]^{4-}$ is unreactive under VIS irradiation. The photoredox-reaction which occurs upon irradiation of $[V_5O_{14}]^{3-}$ once more highlights the structural flexibility of vanadates: upon reduction, the pentanuclear vanadate "dimerizes" to give the two-electron reduced species $[V^{IV}_2V^V_8O_{16}]^{4-}$. The catalytic cycle can be closed by re-oxidation of the system with molecular oxygen or hydrogen peroxide, see Fig. 9.

Based on this early study, further work was directed at the introduction of redox-active heterometals [31, 38, 39, 41] and reactive templates [29] into vanadate frameworks and much understanding has been gained into the structural features which control visible light photoreactivity in vanadium oxide clusters.

Fig. 9 *Left*: Illustration of the manganese vanadate {Mn_4V_4} and the manganese and vanadate components. *Right*: electrochemical water oxidation performance by {Mn_4V_4}
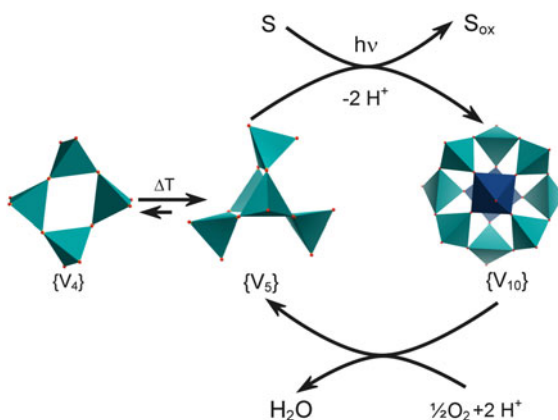
6.3 Magnetism

Mixed valent ($V^{IV/V}$) vanadate clusters have been at the centre of molecular magnetism studies in POM chemistry [42–44]. As the V centres are often in similar all-oxo coordination environments, electron delocalization and thus complex magnetic behaviour is observed. This is nicely exemplified by a recent study presented by Monakhov and Kögerler who used anion templates with varying symmetry such as SCN^- ($C_{\infty v}$) or ClO_4^- (T_d) to template the mixed-valent polyoxovanadate cluster $\{V_{22}O_{54}\}$ which features overall D_{2d} symmetry (see Fig. 4. For $ClO_4^-@\{V_{22}\}$) [45]. The authors analysed the d-electron distribution of the vanadium centres using magnetochemical, crystallographic and computational means. Their results show that significant electronic interactions between anion template and vanadate cluster shell are observed where the structure, symmetry and electronic properties of the template affect the magnetic behaviour and electron distribution within the vanadate shell. The authors note that this represents the first example of supramolecular recognition in a POM host–guest system and could be explored further by systematic variation of the central template.

6.4 Molecular Nanoparticles

For a long time, the design of POM architectures in the >2 nm region was the domain of molybdate and tungstate chemistry. Giant molybdate rings (Bielefeld wheel) and spheres (Keplerates) were pioneered in seminal studies by Müller who showed their fascinating assembly under reductive acidic self-assembly conditions starting from simple sodium molybdate aqueous solutions. In tungstate chemistry, Pope and later Kortz pioneered the linkage of lacunary Keggin anions into giant architectures by linkage with large metal cations such as Ce^{3+}, resulting in impressive yet molecular nanostructures such as $[Ce_{20}Ge_{10}W_{100}O_{376}(OH)_4(H_2O)_{30}]^{56-}$ [46]. For vanadates, these concepts have only recently been explored and first steps were taking into this direction. In an example which uses the metal linkage concept presented above, the authors used large Ba^{2+} cations to link four $\{V_{12}\}$ clusters into a supramolecular tetrahedral architecture. As shown in Fig. 10, a unique and highly symmetric system is observed: at the centre of the supramolecular structure, a bromide anion is observed which might act as a template or "growth point" for the whole structure. Six barium cations form an octahedron; each of the six octahedron faces is capped by either an additional Barium cation or by a $\{V_{12}\}$ anion as shown in Fig. 10. This to-date represents the largest molecular vanadate assembly and the structure features dimensions of ca. $2.2 \times 2.2 \times 2.2$ nm^3 (Fig. 10).
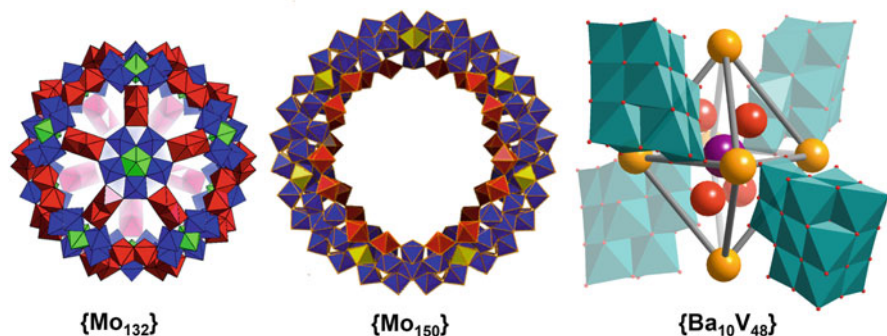
Fig. 10 *Left*: Illustration of the Keplerate cluster {Mo$_{132}$}. *Centre*: Illustration of a Bielefeld wheel cluster {Mo$_{150}$}. *Right*: Illustration of the Barium vanadate {Ba$_{10}$V$_{48}$}

7 Conclusion

In summary, this review highlights recent developments in the development of molecular and supramolecular vanadium oxide based architectures. Assembly principles based on molecular recognition between templates and reactive vanadate fragments are discussed together with the template effects on the resulting cluster architecture. Further prototype applications of vanadates are highlighted to reflect current and future developments, which are possible with this versatile materials class.

References

1. Johnson GK, Murman RK, Bowman B (1985) Isotopic oxygen exchange rates between [V18O42]12− and water. Transit Met Chem 10(5):181–184
2. Casey WH, Rustad JR (2016) Pathways for oxygen-isotope exchange in two model oxide clusters. New J Chem 40(2):898–905. The Royal Society of Chemistry
3. Keggin JF (1934) The structure and formula of 12-phosphotungstic acid. Proc R Soc A Math Phys Eng Sci 144(851):75–100
4. Pope MT (1983) Heteropoly and isopoly oxometalates. Springer, Heidelberg, 180 pp
5. Pope MT, Müller A (1991) Polyoxometalate chemistry: an old field with new dimensions in several disciplines. Angew Chem Int Ed 30(1):34–48
6. Grabau M, Forster J, Heussner K, Streb C (2011) Synthesis and theoretical Hirshfeld analysis of a supramolecular heteropolyoxovanadate architecture. Eur J Inorg Chem 2011 (11):1719–1724
7. Aureliano M, Ohlin CA, Vieira MO, Marques MPM, Casey WH, Batista de Carvalho LAE (2016) Characterization of decavanadate and decaniobate solutions by Raman spectroscopy. Dalt Trans 45(17):7391–7399. The Royal Society of Chemistry
8. Forster J, Rösner B, Fink RH, Nye LC, Ivanovic-Burmazovic I, Kastner K, et al. (2013) Oxidation-driven self-assembly gives access to high-nuclearity molecular copper vanadium oxide clusters. Chem Sci 4(1):418–424

9. Müller A, Sessoli R, Krickemeyer E, Bögge H, Meyer J, Gatteschi D, et al. (1997) Polyoxovanadates: high-nuclearity spin clusters with interesting host-guest systems and different electron populations. synthesis, spin organization, magnetochemistry, and spectroscopic studies. Inorg Chem 36(23):5239–5250

10. Wutkowski A, Niefind F, Näther C, Bensch W (2011) A new mixed-valent high nuclearity polyoxovanadate cluster based on the {V18O42} archetype. Zeitschrift fur Anorg und Allg Chemie 637(14-15):2198–2204

11. Hasenkopf B, Delmont R, Herson P, Gouzerh P (2002) Anderson-type heteropolymolybdates containing tris(alkoxo) ligands: synthesis and structural characterization. Eur J Inorg Chem 5:1081–1087

12. Long D-L, Song Y-F, Wilson EF, Kögerler P, Guo S-X, Bond AM, et al. (2008) Capture of periodate in a {W$_{18}$O$_{54}$} cluster cage yielding a catalytically active polyoxometalate [H$_3$W$_{18}$O$_{56}$(IO$_6$)]$^{6-}$ embedded with high-valent iodine. Angew Chem Int Ed 47(23):4384–4387. WILEY-VCH

13. Yan J, Long D-L, Wilson EF, Cronin L (2009) Discovery of heteroatom-"Embedded" Te⊂ {W$_{18}$O$_{54}$} nanofunctional polyoxometalates by use of cryospray mass spectrometry. Angew Chem Int Ed 48(24):4376–4380. WILEY-VCH

14. Ichida H, Nagai K, Sasaki Y, Pope MT (1989) Heteropolyvanadates containing two and three manganese(IV) ions: unusual structural features of Mn2V22O6410- and Mn3V12O40H35. J Am Chem Soc 111(2):586–591

15. Inami S, Nishio M, Hayashi Y, Isobe K, Kameda H, Shimoda T (2009) Dinuclear manganese and cobalt complexes with cyclic polyoxovanadate ligands: synthesis and characterization of [Mn$_2$V$_{10}$O$_{30}$]$^{6-}$ and [Co$_2$(H$_2$O)$_2$V$_{10}$O$_{30}$]$^{6-}$. Eur J Inorg Chem 2009(34):5253–5258

16. Kurata T, Uehara A, Hayashi Y, Isobe K (2005) Cyclic polyvanadates incorporating template transition metal cationic species: synthesis and structures of hexavanadate [PdV$_6$O$_{18}$]$^{4-}$, octavanadate [Cu$_2$V$_8$O$_{24}$]$^{4-}$, and decavanadate [Ni$_4$V$_{10}$O$_{30}$(OH)$_2$(H$_2$O)$_6$]$^{4-}$. Inorg Chem 44 (7):2524–2530

17. Nishio M, Inami S, Hayashi Y (2013) Early-lanthanide complexes with all-inorganic macrocyclic polyoxovanadate ligands. Eur J Inorg Chem 10–11:1876–1881

18. Nishio M, Inami S, Katayama M, Ozutsumi K, Hayashi Y (2012) Lanthanide complexes of macrocyclic polyoxovanadates by VO4 units: synthesis, characterization, and structure elucidation by X-ray crystallography and EXAFS spectroscopy. Inorg Chem 51(2):784–793

19. Klemperer WG, Marquart TA, Yaghi OM (1992) New directions in polyvanadate chemistry: from cages and clusters to baskets, belts, bowls, and barrels. Angew Chem Int Ed Engl 31 (1):49–51. Hüthig & Wepf

20. Müller A, Reuter H, Dillinger S (1995) Supramolecular inorganic chemistry: small guests in small and large hosts. Angew Chem Int Ed Engl 34(21):2328–2361

21. Müller A, Krickemeyer E, Penk M, Walberg H-J, Bögge H (1987) Spherical mixed-valence [V15O36]$^{5⊖}$, an example from an unusual cluster family. Angew Chem Int Ed Engl 26 (10):1045–1046. Hüthig & Wepf

22. Kastner K, Margraf JT, Clark T, Streb C (2014) A molecular placeholder strategy to access a family of transition-metal-functionalized vanadium oxide clusters. Chemistry 20 (38):12269–12273

23. Kastner K, Forster J, Ida H, Newton GN, Oshio H, Streb C (2015) Controlled reactivity tuning of metal-functionalized vanadium oxide clusters. Chemistry 21(21):7686–7689

24. Chen L, Jiang F, Lin Z, Zhou Y, Yue C, Hong M (2005) A basket tetradecavanadate cluster with blue luminescence. Am Chem Soc 127(24):8588–8589

25. Zhang C-D, Liu S-X, Gao B, Sun C-Y, Xie L-H, Yu M, et al. (2007) Hybrid materials based on metal–organic coordination complexes and cage-like polyoxovanadate clusters: synthesis, characterization and magnetic properties. Polyhedron 26(7):1514–1522

26. Pan C-L, Xu J-Q, Li G-H, Chu D-Q, Wang T-G (2003) A three-dimensional framework of novel vanadium clusters bridged by [Ni(en)$_2$]$^{2+}$: Ni(en)$_3${V$^{IV}_{11}$V$^V_5$O$_{38}$Cl [Ni(en)$_2$]$_3$}· 8.5H$_2$O. Eur J Inorg Chem 2003(8):1514–1517. WILEY-VCH

27. Zhang L, Schmitt W (2011) From platonic templates to Archimedean solids: successive construction of nanoscopic {$V_{16}As_8$}, {$V_{16}As_{10}$}, {$V_{20}As_8$}, and {$V_{24}As_8$} polyoxovanadate cages. J Am Chem Soc 133(29):11240–11248

28. Breen JM, Schmitt W (2008) Hybrid organic-inorganic polyoxometalates: functionalization of V^{IV}/V^V nanosized clusters to produce molecular capsules. Angew Chem 120(36):7010–7014

29. Tucher J, Peuntinger K, Margraf JT, Clark T, Guldi DM, Streb C (2015) Template-dependent photochemical reactivity of molecular metal oxides. Chemistry 21(24):8716–8719

30. Tucher J, Nye LC, Ivanovic-Burmazovic I, Notarnicola A, Streb C (2012) Chemical and photochemical functionality of the first molecular bismuth vanadium oxide. Chemistry 18 (35):10949–10953

31. Tucher J, Streb C (2014) Visible light photooxidative performance of a high-nuclearity molecular bismuth vanadium oxide cluster. Beilstein J Nanotechnol 5:711–716

32. Streb C (2012) New trends in polyoxometalate photoredox chemistry: from photosensitisation to water oxidation catalysis. Dalt Trans 41(6):1651–1659

33. Nishiyama Y, Nakagawa Y, Mizuno N (2001) High turnover numbers for the catalytic selective epoxidation of alkenes with 1 atm of molecular oxygen. Angew Chem Int Ed Engl 40(19):3639–3641

34. Neumann R (2010) Activation of molecular oxygen, polyoxometalates, and liquid-phase catalytic oxidation. Inorg Chem 49(8):3594–3601

35. Sartorel A, Carraro M, Scorrano G, Bonchio M (2011) Water oxidation catalysis by molecular metal-oxides. Energy Procedia 22:78–87

36. Lv H, Geletii YV, Zhao C, Vickers JW, Zhu G, Luo Z, et al. (2012) Polyoxometalate water oxidation catalysts and the production of green fuel. Chem Soc Rev 41(22):7572–7589

37. Forster J, Rosner B, Khusniyarov MM, Streb C, Rösner B, Khusniyarov MM, et al. (2011) Tuning the light absorption of a molecular vanadium oxide system for enhanced photooxidation performance. Chem Commun 47(11):3114–3116

38. Seliverstov A, Streb C (2014) A new class of homogeneous visible-light photocatalysts: molecular cerium vanadium oxide clusters. Chemistry 20(31):9733–9738

39. Seliverstov A, Streb C (2014) Chirality meets visible-light photocatalysis in a molecular cerium vanadium oxide cluster. Chem Commun 50(15):1827–1829

40. Schwarz B, Forster J, Goetz MK, Yücel D, Berger C, Jacob T, et al. (2016) Visible-light-driven water oxidation by a molecular manganese vanadium oxide cluster. Angew Chem Int Ed 55 (21):6329–6333

41. Tucher J, Nye LC, Ivanovic-Burmazovic I, Notarnicola A, Streb C (2012) Chemical and photochemical functionality of the first molecular bismuth vanadium oxide. Chem Eur J 18 (35):10949–10953

42. Daniel C, Hartl H (2009) A mixed-valence V^{IV}/V^V alkoxo-polyoxovanadium cluster series [$V_6O_8(OCH_3)_{11}$]$^{n+/-}$: exploring the influence of a μ-oxo ligand in a spin frustrated structure. J Am Chem Soc 131(14):5101–1514

43. Mu A, Peters F, Pope MT, Gatteschi D (1998) Polyoxometalates: very large clusters-nanoscale magnets. Chem Rev 2665(98):239–271

44. Monakhov KY, Bensch W, Kogerler P (2015) Semimetal-functionalised polyoxovanadates. Chem Soc Rev 44(23):8443–8483. The Royal Society of Chemistry

45. Monakhov KY, Linnenberg O, Kozłowski P, van Leusen J, Besson C, Secker T, et al. (2015) Supramolecular recognition influences magnetism in [X@HV^{IV}_8 $V^V_{14}O_{54}$]$^{6-}$ self-assemblies with symmetry-breaking guest anions. Chemistry 21(6):2387–2397

46. Bassil BS, Dickman MH, Römer I, Von Der Kammer B, Kortz U (2007) The tungstogermanate [Ce20Ge10W100O 376(OH)4(H2O)30]56-: a polyoxometalate containing 20 cerium(III) atoms. Angew Chem Int Ed Engl 46(32):6192–6195

Polyoxometalate-Based Photo-Sensitive Functional Hybrid Materials

Chang-Gen Lin, Wei Chen, and Yu-Fei Song

Abstract The photochemical behaviors of polyoxometalates (POMs) have been extensively studied and widely used in various photo-redox reactions. Incorporating photo-sensitive organic molecules onto the POM platform not only allows the rational design and fine-controlled synthesis of novel organic–inorganic hybrids but also gives the possibility to explore their potential applications in diverse areas such as photochromics, optical switching, and smart self-assemblies. Herein, we summarize the latest progress of photo-sensitive POM hybrids with a particular focus on the photo-induced reversible coloration, polymerization, and supramolecular self-assembly. The mechanisms and the crucial roles of POM clusters in such reversible processes are also considered.

Keywords Azobenzene • Coumarin • Photo-sensitive • Polyoxometalate • Spiropyran

Contents

C.-G. Lin and Y.-F. Song (✉)
State Key Laboratory of Chemical Resource Engineering, Beijing University of Chemical Technology, Beijing 100029, P. R. China

Beijing Advanced Innovation Center for Soft Matter Science and Engineering, Beijing University of Chemical Technology, Beijing 100029, P. R. China
e-mail: songyf@mail.buct.edu.cn; songyufei@hotmail.com

W. Chen
State Key Laboratory of Chemical Resource Engineering, Beijing University of Chemical Technology, Beijing 100029, P. R. China

1   Introduction

Polyoxometalates (POMs) represent a large family of versatile and discrete polyanions, which are usually formed by condensation of early transition metal oxides in acid solution [1–4]. Such oxygen clusters exhibit attractive properties such as dynamic structure complexity, multi-electron redox, and Brønsted acidity, thus leading to a diverse range of applications ranging from catalysis, medicine, to materials science [5–10].

Perhaps one of the most intriguing properties of POMs lies in the photo-redox reactions of such clusters that can be easily processed in the presence of sacrifice and reoxidation agents. The reduced POMs, or the so-called heteropoly blues, have been intensively studied and used for colorimetric analysis and catalysis. The photochemistry of POMs both in solution and in solid state has been well-documented in several excellent reviews [11, 12]. To put it simply, electrons from the low-energy oxygen 2p orbitals (HOMO) will be promoted to the high-energy metal d orbitals (LUMO) upon irradiation due to the $O \rightarrow M$ ligand-to-metal charge transfer (LMCT), thus leading to a photoexcited state of highly oxidized POM clusters which can be readily reduced into heteropoly blues in the presence of sacrifice agents. The reduced form is often possible to be reoxidized into the ground state by using molecular oxygen or hydrogen peroxide. Another advantage of the photoexcited $O \rightarrow M$ LMCT bands is the photoluminescence and intramolecular energy transfer in POM solids, especially in the lanthanide-containing POMs. For example, the photoexcitation of the $O \rightarrow W$ LMCT bands in the Weakley-type POM, $Na_9[EuW_{10}O_{36}] \cdot 32H_2O$, leads to a strong Eu^{3+} emission which arises from the $^5D_0$ excited state of Eu^{3+} and terminates at the ^7F_j ground state [11]. Once the intramolecular energy transfer is interrupted, fluorescence quenching of Eu^{3+} will be observed. Such "on/off" state of lanthanide-containing POMs has been used as an effective tool in sensing [13].

Apart from the extraordinary chemical and physical properties of POM anions, one common problem faced during practical applications is the poor processibility of the highly crystallized POM clusters. Large efforts such as the immobilization of POMs onto supporters have been allocated to solve this problem. However, in most of the cases weak non-covalent interactions between POM anions and the counter-parts are used, which inevitably results in another tricky issue of leaking. Covalent modification of POMs seems to be promising since it offers several advantages that non-covalent interactions can hardly compete [14–16]. Moreover, the covalent strategy gives rise to products with well-defined anchoring modes and stoichiometry, thus leaving the resulting hybrids with predictable architectures and fine-tuned

properties. In this article, we focus on the recent development of covalently modified POM hybrids that exhibit photo-sensitive features and their applications in self-assembly formulation and photochromics will also be discussed. In accordance with previous definition, the term "hybrid" will refer to covalently modified species [16].

2 Covalent Modification Methods

Organically functionalized POM hybrids give rise to materials that possess physical properties fundamentally different from their parent two parts. The resulting synergistic effects between the organic and inorganic moieties often offer extraordinary enhanced performances in practical applications. Moreover, the covalently modified POMs provide building blocks that are capable to be further functionalized into giant self-assembled architectures [17, 18]. However, currently the POM hybrids are still synthetically challenging and only a few types of clusters could be modified. The methodologies of modification of POMs (*direct functionalization* and *post-functionalization*) have been summarized in several outstanding reviews [14–16, 19–21], so here in this section we will give a very brief introduction.

Lindqvist POMs The hexamolybdate anion, $[Mo_6O_{19}]^{2-}$, which is also known as Lindqvist POM, has six reactive terminal oxygen atoms that are apt to be partially [20] or completely [22] substituted with organoimido ligands (Fig. 1). The resulting organoimido hybrids with strong d–pπ covalent bonds dramatically modify the electronic and redox properties of the Lindqvist cluster. Another type of organically modified Lindqvist cluster is the $\{V_6O_{13}((OCH_2)_3CR)_2\}^{2-}$ (R = CH_3, CH_2CH_3, CH_2OH, NO_2, and NH_2), which can be prepared from the $\{H_3V_{10}O_{28}\}^{3-}$ cluster in the presence of tripodal alcohols [23, 24].
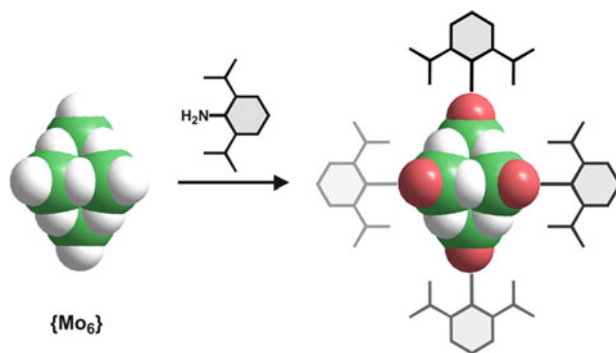
Fig. 1 Schematic view of the organoimido functionalized Lindqvist cluster [22]. {Mo$_6$} stands for $\{Mo_6O_{19}\}^{2-}$
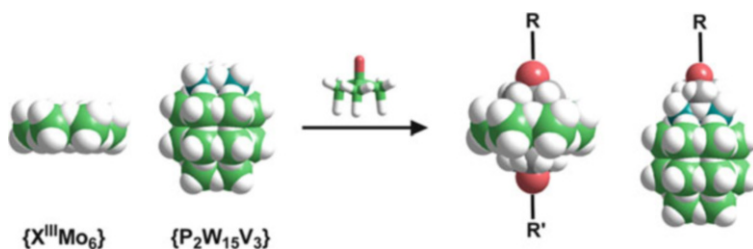
Fig. 2 Schematic illustration of the tripodal alcohol modified Anderson cluster and Dawson cluster. $\{X^{III}Mo_6\}$ is short for $\{X^{III}(OH)_6Mo_6O_{18}\}^{3-}$, where X stands for transition metals such as Mn, Fe, Cr, Al, etc.; $\{P_2W_{15}V_3\}$ represents $\{P_2W_{15}V_3O_{62}\}^{9-}$ Dawson cluster

Anderson POMs The functionalization of Anderson polyanions is first reported by Hasenknopf et al. [25] and then fully developed by Song et al. [26–30] This well-established method is mainly based on the $\{Mn^{III}Mo_6O_{18}((OCH_2)_3CNH_2)_2\}^{3-}$ cluster, which can be easily generated from the $\{\alpha\text{-}Mo_8O_{26}\}^{4-}$ cluster. Latest researches by authors' group and other groups reveal a more facile route for the synthesis of such tripodal alcohol modified hybrids by using the B-type Anderson cluster as parent POM [31–33]. A detailed survey of the functionalization methods of Anderson cluster and the applications of the resulting hybrids have been reviewed recently [21].

Dawson and Keggin POMs Except the V-substituted Dawson cluster [34–36] which can be modified by tripodal alcohols (Fig. 2), the rest of the Dawson and Keggin hybrids are prepared by grafting addenda organometallic compounds onto the lacunary POM clusters. Organosilyl, organostannyl, and organophosphoryl are the most common organometallic reagents used. Readers can refer to those brilliant reviews and the references thereafter for more detailed discussions [14–16].

3 Photo-Sensitive Polyoxometalate Hybrids

Based on the covalent modification methods, various organic photo-sensitive and photochromic molecules have been attached onto POM clusters to investigate the fascinating intramolecular electron transfer and charge separation between the two counterparts under irradiation. Such POM hybrids are considered to be potentially suitable as optical switches, photosensors, and even smart windows. In this section, we will review the latest progresses made in this field.

3.1 Spiropyran-Containing Polyoxometalate Hybrids

Spiropyrans (SPs) are dynamic molecules that can switch reversibly between the two isomers of the closed SP form and the opened merocyanine (MC) form in response to stimuli such as light, temperature, and mechanical stress [37]. SPs have been widely investigated and employed for the construction of light-responsive systems due to their high performance in optical coloration. Oms et al. [38] first studied the photo-/electrochromic properties of SP-containing POM hybrids by tethering SP-Tris derivatives on to Anderson-type cluster (Fig. 3). It was demonstrated that the strong covalent bonds developed a remarkable photochromic effect and a fast coloration speed when compared to the electrostatically associated ones [39]. Moreover, the free amino group in the asymmetrically modified SP-Anderson cluster **1** allows the further functionalization, thus offering the opportunity to elaborate more sophisticated assemblies.

Bearing in this in mind, Chu et al. [40] developed a new type of amphiphiles by combining the SP fragment and a long alkyl chain onto a hydrophilic Anderson cluster (Fig. 4). Due to the amphiphilic nature, the hybrids self-assembled into nanosized vesicles and reverse vesicles in polar solvents and nonpolar solvents, respectively. More importantly, the self-assembly process of the vesicles could be triggered by UV irradiation because of the structural isomerization of SP moieties. The obtained reverse vesicles, on the other hand, remained unaffected when irradiated either with UV or visible light.

Besides the photo-sensitive SP molecules, the same catalogue spironaphthoxazines (SNs) which exhibit more fatigue resistance have also been incorporated into POM hybrids. For example, symmetrically modified SN-Anderson-SN and asymmetrically modified SN-Anderson-SP hybrids have been successfully fabricated (Fig. 5). It was evidenced that the SN-Anderson-SP hybrids were highly effective solid-state photochromic materials. Controlled experiments of the
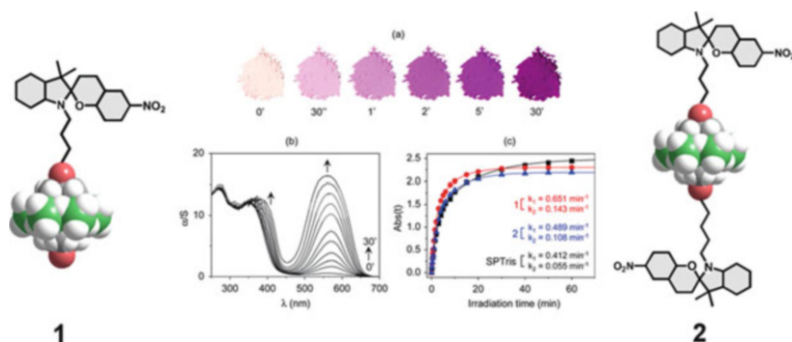
Fig. 3 Schematic representation of asymmetrically modified SP-Anderson cluster (**1**) and symmetrically modified SP-Anderson cluster (**2**). (**a**) *Color changes* of **1** at different UV 365 nm irradiation times; (**b**) Kubelka–Munk transformed reflectivity spectra of **1** under 365 nm irradiation; and (**c**) the absorption/time plots of **1**, **2**, and SP-Tris [38]
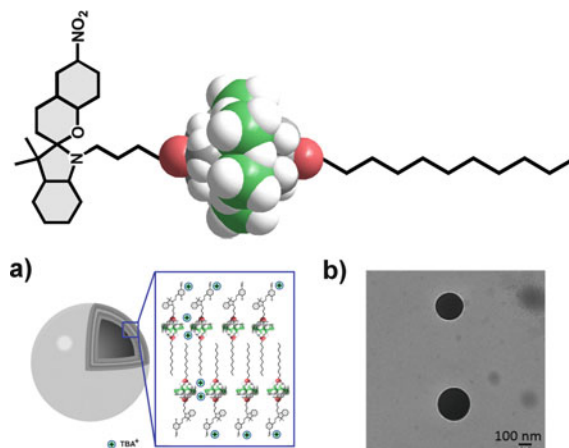
Fig. 4 *Top*: Schematic view of the asymmetrical SP-Anderson amphiphile; *bottom*: (**a**) the self-assembled model of the asymmetrical SP-Anderson hybrid in polar solvents, and (**b**) TEM image of the asymmetrical SP-Anderson hybrid in 2.5 v/v% water/acetonitrile solution [40]
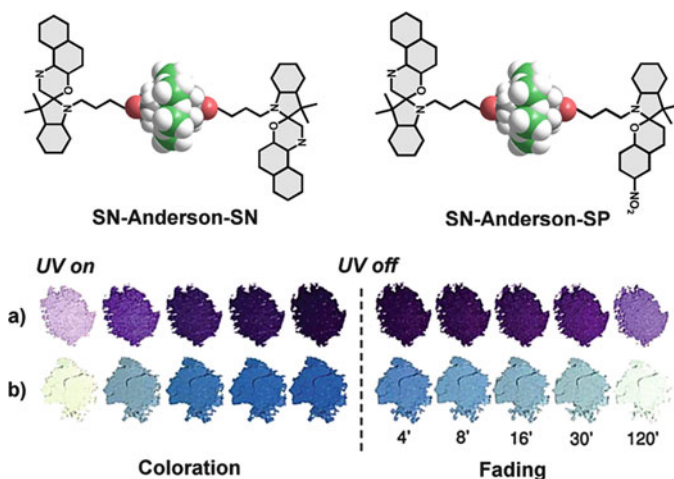
Fig. 5 *Top*: Representation of the SN-Anderson-SN and SN-Anderson-SP hybrids; *bottom*: *color changes* of: (**a**) SN-Anderson-SP powders and (**b**) SN-Anderson-SN powders upon UV 365 nm irradiation (*coloration*) and without irradiation (*fading*). Note: the *pink color* of SN-Anderson-SP is attributed to the initially photo-activated SP group [41]

SN-Tris derivatives showed that such pure organic molecules in solid states were hardly photochromic, which demonstrated the crucial role of POM clusters on the optical properties of such materials. In addition, the SN-Anderson-SN hybrids showed a relatively faster thermal fading process and a better anti-fatigue performance when compared to the SP groups modified ones [41]. Aside from the

aforementioned SP modified Anderson hybrids, the Keggin-type hybrids bearing one or two SP fragments and highly fluorescent boron-dipyrromethene (BODIPY) functionalized Anderson hybrids were also reported [42, 43].

3.2 Coumarin-Containing Polyoxometalate Hybrids

Due to the strong UV absorption and high radiative quantum yield, coumarins have been widely used as laser dyes, fluorescent probes, and photo-sensitizers. Another fascinating property of coumarins lies in the photo-triggered cycloaddition reactions that will lead to photodimerization processes. Recently, authors' group synthesized a series of coumarin-containing POM hybrids and the photochemistry of such materials had been systematically investigated. The first example would be the coumarin-Anderson cluster, which undergoes a remarkable optical behavior when irradiated at UV 365 nm (Fig. 6). [2 + 2] cycloadditions between the coumarin moieties were clearly observed in the UV absorption spectra and had been unambiguously demonstrated in ^{1}H NMR and 2D COSY NMR. Dynamic light scanning analysis before and after UV 365 nm irradiation showed dramatic increase in particle size. Obvious color changes upon irradiation could be also observed from light orange to deep brown. To strengthen the potential applications of such photoswitchable process, the coumarin-Anderson hybrids were embedded into polymer matrix giving rise to a solid-state film sample. Similar to the performance in solution, the film sample exhibited reversible coloration and fading process over five consecutive cycles of UV 365 and 254 nm irradiation [44].

To broaden our understanding of the coumarin-containing POM hybrids during such photo-triggered coloration phenomenon, we chose to modify the V-substituted Dawson cluster with coumarin-Tris derivative (Fig. 7). The obtained hybrids were somehow different from the coumarin-Anderson ones since only one coumarin
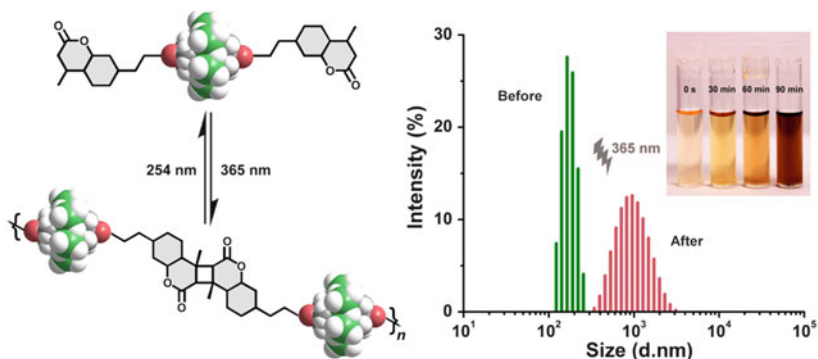
Fig. 6 *Left*: schematic illustration of the reversible photopolymerization process of coumarin-Anderson hybrids; *right*: size distributions of coumarin-Anderson hybrids before and after irradiation. *Inset*: photographs of the *coloration* process of coumarin-Anderson upon 365 nm irradiation [44]
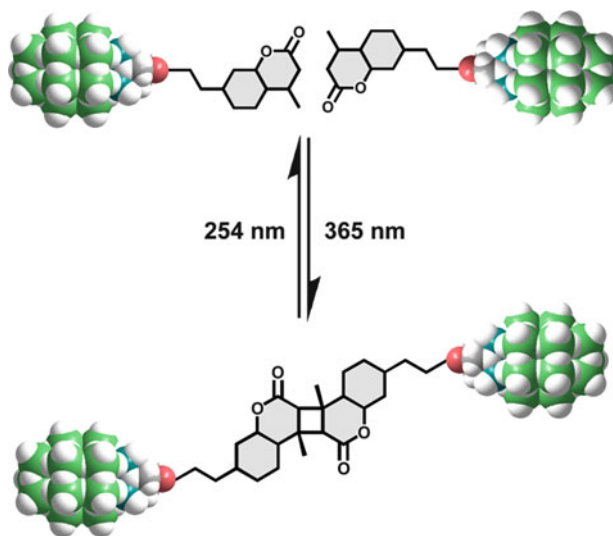
Fig. 7 Schematic view of the photodimerization process of coumarin-Dawson hybrid under UV irradiation

moiety was attached onto the POM platform and photodimerization was implemented instead. The photo-controlled reversible dimerization had been proved by UV-Vis, 2D COSY NMR, and ESI-MS analysis. Moreover, a second photo-assistant process was observed in the Dawson cluster as the reduction of V^{V} to V^{IV} was clearly confirmed by X-ray photoelectron spectroscopy and electron paramagnetic resonance. On the contrary, no clear evidence was obtained in the unmodified Dawson cluster, which verified the importance of the covalent modification and the corresponding synergistic effects between the organic moieties and the inorganic clusters [45].

Similar to coumarins, chalcone molecules also possess photo-sensitive α,β-unsaturated carbonyl groups, which are capable to carry out fast [2 + 2] cyclo-addition reaction under UV initiation. Thus, chalcone-containing POM hybrid was also prepared and fully investigated in our group (Fig. 8). For example, when irradiated at UV 365 nm the hybrid underwent a [2 + 2] cycloaddition reaction, leading to an absorbance decrease at 332 nm and a new absorbance peak at 245 nm attributed to the generated cyclobutane structure. This process gave a total photopolymerization conversion of 37.45% and was found able to restore when exposed to UV light of 254 nm. After five cycles of alternative irradiation at 365 and 254 nm, the amount of the hybrid monomer still maintained at 85%. ^{1}H NMR spectrum of the hybrid also exhibited significant changes when irradiated at 365 nm. Signals of the unsaturated carbonyl group of the chalcone moieties at $\delta = 7.83$ and 7.73 ppm shifted to high field after irradiation and gave corresponding cyclobutane signal at $\delta = 4.80$ ppm. These results were in good agreement with the UV-Vis analysis. The weight-average molecular weight of the hybrid polymer was examined to be
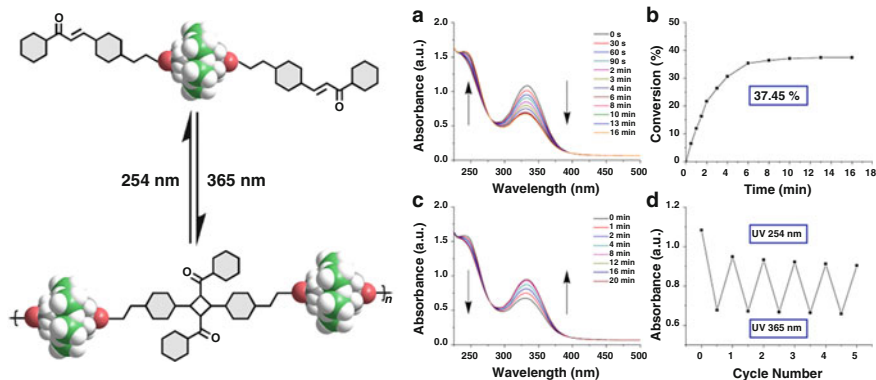
Fig. 8 *Left*: representation of photo-controlled polymerization of chalcone-Anderson hybrids; *right*: (**a**) UV-Vis spectra of chalcone-Anderson under UV 365 nm irradiation, (**b**) the photopolymerization conversion ratio of chalcone-Anderson hybrid, (**c**) UV-Vis spectra of the photo-disassociation under UV 254 nm irradiation, and (**d**) cycle experiment of alternative irradiation at 365 and 254 nm [46]

9.78×10^5 g/mol as demonstrated by the gel permeation chromatography analysis [46].

3.3 Azobenzene-Containing Polyoxometalate Hybrids

Azobenzene derivatives constitute a large family of photo-sensitive molecules and have been intensively investigated as promising candidates in various applications such as photo-switches, optical memory materials, and protein probes. Azobenzene derivatives can undergo reversible *trans/cis* isomerizations when irradiated with appropriate light sources and exhibit remarkable photo-stability [47].

We recently prepared a category of azobenzene-Anderson hybrids and carefully examined their polymolecular aggregation processes with ion-mobility mass spectrometry (IMS-MS) [48]. IMS-MS emerged as an efficient tool in monitoring the structure and conformational dynamics of proteins and coordination compounds. By using this powerful technique, we were able to investigate the conformational changes of the photo-sensitive azobenzene-Anderson hybrids in solution (Fig. 9). After 5 min consecutive irradiation under UV 365 nm light, the azobenzene-Anderson hybrids were then quickly transferred into the IMS-MS device for measurements. To our surprise, only quaternary structures of the hybrids with four or more TBA counter cations were observed, which strongly indicated the existence of high π–π interactions between azobenzene moieties. The conformational changes resulted in a significant difference in the drift time spectra where the equilibria for the formation of quaternary structures clearly shifted. The much higher intensity for the peak of dimeric assembly centered on a drift time of
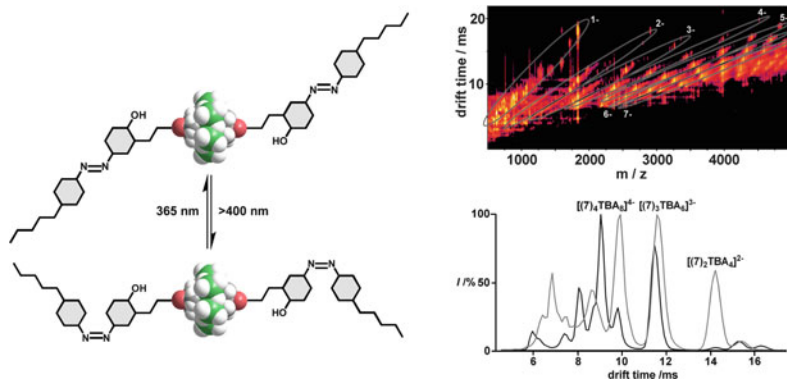
Fig. 9 *Left*: switching of the photo-sensitive azobenzene-containing Anderson cluster; *right*: 2D IMS/MS spectrum of azobenzene-containing Anderson cluster and the comparison of drift time before and after UV irradiation [48]

14.22 ms after 365 nm irradiation clearly indicated a higher stability of the azobenzene-Anderson hybrids in the *cis* conformation when compared to that in the *trans* conformation. As demonstrated above, π–π stacking of the azobenzene molecules plays a crucial role during the self-assembly or aggregation process of azobenzene-containing POM hybrids. More convincing evidences could be obtained by investigating the assembly behaviors of such amphiphilic hybrids in mixed polar solvents. To this end, photo-responsive azobenzene moieties had been grafted onto the lacunary Keggin cluster [49]. The hydrophilic/hydrophobic interactions of the azobenzene-containing Keggin POMs drove the hybrid assembled into 0D nanospheres in acetonitrile-dominating acetonitrile/water mixture. Gradually increasing the water contents in mixed solvents would induce the hydrophobic packing of azobenzene moieties and thus enhance the π–π interactions among them. Such variations allowed the switching of assembled structures from 0D nanospheres into 1D nanorods.

Liquid crystals (LCs) represent a diverse class of soft matter materials that exhibit anisotropic and switching properties. The inherent rigidity of azobenzene groups renders them as mesogens in the construction of LCs. As such, we adopted a straightforward procedure to prepare liquid crystalline azobenzene-containing POM hybrids by anchoring dendritic gallic acid derivatives on to lacunary Keggin clusters [50]. As demonstrated by the differential scanning calorimetry (DSC), optical polarized microscopy (OPM), and small-angle X-ray scattering (SAXS) analyses, all the POM hybrids exhibited a lamellar smectic A phase with interlayer distances independent of temperature and a neighboring POM cluster distance of 12.4 Å. It should be underlined that the pure organic azobenzene-embedded gallic acid derivatives were found to display no liquid crystalline properties at all, which manifested the importance of POM clusters in the construction of LCs.

Besides the advantages of azobenzene fragments in the preparation of liquid crystalline soft materials, the *trans/cis* isomerization of such functional groups also
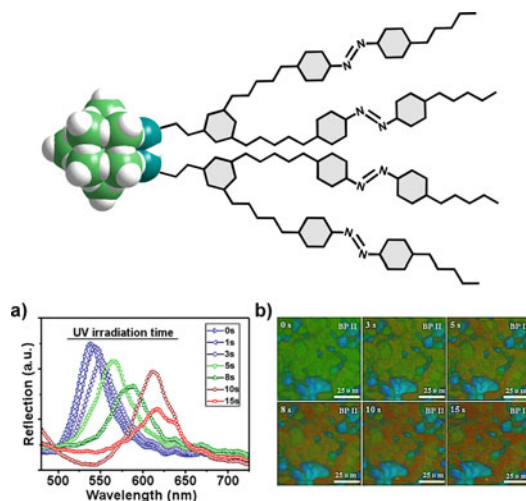
Fig. 10 *Top*: schematic presentation of the azobenzene-containing Keggin cluster; *bottom*: (**a**) the reflectance spectrum of POM-doped blue phase liquid crystals under UV irradiation, and (**b**) the *reflective color* of POM-doped blue phase liquid crystals in polarized microscopy under UV irradiation [50]

leaves the possibility to finely control the transformation of mesogenic phases and optical switching of LCs. To this end, a similar type of dendritic azobenzene-containing POM hybrid was fabricated, and its applications in stabilizing the blue phase (BP) LCs as well as in optically switching the Bragg reflection band of BPs were also investigated (Fig. 10). BPs are 3D ordered phases which can be observed in cholesteric LCs with strong chirality strength. In despite of their promising efficient LC display and emerging photonic applications, the fact that BP LCs are limited to only one or two degrees temperature range due to their high free energies of the disclination lines drastically restricts the application of BP LCs. When POM hybrids were physically doped into the BP samples, the stabilization temperature range of BP was expanded to 7.5 °C. Moreover, when the POM hybrids doped BP samples were exposed to UV 365 nm light, a clear red shift from 539 to 617 nm of the Bragg reflection bands was observed because of the *trans* to *cis* isomerization of azobenzene moieties. Various BP platelet colors from green to red were also observed with UV irradiation under polarized microcopy. Such stabilization and optical switching of BP LCs could be explained as follows: firstly, the azobenzene-containing POM hybrids induced the increase of bending K_{33} elastic constant, which was beneficial in stabilizing BP samples; secondly, the transformation from *trans* to *cis* isomer of the azobenzene groups in POM hybrids resulted in the extension of the double twisted cylinder structure of BPs, thus leading to an increase in the lattice constant [51].

Self-assemblies that can be modulated by external stimuli and gave dynamic morphological transitions are of great interests in smart functional materials. In
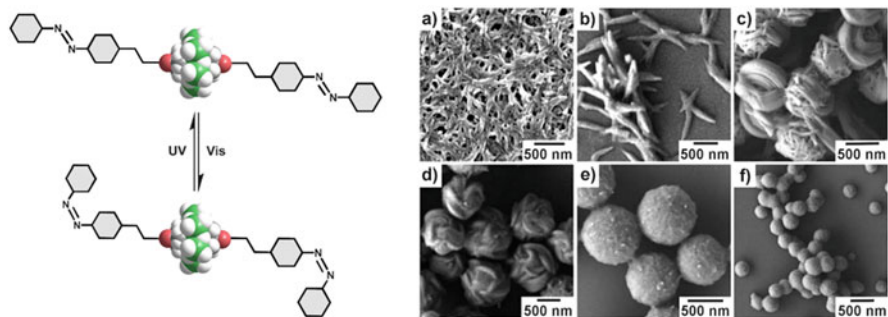
Fig. 11 *Left*: the structural isomerization of azobenzene-Anderson hybrid under UV and visible light; *right*: SEM images of surfactant encapsulated azobenzene-Anderson hybrids in CHCl₃/CH₃OH solution after: (**a**) 0, (**b**) 1, (**c**) 5, (**d**) 15, (**e**) 30, and (**f**) 120 min of UV 365 nm irradiation [52]

2010, Yan et al. [52] reported an example of azobenzene-functionalized Anderson cluster, which exhibited reversible aggregation changes as a result of photo-controlled structure alternation. As shown in Fig. 11, surfactant dimethyl-dioctadecylammonium encapsulated azobenzene-Anderson hybrids gave a fiber-like morphology in the *trans* state, while upon UV irradiation such fiber-like structures gradually transferred into spheres. Leaving the self-assembled spherical structure either in visible light or in the dark, it could switch back to fibers. Such reversible photo-controlled morphological changes were revealed to be manipulated by the destruction and rebuilding of the hydrogen bonds between azobenzene moieties and the Anderson cluster through photo-irradiation. By using the same azobenzene-containing Anderson hybrid and a pyridine-modified cyclodextrin cation, the same group constructed a self-crosslinking complex system which showed a photo-controllable chiral assembly process [53].

3.4   Other π-Conjugated Polyoxometalate Hybrids

Thanks to the versatile covalent modification methods, a large amount of π-conjugated organic molecules have been tethered onto the skeletons of POM clusters up to date. These functional molecules include pyrene [54], porphyrin [55–58], perylene [59], fullerene [60, 61], and polypyridinyl complexes [62–65]. Since the photochemistry and photophysics of these POM hybrids have been well-documented in several remarkable reviews [66–68], we will not give further statements here.

4 Conclusion

In summary, we have discussed the synthetic methodologies and the recent developments of photo-sensitive POM-based hybrid materials in photochromics, optical switching, and smart self-assembly. Interestingly, the choice of methodology and the type of POM clusters have a profound influence on the functional performance of such POM hybrids. In addition, the close interactions between POM clusters and the covalently attached organic fragments favor the electron transfer process between the two subunits, which might be of great potential in photocatalysis, water oxidation, photovoltaics, and even solar cells.

References

 1. Long D-L, Burkholder E, Cronin L (2007) Chem Soc Rev 36:105–121
 2. Long D-L, Tsunashima R, Cronin L (2010) Angew Chem Int Ed Engl 49:1736–1758
 3. Hill CL (1998) Chem Rev 98:1–2
 4. Cronin L, Müller A (2012) Chem Soc Rev 41:7333–7334
 5. Wang S-S, Yang G-Y (2015) Chem Rev 115:4893–4962
 6. Omwoma S, Chen W, Tsunashima R, Song Y-F (2014) Coord Chem Rev 258–259:58–71
 7. Rhule JT, Hill CL, Judd DA (1998) Chem Rev 98:327–357
 8. Bijelic A, Rompel A (2015) Coord Chem Rev 299:22–38
 9. Song Y-F, Tsunashima R (2012) Chem Soc Rev 41:7384–7402
10. Ji Y, Huang L, Hu J, Streb C, Song Y-F (2015) Energy Environ Sci 8:776–789
11. Yamase T (1998) Chem Rev 98:307–325
12. Streb C (2012) Dalton Trans 41:1651–1659
13. Wang X, Wang J, Tsunashima R, Pan K, Cao B, Song Y-F (2013) Ind Eng Chem Res 52:2598–2603
14. Proust A, Thouvenot R, Gouzerh P (2008) Chem Commun 1837–1852
15. Dolbecq A, Dumas E, Mayer CR, Mialane P (2010) Chem Rev 110:6009–6048
16. Proust A, Matt B, Villanneau R, Guillemot G, Gouzerh P, Izzet G (2012) Chem Soc Rev 41:7605–7622
17. Macdonell A, Johnson NAB, Surman AJ, Cronin L (2015) J Am Chem Soc 137:5662–5665
18. Izzet G, Abécassis B, Brouri D, Piot M, Matt B, Serapian SA, Bo C, Proust A (2016) J Am Chem Soc 138:5093–5099
19. Peng Z (2004) Angew Chem Int Ed Engl 43:930–935
20. Zhang J, Xiao F, Hao J, Wei Y (2012) Dalton Trans 41:3599–3615
21. Blazevic A, Romel A (2016) Coord Chem Rev 307:42–64
22. Strong JB, Haggerty BS, Rheingold AL, Maatta EA (1997) Chem Commun 1137–1138
23. Chen Q, Goshorn DP, Scholes CP, Tan X-L, Zubieta J (1992) J Am Chem Soc 114:4667–4681
24. Li D, Song J, Yin P, Simotwo S, Bassler AJ, Aung Y, Roberts JE, Hardcastle KI, Hill CL, Liu T (2011) J Am Chem Soc 133:14010–14016
25. Hasenknopf B, Delmont R, Herson P, Gouzerh P (2002) Eur J Inorg Chem 1081–1087

26. Song Y-F, Long D-L, Cronin L (2007) Angew Chem Int Ed Engl 46:3900–3904
27. Song Y-F, Long D-L, Kelly SE, Cronin L (2008) Inorg Chem 47:9137–9139
28. Song Y-F, McMillan N, Long D-L, Kane S, Malm J, Riehle MO, Pradeep CP, Gadegaard N, Cronin L (2009) J Am Chem Soc 131:1340–1341
29. Song Y-F, Long D-L, Cronin L (2010) CrystEngComm 12:109–115
30. Yvon C, Macdonell A, Buchwald S, Surman AJ, Follet N, Alex J, Long D-L, Cronin L (2013) Chem Sci 4:3810–3817
31. Wu P, Yin P, Zhang J, Hao J, Xiao Z, Wei Y (2011) Chem Eur J 17:12002–12005
32. Lin C-G, Chen W, Long D-L, Cronin L, Song Y-F (2014) Dalton Trans 43:8587–8590
33. Ai H, Wang Y, Li B, Wu L (2014) Eur J Inorg Chem 2766–2772
34. Zeng H, Newkome GR, Hill CL (2000) Angew Chem Int Ed Engl 39:1772–1774
35. Pradeep CP, Long D-L, Newton GN, Song Y-F, Cronin L (2008) Angew Chem Int Ed Engl 47:4388–4391
36. Pradeep CP, Misdrahi MF, Li F-Y, Zhang J, Xu L, Long D-L, Liu T, Cronin L (2009) Angew Chem Int Ed Engl 48:8309–8313
37. Klajn R (2014) Chem Soc Rev 43:148–184
38. Oms O, Hakouk K, Dessapt R, Deniard P, Jobic S, Dolbecq A, Palacin T, Nadjo L, Keita B, Marrot J, Mialane P (2012) Chem Commun 48:12103–12105
39. Mialane P, Zhang G, Mbomekalle IM, Yu P, Compain J-D, Dolbecq A, Marrot J, Sécheresse F, Keita B, Nadjo L (2010) Chem Eur J 16:5572–5576
40. Chu Y, Saad A, Yin P, Wu J, Oms O, Dolbecq A, Mialane P, Liu T (2016) Chem Eur J 22:11756–11762
41. Saad A, Oms O, Marrot J, Dolbecq A, Hakouk K, El Bekkachi H, Jobic S, Deniard P, Dessapt R, Garrot D, Boukheddaden K, Liu R, Zhang G, Keita B, Mialane P (2014) J Mater Chem C 2:4748–4758
42. Parrot A, Izzet G, Chamoreau L-M, Proust A, Oms O, Dolbecq A, Hakouk K, El Bekkachi H, Deniard P, Dessapt R, Mialane P (2013) Inorg Chem 52:11156–11163
43. Saad A, Oms O, Dolbecq A, Menet C, Dessapt R, Serier-Brault H, Allard E, Baczko K, Mialane P (2015) Chem Commun 51:16088–16091
44. Tong U, Chen W, Ritchie C, Wang X, Song Y-F (2014) Chem Eur J 20:1500–1504
45. Chen W, Tong U, Zeng T, Streb C, Song Y-F (2015) J Mater Chem C 3:4388–4393
46. Zhang J, Long Y, Xuan W, Lin C-G, Song Y-F (2017) Chin Sci Bull 62:685–692
47. Bandara HMD, Burdette SC (2012) Chem Soc Rev 41:1809–1825
48. Thiel J, Yang D, Rosnes MH, Liu X, Yvon C, Kelly SE, Song Y-F, Long D-L, Cronin L (2011) Angew Chem Int Ed Engl 50:8871–8875
49. Chen W, Ma D, Yan J, Boyd T, Cronin L, Long D-L, Song Y-F (2013) ChemPlusChem 78:1226–1229
50. Lin C-G, Chen W, Omwoma S, Song Y-F (2015) J Mater Chem C 3:15–18
51. Wang J, Lin C-G, Zhang J, Wei J, Song Y-F, Guo J (2015) J Mater Chem C 3:4179–4187
52. Yan Y, Wang H, Li B, Hou G, Yin Z, Wu L, Yam VWW (2010) Angew Chem Int Ed Engl 49:9233–9236
53. Yue L, Ai H, Yang Y, Lu W, Wu L (2013) Chem Commun 49:9770–9772
54. Matt B, Renaudineau S, Chamoreau L-M, Afonso C, Izzet G, Proust A (2011) J Org Chem 76:3107–3112
55. Harriman A, Elliott KJ, Alamiry MAH, Le Pleux L, Séverac M, Pellegrin Y, Blart E, Fosse C, Cannizzo C, Mayer CR, Odobel F (2009) J Phys Chem C 113:5834–5842
56. Elliott KJ, Harriman A, Le Pleux L, Pellegrin Y, Blart E, Mayer CR, Odobel F (2009) Phys Chem Chem Phys 11:8767–8773
57. Allain C, Schaming D, Karakostas N, Erard M, Gisselbrecht J-P, Sorgues S, Lampre I, Ruhlmann L, Hasenknopf B (2013) Dalton Trans 42:2745–2754
58. Ahmed I, Farha R, Huo Z, Allain C, Wang X, Xu H, Goldmann M, Hasenknopf B, Ruhlmann L (2013) Electrochim Acta 110:726–734

59. Odobel F, Séverac M, Pellegrin Y, Blart E, Fosse C, Cannizzo C, Mayer CR, Elliott KJ, Harriman A (2009) Chem Eur J 15:3130–3138
60. Bonchio M, Carraro M, Scorrano G, Bagno A (2004) Adv Synth Catal 346:648–654
61. Zhou S, Feng Y, Chen M, Li Q, Liu B, Cao J, Sun X, Li H, Hao J (2016) Chem Commun 52:12171–12174
62. Duffort V, Thouvenot R, Afonso C, Izzet G, Proust A (2009) Chem Commun 6062–6064
63. Matt B, Coudret C, Viala C, Jouvenot D, Loiseau F, Izzet G, Proust A (2011) Inorg Chem 50:7761–7768
64. Matt B, Moussa J, Chamoreau L-M, Afonso C, Proust A, Amouri H, Izzet G (2012) Organometallics 31:35–38
65. Santoni M-P, Pal AK, Hanan GS, Tang M-C, Furtos A, Hasenknopf B (2014) Dalton Trans 43:6990–6993
66. Santoni M-P, Hanan GS, Hasenknopf B (2014) Coord Chem Rev 281:64–85
67. Walsh JJ, Bond AM, Forster RJ, Keyes TE (2016) Coord Chem Rev 306:217–234
68. Izzet G, Volatron F, Proust A (2017) Chem Rec 17:250–266

Porous Ionic Crystals
Based on Polyoxometalates

Sayaka Uchida

Abstract The properties of porous ionic crystals based on polyoxometalate (POM) anions, which are different from conventional porous crystalline materials such as zeolites and metal-organic frameworks (MOFs), can be summarized as follows: (a) POMs show reversible redox properties, which can lead to the formation of "redox-active" porous ionic crystals. (b) Specific functions such as guest binding and catalytically active sites can be incorporated beforehand into the ionic components, and these functions can be maintained and utilized after complexation of the ionic components since they still exist as discrete molecules in the crystal lattice. (c) The ionic components create strong electrostatic fields at internal surfaces, which are suitable for accommodation and stabilization of polar guests and cationic intermediates. (d) Since Coulomb interaction works isotropically in a long range, the crystal structures are often flexible and can transform to adapt to specific guests. Crystal structures of porous ionic crystals can be controlled by the appropriate choice of elements, charges, sizes, symmetry, or ligands of the ionic components. These properties and control of structural features lead to interesting functions in gas adsorption/separation, ion-exchange and conduction, heterogeneous catalysis, reduction-induced highly selective ion uptake, etc., which are unique to porous ionic crystals.

Keywords Adsorption • Heterogeneous catalysis • Ionic crystal • Metal carboxylate • Polymorph • Polyoxometalate • Porous structure • Redox • Self-assembly

S. Uchida (✉)
School of Arts and Sciences, The University of Tokyo, Tokyo, Japan
e-mail: csayaka@mail.ecc.u-tokyo.ac.jp

Contents

1 Introduction

Porous crystalline materials such as zeolites and metal-organic frameworks (MOFs) have attracted wide attention due to their well-defined porous structures and high surface area, which are useful in gas storage and separation, heterogeneous catalysis, ion-exchange and conduction, etc. Polyoxometalates (POMs) are nano-sized metal-oxide molecular anions (macroanions) with unique catalytic, electrochemical, magnetic, and luminescent properties and have stimulated research in broad fields of science. Recently, incorporation of POMs in nano-sized cavities of MOFs have been reported, and these POM–MOFs show unique functions such as oxidative removal of hydrogen sulfide, selective adsorption of cationic dyes, visible-light driven hydrogen production, etc. [1–5]. On the other hand, we have reported that the complexation of POMs with molecular cations (macrocations) having appropriate elements, charges, sizes, symmetry, or ligands enables anisotropic packing and/or utilization of anisotropic interactions such as π–π and hydrogen-bonding interactions, resulting in the formation of voids and channels in the crystal lattice.

The properties of porous ionic crystals based on POMs can be summarized as follows: (a) POMs show reversible redox properties, which can lead to the formation of "redox-active" porous ionic crystals. On the other hand, the components of zeolites (mainly Si and Al) are non-redox active, and MOFs can rarely withstand the geometry changes in the framework which often accompany the redox reactions. (b) Specific functions such as guest binding and catalytically active sites can be incorporated beforehand into the ionic components, and these functions can be maintained and utilized after complexation of the ionic components since they still exist as discrete molecules in the crystal lattice. (c) The ionic components create strong electrostatic fields at internal surfaces, which are suitable for accommodation and stabilization of polar guests and cationic intermediates. (d) Since Coulomb interaction works isotropically in a long range, the crystal structures are often flexible and can transform to adapt to specific guests.

2 Chromium(III)-Carboxylates [Cr₃O(OOC*R*)₆(*L*)₃]⁺ as Counter Cations of Polyoxometalates and Selective Guest Adsorption in Porous Ionic Crystals

M(III)-carboxylates (M = Cr, Fe, Mn, Ru, etc.) with a general formula of $[M_3O(OOCR)_6(L)_3]^+$ have been studied as building blocks of solid materials because selection of metal ions (M^{III}) and ligands (R, L) leads to versatile functions [6–8]. Among the trivalent metal ions (M^{III}), octahedral Cr^{III} complexes are chemically inert due to the large crystal field stabilization energy of d^3 electronic configuration [9], so that $[Cr_3O(OOCR)_6(L)_3]^+$ is stable and would be a suitable ionic component for porous ionic crystals.

According to these considerations, a porous ionic crystal $K_3[Cr_3O(OOCH)_6(H_2O)_3][\alpha\text{-}SiW_{12}O_{40}]\bullet16H_2O$ (**1**) was synthesized with a simple Cr(III)-carboxylate $[Cr_3O(OOCH)_6(H_2O)_3]^+$ and a α-Keggin-type POM $[\alpha\text{-}SiW_{12}O_{40}]^{4-}$ [10]. In the crystal structure of **1**, the molecular ions lined up and formed a column, and three K^+ compensated the minus charge. The columns were hexagonally placed by hydrogen bonding between $[Cr_3O(OOCH)_6(H_2O)_3]^+$ with D_{3h} molecular symmetry and $[\alpha\text{-}SiW_{12}O_{40}]^{4-}$. As a result, straight channels with an opening of ca. 0.5×0.8 nm were formed (Fig. 1a). The large size and small charge (+1) of $[Cr_3O(OOCH)_6(H_2O)_3]^+$ reduced the Coulomb interaction among the ionic components and probably contributed to the formation of channels, where the water of crystallization existed. The porous structure was lost by removing the water of crystallization, and the empty host selectively sorbed methanol from a mixture of alcohols followed by the restoration of the porous structure.

Increasing the charge of ionic components increases cation–anion interaction and closer packing would be achieved, which would reduce the size and volume of pores in the crystal lattice. This reduction may lead to the selective sorption of water from alcohols. Based on these considerations, the POM was changed from $[\alpha\text{-}SiW_{12}O_{40}]^{4-}$ to $[\alpha\text{-}CoW_{12}O_{40}]^{6-}$, and an ionic crystal of $Cs_5[Cr_3O(OOCH)_6(H_2O)_3][\alpha\text{-}CoW_{12}O_{40}]\bullet7.5H_2O$ (**2**) was obtained [11]. The space volume
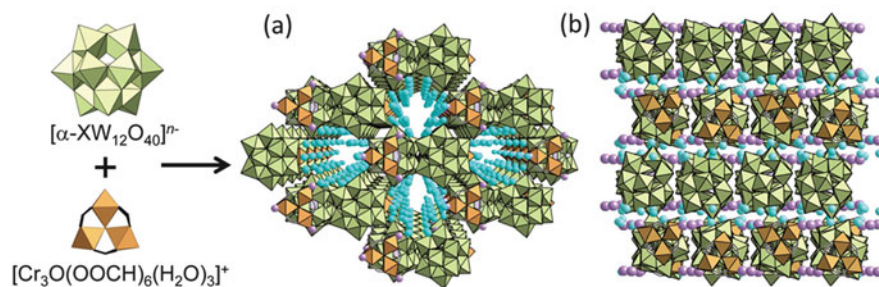
Fig. 1 Crystal structures of (**a**) **1** and (**b**) **2**. [WO₆] and [CrO₆] are shown by the *green and orange polyhedra*, respectively. *Purple and light blue spheres* show the alkali metal ions (K⁺, Cs⁺) and oxygen atom of the water of crystallization, respectively

of **2** was 17% of the crystal lattice and was much smaller than that of **1** (36%), and **2** possessed one-dimensional winding channels filled with the water of crystallization (Fig. 1b). The narrowest cross diameter of the channel was ca. 0.27 nm and comparable to the van der Waals diameter of oxygen (0.30 nm). Compound **2** showed selective sorption of water and separation of water from an ethanol/water azeotropic mixture.

From the viewpoint of storage and utilization of organic resources, controlled sorption of organic guests is important. Since most organic guests contain hydrophobic (e.g., alkyl and phenyl, etc.) and/or hydrophilic (e.g., hydroxyl) functional groups, construction of both hydrophilic and hydrophobic spaces by the fine tune of the ionic components would be a solution. According to this idea, the bridging ligand ($-OOCR$) of the molecular cation was changed from $-OOCH$ to $-OOCC_2H_5$, and an ionic crystal of $K_2[Cr_3O(OOCC_2H_5)_6(H_2O)_3]_2[\alpha\text{-}SiW_{12}O_{40}]\cdot4H_2O$ (**3**) was obtained [12] (Fig. 2). Compound **3** was composed of two-dimensional layers of $[\alpha\text{-}SiW_{12}O_{40}]^{4-}$ and $[Cr_3O(OOCC_2H_5)_6(H_2O)_3]^+$ in the *ac*-plane. The layers were stacked along the *b*-axis with an offset of *a*/2 with respect to each other, and alkali metal ions resided between the adjacent layers. Compound **3** possessed both hydrophilic and hydrophobic channels in the crystal lattice, with an opening of ca. 0.25×0.25 nm and 0.25×0.51 nm, respectively. IR and NMR studies have shown that ethanol molecules can enter both hydrophobic and hydrophilic channels, while water molecules can enter only the hydrophilic channel. The increase in the size of the alkali metal ion from K^+ ($r = 0.152$ nm, compound **3**) to Rb^+ ($r = 0.166$ nm, compound **4**) or Cs^+ ($r = 0.181$ nm, compound **5**) increased the interlayer spacing, and the size of the opening of the hydrophobic channel increased in the order of **3** (0.25×0.51 nm) < **4** (0.34×0.51 nm) < **5** (0.40×0.52 nm). In particular, **5** sorbed water and dichloromethane into the hydrophilic and

Fig. 2 Crystal structure of **3**. $[WO_6]$ and $[CrO_6]$ are shown by the *green and orange polyhedra*, respectively. K^+ is shown by the *purple spheres*. The hydrophobic and hydrophilic channels are surrounded by the *orange and blue broken lines*, respectively

0.25 nm × 0.25 nm

0.25 nm × 0.51 nm
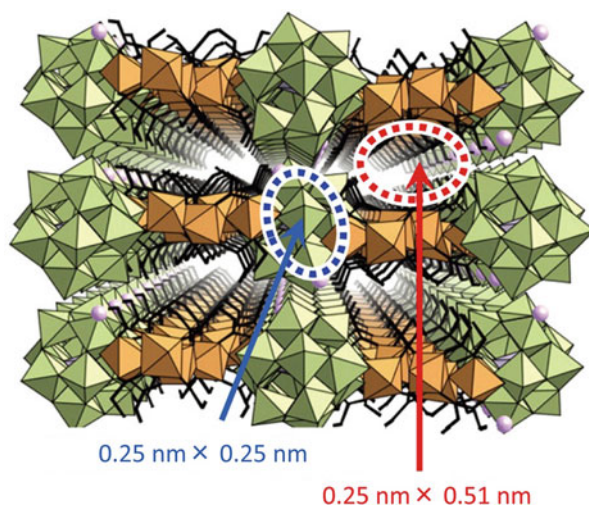
hydrophobic channel, respectively, and realized the adsorptive separation of a gas mixture of water and dichloromethane [13].

In order to further functionalize these compounds, the adsorptive separation of olefin/paraffin, which is both industrially and scientifically important, was targeted. It has been long recognized that the utilization of π-complexation between the π^* orbital of $C = C$ ($C \equiv C$) and the d orbital of the metal cation with d^{10}-electronic configuration (e.g., Ag^+) is promising for the selective sorption of olefins [14]. Based on this consideration, $Ag_2[Cr_3O(OOCC_2H_5)_6(H_2O)_3]_2[\alpha\text{-}SiW_{12}O_{40}]\cdot6H_2O$ (6) was synthesized by the exchange of alkali metal ions with Ag^+ [15]. While 6 was isostructural with 3–5, the interlayer spacing was small and no channels existed because of the smaller size of Ag^+ ($r = 0.129$ nm) compared with the alkali metal ions ($r = 0.152$–0.181 nm). While 6 is nonporous, the amounts of sorption of small unsaturated hydrocarbons such as ethylene, propylene, n-butene, acetylene, and methyl acetylene were >1 mol mol^{-1} (i.e., 1 mol of acetylene per mole of 6) while those of paraffins and larger unsaturated hydrocarbons were quite small (<0.2 mol mol^{-1}) (Fig. 3). The sorption property could be applied to the collection of ethylene from the gas mixture of ethane and ethylene. Kinetic analysis of the sorption profile of ethylene showed that ethylene molecules in the gas phase were adsorbed on the external surface and subsequently diffused into the solid bulk. In situ powder X-ray diffraction (XRD) studies showed that the lattice volume of 6 increased by 0.766 nm^3 per unit cell with the sorption of 2 mol mol^{-1} of ethylene (0.655 nm^3) suggesting that the framework of 6 is flexible (Fig. 4). These results show that paraffins can be only sorbed on the external surface while small unsaturated hydrocarbons can penetrate into the solid bulk with an increase in the lattice volume through the π-complexation with Ag^+, resulting in the high olefin/paraffin sorption ratios.

The use of aromatics as terminal ligands (L) of metal carboxylates would induce π–π interaction leading to the formation of rigid channels. Pyridine (py) was used as a terminal ligand ($[Cr_3O(OOCH)_6(py)_3]^+$), and an ionic crystal of $K_{1.5}[Cr_3O(OOCH)_6(py)_3]_2$ $[Cr_3O(OOCH)_6(py)(CH_3OH)_2]_{0.5}[\alpha\text{-}SiW_{12}O_{40}]\cdot2CH_3OH\cdot8H_2O$ (7) was obtained [16]. Compound 7 possesses one-dimensional winding channels with a
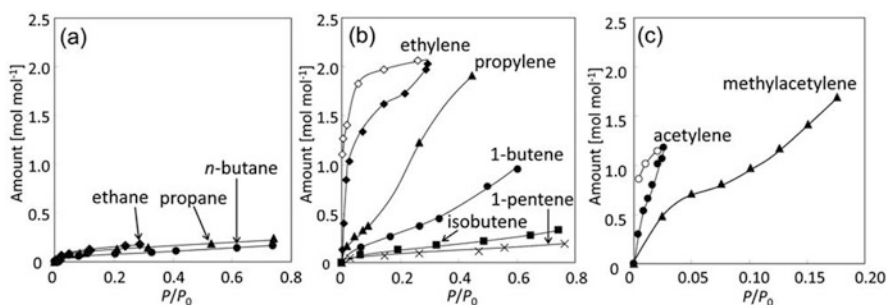
Fig. 3 Hydrocarbon gas sorption isotherms of 6 at 298 K. (a) Paraffins, (b) olefins, and (c) acetylenes. The *closed and open symbols* for ethylene and acetylene show the sorption and desorption plots, respectively

narrowest cross section of ca. 3.0×10^{-2} nm^2, and small hydrocarbons, alcohols, and halocarbons are shape-selectively sorbed regardless of their polarity and functional groups (Fig. 5). When 4-methylpyridine (mepy) was used instead of pyridine, an ionic crystal of K$_2$[Cr$_3$O(OOCH)$_6$(mepy)$_3$]$_2$[α-SiW$_{12}$O$_{40}$]•2H$_2$O•CH$_3$OH (**8**) with one-dimensional channels occupied by K$^+$ was formed (Fig. 6a) [17]. Similar to zeolites, K$^+$ in **8** can be exchanged with other alkali metal ions in water at room temperature without any structure change, and the guest sorption properties of the alkali metal ion-exchanged ionic crystals largely depended on the ionic potential of alkali metal ions ion–dipole interaction between the host–guest (Fig. 6b).

3   Heterogeneous Catalysis in Porous Ionic Crystals

Compared with guest sorption, little is known of heterogeneous catalysis in porous ionic crystals. Ionic crystals of [M_3O(OOCC$_6$H$_5$)$_6$(H$_2$O)$_3$]$_4$[α-SiW$_{12}$O$_{40}$]•nH$_2$O•mCH$_3$COCH$_3$ (M = Cr^{III} (**9**), Fe^{III} (**10**)) were synthesized, and these crystals heterogeneously catalyzed pinacol rearrangement to pinacolone with high conversion at 373 K and the catalysis proceeds size-selectively in the solid bulk (Fig. 7) [18]. Notably, **9** showed higher catalytic activity than **10**, which can be explained as follows: Pinacol rearrangement is generally catalyzed by Brønsted acids [19], and it is well known that metal aqua ions [M(H$_2$O)$_6$]$^{n+}$ dissociate protons and act as Brønsted acids [9]. The pKa of [Cr(H$_2$O)$_6$]$^{3+}$ and [Fe(H$_2$O)$_6$]$^{3+}$ are 4.2 and 2.2, respectively, and the acidity of [Fe(H$_2$O)$_6$]$^{3+}$ is higher because of the higher electronegativity of Fe: Fe–O bonds are more covalent and stronger, and dissociation of protons proceeds easier [9].
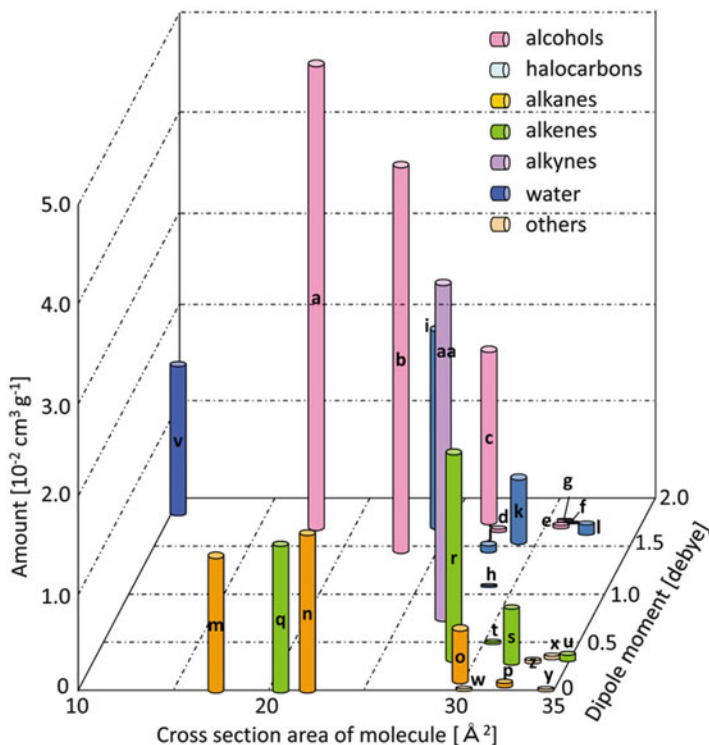
Fig. 5 Effects of sizes and dipole moments of guest molecules on the amounts of sorption by **7** at 298 K. The amounts are measured at $P/P_0 = 0.40$ or at the following pressures shown in *parentheses*. (a) Methanol, (b) ethanol, (c) 1-propanol, (d) 2-propanol, (e) 1-butanol, (f) 2-methyl-1-propanol, (g) 2-butanol, (h) chloroform, (i) dichloromethane, (j) 1,2-dichloroethane, (k) 1-bromo-2-chloroethane, (l) 1,2-dichloropropane, (m) methane (9.0 MPa), (n) ethane, (o) propane, (p) *n*-butane, (q) ethylene ($P/P_0 = 0.32$), (r) propylene, (s) 1-butene, (t) isobutene, (u) - 1-pentene, (v) water, (w) benzene, (x) toluene, (y) cyclohexane, (z) cyclohexene, and (aa) methyl acetylene

Aluminum is the most abundant metal in the earth's crust and one of the most widely used metals in the world. Cationic aluminum (III) complexes are naturally electron deficient, and the choice of loosely coordinating ligands such as water may generate Brønsted and/or Lewis acid sites. In particular, planar Al(III)-Schiff base complexes enable loose coordination of solvent molecules or anions at the axial positions (Fig. 8a), which have been found to show high catalytic activities in the synthesis of cyclic carbonates from a range of epoxides and carbon dioxide [20, 21]. According to these considerations, a porous ionic crystal [Al(salphen) $(H_2O)_2]_3[\alpha-PW_{12}O_{40}] \cdot mC_8H_{10} \cdot nCH_3COCH_3$ (**11**) (salphen = N,N'-phenylenebis (salicylideneimine)) with a cationic Al(III)-Schiff base complex [Al(salphen) $(H_2O)_2]^+$ (Al(III)-salphen) and $[\alpha-PW_{12}O_{40}]^{3-}$ was synthesized [22]. Compound **11** possessed a stable three-dimensional porous structure (channel opening
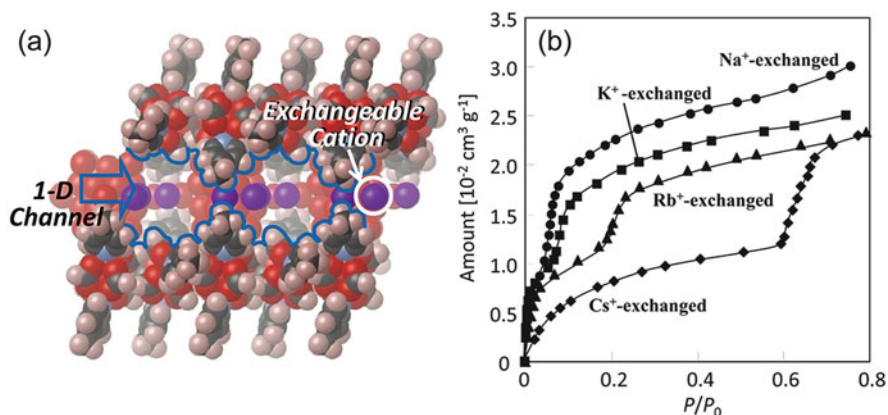
Fig. 6 (**a**) Crystal structure of **8**. (**b**) Water sorption isotherms of the alkali metal ion-exchanged compounds at 298 K
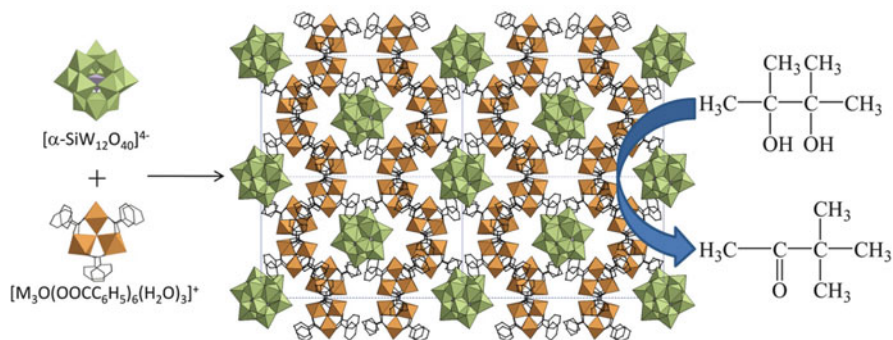
Fig. 7 Crystal structure of **9** and **10** and the heterogeneous catalysis (pinacol rearrangement). [WO$_6$] and [CrO$_6$] are shown by the *green and orange polyhedra*, respectively

0.6 × 1.2 nm) and showed high activity as a heterogeneous catalyst in pinacol rearrangement (Fig. 8b). Notably, Al(III)-salphen, POM, and a physical mixture of the two components were much less active, suggesting a synergetic effect of Al (III)-salphen (acid site) and POM (stabilization of cationic intermediate) in a porous framework.

These microporous materials (**9**–**11**) (IUPAC classification: pore size < 2 nm) have limitation in diffusion especially when large guest molecules are involved, so that an important line of research has focused on the enlargement of pore sizes into the mesopore range (pore size > 2 nm). However, in order to construct mesopores, a strategy is required to prevent close-packing of ionic building blocks. In supramolecular chemistry, it is well known that hydrogen-bonded water clusters serve as templates in the formation of nano-sized cavities, and polar functional groups or hydrogen-bonding sites are often required to stabilize the water clusters [23].

Fig. 8 (**a**) Crystal structure of **11**. The water ligands at the axial position of the Al (III)-salphen are surrounded by the *red broken circles*. Void spaces are shown in *brown*. (**b**) Synergy effect in the catalysis of **11**
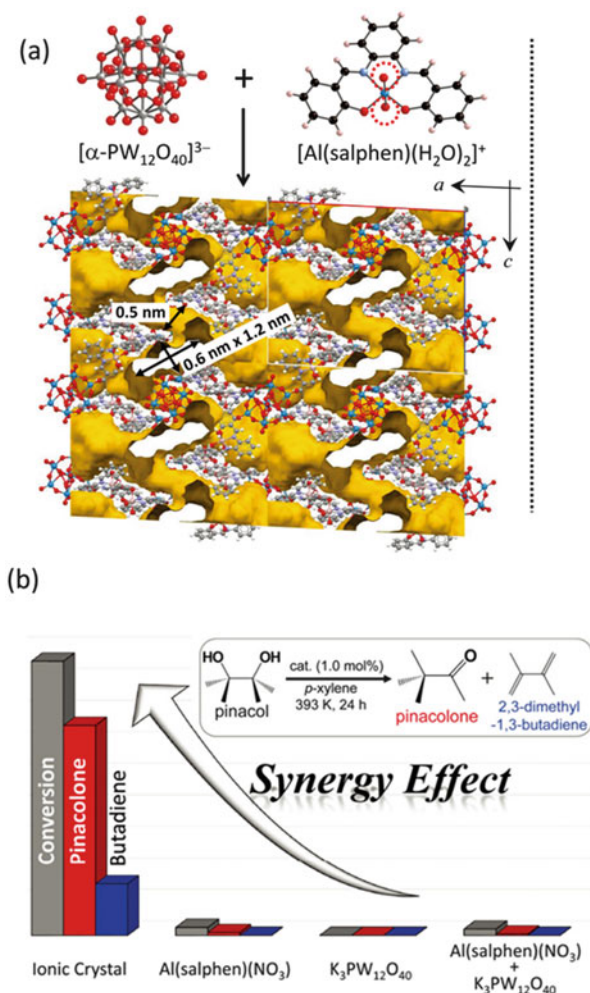
Based on these considerations, a mesoporous ionic crystal Cr[Cr$_3$O (OOCCH$_2$CN)$_6$(H$_2$O)$_3$]$_3$[α-PW$_{12}$O$_{40}$]$_2$•69H$_2$O (**12**) was synthesized with [α-PW$_{12}$O$_{40}$]$^{3-}$ and macrocation [Cr$_3$O(OOCCH$_2$CN)$_6$(H$_2$O)$_3$]$^+$ with polar cyano groups (CN) (Fig. 9) [24]. Compound **12** possessed one-dimensional mesopores with an opening of 3.0 × 2.0 nm, and the mesoporous structure was maintained by water molecules acting as templates. The compound showed high catalytic activity toward allylation of benzaldehyde with allytin.
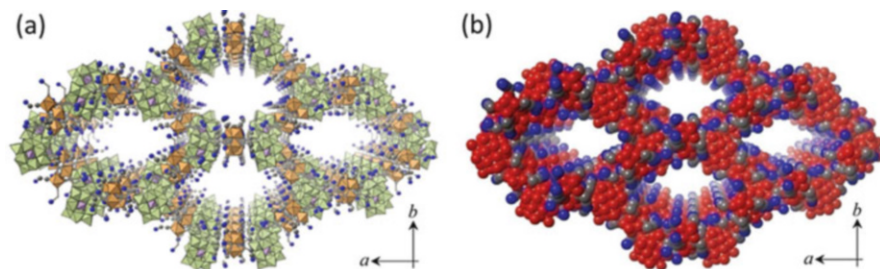
Fig. 9 (**a**) Polyhedral and (**b**) space filling model of **12**. [WO$_6$] and [CrO$_6$] are shown by the *green and orange polyhedra*, respectively, in (**a**). Oxygen, nitrogen, and carbon atoms are shown by the *red, blue, and gray spheres*, respectively, in (**b**)

4 Control of Pore Dimensions in Porous Ionic Crystals

Conventional crystalline porous materials such as zeolites and MOFs have large varieties of pore dimensions. For example, mordenite zeolite with one-dimensional channels catalyzes the disproportionation of *m*-xylene via a transition state that is conformationally restricted [25], while faujasite zeolite with three-dimensional channels is suited for uniform guest diffusion and utilized as a template to produce porous carbon [26].

As described in previous sections, the use of aromatics as terminal ligands of metal carboxylates enables the formation of one-dimensional channels via π–π interaction in ionic crystals. Since the sizes of voids and channel apertures in the ionic crystals are generally small and similar to those of industrially important small inorganic and hydrocarbon gases, ionic crystals are potentially suitable for the storage and separation of these gases. For example, the crystal structure of K$_2$[Cr$_3$O (OOCH)$_6$(etpy)$_3$]$_2$[α-SiW$_{12}$O$_{40}$]•4CH$_3$OH (**13**) (etpy = 4-ethylpyridine) is shown in Fig. 10 [27]. The opening of the one-dimensional channel was 0.35 nm. Two potassium ions per formula were disordered among three positions K1, K2, and K3 with occupancies of 0.6, 0.5, and 0.4, respectively, and were located either in the vicinity of POMs (K1 and K3) or in the space surrounded by the etpy ligands (K2). One potassium ion per formula (K2) existed in the space surrounded by the etpy ligands and interacted with two etpy ligands (K2-C = 0.356–0.364 nm), showing weak cation–π interaction. Compound **13** exhibited only surface adsorption of N$_2$, O$_2$, and CO (77 K) while sorption isotherms of CO$_2$ and C$_2$H$_2$ (195 K) were type-I (IUPAC classification) indicative of physisorption by microporous materials (Fig. 11a). Saturated sorption amounts of CO$_2$ and C$_2$H$_2$ sorption were 3 and 1 mol mol^{-1}, respectively, and **13** especially showed high affinity toward CO$_2$. The sorption isotherm of CO$_2$ at 278 K consisted of two steps and a large hysteresis loop, suggesting guest-induced phase transition (Fig. 11b). Sorption isotherm of C$_2$H$_2$ consisted of a single step and a hysteresis loop, while the amount of sorption was smaller. The CO$_2$/C$_2$H$_2$ sorption amount ratio reached up to 4.8 at 278 K and 100 kPa and is the inverse and highest selectivity in comparison with those of
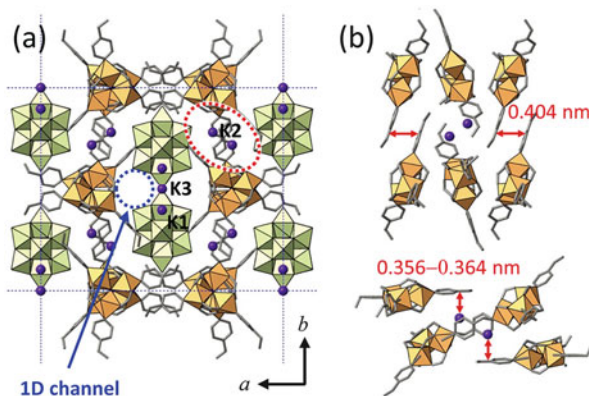
Fig. 10 Crystal structure of **13**. (**a**) Arrangements of the ionic components in the *ab*-plane and (**b**) local structure of the space surrounded by the etpy ligands. [WO$_6$] and [CrO$_6$] are shown by the *green and orange polyhedra*, respectively. K$^+$ are shown by the *purple spheres*
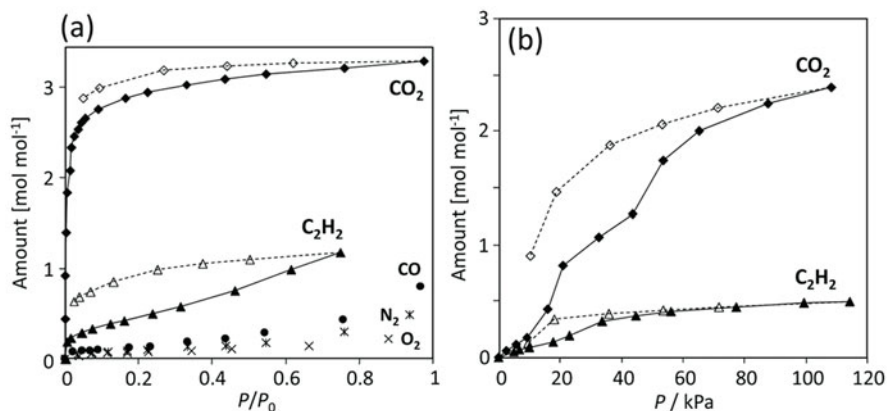
Fig. 11 Gas sorption isotherms of **13** at (**a**) 77 K (CO, N$_2$, and O$_2$) and 195 K (CO$_2$ and C$_2$H$_2$), and (**b**) 278 K. *Closed and open symbols* show the sorption and desorption branches, respectively

zeolites, carbon materials, and MOFs. These results suggest that **13** accommodates CO$_2$ molecules by expanding its lattice by two steps and shows higher structural flexibility for the sorption of CO$_2$ than that of C$_2$H$_2$. The key for the high affinity toward CO$_2$ is the combination of structural flexibility and strong binding sites (i.e., K$^+$).

Next, two-dimensional porous structure was focused on by the utilization of trifluoroacetate groups, and an ionic crystal of [Cr$_3$O(OOCCF$_3$)$_6$(H$_2$O)$_3$]$_3$[α-PW$_{12}$O$_{40}$]•8CH$_3$COCH$_3$•8H$_2$O•CHCl$_3$ (**14**) was obtained (Fig. 12) [28]. Compound **14** possessed a layered structure (= two-dimensional) composed of molecular cations and POMs. The interlayer distance was ca. 0.35 nm and the inner surface

Fig. 12 Crystal structure of **14**. [WO$_6$], [SiO$_4$], and [CrO$_6$] are shown by the *green, purple, and orange polyhedra*, respectively. Fluorine atoms are shown by the *green spheres*

$[\alpha\text{-PW}_{12}\text{O}_{40}]^{3-}$ $[\text{Cr}_3\text{O}(\text{OOCCF}_3)_6(\text{H}_2\text{O})_3]^+$
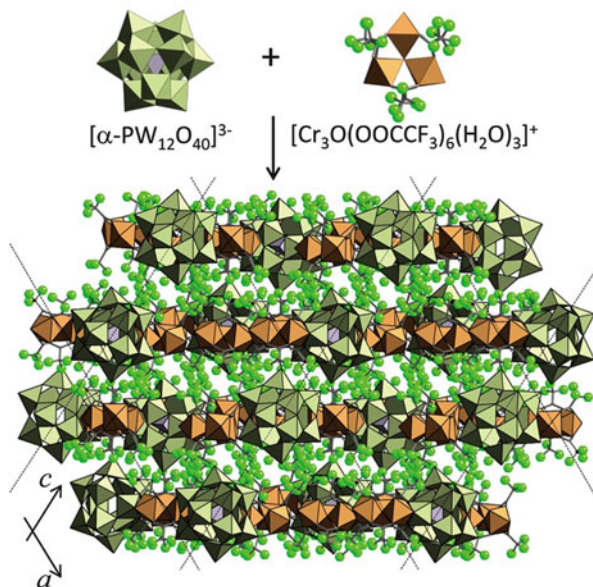
was decorated with CF$_3$ groups of the macrocations. The shortest F–F distances between the macrocations of adjacent layers were 0.28–0.32 nm, which were comparable to the sum of van der Waals radius of fluorine (0.15 nm). Small voids of ca. 0.35 nm existed within the layer, which were connected to the interlayer space, and chloroform existed in the void. Compound **14** sorbed CO$_2$ and unsaturated hydrocarbons, while saturated hydrocarbons such as ethane and methane were almost excluded despite the similar kinetic diameters. Typical Monte Carlo-based optimized geometries of acetylene and CO$_2$ showed different alignments in the structure of **14** despite the similar amounts of sorption and molecular sizes: Acetylene and CO$_2$ were aligned mainly parallel and perpendicular, respectively, to the layer, which is probably due to the differences in the electron density distributions of the HOMO orbitals.

In order to construct three-dimensional channels in ionic crystals, incorporation of acrylate ligands (CHCH$_2$OOC$^-$) into metal carboxylate was effective. It is well recognized that π–π interaction between aromatic groups with multiple π-electrons and large planar molecular surfaces is suitable for constructing rigid one-dimensional structures. On the other hand, olefin moieties in acrylate ligands possess large flexibility and "olefin–olefin interaction" may link multiple sites to construct stable three-dimensional structures [29]. The complexation of $[\alpha\text{-PW}_{12}\text{O}_{40}]^{3-}$ and $[\text{Cr}_3\text{O}(\text{OOCCHCH}_2)_6(\text{H}_2\text{O})_3]^+$ formed an ionic crystal $[\text{Cr}_3\text{O}(\text{OOCCHCH}_2)_6(\text{H}_2\text{O})_3]_3[\alpha\text{-PW}_{12}\text{O}_{40}]\cdot15\text{H}_2\text{O}$ (**15**) with three-dimensional micropores showing shape-selective guest sorption properties (Fig. 13) [30]. Stable three-dimensional micropores were constructed for the first time with discrete and precisely located molecular ionic components.
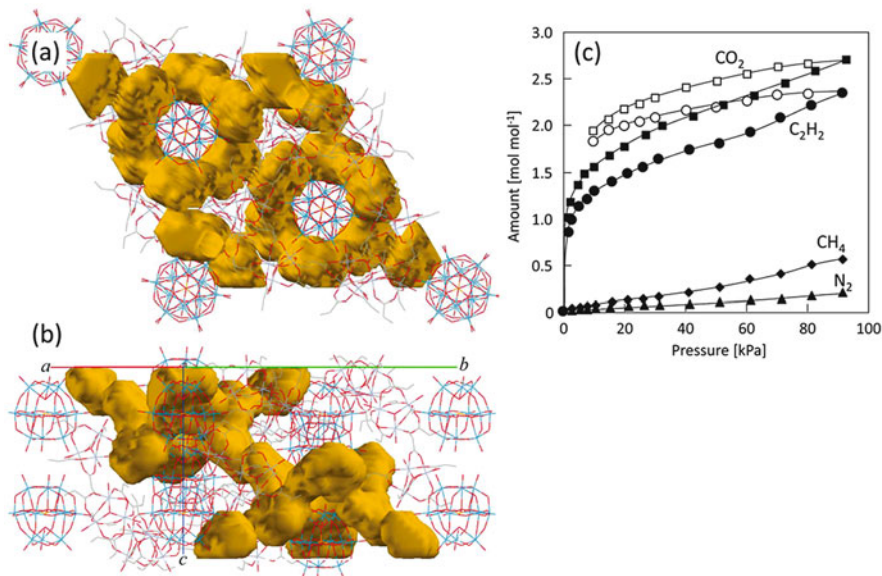
Fig. 13 Void analyses of **15** with a probe diameter of 0.33 nm. Viewed (**a**) parallel and (**b**) perpendicular to the *ab*-plane. Void spaces are shown in *brown*. (**c**) Gas sorption isotherms of CO_2 (198 K), C_2H_2 (198 K), CH_4 (115 K), and N_2 (77 K). *Closed and open symbols* show the sorption and desorption branches, respectively

5 Post-synthetic Modification of Porous Ionic Crystals

While the porous ionic crystals described in previous sections were easily synthesized by one-pot reactions in a solution containing the constituent ions, precise prediction and control of structures are difficult because Coulomb interaction works isotropically in a long range. A solution to this problem is to utilize post-synthesis modification to incorporate additional functions that could not be achieved during synthesis. In the case of MOFs, functional groups of organic linkers can be exchanged, removed, or extended post-synthetically [31–33]. For example, chiral azides are attached post-synthetically onto external alkynes of an organic linker, and the resulting compound catalyzed asymmetric aldol reactions [34].

Based on these considerations, the porous ionic crystal $K_2[Cr_3O(OOCH)_6(etpy)_3]_2[\alpha\text{-}SiW_{12}O_{40}]\cdot 8H_2O$ (**13**) was modified to increase guest capacity by post-synthesis in a single-crystal-to-single-crystal manner [35]. Post-synthesis modification of a porous ionic crystal proceeded via two steps (acid treatment followed by ion-exchange) in an aqueous solution. Compound **13** is a porous ionic crystal with one-dimensional channels, which can accommodate guests such as water, alcohols, and halocarbons. Crystals of **13** were immersed in an aqueous HCl solution (acid treatment), and the etpy ligand which was exposed to the one-dimensional channel was removed and exchanged with water. The formula
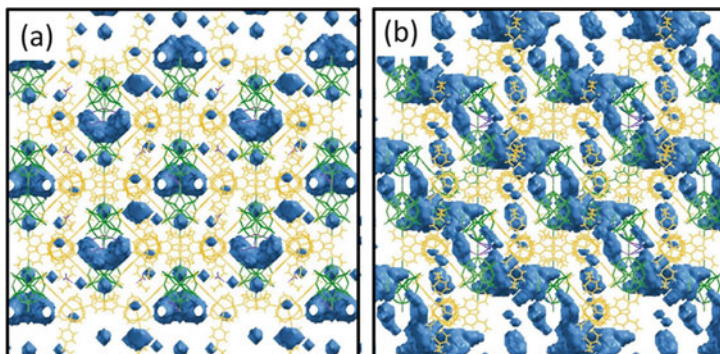
Fig. 14 Void spaces (*blue*) in (**a**) **13** (before post-synthesis, void space is 0.74 nm^3 per unit cell) and (**b**) **15** (after post-synthesis, void space is 1.02 nm^3 per unit cell)

of the resulting compound was $(etpyH^+)_2[Cr_3O(OOCH)_6(etpy)_2(H_2O)]_2[\alpha\text{-}SiW_{12}O_{40}]\cdot6H_2O$ (**14**), and K^+, which are potential guest binding sites, were simultaneously removed by this treatment. Reincorporation of K^+ was attempted by immersion of **14** into an aqueous CH_3COOK solution (ion-exchange), and $K_2[Cr_3O(OOCH)_6(etpy)_{2.5}(H_2O)_{0.5}]_2[\alpha\text{-}SiW_{12}O_{40}]\cdot8H_2O$ (**15**) was formed. Increase in void volume from **13** (0.74 nm^3 per unit cell) to **15** (1.02 nm^3 per unit cell) by the two-step post-synthesis modification was confirmed by sorption isotherms and Monte Carlo-based simulations using water as a probe molecule (Fig. 14). The role of K^+ as water binding sites was confirmed by water sorption isotherms of alkali metal ion-exchanged compounds. The same kind of post-synthetic treatment can be carried out with **6** [36].

6   Utilization of Crystal Polymorphs

Polymorphism is the ability of a solid to exist in more than one crystal structure. Polymorphs can exhibit different physicochemical properties, and one of the long-standing challenges in science is prediction and control of polymorphism. Especially, polymorphism of TiO_2 has also been a popular topic due to its high photocatalytic activity, high stability, low cost, and low toxicity [37].

Toward this end, molecular ions with a Keggin-type structure have been a popular motif because of its easy synthesis and high molecular symmetry (T_d), which may lead to formation of polymorphs with different functions. For example, Kwon et al. have studied the structures and water adsorption properties of porous ionic crystals composed of POMs and Keggin-type polyaluminum hydroxide ($[\varepsilon\text{-}Al_{13}O_4(OH)_{24}(H_2O)_{12}]^{7+}$, **Al$_{13}$**) [38–40]. In one of their studies, two kinds of polymorphs with **Al$_{13}$** and $[\alpha\text{-}H_2W_{12}O_{40}]^{6-}$ as molecular building blocks crystallized from the same aqueous solution [40]. Mellot-Draznieks et al. have predicted that the crystal structures of polymorphs composed of $[\varepsilon\text{-}PMo_{12}O_{36}(OH)_4]^{7-}$,

benzenedicarboxylates, and Zn(II) ions by computational simulations, and some of the polymorphs were actually synthesized and applied as an electrocatalyst for reduction of bromate [41, 42].

Based on these considerations, an attempt was carried out to control not only the polymorphism but also the functions of all-inorganic porous ionic crystals. Two kinds of polymorphs (needle and plate-type crystals) with a chemical formula of $[\varepsilon\text{-}Al_{13}O_4(OH)_{25}(H_2O)_{11}][\alpha\text{-}CoW_{12}O_{40}]\cdot nH_2O$ (**16**) were obtained by the combination of oppositely charged macroions with T_d symmetry (**Al$_{13}$** and $[\alpha\text{-}CoW_{12}O_{40}]^{6-}$) in an aqueous solution (Fig. 15) [43]. The needle-type crystal was grown by dissolution–recrystallization of the precipitates, which formed immediately by combining **Al$_{13}$** with POM. On the other hand, the plate-type crystal was obtained by adding inorganic salts (e.g., NaCl) into the aqueous solution containing the needle-type crystals: Dissolution of the needle-type crystal occurred followed by precipitation of the plate-type crystal, which is the more insoluble and stable polymorph with larger numbers of hydrogen bonds between the constituent ions. The plate-type crystal possessed one-dimensional channels with large apertures (ca. 1.2×0.6 nm) and showed high activity as a heterogeneous solid acid catalyst in pinacol rearrangement.

crystal system :	tetragonal		orthorhombic
hydrogen-bonds per Al$_{13}$:	12	<	20
pore opening:	0.6 x 0.6 nm^2	<	0.6 x 1.2 nm^2
conversion of pinacol:	8—18%	<	26—54%
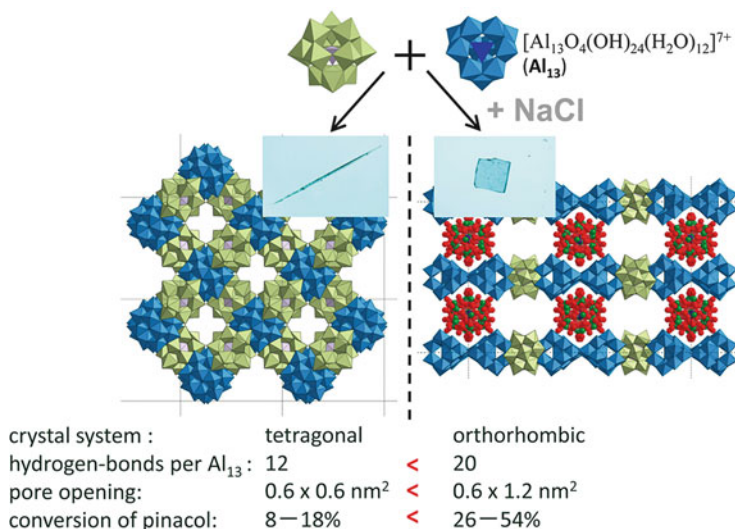
Fig. 15 Crystal structures and photo images of the polymorphs: needle-type crystal (*left*) and plate-type crystal (*right*). *Green, purple, light blue, and dark blue polyhedra* show the [WO$_6$], [CoO$_4$], [AlO$_6$], and [AlO$_4$] units, respectively. The disordered polyoxometalates (POMs) in the plate-type crystal are depicted with a ball-and-stick model, where *red, green, and purple spheres* show the oxygen, tungsten, and cobalt atoms, respectively

7   Redox-Active Porous Ionic Crystals

Reversible redox properties of POMs have been utilized as catalysts, single-molecule magnets, cathodes, and electro-optical devices, etc. For example, Yoshikawa and Awaga et al. have reported the preparation of a molecular cluster battery utilizing $[\alpha\text{-}PMo_{12}O_{40}]^{3-}$ as a cathode: 12 Mo^{IV} were reduced to Mo^{IV}, and 24 electrons can be stored in the POM [44]. A redox-active porous ionic crystal of $(mepyH)[Cr_3O(OOCH)_6(mepy)_3]_2[\alpha\text{-}PMo^{IV}_{12}O_{40}]\bullet 5H_2O$ (mepy = 4-methylpyridine, $mepyH^+$ = 4-methylpyridinium ion) (**17**) was synthesized with $[\alpha\text{-}PMo_{12}O_{40}]^{3-}$ and $[Cr_3O(OOCH)_6(mepy)_3]^+$ (Fig. 16) [45]. Compound **17** possessed one-dimensional channels with an aperture of 0.32 nm due to π–π interaction between the molecular cations. The treatment of **17** with an aqueous solution containing ascorbic acid as a reducing reagent and KCl resulted in a color change from yellow to blue: One-electron reduction of $[\alpha\text{-}PMo^{VI}_{12}O_{40}]^{3-}$ to $[\alpha\text{-}PMo^{V}Mo^{VI}_{11}O_{40}]^{4-}$ occurred followed by simultaneous uptake of K^+, and $K_2[Cr_3O(OOCH)_6(mepy)_3]_2[\alpha\text{-}PMo^{V}Mo^{VI}_{11}O_{40}]\bullet 5H_2O$ (**18**) was formed. The reduced crystal (**18**) could be oxidized with aqueous chlorine solution followed by the release of K^+ in the aqueous solution, and $K[Cr_3O(OOCH)_6(mepy)_3]_2[\alpha\text{-}PMo^{VI}_{12}O_{40}]\bullet 5H_2O$ (**19**) was formed. The redox cycles were reversible and proceeded in a single-crystal-to-single-crystal manner. Compound **18** can incorporate other alkali metal ions by the same
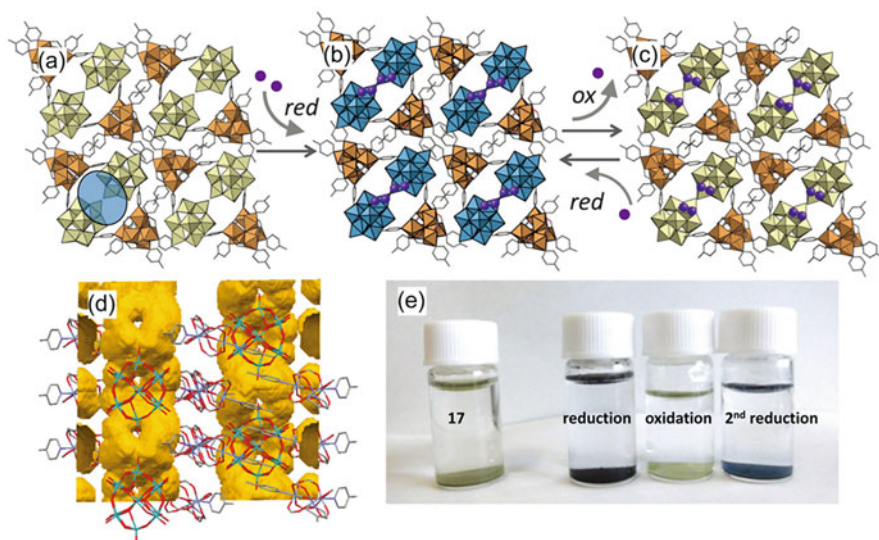
Fig. 16 Schematic illustration of the redox-induced reversible uptake-release of cations (K^+). Crystal structures of (**a**) **17**, (**b**) **18**, and (**c**) **19**. The opening of the one-dimensional channel is indicated by the *blue oval* in (**a**). The molecules in *light green and blue* show the $[\alpha\text{-}PMo^{VI}_{12}O_{40}]^{3-}$ and $[\alpha\text{-}PMo^{V}Mo^{VI}_{11}O_{40}]^{4-}$, respectively. The molecule in *orange* shows the macrocation. (**d**) Void analyses of **17** with a probe diameter of 0.32 nm (void spaces are shown in *brown*). (**e**) Photo images of **17** in water, and aqueous mixtures after the redox reactions

method, and Cs^+ uptake and the simultaneous reduction of the crystal proceeded much faster than in the case of K^+, which is in line with the trends in the Gibbs energies of hydration of alkali metal ions (K^+ (-352 kJ mol^{-1}) < Cs + (-306 kJ mol^{-1})) [46]: It is easier to remove the water of hydration from Cs^+ than K^+, so that Cs^+ can enter and diffuse through the one-dimensional channels of **18** easily.

Selective Cs^+ uptake from aqueous solutions is especially important because Cs^+ is expensive and found in radioactive wastes. Besides zeolites, Prussian blues and layered compounds have been researched and applied as Cs^+ adsorbents [47, 48]. Prussian blue, which is a classical coordination polymer with a general formula of {Fe(III)$_4$[Fe(II)(CN)$_6$]$_3$}, can capture Cs^+ with high selectivity against Na^+ and K^+ by physical adsorption with an anion or chemical adsorption via lattice defect [47]. Among the layered compounds, $K_{2x}Mn_xSn_{3-x}S_6$ shows high Cs^+ uptake under a wide pH range due to the soft Lewis acid–Lewis base interaction ($Cs^+\cdots S^{2-}$) [48]. However, these materials adsorb Rb^+ as well as Cs^+, and an adsorbent with high selectivity toward Cs^+ has not yet been reported.

To solve this problem, an ionic crystal (etpyH)$_2$[Cr$_3$O(OOCH)$_6$(etpy)$_3$]$_2$[α-SiMo$_{12}$O$_{40}$]•3H$_2$O (etpy = 4-ethylpyridine, etpyH$^+$ = 4-ethylpyridinium ion) (**20**) with closed pores was synthesized [49]. Compound **20** incorporated up to 3.8 mol mol^{-1} of Cs^+ via cation-exchange with etpyH$^+$ and reduction of silicododecamolybdate [α-SiMo$^{VI}_{12}$O$_{40}$]$^{4-}$ to [α-SiMo^V_nMo$^{VI}_{12-n}$O$_{40}$]$^{(4+n)-}$ with ascorbic acid (Fig. 17). Other alkali metal (Na^+, K^+, and Rb^+) and alkaline earth metal (Mg^{2+}, Ca^{2+}, Sr^{2+}, and Ba^{2+}) cations were almost completely excluded (<0.2 mol mol^{-1}). As stated above, hydration radius and Gibbs energy of dehydration of alkali metal cations decrease in the order of $Na^+ > K^+ > Rb^+ > Cs^+$ [46]. Therefore, it is easier to remove the water of hydration from Cs^+, and Cs^+ can enter and diffuse through the crystal lattice easily. Notably, **18** exhibits continuous one-dimensional channels and could incorporate K^+ and Rb^+ as well as Cs^+ [45]. Therefore, the high selectivity toward Cs^+ for **20** is due to the existence of closed pores instead of open channels. In addition, flexibility of the crystal lattice
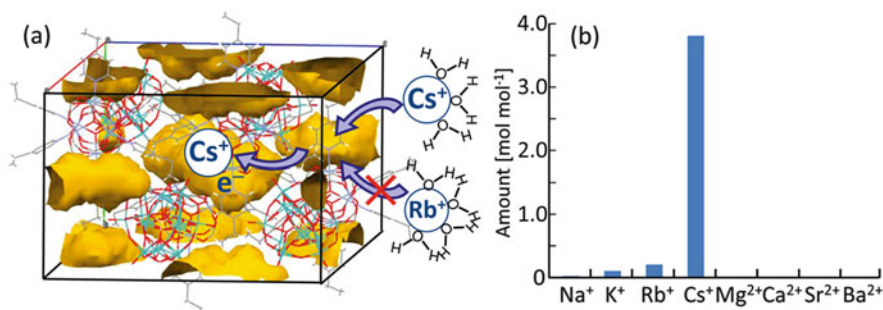
Fig. 17 (**a**) Crystal structure of **20** (closed pores are shown in *brown*) and schematic model of the reduction-induced selective adsorption of Cs^+. (**b**) Amount of various cations incorporated into **20** by the reduction-induced method

caused by isotropic and long-range Coulomb interactions among the constituent
ions may have contributed to the diffusion of Cs^+ between the closed pores.

8   Introducing Porosity by Controlling Self-assembly and Crystal Growth Processes

All the results described in previous sections show the construction and utilization
of intrinsic pores within the crystal lattice. Since the thermodynamically stable
single crystal does not always possess intrinsic pores, methods to introduce pores
into dense nonporous single crystals are of importance. For example, a single
crystal of $(NH_4)_3[\alpha\text{-}PW_{12}O_{40}]$ grown at 473 K (**21**) is nonporous [50]. The crystal
structure of **21** can be explained by a spherical approximation of anions:
$[\alpha\text{-}PW_{12}O_{40}]^{3-}$ are packed in a body-centered cubic (bcc) cell, cations exist at
the center of each plane and edge of the cell, and thus two anions and six cations
exist in the unit cell, resulting in an anion to cation site ratio of 1:3. In a bcc cell,
{110} planes are most densely packed and thus the most stable (Fig. 18a). There-
fore, the rhombic dodecahedron faceted with 12 {110} planes is the thermodynam-
ically stable morphology (Fig. 18b).

By changing the synthetic temperature from 473 to 298 K, spherical particles of
100–400 nm in size were formed (denoted as **22**, Fig. 18c). Compound **22** showed a
large BET surface area of 91 $m^2 g^{-1}$ (pore diameter: 0.7–1.2 nm), suggesting that
the spherical particles are aggregates of nanocrystallites of ca. 10 nm in size. The
existence of nanocrystallites was confirmed by the high resolution SEM and AFM
images. Based on these observations, the formation and growth mechanism of
$(NH_4)_3[\alpha\text{-}PW_{12}O_{40}]$ was suggested as follows: (1) formation of nanocrystallites,
(2) assembly of the nanocrystallites to form aggregates, and (3) growth of aggre-
gates by the attachment of nanocrystallites [51]. This mechanism can explain the
time courses of turbidity of the synthetic solution and the averaged particle sizes of
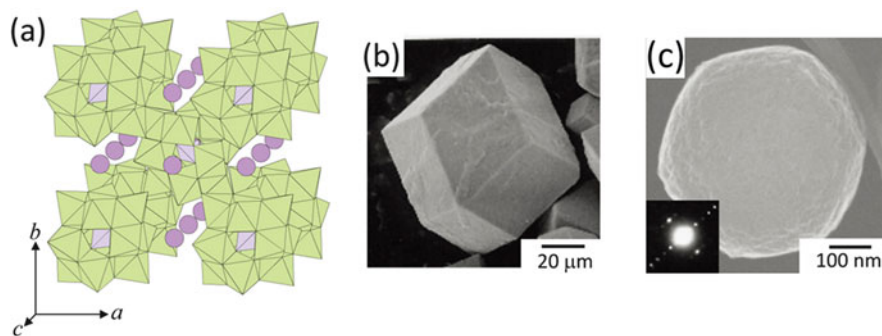
Fig. 18 (**a**) Crystal structure and (**b**) SEM image of **21**. (**c**) SEM image of **22** (*inset* shows the
electron diffraction (ED) pattern)

$(NH_4)_3[\alpha-PW_{12}O_{40}]$. The decrease in the crystallinity and the increase in the porosity (= BET surface area) by the decrease in the synthetic temperature from 473 to 298 K could be explained by the increase in the rate constant of (3), which probably disturbed the formation of epitaxial interfaces between the nanocrystallites. These results show the kinetic control of the self-organization process to change the morphology, crystallinity, and porosity of POM-based compounds.

Among the POM-based compounds, cesium-hydrogen phosphododecatungstates $Cs_xH_{3-x}[\alpha-PW_{12}O_{40}]$ have been widely studied as proton conductors [52], cation-exchangers [53], and catalysts [54, 55]. It has been reported that use of −4-charged anions such as $[\alpha-SiW_{12}O_{40}]^{4-}$ and $[\alpha-PVMo_{11}O_{40}]^{4-}$ instead of −3-charged $[\alpha-PW_{12}O_{40}]^{3-}$ generates anion (i.e., POM) vacancies in the bcc cell to compensate excess anion charges [56–58]. However, constructive use of anion vacancies as nanospaces has not yet been reported. Based on these considerations, a cesium-hydrogen silicododecatungstate $Cs_{3.0}H_{0.3}[\alpha-SiW_{12}O_{40}]_{0.83} \cdot 3.0H_2O$ (**23**) with a bcc cell and anion vacancies was synthesized, and the anion vacancies could be utilized for selective water sorption and cation-exchange (Fig. 19) [59]. Compound **23** consisted of highly crystalline particles with a flat rhombic bipyramidal morphology, and the anisotropic morphology was reported for the first time among the cubic solid POM compounds. Due to high crystallinity and flatness of **23**, direct atomic images (heavy cesium and tungsten atoms) were observed for the first time in solid POM compounds.

Unique properties associated with facets and morphologies have been reported for various cubic metal and metal-oxide particles. For example, catalytic activities of the crystal faces of bcc iron in ammonia synthesis increase in the order of {110} < {100} < {111} [60]. Octahedral particles of Cu_2O show higher catalytic activity in *N*-arylation than those with cubic morphologies [61], and hexagonal platelet particles of Co_3O_4 exhibit higher capacitance performance than those with spherical morphologies [62]. In ionic crystals, charge neutralization as well as atomic density is an important parameter to discuss the stability of facets and morphologies: NaCl with face-centered cubic (fcc) packing of Na^+ and Cl^- prefers a cube faceted with six {100} planes, since charge neutralization is attained in {100} planes while {111} planes are composed of alternate arrangements of oppositely charged planes [63].

In this context, synthesis of bcc particles of cesium-hydrogen silico-dodecatungstates faceted with {100} planes seems possible, since it is an ionic crystal and charge neutralization is attained in a {100} plane while charge density in a {110} plane is ± 0.0203 e A^{-2}. Based on these considerations, cubic particles as well as rhombic dodecahedron particles of cesium-hydrogen silicododecatungstate were obtained from spherical seed crystals by the control of the Cs^+ to $[\alpha-SiW_{12}O_{40}]^{4-}$ (Cs/SiW) ratio in the synthetic solution (Fig. 20) [64]. STEM-EDS analysis of the cross section showed that the cubes possessed a core-shell structure with anion vacancies in the shell. Spectroscopic and sorption measurements of the cubes showed that the porous core was covered by the dense shell, and only water molecules could diffuse through the dense shell via the anion vacancies (Fig. 20). Despite the small amounts of acidic protons, the cubes exhibited
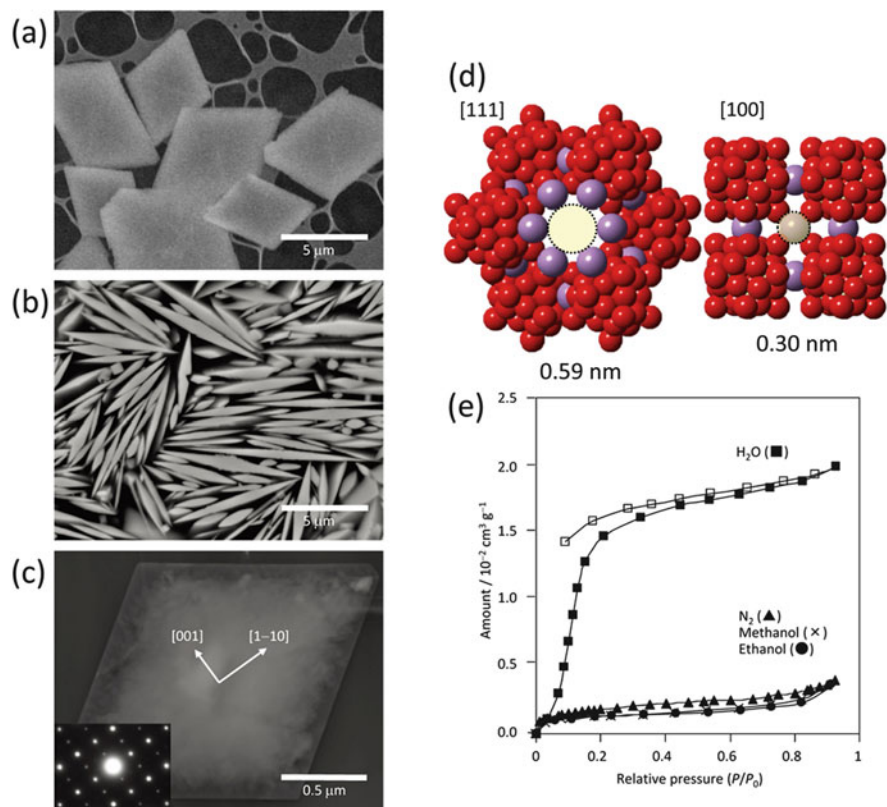
Fig. 19 (**a**) SEM image of **23**. (**b**) Cross section SEM image and (**c**) TEM image (*inset* shows the ED pattern) of **23**. (**d**) Illustration of openings between anion vacancies. *Red and purple spheres* show the oxygen and cesium atoms, respectively. (**e**) Water (298 K), methanol (298 K), ethanol (298 K), and N_2 (77 K) sorption isotherms. *Closed and open symbols* show the sorption and desorption plots, respectively

moderate proton conductivity at room temperature under water vapor, suggesting that mobile water molecules in the anion vacancies contributed to the proton conduction.

9 Summary and Concluding Remark

This review described recent studies on the design and functions of porous ionic crystal based on POMs. Kinetic control of self-assembly and crystal growth processes to form porous aggregates as well as design of intrinsic pores in the crystal lattice was presented. Long-term goals of ionic crystals can be summarized as follows: (a) Multi-electron redox-active porous ionic crystals that can sorb and
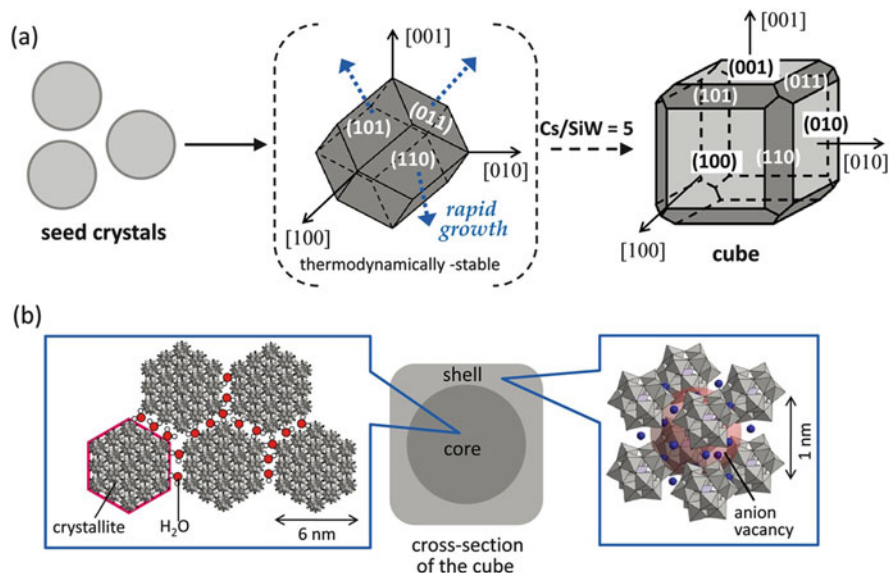
Fig. 20 (**a**) Crystal growth mechanism and (**b**) core-shell structure model of the cube

activate chemically inert molecules such as methane and carbon dioxide. (b) Synergetic effect of POM and counter cation in heterogeneous catalysis. (c) Introduction of chirality in the porous structure for the separation of enantiomers from racemic mixtures and asymmetric reactions.

References

1. Ma F-J, Liu S-X, Sun C-Y, Liang D-D, Ren G-J, Wei F, Chen Y-G, Su Z-M (2011) J Am Chem Soc 133(12):4178–4181
2. Song J, Luo Z, Britt DK, Furukawa H, Yaghi OM, Hardcastle KI, Hill CL (2011) J Am Chem Soc 133(42):16839–16846
3. Yan A-X, Yao S, Li Y-G, Zhang Z-M, Lu Y, Chen W-L, Wang E-B (2014) Chem Eur J 20 (23):6927–6933
4. Zhang Z-M, Zhang T, Wang C, Lin Z, Long L-S, Lin W (2015) J Am Chem Soc 137 (9):3197–3200
5. Kong X-J, Lin Z, Zhang Z-M, Zhang T, Lin W (2016) Angew Chem Int Ed Engl 55 (22):6411–6416
6. Fujihara T, Aonahata J, Kumakura S, Nagasawa A, Murakami K, Ito T (1998) Inorg Chem 37 (15):3779–3784
7. Sreerama SG, Pal S (2002) Inorg Chem 41(19):4843–4845

8. Vimont A, Goupil JM, Lavalley JC, Daturi M, Surble S, Serre C, Millange F, Férey G, Audebrand N (2006) J Am Chem Soc 128(10):3218–3227
9. Weller M, Overton T, Rourke J, Armstrong F (2014) Shriver-Atkins inorganic chemistry, 6th edn. Oxford University Press, Oxford
10. Uchida S, Hashimoto M, Mizuno N (2002) Angew Chem Int Ed Engl 41(15):2814–2817
11. Uchida S, Mizuno N (2004) J Am Chem Soc 126(6):1602–1603
12. Kawamoto R, Uchida S, Mizuno N (2005) J Am Chem Soc 127(30):10560–10567
13. Jiang C, Lesbani A, Kawamoto R, Uchida S, Mizuno N (2006) J Am Chem Soc 128(44):14240–14241
14. Yang RT, Kikkinides ES (1995) AICHE J 41(3):509–517
15. Uchida S, Kawamoto R, Tagami H, Nakagawa Y, Mizuno N (2008) J Am Chem Soc 130(37):12370–12376
16. Tagami H, Uchida S, Mizuno N (2009) Angew Chem Int Ed Engl 48(33):6160–6164
17. Uchida S, Eguchi R, Mizuno N (2010) Angew Chem Int Ed Engl 49(51):9930–9934
18. Uchida S, Lesbani A, Ogasawara Y, Mizuno N (2012) Inorg Chem 51(2):775–777
19. Berson JA (2002) Angew Chem Int Ed Engl 41(24):4655–4660
20. Atwood DA, Jegier JA, Rutherford D (1995) J Am Chem Soc 117(25):6779–6780
21. Castro-Osma JA, North M, Wu X (2016) Chem Eur J 22(6):2100–2107
22. Kawahara R, Osuga R, Kondo JN, Mizuno N, Uchida S (2017) Dalton Trans 46(10):3105–3109
23. Barbour LJ, Orr GW, Atwood JL (1998) Nature 393:671–673
24. Kawahara R, Niinomi K, Kondo JN, Hibino M, Mizuno N, Uchida S (2016) Dalton Trans 45(7):2805–2809
25. Csicsery SM (1984) Zeolites 4(3):202–213
26. Nishihara H, Kyotani T (2012) Adv Mater 24(33):4473–4498
27. Eguchi R, Uchida S, Mizuno N (2012) Angew Chem Int Ed Engl 51(7):1635–1639
28. Uchida S, Kawahara R, Ogasawara Y, Mizuno N (2013) Dalton Trans 42(45):16209–16215
29. Wakabayashi R, Ikeda T, Kubo Y, Shinkai S, Takeuchi M (2009) Angew Chem Int Ed Engl 48(36):6667–6670
30. Kawahara R, Uchida S, Mizuno N (2014) Inorg Chem 53(7):3655–3661
31. Kim M, Cahill JF, Fei H, Prather KA, Cohen SM (2012) J Am Chem Soc 134(43):18082–18088
32. Yamada T, Kitagawa H (2009) J Am Chem Soc 131(18):6312–6313
33. Wang Z, Cohen SM (2007) J Am Chem Soc 129(41):12368–12369
34. Zhu W, He C, Wu P, Wu X, Duan C (2012) Dalton Trans 41(10):3072–3077
35. Uchida S, Takahashi E, Mizuno N (2013) Inorg Chem 52(16):9320–9326
36. Uchida S, Mizuno K, Kawahara R, Takahashi E, Mizuno N (2014) Chem Lett 43(8):1192–1194
37. Hanaor DAH, Sorrell CC (2011) J Mater Sci 46(4):855–874
38. Son J-H, Choi H, Kwon Y-U (2000) J Am Chem Soc 122(30):7432–7433
39. Son J-H, Kwon Y-U (2004) Inorg Chem 43(6):1929–1932
40. Son J-H, Kwon Y-U (2005) Inorg Chim Acta 358(2):310–314
41. Rodriguez-Albelo LM, Ruiz-Salvador AR, Sampieri A, Lewis DW, Gómez A, Nohra B, Mialane P, Marrot J, Sécheresse F, Mellot-Draznieks C, Biboum RN, Keita B, Nadjo L, Dolbecq A (2009) J Am Chem Soc 131(44):16078–16087
42. Rodriguez-Albelo LM, Ruiz-Salvador AR, Lewis DW, Gómez A, Mialane P, Marrot J, Dolbecq A, Sampieri A, Mellot-Draznieks C (2010) Phys Chem Chem Phys 12(30):8632–8639
43. Mizuno K, Mura T, Uchida S (2016) Cryst Growth Des 16(9):4968–4974
44. Wang H, Hamanaka S, Nishimoto Y, Irle S, Yokoyama T, Yoshikawa H, Awaga K (2012) J Am Chem Soc 134(10):4918–4924
45. Kawahara R, Uchida S, Mizuno N (2015) Chem Mater 27(6):2092–2099
46. Fawcett WR (1999) J Phys Chem B 103(50):11181–11185

47. Ishizaki M, Akiba S, Ohtani A, Hoshi Y, Ono K, Matsuba M, Togashi T, Kananizuka K, Sakamoto M, Takahashi A, Kawamoto T, Tanaka H, Watanabe M, Arisaka M, Nankawa T, Kurihara M (2013) Dalton Trans 42(45):16049–16055
48. Manos MJ, Kanatzidis MG (2009) J Am Chem Soc 131(18):6599–6607
49. Seino S, Kawahara R, Ogasawara Y, Mizuno N, Uchida S (2016) Angew Chem Int Ed Engl 55 (12):3987–3991
50. Ito T, Hashimoto M, Uchida S, Mizuno N (2001) Chem Lett 1272–1273
51. Okamoto K, Uchida S, Ito T, Mizuno N (2007) J Am Chem Soc 129(23):7378–7384
52. Kukino T, Kikuchi R, Takeguchi T, Matsui T, Eguchi K (2005) Solid State Ionics 176 (23–24):1845–1848
53. Caron HL, Sugihara TT (1962) Anal Chem 34(9):1082–1086
54. Misono M (2001) Chem Commun 1141–1152
55. Kamiya Y, Okuhara T, Misono M, Miyaji A, Tsuji K, Nakajo T (2008) Catal Sur Asia 12:101–113
56. Berndt S, Herein D, Zemlin F, Beckmann E, Weinberg G, Schütze J, Mestl G, Schlögl R (1998) Ber Bunsenges Phys Chem 102:763–774
57. Laronze N, Marchal-Roch C, Guillou N, Liu FX, Hervé G (2003) J Catal 220(1):172–181
58. Kamiya Y, Sano S, Miura Y, Uchida Y, Ogawa Y, Watase Y, Okuhara T (2010) Chem Lett 39 (8):881–883
59. Ogasawara Y, Uchida S, Maruichi T, Ishikawa R, Shibata N, Ikuhara Y, Mizuno N (2013) Chem Mater 25(6):905–911
60. Spencer ND, Schoonmaker RC, Somorjai GA (1981) Nature 294(5842):643–644
61. Xu Y, Wang H, Yu Y, Tian L, Zhao W, Zhang B (2011) J Phys Chem C 115(31):15288–15296
62. Deori K, Ujjain SK, Sharma RK, Deka S (2013) ACS Appl Mater Interfaces 5 (21):10665–10672
63. Paetero L, Aquilano D, Moret M (2012) Cryst Growth Des 12(5):2306–2314
64. Uchida S, Ogasawara Y, Maruichi T, Kumamoto A, Ikuhara Y, Yamada T, Kitagawa H, Mizuno N (2014) Cryst Growth Des 14(12):6620–6626

Polyoxometalates Assemblies and Their Electrochemical Applications

Wenjing Liu, Xiao-Li Wang, and Ya-Qian Lan

Abstract Polyoxometalates (POMs) possess a large structural and compositional variety, coupled with their highly redox activity, leading to applications in deriving advanced materials for clean and renewable energy storage and conversion. The synthetic strategies used to prepare POM-assisted nanocomposites are discussed. The principal classes of POM derived electrocatalysts reported so far, such as polyoxometalates based metal-organic framework (POMOFs) materials, metal carbides, metal oxides, metal sulfides, and heteroatom-doped carbon materials for hydrogen evolution reaction (HER), oxygen evolution reaction (OER), and the overall water splitting are reviewed. These composites provide a chemist's way to prepare highly efficient and low-cost non-noble metal electrocatalysts.

Contents

W. Liu, X.-L. Wang, and Y.-Q. Lan (✉)
Nanjing Normal University, Nanjing, China
e-mail: yqlan@njnu.edu.cn

1   Introduction

The development of clean and efficient new energy has attracted great research
interest in recent years because of fast exhaustion of fossil fuels, environmental
contamination, greenhouse effect, etc. The preparation of clean energy by electro-
lyzing water is an efficient and effective alternative to fossil fuels [1]. Electrochem-
ical energy conversion systems including chlor-alkali electrolyzer [2], water-alkali
electrolyzer [3], metal-air batteries [4–8], solar water-splitting devices [9, 10],
artificial leaves [11], and proton exchange membrane electrolyzer [12–15] are
expected to produce contemporary clean energy. However, in the practical appli-
cation, their performance is hindered by high activation barriers, leading to large
overpotentials [16]. It is thus attractive to develop active, cost-effective, and earth-
abundant electrocatalysts for the water electrolysis industry that can be commer-
cialized at a large scale. Progress has been made in recent years in designing such
active electrocatalysts including metal carbide (e.g., Mo_2C, W_2C) [17–20], metal
nitrides (e.g., MoN) [21–24], metal oxide (e.g., CoO, Co_3O_4, and MoO_2), metal
sulfide (e.g., MoS_2, WS_2, CoS_2, and VS_2) [25–30], metal phosphide (e.g., MoP,
Ni_2P, FeP, and CoMoP) [31–35], metal layered double hydroxides (e.g., NiFe LDH,
NiV LDH) [36–39], heteroatom-doped carbon (e.g., N,P-codoped nanocarbon)
[40–43], etc.

1.1   General Considerations of Water Splitting

As shown in Fig. 1, an electrolyzer in which the overall water-splitting reaction
happens can be divided into two-half reactions: the hydrogen evolution reaction
(HER) of the cathode and the oxygen evolution reaction (OER) of the anode. When
an external voltage is applied to the electrodes, water molecules are electrolyzed
into hydrogen occurring in HER and oxygen accompanied with OER. According to
the electrolytes with various pHs in which water splitting carries out, the water
splitting can be described as follows:

The whole reaction:

$$2H_2O \rightarrow 2H_2 + O_2$$

$$E_{cell} = 1.23 \text{ V vs. RHE}$$
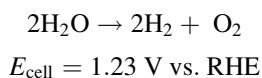
Fig. 1 Schematic diagram illustrating the two-electrode water electrolyzer

In acidic media,

$$\text{OER}: \quad 2H_2O \rightarrow O_2 + 4H^+ + 4e^-$$
$$\text{HER}: \quad 2H^+ + 2e^- \rightarrow H_2$$
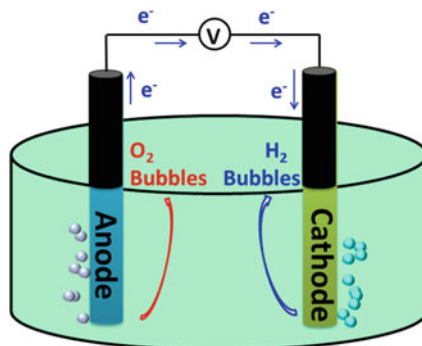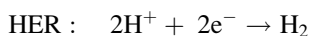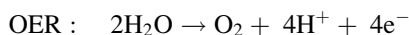
In neutral or alkaline media,

$$\text{HER}: \quad 2H_2O + 2e^- \rightarrow H_2 + 2OH^-$$
$$\text{OER}: \quad 4OH^- \rightarrow 2H_2O + O_2 + 4e^-$$
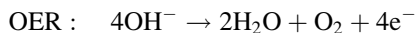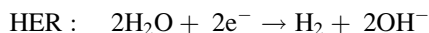
The theoretical minimum voltage required for the electrochemical water splitting is 1.23 V at 25°C regardless of the electrolytes in which water splitting takes place. The practical operational voltage is larger than the theoretical potential due to the existence of the resistances which would consume lots of electricity. Thus, the applied voltage for water splitting can be described as [44, 45]:

$$E_a = 1.23 \text{ V} + \eta,$$

where η includes the overpotentials desired for overcoming intrinsic activation obstacles of both anode and cathode, and the external potentials required for compensating the systematic resistances, e.g., electrolyte resistance and contact resistance. From this point of view, highly active electrocatalysts are desirable in water electrolyzers if they could reduce the overpotential and improve the efficiency of water electrolysis.

1.2 Advantages of Polyoxometalates for Hydrogen Evolution Reaction and Oxygen Evolution Reaction

Polyoxometalates (abbreviated POMs), as its name suggests, represent a class of multi-metal oxyanions usually formed by early transition metals pertaining a d^0 or d^1 electron configuration (e.g., V^V, Mo^V, Nb^V, Ta^V, Mo^{VI}, and W^{VI}). According to this definition, we can use a general formula $[M_m O_y]^{p-}$ to describe them, where M can be visualized as the central metal of a polyhedron, and O can be regarded as the vertices of that polyhedron. These polyhedra can be connected to each other via corner- or edge-sharing modes (face sharing is rarely seen). These structural building blocks may be used to prepare or conceptualize the primary, secondary, and tertiary structures of the POM clusters [46]. Therefore, the different structural POM assemblies can be formed by the linking or aggregation of these polyhedra via a self-assembly process. POM chemistry has developed exponentially due to the modern instrumentation and novel synthetic approaches, starting from the 1991 review [47]. The development of single crystal X-ray diffraction technique has allowed collecting the diffraction data to obtain the aesthetically beautiful structure and the availability of multinuclear NMR spectroscopy has led to a clearer understanding of the structure solution chemistry. The most common and widely studied POMs with dimensions of ca. 1–6 nm are as follows: (a) The Anderson-Evans $[XM_6 O_{24}]^{n-}$ is a planar arrangement of six MO_6 octahedra with a central heteroatom XO_6 octahedron, resulting in an overall D_{3h}-symmetric shape (Fig. 2a) [48–50]. (b) The Keggin $[XM_{12} O_{40}]^{n-}$ is composed of a central XO_4 tetrahedron surrounded by four corner-shared $\{M_3 O_{13}\}$ groups with each triad being composed of three edge-shared MO_6 octahedra, resulting in an overall T_d-symmetry (Fig. 2b) [51]. (c) The Wells-Dawson $[(XO_4)_2 M_{18} O_{54}]^{n-}$ is assembled by the fusion of two trilacunary Keggin-type units $[XM_9 O_{34}]^{n-}$ via corner sharing at the vacant sites. This structure consists of two unequivalent metal centers, the caps (polar positions) and belts (equatorial regions), where the cap is composed of three edge-shared MO_6 octahedra forming an $\{M_3 O_{13}\}$ triad and the belt is formed by alternating corner- and edge-shared MO_6 octahedra, as shown in Fig. 2c [52]. (d) The famous Kelperate structure $[Mo_{72}^{VI} Mo_{60}^{V} O_{372}(CH_3 COO)_{30}(H_2 O)_{72}]^{42-}$ could be abbreviated as $\{Mo_{11}\}_{12}$ with remarkable equivalent stoichiometrical building blocks. The Keggin $\{Mo_{11}\}$ is composed of a central $\{(Mo)^{VI} Mo_5^{VI}\}$ pentagonal bipyramid surrounded by five $\{Mo_1^V\}$ as linkers [53]. Müller pioneered the study of Kelperate spherical POMs (Fig. 2d).

One of the most striking features of POMs is that they could configure and tailor their redox characteristics, reversibly gain and lose up to 24 electrons per unit for the Keggin ion $[PMo_{12} O_{40}]^{3-}$. This phenomenon has been verified by in operando X-ray absorption studies [54]. POMs, structurally well-defined molecular species, together with their unique redox properties, have led to a myriad of applications in electrocatalysis [51, 55–58], electronic and energy storage devices [59], magnetic science [60], as wells as in analytical and clinical chemistry including spectroscopy [61], biology [62–64], and catalysis [65–69].

Fig. 2 Polyhedral representations of polyoxometalate (POM) anions, highlighting their structural variety. (**a**) Anderson anion; (**b**) Keggin anion; (**c**) Dawson anion; and (**d**) {Mo$_{132}$} ball shaped cluster
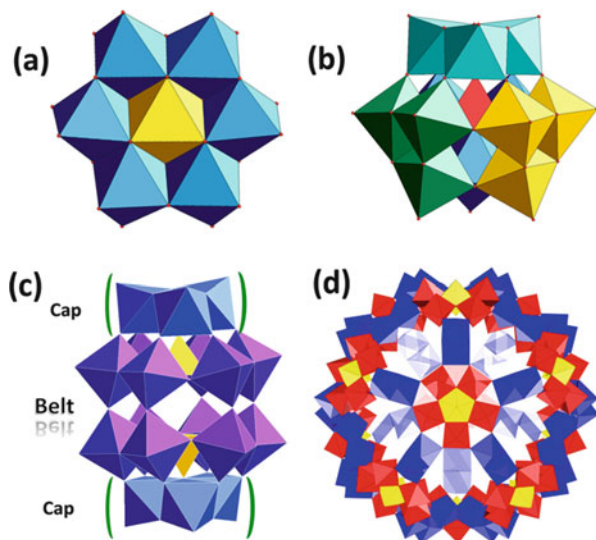
1.3 Scope of This Chapter

Though vast breakthroughs had been achieved in designing and applying POM-based composites [70–73], it was not until the contemporary time that scientific communities have paid attention to their potentials in the field of electro-chemical catalysis. In this chapter, we will briefly introduce the principle of water electrolysis and the regular parameters for the determination of the catalytic activity. Then, we will give an overview of the principal synthetic strategy for POM-based composites including polyoxometalates based metal-organic frame-works (POMOFs), and POMs encapsulated in nanocarbon materials. Meanwhile, we will systematically summarize the performance of POM-based composites. More importantly, we expect that this chapter could provide guidance to rational design and controllable syntheses of POM-based electrocatalysts, which are useful for the further applications in mediators for electrochemical water splitting.

2 Measurement Criteria for Characterizing the Electrochemical Activity

To evaluate the performance of electrocatalysts fairly, the kinetic parameters such as overpotential (η), exchange current density (j_0) and Tafel slope (b) are required to be measured or calculated carefully. The overpotential (η) is one of the most important benchmarks to elucidate the catalytic activity of the target electrocatalysts. It is generally logarithmically related to the current density (j) as given by Tafel equation: $\eta = a + b \log (j)$. The exchange current density (j_0) is

yielded when this linear relationship η is extrapolated to be zero, describing the intrinsic activity of the electrode under equilibrium conditions [74]. The desirable electrocatalysts should possess a high exchange current density (j_0) and a low Tafel slope (b) in order to be useful at the applied current densities. In practice, the most convenient way to determine the electrocatalytic ability for the target reaction is stating the overpotential at a current density of 10 mA cm^{-2}. Here, precautions have to be taken because different current densities are referred to different overpotential. Therefore, the current density of the reported overpotential should be stated.

Apart from the above discussed parameters used for developing excellent electrocatalysts, some other factors for designing catalytic materials are also very important. The construction of an ideal electrocatalyst should be considered in the light of the following three principles: (1) high activity; the more active sites (the part where catalysis reaction can happen) that the catalysts have, the better they are for evolution reactions. (2) Long-term stability; the continuous hydrogen evolution or oxygen evolution could last for over 8 h while the catalyst activity would not be reduced. There are two approaches for characterizing its stability. One way is to measure the current variation with time (I–t curve). The other method is to conduct the cycling experiment by using linear sweep voltammetry (LSV) and cyclic voltammetry (CV). More precisely, if the number of cycles is over 5,000, it indicates that the material has good stability [44]. (3) High selectivity; the Faraday efficiency of the reaction process is calculated by comparing the ratio of the experimentally detected hydrogen or oxygen amount to the theoretically calculated hydrogen or oxygen amount, which should be close to 100%. Currently, industrial electrolytic water catalysts include commercially available Pt/C electrocatalysts for HER and IrO$_2$ or RuO$_2$ catalysts for OER. These two types of precious metals are the most important benchmarks to determine the performance of the catalysts. However, the noble metals are exorbitantly costly. There is an urgent need to develop highly efficient, cost-effective, and earth-abundant non-precious metal catalysts.

3 Synthetic Strategies Used for Constructing Polyoxometalates Based Materials

Due to the rich composition of the high oxidation states of V, Mo, and W (V^V, Mo^{VI}, and W^{VI}), POMs are supposed to be a perfect candidate to prepare high efficient electrocatalysts. Cronin et al. have introduced the concept of electron-coupled-proton buffer (ECPB), whereby the OER was decoupled from the HER, O$_2$ and H$_2$ can be produced separately in both space and time [75]. It broke through the conventional water electrolysis producing H$_2$ and O$_2$ simultaneously, but the catalysis of {PMo$_{12}$} was weak. Moreover, it had high requirement regarding the catalysts, e.g., they should have reversible redox waves between OER and HER, should be highly soluble in

water, and should effectively buffer the pH variations without any degradation during the water-splitting process. Indeed, most of POMs as electron and proton reservoir could undergo reversible multi-electron processes in the homogeneous liquid media. However, their applications as very efficient heterogeneous electrocatalysts are circumvented by the following drawbacks: (1) they are very soluble in water or electrolyte, which is not good for isolating and recycling them from the solution; and (2) they have low specific surface area (<10 m^2 g^{-1}), which are not conductive to catalytic performance.

There are two synthetic strategies here for solving this problem. One method is to immobilize POMs in porous metal-organic framework (MOF). MOFs represent a branch of porous materials with high surface area, highly ordered permanent porosity, and tunable chemical structures, and they are excellent candidates for carriers. Because POMs are either as a template occupied in the cavities of MOFs or directly part of the frameworks of MOFs, such kinds of materials are termed as POMOFs materials. The other method is to load POMs evenly between graphene oxide (GO) or some other carbon materials. Furthermore, GO-based materials are nontoxic, chemically tolerant, which is possible to be exfoliated into single layers as carrier uniformly in aqueous solution. Because of the insolubility of the POMOFs and POM-based carbon materials, the electrochemistry of the composites is allowed to be performed in the solid state by entrapping them in a perfluorinated polymer (Nafion). Those composites are anticipated to be useful for efficient electrocatalysts elaboration. Furthermore, on theoretical grounds, the entrapment of POMs in a 3D configuration could increase their electrocatalytic activity [56, 76]. Those strategies Su and Lan adopted here offer an effective and feasible way for preparing electrocatalytic materials with low solubility and high surface area.

4 Polyoxometalates Based Metal-Organic Framework Materials

4.1 Polyoxometalates Based Metal-Organic Framework Single Crystal Materials

Hybrid materials involving the combination of metal–organic complexes and POMs have been met in the past few decades. There are essentially two key factors, stability and porosity, utilizing POMOF as electrocatalysts. Compared with the traditional MOFs, though vast examples of POMOFs have been usually synthesized in water with good stability, the porosity of the synthesized single crystals is small due to the lack of organic solvent as template during the synthetic process. It is natural to ask the question: how to synthesize porous and stable POMOFs? According to the structural diversity, POMOFs could be classified into three categories: (1) POMs serving as nodes connected with the rigid ligand, (2) POMs

serving as a template encapsulated within the cavities of MOFs, and (3) POMs anions serving as pillars. As shown in Fig. 3, the second one and the third one are easier to support the channel compared to the first one where the cavities of the resulting porous materials are partially occupied. Therefore, researchers draw this idea to design POMOFs. Then, a new synthetic challenge came: how do the anionic POMs coordinate to organic ligands?

POMOFs are usually prepared by utilizing POMs precursors, organic ligands, and metal ions via conventional bottom-up aqueous solution methods or hydro-/solvo-/iono-thermal methods [77]. Although POMOFs-based materials have been studied extensively as catalysts [77–79], there were only a few reports on POMOFs utilized as electrocatalysts [80]. Dolbecq et al. primarily studied the cation effect on the electrocatalytic activities of $(TBA)_3[PMo^V_8Mo^{VI}_4O_{36}(OH)_4Zn_4]$ $[C_6H_3(COO)_3]_{4/3} \cdot 6H_2O$ ($\varepsilon(trim)_{4/3}$, TBA^+ = tetrabutylammonium ion) in XCl (X = Li, Na, K, Cs) media [80]. The material represented the first example of non-noble POM-based materials and showed a turnover frequency (TOF) as high as ca. 6.7 s^{-1} with $\eta = 200$ mV for HER. Dolbecq et al. synthesized five compounds. These compounds all contain {Zn-ε-Keggin} fragments and organic ligands, in which {$C_6H_3(COO)_3$} of $\varepsilon(trim)_{4/3}$ was substituted by some other types of organic

POM-based MOF single-crystal materials
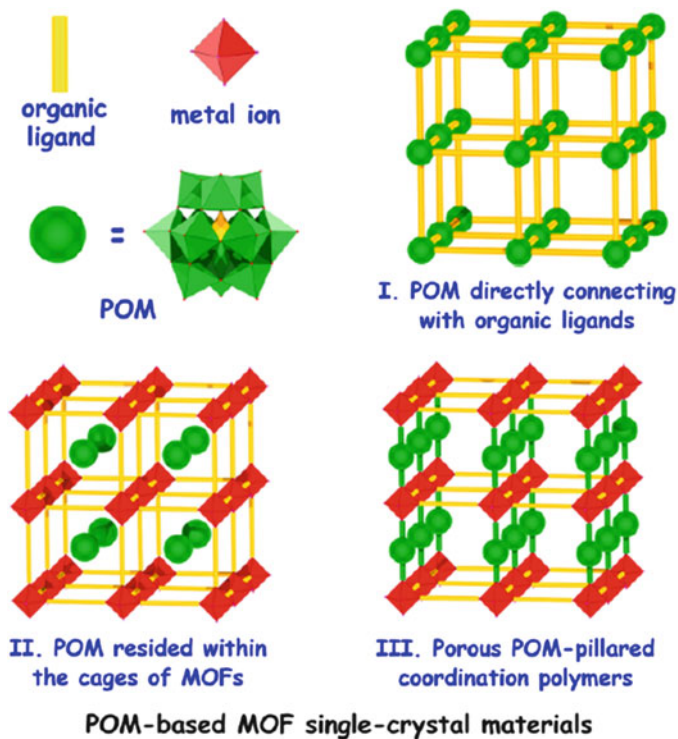
Fig. 3 Schematic views of three main forms of polyoxometalates based metal-organic framework (POMOFs) materials. Reprinted with permission [77]. Copyright 2014, Royal Society of Chemistry

linkers. Those hybrids also showed remarkable behaviors for HER which is mainly due to the presence of {Zn-ε-Keggin} units as well as their special structures.

Lan's group modified the Keggin type of {PMo$_{12}$} through the decoration of transition metal to synthesize the coordinated chloride ion and zinc modified Zn-ε-Keggin-Cl (**NENU-499**, (TBA)$_4$[ε-PMo$^V_8$Mo$^{VI}_4$O$_{37}$(OH)$_3$Zn$_4$]Cl$_4$). After that, chloride ions were substituted by the carboxylate group. Density functional calculations showed that the binding energy value of POMs coordinated chloride ions was smaller than that of carboxylate group and demonstrated that POMs with carboxylate groups were more stable than those with chloride ions. This provided a theoretical basis for the next step in the construction of porous POMOFs (Fig. 4).

In view of the above discussed strategies, {Zn-ε-keggin} fragments [81] serving as nodes were linked to ligands with different sizes, respectively, to form POMOFs with different frameworks, **ε(trim)**$_{4/3}$ [80], (TBA)$_3$[ε-PMo$^V_8$Mo$^{VI}_4$O$_{36}$(OH)$_4$Zn$_4$] [BTB]$_{4/3}$·xGuest (**NENU-500**, BTB = benzene tribenzoate) [81], and (TBA)$_3$[ε-PMo$^V_8$Mo$^{VI}_4$O$_{36}$(OH)$_4$Zn$_4$][BPT]$_{4/3}$·xGuest (**NENU-501**, BPT = (1,1'-biphenyl)-3,4',5-tricarboxylate) [81] (Fig. 5). The N$_2$ adsorption curve showed that the crystal structure changes from nonporous to microporous as the rigidity of the ligand increases. Powder X-ray diffraction (PXRD) of the compounds under different pH values showed that they had good chemical stability. As an electrochemical hydrogen evolution catalyst, porous POMOF **NENU-500** had the best electrochemical activity compared to other MOFs and POMOFs (**NENU-501**, **ε(trim)**$_{4/3}$,
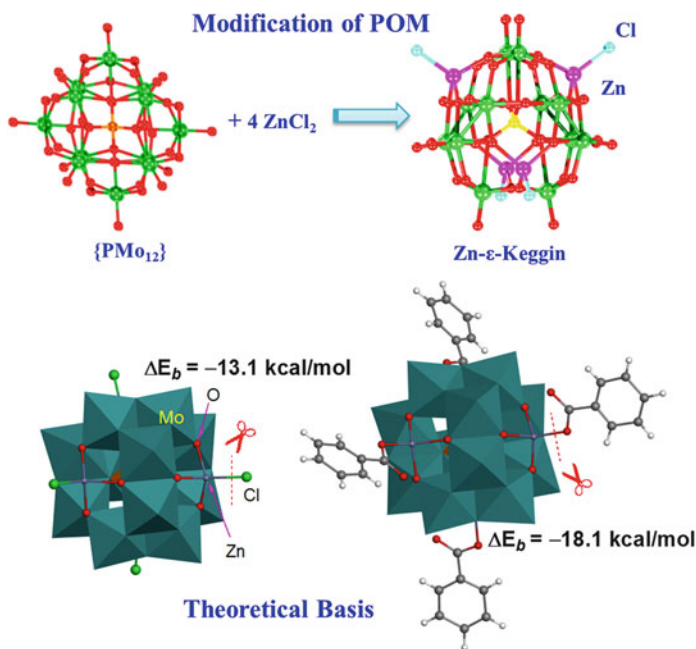
Fig. 4 Theoretical basis of designing POMOFs. Reprinted with permission [81]. Copyright 2015, American Chemical Society
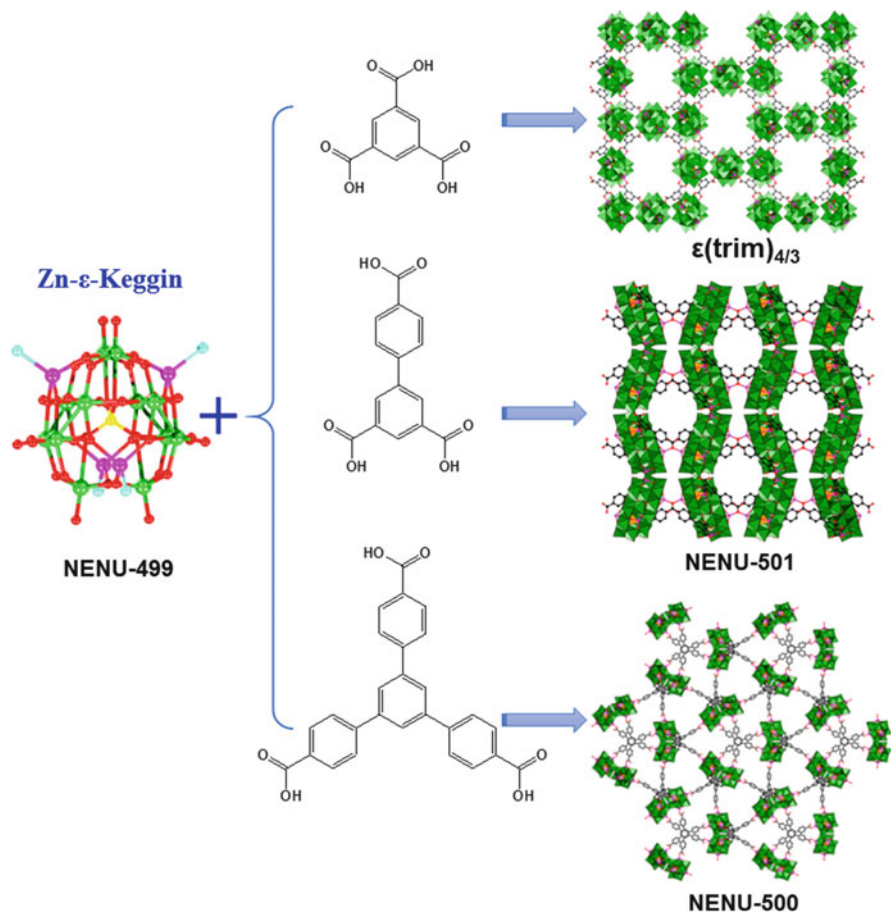
Fig. 5 Schematic views of three types of POMOFs single crystal materials with different sizes of pores

NENU-499, **NENU-5**, and **HKUST-1**) due to its good stability, highly porosity, and exposed active sites. It showed an onset potential of 180 mV and an overpotential of 237 mV at the current density of 10 mA cm^{-2} (Fig. 6a). The performance comparison showed that the extensive porosity has a great influence on the electrochemical activity of POMOFs. Tafel slope is also a very important parameter for evaluating an inherent property of electrocatalytic materials and elucidating HER mechanism involved. Figure 6b displayed the Tafel plots for the corresponding materials. The Tafel slopes of commercially available Pt/C, **NENU-500**, **NENU-501**, **ε(trim)$_{4/3}$**, **NENU-499**, **NENU-5**, and **HKUST-1** obtained from the Tafel plots are 30, 96, 137, 142, 122, 94, and 127 mV dec^{-1}, respectively. In summary, POMOFs single crystal materials are successful examples that POMs could be immobilized in MOFs evenly at the atomic or molecular level. This unique feature of POMOFs combining the redox activity of POMs and the porosity of MOFs opens up a new path for designing more efficient catalysts.
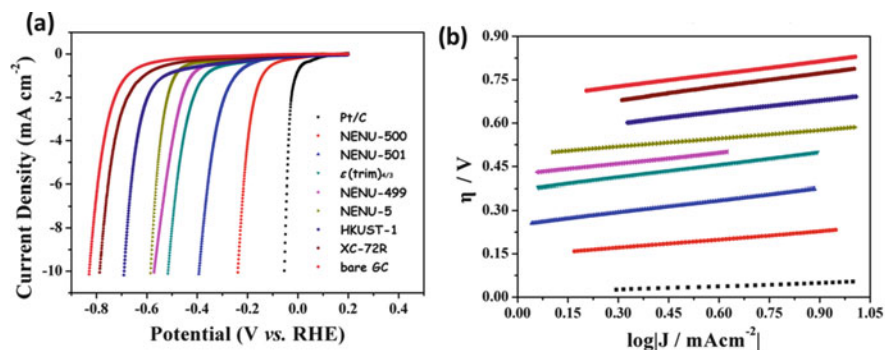
Fig. 6 (**a**) Hydrogen evolution reaction (HER) polarization curves of various electrocatalysts in 0.5 M H_2SO_4 aqueous solution. (**b**) Tafel plots of the corresponding catalysts. Reprinted with permission [81]. Copyright 2015, American Chemical Society

4.2 Polyoxometalates Based Metal-Organic Framework-Based Composites as Electrocatalysts

POMOFs have the advantage of POMs (redox activity) and the advantage of MOFs (porosity). Hence, they form appealing structures and show potential applications. Moreover, due to the inherent presence of Mo, P, and N-moieties in POMOF structures, the POMOFs present ideal sacrificial precursors to derive bimetallic composite electrode materials. The research of POMOFs has been extended from single crystal synthesis to material application. POMOFs as the precursors to prepare the electrochemically active carbon-based composite provide a new idea for the synthesis of the electrocatalysts. Lou et al. prepared porous molybdenum carbide octahedral nanoparticles (MoC_x nano-octahedrons) starting from NENU-5 in situ carburization reaction as a proof of concept exhibiting remarkable electrocatalytic performance for HER in both acidic and basic solutions with good stability (Fig. 7) [82]. It showed an onset potential of 25 mV, an overpotential of 142 mV at the current density of 10 mA cm^{-2}, and a small Tafel slope of 53 mV dec^{-1} in acidic condition. The HER performance in basic solution was also favorable with an onset potential of 80 mV, an overpotential of 151 mV at the current density of 10 mA cm^{-2}, and a small Tafel slope of 59 mV dec^{-1} (Fig. 8).

The study on POMOFs-based catalysts has been further extended to explore porous heteroatom-doped carbon hybrids because the dopant of heteroatoms has the advantage of offering more active sites to enhance their catalytic performance. Lan et al. synthesized the Fe_3C/Mo_2C-containing N,P-codoped graphitic carbon derived from POM@MOF-100 (Fe) (denoted as $Fe_3C/Mo_2C@NPGC$) catalyst by carbonizing the mixture of $PMo_{12}@MIL$-100 (Fe) and melamine at 900°C in a flow of ultrapure N_2 atmosphere (Fig. 9) [83]. By the ingenious synthetic strategy "killing three birds with one stone" the author adopted here, the as-synthesized catalyst had the characteristics of uniform distribution, mesoporous structures, and N, P-heteroatom codoped graphitic carbon. The contradistinctive catalysts $Fe_3C@C$
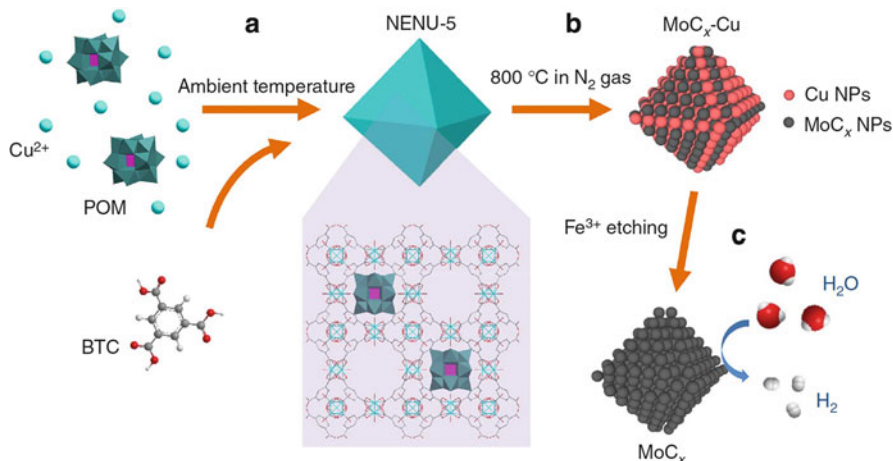
Fig. 7 Preparation processes of porous MoC_x nano-octahedrons. (**a**) Synthesis of NENU-5 nano-octahedrons with {PMo_{12}} residing in the pores of HKUST-1 host. (**b**) Formation of MoC_x-Cu nano-octahedrons after carburization reaction. (**c**) Removal of Cu nanoparticles by Fe^{3+} etching to prepare porous MoC_x nano-octahedrons for HER [82]. Copyright 2015, Nature Publishing group
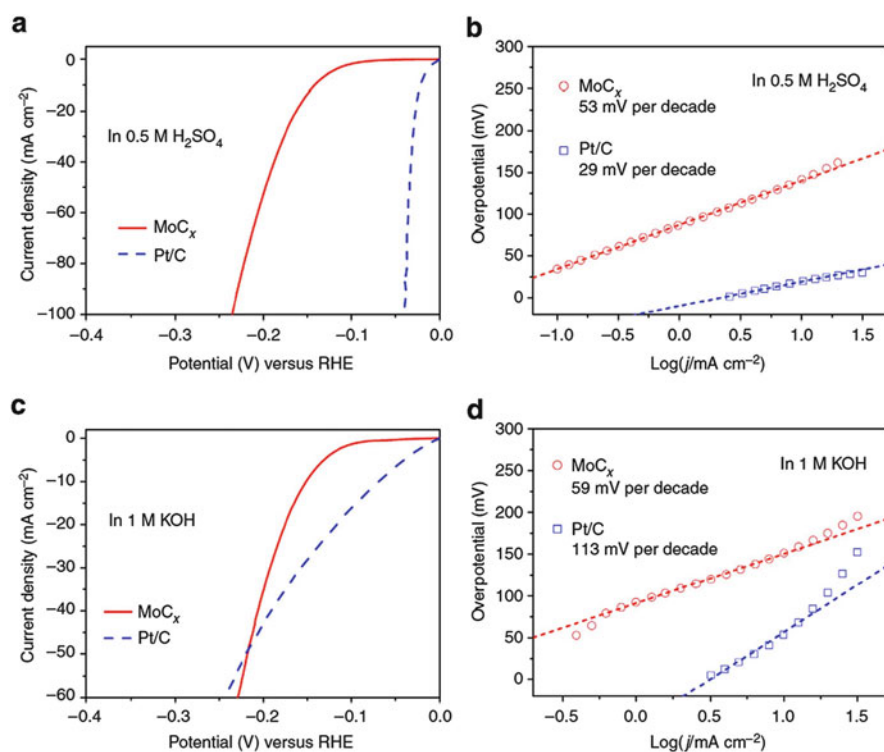
Fig. 8 (**a**) Polarization curves at 2 mV s^{-1} of porous MoC_x nano-octahedrons and Pt/C in 0.5 M H_2SO_4 solution. (**b**) Tafel plots in 0.5 M H_2SO_4. (**c**) Polarization curves at 2 mV s^{-1} in 1 M KOH. (**d**) Tafel plots in 1 M KOH [82]. Copyright 2015, Nature Publishing group
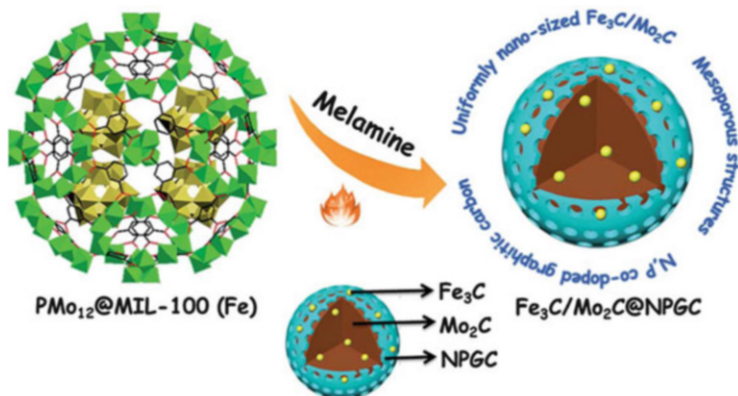
Fig. 9 Preparation process of the Fe$_3$C/Mo$_2$C@NPGC nanocomposite. Reproduced from [83] with permission from The Royal Society of Chemistry

and Fe$_3$C/FeMo/Mo$_2$C were also synthesized via the carbonization of the pure MIL-100 (Fe) or PMo$_{12}$@MIL-100 (Fe) under the same conditions, respectively (Fig. 10). The material Fe$_3$C/Mo$_2$C@NPGC exhibited high HER activity with a low onset potential of 18 mV (vs. RHE), an overpotential of 98 mV at the current density of 10 mA cm^{-2}, a small Tafel slope of 45.2 mV dec^{-1} as well as long-term durability for 10 h.

The noble metal-free HER catalysts still could not replace the Pt or Pt-based nanomaterials because the performances of POMOFs-based catalysts are worse than Pt-group metals. Then, Lan's group have fabricated a hybrid material consisting of MoO$_2$, phosphorus-doped nanoporous carbon, and reduced graphene oxide (RGO) substrates (denoted as MoO2@PC-RGO, Fig. 11) by using a POMOFs/GO-assisted strategy for the following considerations: First, {PMo$_{12}$} is rich in molybdenum and phosphorus moieties [84]. Second, graphene sheets as support have been introduced into POMOFs for electrocatalysts, which are one of the most promising components because of their characteristics of large surface area, chemical toleration, good conductivity, and high stability [85]. Third, the agglomeration of MoO$_2$ can be hindered by confining the carbon skeleton, and MoO$_2$@PC hybrids are loaded onto RGO evenly because of the defined and distinct structure of the POMOFs/GO composite. Phosphorus is doped with MoO$_2$@PC-RGO through P–C and P–O bonds and it offers the active sites for catalysts. The nanosized POMOF/GO composites were prepared first by utilizing the NENU-5 as precursors and GO. The final product was successfully synthesized by carbonizing the mixture of POMOF/GO composites at 800°C in a flow of ultrapure N$_2$ atmosphere and successively by acid-leaching with 3 M HCl. We have to mention that the calcination duration played a key role in obtaining the final product because MoO$_2$ species were reduced to MoC$_2$ upon increasing the carbonizing time to 5 h. The MoO$_2$@PC-RGO nanocomposite exhibited an excellent HER electrochemical activity in acidic solution, with the onset potential close to 0 mV, approaching that
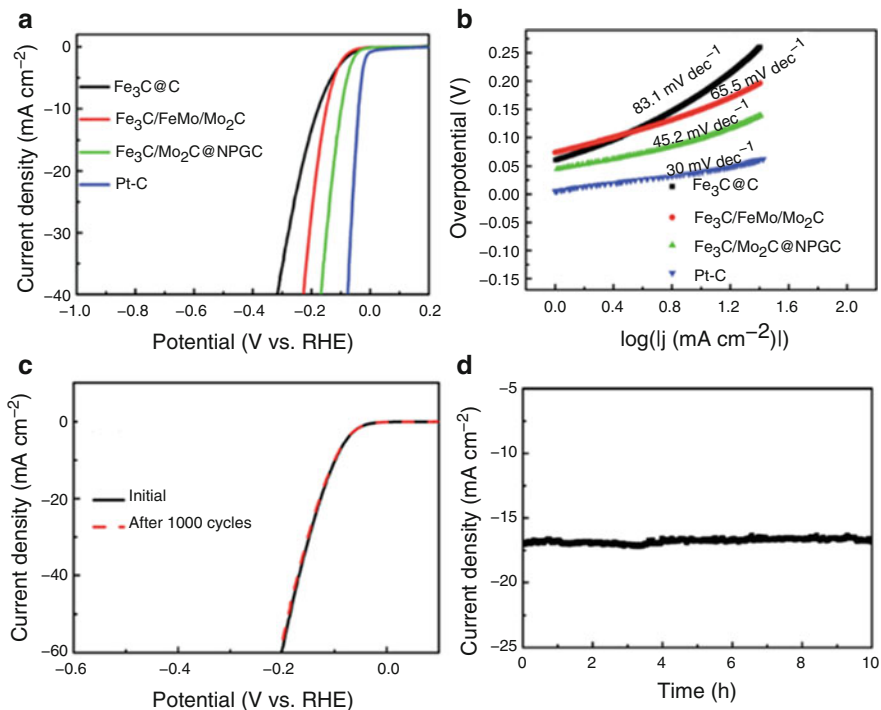
Fig. 10 (**a**) Polarization curves of different samples. (**b**) Corresponding Tafel plots of the polarization curves. (**c**) Polarization curves of Fe$_3$C/Mo$_2$C@NPGC initially and after 1,000 cycles. (**d**) Time dependence of current density under a static overpotential of 120 mV for 10 h. Reproduced from [83] with permission from The Royal Society of Chemistry

of commercially available Pt/C, an overpotential of 38 mV at the current density of 10 mA cm^{-2}, a small Tafel slope of 41 mV dec^{-1} as well as remarkable long-term cycle stability (Fig. 12).

Li et al. also devoted efforts on exploring non-noble metal substitutes derived from POMs precursors instead of Pt-based electrocatalysts [86]. The molybdenum carbide nanoparticles MoC$_x$@C-1 and MoC$_x$-2 were prepared from the starting two types of POMOFs as precursors which were further carbonized at 800°C in a flow of ultrapure N$_2$ atmosphere and acid-leached with 1 M HCl so as to remove the inactive metallic metal (Fig. 13). The measurements showed that the MoC$_x$@C-1 with N dopants and graphene coatings were superior to that of uncoated MoC$_x$-2 nanoparticles. MoC$_x$@C-1 exhibited a low onset potential of 21 mV and an overpotential of 79 mV at the current density of 10 mA cm^{-2}, a small Tafel slope of 56 mV dec^{-1} as well as remarkable long-term cycle stability (Fig. 14). Hence, the confined carburization strategy by using POMOFs as precursors is an extremely promising method for synthesizing other non-noble metal oxides or carbides confined carbon skeletons used as electrocatalysts for water splitting.
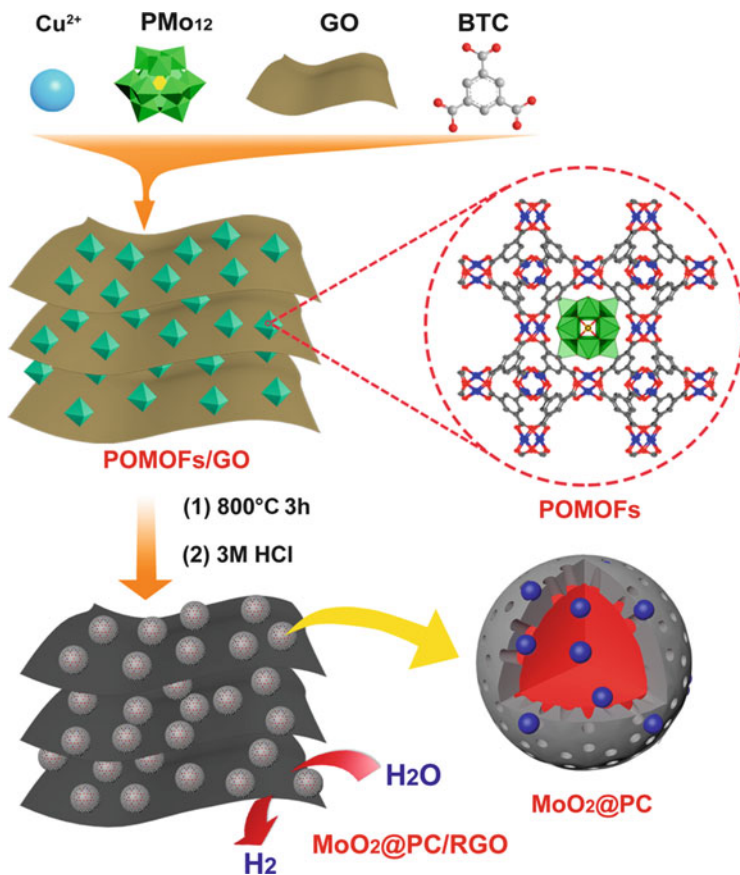
Fig. 11 Schematic construction of the MoO_2@PC-RGO nanocomposite. Copyright 2015, [84] Wiley
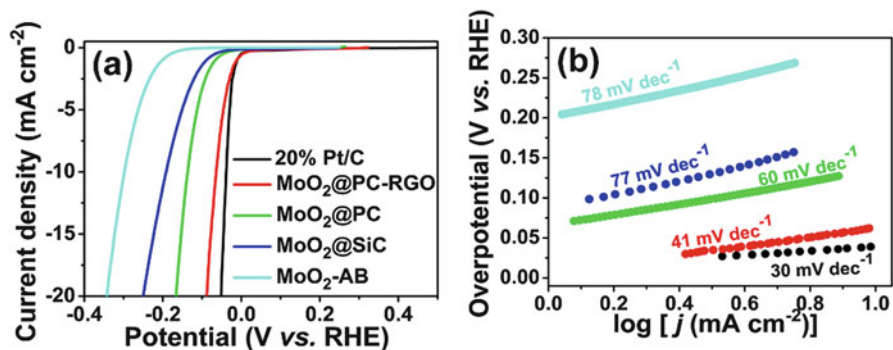
Fig. 12 (**a**) Polarization curves for four electrocatalysts and 20% Pt/C. (**b**) Tafel plots of the corresponding polarization curves. Copyright 2015, [84] Wiley
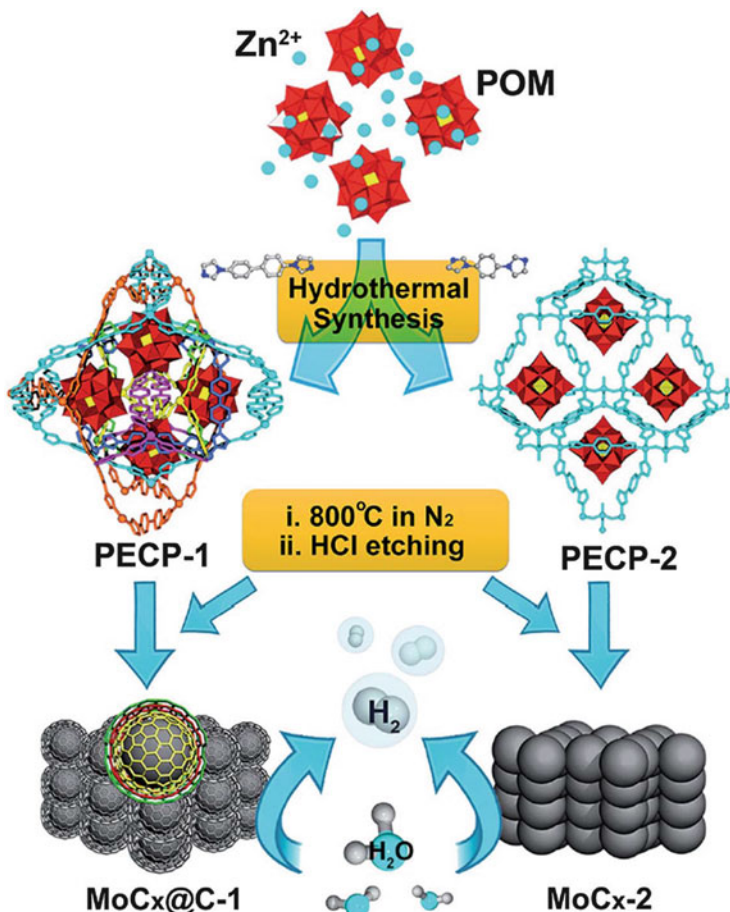
Fig. 13 Schematic constructions of molybdenum carbide nanoparticles [86]. Copyright 2016, Royal Society of Chemistry

5 Polyoxometalate–Carbon Composites

The attachment of POMs in a 3D configuration could boost their electrocatalytic activity. This trend was termed as "microenvironment effect." It was verified not only by theory but also by experiment evidence. Take several effective POM-based electrocatalysts, for example, Kortz's polyanions, $[Cu^{II}_2Pd^{II}_{22}P^V_{12}O_{60}(OH)_8]^{20-}$ [87], $[Co_6(H_2O)_{30}\{Co_9Cl_2(OH)_3(H_2O)_9(\beta\text{-}SiW_8O_{31})_3\}]^{5-}$, $[\{Co_3(B\text{-}\beta\text{-}SiW_9O_{33}(OH))(B\text{-}\beta\text{-}SiW_8O_{29}OH)_2\}_2]^{22-}$ [56], which were fixed on the low-cost carbon material Vulcan XC-72 for the HER in acidic aqueous solutions; $\{Co_7(AlePy)_2\}$, which was immobilized on Vulcan XC-72 for oxygen reduction reactions in basic aqueous solutions with superior durability than that of commercially available Pt/C [88]. As we all know, atom doping has great effect on HER performance because of electronic
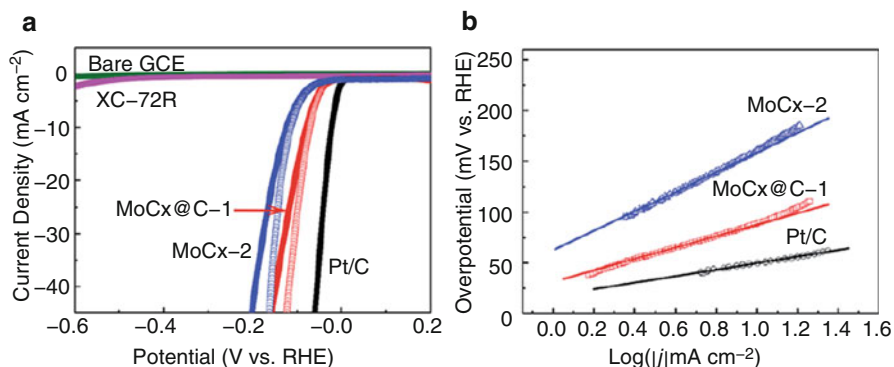
Fig. 14 Electrochemical characterization of the prepared catalysts: (**a**) polarization curves of MoC$_x$@C-1, MoC$_x$-2, 20%Pt/C, and pure carbon black (XC-72R). (**b**) Tafel plots of the corresponding composites [86]. Copyright 2016, Royal Society of Chemistry

structural modification [89]. Wang et al. reported 3D urchin-like Mo doping-$W_{18}O_{49}$ nanocomposite as an efficient HER catalysts with an onset potential of 23 mV, an overpotential of 40 mV at the current density of 10 mA cm^{-2}, a small Tafel slope of 54 mV dec^{-1} as well as long-term durability [90]. Density functional theory calculations revealed that such impressive HER performance is due to the existence of Mo dopant to increase the number of active sites, leading to optimal hydrogen adsorption on the active sites because of the electronic and geometric modulation. In addition, carbon nanotubes (CNTs) have the particularities of hollow geometry, high surface area, and high electronic conductivity. Xu et al. reported a hybrid based on CNTs and the classical 12-tungstophosphate $[PW_{12}O_{40}]^{3-}$ Keggin ion as effective electrocatalysts for HER [91]. Spectra and electrochemical results demonstrated that the electroactive sites were the tungstate oxycarbides formed on nanotubes by W–C covalent bonds. Bonchio et al. entrapped {Ru_4SiW_{10}} on multiwall CNTs to obtain high efficient catalyst with low overpotential for OER [92]. Very recently, Li et al. fabricated a cobalt molybdenum phosphide nanocrystal coated by few-layer N-doped carbon shell (donated as CoMoP@C) on a large scale by utilizing {$Co_{16}Mo_{16}P_{24}$} as precursor [93]. The mixture of {$Co_{16}Mo_{16}P_{24}$} and dicyandiamide was initially heated at 500°C for 30 min and then heated at 800°C in a flow of ultrapure N_2 atmosphere with different N_2 flow rate to obtain CoMoP@C. It could be used directly in seawater. It exhibited excellent electrocatalytic activity for HER over the whole pH range, which was close to 20% Pt/C in pH = 0–1 media and superior to 20% Pt/C in pH = 2–14 solution. Theoretical investigation demonstrated that the carbon shell acted as a template, prevented the catalyst from agglomeration, and facilitated the porousness and electroconductivity of the catalysts.

GO-based materials are quite intriguing because of their good conductivity, chemically toleration, and large surface area. Such properties suggest wide applications of GO-based materials [94, 95]. More recently, a class of green materials based on the cyclic 48-tungsto-8-phosphate $[H_7P_8W_{48}O_{184}]^{33-}$ and the reduced GO was used for highly active HER electrocatalyst by Zhang and coworkers [96]. P_8W_{48}/rGO was prepared by one-step electrochemical reduction method

(Fig. 15) and it exhibited an exceptionally low overpotential of 28 mV at a current density of 10 mA cm^{-2}, a small Tafel slope of 38 mV dec^{-1} as well as remarkable long-term cycle stability during prolonged potential cycling (Fig. 16). The choice of the macrocyclic POM {P_8W_{48}} serving as an efficient graphite oxide reductant as precursors was very important [96]. In comparison, a much higher overpotential of 188 mV was obtained for H_2W_{12}/rGO at a current density of 10 mA cm^{-2}. The electrochemical behavior of P_8W_{48}/rGO was comparable well with those of Pt/C, which represented the most convincing experimental examples of the predicted "microenvironment effect."

Dispersing POMs on specific substrates (e.g., graphene or RGO) could greatly improve the catalyst activities due to the enhancement of conductivity and enlargement of specific surface area of POMs. The above example provided a good synthetic path for synthesizing POM-based GO composites by electrochemical reduction [96]. Then, the question is that how to simply mix POMs and GO without extra voltage? And this is unfortunate, because the interaction between POMs and carbon materials is weak, and thus POMs fall off easily. To solve this problem, conducting organic polymer, ionic liquid, or dye were introduced. Then, Lan et al. prepared a family of hybrid materials consisting of POMs, conducting polymer, and
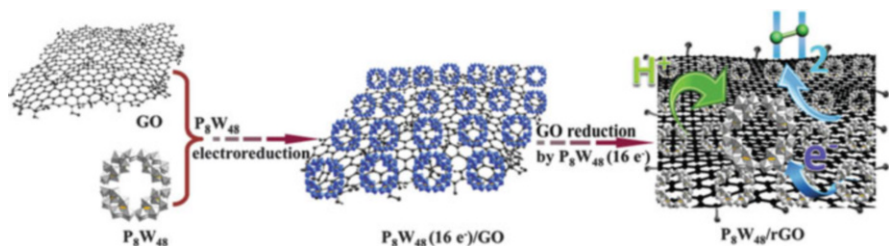
Fig. 15 Schematic view of the one-step electrochemical reduction synthesis of the P_8W_{48}/rGO nanocomposite [96]. Copyright 2016, Royal Society of Chemistry
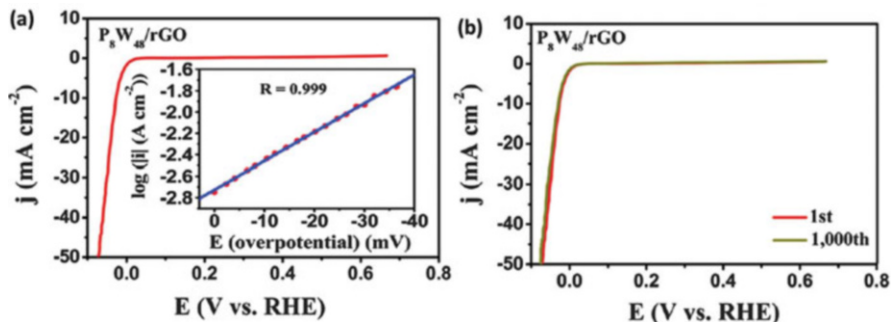
Fig. 16 Electrochemical characterization of the prepared P_8W_{48}/rGO: (**a**) polarization curves of P_8W_{48}/rGO, and the *inset* shows the corresponding Tafel plot obtained from the polarization curve, and (**b**) catalyst stability tests for the composite initially and after 1,000 CV sweeps [96]. Copyright 2016, Royal Society of Chemistry
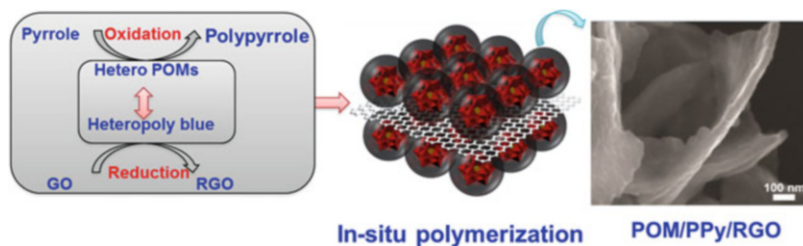
Fig. 17 Synthetic strategy of designing POM/conducting polymer/GO (abbreviated as PCG) substrates (taking conducting polymer of polypyrrole as an example)

RGO substrates (denoted as PCG, Fig. 17) for the following considerations: First, the stacking and aggregation of graphene could be avoided by the introduction of polymer-functionalized POMs. Second, taking pyrrole monomer as an example, it is polymerized into polypyrrole owing to the acidic and oxidative properties of heteropoly acid. Meanwhile the heteropoly acid is reduced to heteropoly blue, and the graphene oxide is reduced to the RGO by the reducing agent-heteropoly blue (Fig. 17). With the polymerization of the pyrrole monomers, POMs are dispersed into the polypyrrole framework. Meanwhile, the RGO is homogeneously distributed and segregated by POMs with wrapped polypyrrole. Third, conducting organic polymers such as polyaniline, polypyrrole, and polythiophene provide C and N sources, and POMs can function as the Mo and P sources, etc. Overall, POMs encapsulated by polypyrrole would be evenly sandwiched between the graphene which is able to be exfoliated to single sheets to form an alternately stacked conformation. This synthetic strategy Lan introduced here not only increases the number of active sites on the materials but also enhances their intrinsic properties such as energy adsorption, electroconductivity, and so on.

Lan's group obtained a ternary POMs-polypyrrole/RGO nanocomposite (POMs-PPy/RGO) by the new synthetic strategy to integrate POMs and pyrrole on graphene sheets via one-pot approach [97]. The homogeneous dispersion of the ternary POMs-PPy/RGO as a precursor was further carbonized at high-reaction temperature, leading to a porous uniform thin layer RGO-supported Mo-based two-dimensional coupled hybrid ($Mo_2C@NPC/NPRGO$) (Fig. 18). The hybrid consists of Mo_2C encapsulated by N,P-codoped carbon shells and N,P-codoped RGO, exhibiting outstanding electrocatalytic activity for HER with a low onset potential of 0 mV, a low overpotential of 34 mV at a current density of 10 mA cm^{-2}, and a small Tafel slope of 33.6 mV dec^{-1} (Fig. 19). There are three main advantages for these excellent electrocatalysts: (1) the Mo_2C NPs are nanosized and uniformly embedded in the carbon shells without aggregation; (2) the Mo_2C NPs are coated with carbon matrices, which prevent Mo_2C NPs from aggregating or oxidizing and impart them with fast electron transfer ability; and (3) the heteroatom dopants (N, P) provide a large number of exposed active sites. Such efficient catalysts were further verified by theoretical studies, which demonstrated that the reason ascribes to the synergistic effect between
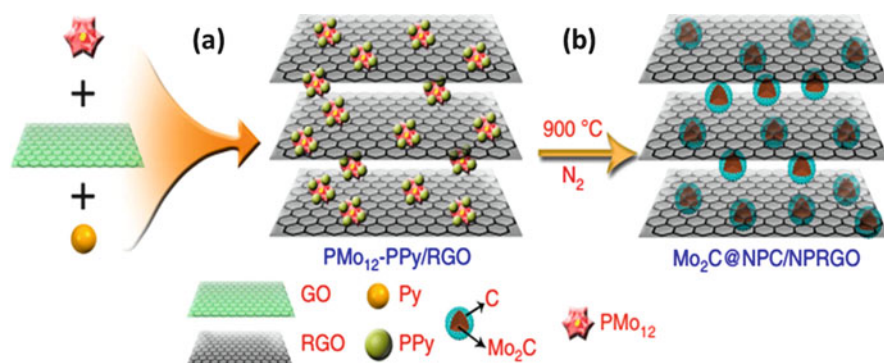
Fig. 18 Schematic construction of $Mo_2C@NPC/NPRGO$. (**a**) Synthesis of POMs-PPy/RGO via one-pot reaction. (**b**) Formation of $Mo_2C@NPC/NPRGO$ after carbonizing at 900°C in a flow of ultrapure N_2 atmosphere [97]. Copyright 2016, Nature Publishing group
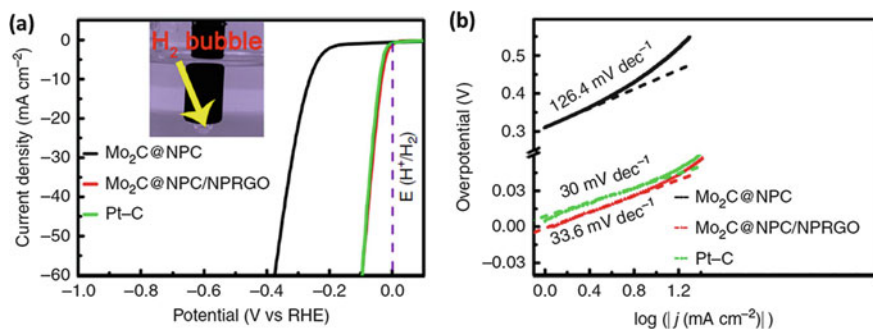
Fig. 19 (**a**, **b**) Polarization curves and Tafel plots of the prepared $Mo_2C@NPC/NPRGO$, and the *inset* shows the production of H_2 bubbles on the surface of $Mo_2C@NPC/NPRGO$ [97]. Copyright 2016, Nature Publishing group

Mo_2C and C-pyridinic N. $Mo_2C@C$-pyridinic N had an appropriate ΔG_{H*} value for the adsorption and desorption of hydrogen.

The PCG composites, which combined the advantages of conductive polymers and graphene film, can be prepared in large scales through a simple one-pot stirring or hydrothermal method. In addition, introducing the second transition metal to PCG systems (denoted as metal–PCG) not only retains the structure and morphology of PCG but also fine-tunes the structure of carbides together with the bimetallic effect and eventually to enhance simultaneously the electrocatalytic activity for the obtained bimetallic carbide-based materials [98–100]. Recently, Lan et al. have synthesized Co-Mo-C/NRGO-1 by the temperature programmed reduction (TPR) method utilizing the metal–PCG system as precursor (Fig. 20) [101]. The Co–PCG composite was simply prepared by a simple mixture of PMo_{12}, Py, GO films, and $Co(NO_3)_2$ using a hydrothermal method, which was further carbonized directly in a horizontal tube furnace at 800°C in a flow of ultrapure N_2 atmosphere. The resulting

Fig. 20 Schematic construction of Co–Mo–C/ NRGO-1 composite [101]. Copyright 2016, Nature Publishing group
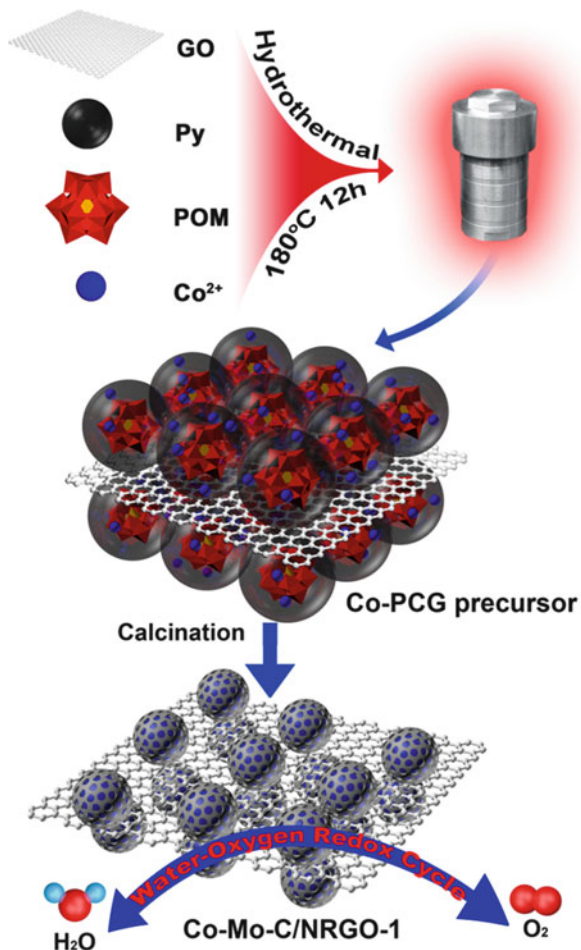
Co–Mo–C/NRGO-1 composite exhibited surprisingly high OER and ORR performance as a bifunctional electrocatalyst (Fig. 21). The OER performance of Co–Mo–C/NRGO-1 was the best among all the reported carbide-based materials and was comparable to the best OER electrodes with an ultra-low Tafel slope of 42 mV dec^{-1}, a small overpotential of 330 mV vs. RHE at the current density of 10 mA cm^{-2}, and long-term stability in alkaline electrolyte. The ORR performance was also investigated with a positive onset potential ($\sim$−95 mV vs. Ag/AgCl), remarkable stability over 30,000 s, and good tolerance to methanol crossover.

POMs are a class of structurally well-defined metal-oxygen (usually composed of MoO_6, WO_6, and V_2O_5) anionic clusters. Polyoxomolybdenum as precursors have been studied in PCG systems for HER, for the analogue structure of polyoxomolybdenum which gave impetus to study on the preparation and characterization of polyoxotungstate based composites. In particular, in recent years considerable efforts have been devoted to enhance the activity of tungsten carbides
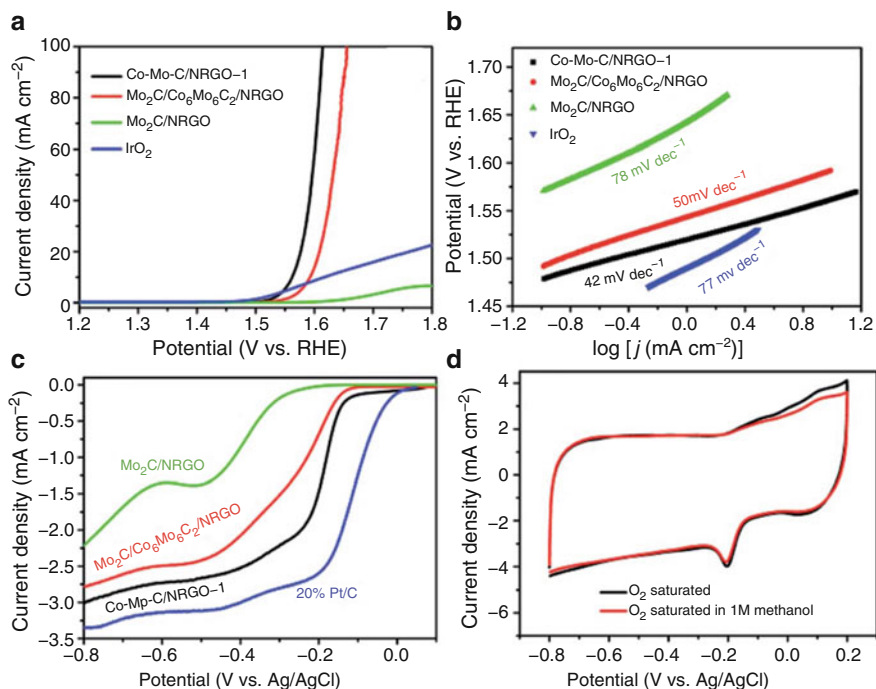
Fig. 21 Electrochemical characterization of the prepared Co–Mo–C/NRGO-1 composite: (**a**) linear sweep voltammetry (LSV) curves of Co–Mo–C/NRGO-1 composite and the comparable samples with a scan rate of 5 mV s^{-1} for oxygen evolution reaction (OER). (**b**) The corresponding Tafel plots derived from (**a**). (**c**) LSV curves of Co–Mo–C/NRGO-1 and the comparable samples with a scan rate of 5 mV s^{-1} and a rotation speed of 1,600 rpm. (**d**) CV curves of Co–Mo–C/NRGO-1 in 0.1 M KOH without and with 1 M MeOH [101]. Copyright 2016, Royal Society of Chemistry
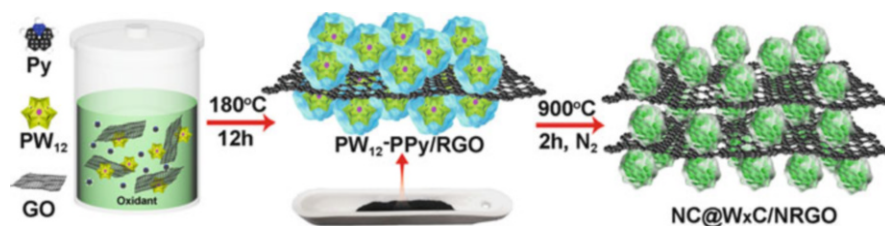
Fig. 22 Schematic construction of NC@W$_x$C/NRGO composite [106]. Copyright 2017, Wiley

which have been actively studied for its Pt-like behavior [102–105]. Lan et al. have carefully fabricated a two-dimensional coupled hybrid NC@W$_x$C/NRGO [106] consisting of tungsten carbide (WC, W$_2$C) encapsulated by N-doped RGO (Fig. 22). First, {PW$_{12}$}, pyrrole monomer, the assisted oxidant FeCl$_3$·6H$_2$O, and graphene oxide were mixed according to the corresponding ratios to synthesize PCG system by one-pot hydrothermal method. Then, the obtained sample was

further carbonized in a horizontal tube furnace at 900°C in a flow of ultrapure N_2 atmosphere. The resulting NC@W$_x$C/NRGO composite exhibited excellent HER performance in acidic media, with an onset potential of 24 mV and an overpotential of 100 mV at the current density of 10 mA cm^{-2}, a small Tafel slope of 58.4 mV dec^{-1} as well as remarkable long-term cycle stability (Fig. 23). This has been one of the highest HER catalysts among the tungsten carbides-based materials ever reported. Very recently, Li et al. reported tungsten carbide NPs encapsulated in N-carbon (donated as P-W$_2$C@NC) by utilizing PW$_{12}$ as precursor [107]. The mixture of {PW$_{12}$} and dicyandiamide was initially heated at 400°C for 30 min and then heated at 800°C in a flow of ultrapure N_2 atmosphere with different N_2 flow rates to obtain the N-carbon coated P-modified tungsten carbide composite, which exhibited excellent electrocatalytic activity for HER over the whole pH range, with a low overpotential of 63 mV in alkaline medium, 89 mV in acid solution, and 185 mV in neutral electrolyte, all at a current density of 10 mA cm^{-2}.

Beyond the excitement for POM-based metal carbides, metal oxides, the class of transition metal dichalcogenides is of particular interest because of their low economic cost and edge-terminated structure among 2D materials, showing remarkable performance as HER electrocatalysts [108–110]. MoS$_2$ showing S-Mo-S layers through weak van der Waals interaction has the catalytic active sites, which has been verified by theoretical studies [111–114]. Lan's group devoted efforts to increase the interlayer spacing of MoS$_2$ and avoid the severe stacking of MoS$_2$-based materials by introducing small molecules, and further to improve the HER activity. Lan et al. have carefully fabricated a family of uniformly MoS$_2$/nitrogen-doped RGO nanocomposites MoS$_2$/N-RGO-T consisting of an ultrathin molybdenum disulfide encapsulated by N-doped RGO with interlayer spacing ranging from 6.2 to 9.5 Å (Fig. 24) [108]. First, PMo$_{12}$ was dissolved in homogenous GO solution by ultra-sonication for a few minutes. Then, thiourea was added to the above solution and the mixtures with different molar ratios and concentration ratios were heated in a Teflon-lined autoclave by one-pot hydrothermal method. Experimental study showed that when the reaction was heated at 160 or 180°C for
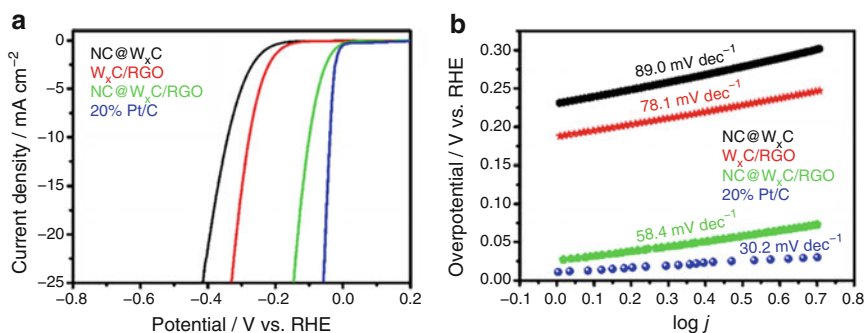
Fig. 23 Electrochemical characterization of the prepared NC@W$_x$C/NRGO composite: (**a**) LSV curves of NC@W$_x$C/NRGO composite and the comparable samples. (**b**) The corresponding Tafel plots derived from (**a**) [106]. Copyright 2017, Wiley
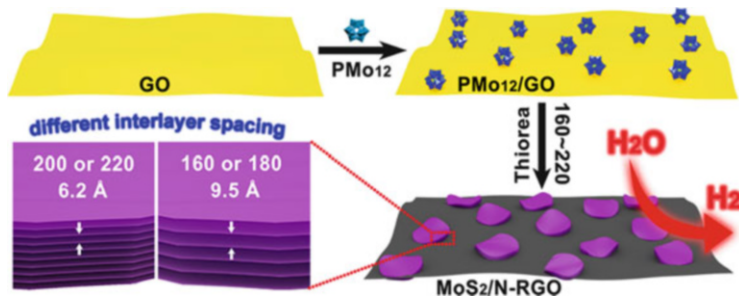
Fig. 24 Schematic constructions of MoS$_2$/N-RGO-*T* composite [108]. Copyright 2016, Wiley
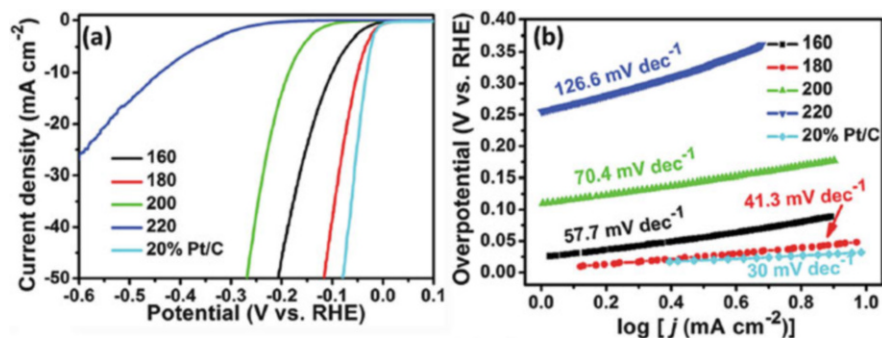
Fig. 25 Electrochemical characterization of the prepared MoS$_2$/N-RGO-*T* composites: (**a**) LSV curves of MoS$_2$/N-RGO-*T* composites at different temperatures; and (**b**) the corresponding Tafel plots [108]. Copyright 2016, Wiley

24 h, the MoS$_2$ nanosheet for MoS$_2$/N-RGO had the most enlarged interlayer spacing of 9.5 Å, whereas, the reaction temperature was higher than 180°C, the interlayer spacing decreased to 6.2 Å. The resulting MoS$_2$/N-RGO-180 composite exhibited excellent HER performance in acidic media, with an onset potential of −5 mV and an overpotential of 56 mV at the current density of 10 mA cm^{-2}, a small Tafel slope of 41.3 mV dec^{-1} as well as remarkable long-term cycle stability (Fig. 25).

6 Summary and Outlooks

In this chapter, we have presented an overview of progress in POMs, POMOFs, and POM-based materials for electrochemical catalysis applications. The pure POMs have been exploited for catalysis due to their rich electronic properties and high redox activity. However, the design of an ideal electrocatalyst with low-cost, high activity, high porosity, and large number of exposed active sites is quite challenging. The major drawbacks associated with POMs are their high solubility and low

surface area, which have been addressed by either compositing with tunable porous MOFs or coating POMs on highly conductive, porous carbon materials. The developed composites will provide several advantages, for example: (1) the introduction of MOFs or porous substrates will help maintain the porosity for mass transport. (2) The calcination of POMs or POMOFs will lead to formation of highly active sites on the template surface, and thus for stabilizing structure and diffusing mass faster. Such design could be summarized to three steps: (1) Functional orientation selection and synthesis of stable POMs; (2) making POM-based materials; and (3) applying to energy storage and conversion. Due to the multifunctional nature of POMs materials, it is certain that the versatility and generality of this POMs-assisted strategy would continue to expand and the application of such materials would be significantly broadened to other areas, such as lithium battery, lithium-sulfur battery, and so on.

References

1. Turner JA (2004) Sustainable hydrogen production. Science 305(5686):972–974
2. Subbaraman R, Tripkovic D, Strmcnik D, Chang K-C, Uchimura M, Paulikas AP, Stamenkovic V, Markovic NM (2011) Enhancing hydrogen evolution activity in water splitting by tailoring Li^+-$Ni(OH)_2$-Pt interfaces. Science 334(6060):1256
3. Subbaraman R, Tripkovic D, Chang K-C, Strmcnik D, Paulikas AP, Hirunsit P, Chan M, Greeley J, Stamenkovic V, Markovic NM (2012) Trends in activity for the water electrolyser reactions on 3d M(Ni,Co,Fe,Mn) hydr(oxy)oxide catalysts. Nat Mater 11(6):550–557
4. Lim H-D, Yun YS, Cho SY, Park K-Y, Song MY, Jin H-J, Kang K (2017) All-carbon-based cathode for a true high-energy-density Li-O_2 battery. Carbon 114:311–316
5. Lee G-H, Lee S, Kim J-C, Kim DW, Kang Y, Kim D-W (2017) $MnMoO_4$ electrocatalysts for superior long-life and high-rate lithium-oxygen batteries. Adv Energy Mater 7(6):1601741
6. Wu X, Han X, Ma X, Zhang W, Deng Y, Zhong C, Hu W (2017) Morphology-controllable synthesis of Zn–Co-mixed sulfide nanostructures on carbon fiber paper toward efficient rechargeable zinc–air batteries and water electrolysis. ACS Appl Mater Interfaces 9 (14):12574–12583
7. Cheng Y, Dou S, Veder J-P, Wang S, Saunders M, Jiang SP (2017) Efficient and durable bifunctional oxygen catalysts based on NiFeO@MnOx core–shell structures for rechargeable Zn–Air batteries. ACS Appl Mater Interfaces 9(9):8121–8133
8. Lin D, Liu Y, Cui Y (2017) Reviving the lithium metal anode for high-energy batteries. Nat Nanotechnol 12(3):194–206
9. Walter MG, Warren EL, McKone JR, Boettcher SW, Mi Q, Santori EA, Lewis NS (2010) Solar water splitting cells. Chem Rev 110(11):6446–6473
10. Wang J, Yang J-Y, Fazal IM, Ahmed N, Yan Y, Huang H, Ren Y, Yue Y, Dolinar S, Tur M, Willner AE (2012) Terabit free-space data transmission employing orbital angular momentum multiplexing. Nat Photonics 6(7):488–496
11. Reece SY, Hamel JA, Sung K, Jarvi TD, Esswein AJ, Pijpers JJH, Nocera DG (2011) Wireless solar water splitting using silicon-based semiconductors and earth-abundant catalysts. Science 334(6056):645
12. Carmo M, Fritz DL, Mergel J, Stolten D (2013) A comprehensive review on PEM water electrolysis. Int J Hydrogen Energy 38(12):4901–4934
13. Peighambardoust SJ, Rowshanzamir S, Amjadi M (2010) Review of the proton exchange membranes for fuel cell applications. Int J Hydrogen Energy 35(17):9349–9384

14. Zeng K, Zhang D (2010) Recent progress in alkaline water electrolysis for hydrogen production and applications. Prog Energy Combust Sci 36(3):307–326
15. Barbir F (2005) PEM electrolysis for production of hydrogen from renewable energy sources. Sol Energy 78(5):661–669
16. Liang Y, Li Y, Wang H, Dai H (2013) Strongly coupled inorganic/nanocarbon hybrid materials for advanced electrocatalysis. J Am Chem Soc 135(6):2013–2036
17. Vrubel H, Hu X (2012) Molybdenum boride and carbide catalyze hydrogen evolution in both acidic and basic solutions. Angew Chem Int Ed 51(51):12703–12706
18. Song J, Li GR, Xiong FY, Gao XP (2012) Synergistic effect of molybdenum nitride and carbon nanotubes on electrocatalysis for dye-sensitized solar cells. J Mater Chem 22 (38):20580–20585
19. Weidman MC, Esposito DV, Hsu Y-C, Chen JG (2012) Comparison of electrochemical stability of transition metal carbides (WC, W_2C, Mo_2C) over a wide pH range. J Power Sources 202:11–17
20. Wan C, Regmi YN, Leonard BM (2014) Multiple phases of molybdenum carbide as electrocatalysts for the hydrogen evolution reaction. Angew Chem Int Ed 53(25):6407–6410
21. Dong S, Chen X, Zhang X, Cui G (2013) Nanostructured transition metal nitrides for energy storage and fuel cells. Coord Chem Rev 257(13–14):1946–1956
22. Hargreaves JSJ (2013) Heterogeneous catalysis with metal nitrides. Coord Chem Rev 257 (13–14):2015–2031
23. Chen W-F, Sasaki K, Ma C, Frenkel AI, Marinkovic N, Muckerman JT, Zhu Y, Adzic RR (2012) Hydrogen-evolution catalysts based on non-noble metal nickel–molybdenum nitride nanosheets. Angew Chem Int Ed 51(25):6131–6135
24. Cao B, Veith GM, Neufeind JC, Adzic RR, Khalifah PG (2013) Mixed close-packed cobalt molybdenum nitrides as non-noble metal electrocatalysts for the hydrogen evolution reaction. J Am Chem Soc 135(51):19186–19192
25. Zhang X, Zhang Q, Sun Y, Zhang P, Gao X, Zhang W, Guo J (2016) MoS_2-graphene hybrid nanosheets constructed 3D architectures with improved electrochemical performance for lithium-ion batteries and hydrogen evolution. Electrochim Acta 189:224–230
26. Ganesan R, Lee JS (2005) Tungsten carbide microspheres as a noble-metal-economic electrocatalyst for methanol oxidation. Angew Chem Int Ed 44(40):6557–6560
27. Zhang Y, Zhang Y, Ji Q, Ju J, Yuan H, Shi J, Gao T, Ma D, Liu M, Chen Y (2013) Controlled growth of high-quality monolayer WS_2 layers on sapphire and imaging its grain boundary. ACS Nano 7(10):8963–8971
28. Voiry D, Yamaguchi H, Li J, Silva R, Alves DCB, Fujita T, Chen M, Asefa T, Shenoy VB, Eda G, Chhowalla M (2013) Enhanced catalytic activity in strained chemically exfoliated WS_2 nanosheets for hydrogen evolution. Nat Mater 12(9):850–855
29. Yang J, Voiry D, Ahn SJ, Kang D, Kim AY, Chhowalla M, Shin HS (2013) Two-dimensional hybrid nanosheets of tungsten disulfide and reduced graphene oxide as catalysts for enhanced hydrogen evolution. Angew Chem Int Ed 52(51):13751–13754
30. Peng S, Li L, Han X, Sun W, Srinivasan M, Mhaisalkar SG, Cheng F, Yan Q, Chen J, Ramakrishna S (2014) Cobalt sulfide nanosheet/graphene/carbon nanotube nanocomposites as flexible electrodes for hydrogen evolution. Angew Chem Int Ed 126(46):12802–12807
31. Jiang P, Liu Q, Liang Y, Tian J, Asiri AM, Sun X (2014) A cost-effective 3D hydrogen evolution cathode with high catalytic activity: FeP nanowire array as the active phase. Angew Chem Int Ed 53(47):12855–12859
32. Popczun EJ, McKone JR, Read CG, Biacchi AJ, Wiltrout AM, Lewis NS, Schaak RE (2013) Nanostructured nickel phosphide as an electrocatalyst for the hydrogen evolution reaction. J Am Chem Soc 135(25):9267–9270
33. Pu Z, Liu Q, Tang C, Asiri AM, Sun X (2014) Ni2P nanoparticle films supported on a Ti plate as an efficient hydrogen evolution cathode. Nanoscale 6(19):11031–11034

34. Huang Z, Chen Z, Chen Z, Lv C, Meng H, Zhang C (2014) $Ni_{12}P_5$ nanoparticles as an efficient catalyst for hydrogen generation via electrolysis and photoelectrolysis. ACS Nano 8 (8):8121–8129

35. Jiang P, Liu Q, Sun X (2014) NiP2 nanosheet arrays supported on carbon cloth: an efficient 3D hydrogen evolution cathode in both acidic and alkaline solutions. Nanoscale 6(22):13440

36. Zhan T, Liu X, Lu S, Hou W (2017) Nitrogen doped NiFe layered double hydroxide/reduced graphene oxide mesoporous nanosphere as an effective bifunctional electrocatalyst for oxygen reduction and evolution reactions. Appl Catal B 205:551–558

37. Jia Y, Zhang L, Gao G, Chen H, Wang B, Zhou J, Soo MT, Hong M, Yan X, Qian G (2017) A heterostructure coupling of exfoliated Ni-Fe hydroxide nanosheet and defective graphene as a bifunctional electrocatalyst for overall water splitting. Adv Mater 29:1700017

38. Weng B, Xu F, Wang C, Meng W, Grice CR, Yan Y (2016) A layered $Na_{1-x}Ni_yFe_{1-y}O_2$ double oxide oxygen evolution reaction electrocatalyst for highly efficient water-splitting. Energy Environ Sci 10:121–128

39. Candelaria SL, Bedford NM, Woehl TJ, Rentz NS, Showalter AR, Pylypenko S, Bunker BA, Lee S, Reinhart B, Ren Y, Ertem SP, Coughlin EB, Sather NA, Horan JL, Herring AM, Greenlee LF (2017) Multi-component Fe-Ni hydroxide nanocatalyst for oxygen evolution and methanol oxidation reactions under alkaline conditions. ACS Catal 7(1):365–379

40. Zheng Y, Jiao Y, Li LH, Xing T, Chen Y, Jaroniec M, Qiao SZ (2014) Toward design of synergistically active carbon-based catalysts for electrocatalytic hydrogen evolution. ACS Nano 8(5):5290–5296

41. Gao S, Li GD, Liu Y, Chen H, Feng LL, Wang Y, Yang M, Wang D, Wang S, Zou X (2014) Electrocatalytic H_2 production from seawater over Co, N-codoped nanocarbons. Nanoscale 7 (6):2306

42. Zou X, Huang X, Goswami A, Silva R, Sathe BR, Mikmeková E, Asefa T (2014) Cobalt-embedded nitrogen-rich carbon nanotubes efficiently catalyze hydrogen evolution reaction at all pH values. Angew Chem Int Ed 53(17):4372–4376

43. Deng J, Ren P, Deng D, Yu L, Yang F, Bao X (2014) Highly active and durable non-precious-metal catalysts encapsulated in carbon nanotubes for hydrogen evolution reaction. Energy Environ Sci 7(6):1919–1923

44. Zou X, Zhang Y (2015) Noble metal-free hydrogen evolution catalysts for water splitting. Chem Soc Rev 44(15):5148–5180

45. Cook TR, Dogutan DK, Reece SY, Surendranath Y, Teets TS, Nocera DG (2010) Solar energy supply and storage for the legacy and nonlegacy worlds. Chem Rev 110 (11):6474–6502

46. Mizuno N, Misono M (1998) Heterogeneous catalysis. Chem Rev 98(1):199–218

47. Pope MT, Müller A (1991) Polyoxometalate chemistry: an old field with new dimensions in several disciplines. Angew Chem Int Ed Engl 30(1):34–48

48. Naruke H, Yamase T (1992) Structure of a photoluminescent polyoxotungstoantimonate. Acta Cryst Sect C 48(4):597–599

49. Schmidt KJ, Schrobilgen GJ, Sawyer JF (1986) Hexasodium hexatungstotellurate(VI) 22-hydrate. Acta Cryst Sect C 42(9):1115–1118

50. Nolan AL, Burns RC, Lawrance GA, Craig DC (2000) Octasodium hexatungstomanganate (IV) octadecahydrate. Acta Cryst Sect C 56(7):729–730

51. Pope MT (1983) Heteropoly and isopoly oxometalates. Springer, Berlin

52. Dawson B (1953) The structure of the 9(18)-heteropoly anion in potassium 9(18)-tungstophosphate, $K_6(P_2W_{18}O_{62}).14H_2O$. Acta Crystallogr 6(2):113–126

53. Müller A, Krickemeyer E, Bögge H, Schmidtmann M, Peters F (1998) Organizational forms of matter: an inorganic super fullerene and keplerate based on molybdenum oxide. Angew Chem Int Ed 37(24):3359–3363

54. Wang H, Hamanaka S, Nishimoto Y, Irle S, Yokoyama T, Yoshikawa H, Awaga K (2012) In operando X-ray absorption fine structure studies of polyoxometalate molecular cluster batteries: polyoxometalates as electron sponges. J Am Chem Soc 134(10):4918–4924

55. Keita B, Nadjo L (2006) In: Bard AJ, Stratmann M (eds) Encyclopedia of electrochemistry, vol 7. Wiley-VCH, Weinheim

56. Keita B, Kortz U, Holzle LRB, Brown S, Nadjo L (2007) Efficient hydrogen-evolving cathodes based on proton and electron reservoir behaviors of the phosphotungstate $[H_7P_8W_{48}O_{184}]^{33-}$ and the Co(II)-containing silicotungstates $[Co_6(H_2O)_{30}\{Co_9Cl_2(OH)_3(H_2O)_9(\beta\text{-}SiW_8O_{31})_3\}]^{5-}$ and $[\{Co_3(B\text{-}\beta\text{-}SiW_9O_{33}(OH))(B\text{-}\beta\text{-}SiW_8O_{29}OH)_2\}_2]^{22-}$. Langmuir 23(19):9531–9534

57. Keita B, Lu YW, Nadjo L, Contant R (2000) Salient electrochemical and electrocatalytic behaviour of the crown heteropolyanion $K_{28}Li_5H_7P_8W_{48}O_{184}\cdot92H_2O$. Electrochem Commun 2(10):720–726

58. Banerjee A, Bassil BS, Roschenthaler G-V, Kortz U (2012) Diphosphates and diphosphonates in polyoxometalate chemistry. Chem Soc Rev 41(22):7590–7604

59. Prabhakaran V, Mehdi BL, Ditto JJ, Engelhard MH, Wang B, Gunaratne KDD, Johnson DC, Browning ND, Johnson GE, Laskin J (2016) Rational design of efficient electrode–electrolyte interfaces for solid-state energy storage using ion soft landing. Nat Commun 7:11399

60. Barras-Almenar JJ, Coronado E, Müller A, Pope MT (2003) Polyoxometalate molecular science, vol 35. Springer, Dordrecht

61. Dolbecq A, Mialane P, Secheresse F, Keita B, Nadjo L (2012) Functionalized polyoxometalates with covalently linked bisphosphonate, N-donor or carboxylate ligands: from electrocatalytic to optical properties. Chem Commun 48(67):8299–8316

62. Rhule JT, Hill CL, Judd DA, Schinazi RF (1998) Polyoxometalates in medicine. Chem Rev 98(1):327–358

63. Nomiya K, Torii H, Hasegawa T, Nemoto Y, Nomura K, Hashino K, Uchida M, Kato Y, Shimizu K, Oda M (2001) Insulin mimetic effect of a tungstate cluster. Effect of oral administration of homo-polyoxotungstates and vanadium-substituted polyoxotungstates on blood glucose level of STZ mice. J Inorg Biochem 86(4):657–667

64. Yamase T (2005) Anti-tumor, -viral, and -bacterial activities of polyoxometalates for realizing an inorganic drug. J Mater Chem 15(45):4773–4782

65. Vasylyev MV, Neumann R (2003) New heterogeneous polyoxometalate based mesoporous catalysts for hydrogen peroxide mediated oxidation reactions. J Am Chem Soc 126(3):884–890

66. Mbomekalle IM, Keita B, Nadjo L, Berthet P, Hardcastle KI, Hill CL, Anderson TM (2003) Multi-iron tungstodiarsenates. Synthesis, characterization, and electrocatalytic studies of $\alpha\beta\beta\alpha\text{-}(Fe^{III}OH_2)_2Fe^{III}2(As_2W_{15}O_{56})_2^{12-}$. Inorg Chem 42(4):1163–1169

67. Sartorel A, Bonchio M, Campagna S, Scandola F (2013) Tetrametallic molecular catalysts for photochemical water oxidation. Chem Soc Rev 42(6):2262–2280

68. Berardi S, La Ganga G, Natali M, Bazzan I, Puntoriero F, Sartorel A, Scandola F, Campagna S, Bonchio M (2012) Photocatalytic water oxidation: tuning light-induced electron transfer by molecular Co_4O_4 cores. J Am Chem Soc 134(27):11104–11107

69. Hill CL, Gueletii YV, Musaev DG, Yin Q, Botar B (2012) Polyoxometalate water oxidation catalysts and methods of use thereof. US20120027666A1

70. Miras HN, Yan J, Long DL, Cronin L (2012) Engineering polyoxometalates with emergent properties. Chem Soc Rev 41(22):7403–7430

71. Long DL, Burkholder E, Cronin L (2007) Polyoxometalate clusters, nanostructures and materials: from self assembly to designer materials and devices. Chem Soc Rev 36(1):105–121

72. Nyman M (2011) Polyoxoniobate chemistry in the 21st century. Dalton Trans 40(32):8049–8058

73. Song YF, Tsunashima R (2012) Recent advances on polyoxometalate-based molecular and composite materials. Chem Soc Rev 41(22):7384–7402

74. Conway BE, Bai L, Sattar MA (1987) Role of the transfer coefficient in electrocatalysis: applications to the H_2 and O_2 evolution reactions and the characterization of participating adsorbed intermediates. Int J Hydrogen Energy 12(9):607–621

75. Rausch B, Symes MD, Chisholm G, Cronin L (2014) Decoupled catalytic hydrogen evolution from a molecular metal oxide redox mediator in water splitting. Science 345(6202):1326

76. Keita B, Nadjo L (2007) Electrochemical reactions on modified electrodes. In: Bard AJ, Stratmann M (eds) Encyclopedia of electrochemistry, vol 11. Wiley-VCH, Weinheim, pp 685–728

77. Du D-Y, Qin J-S, Li S-L, Su Z-M, Lan Y-Q (2014) Recent advances in porous polyoxometalate-based metal-organic framework materials. Chem Soc Rev 43(13):4615–4632

78. Striegler K, Glaeser R (2016) Strategies towards improved efficiency in photocatalytic hydrogen evolution from aqueous media. Prepr Am Chem Soc Div Energy Fuels 61 (1):214–215

79. Schoenweiz S, Rommel SA, Kuebel J, Micheel M, Dietzek B, Rau S, Streb C (2016) Covalent photosensitizer-polyoxometalate-catalyst dyads for visible-light-driven hydrogen evolution. Chem Eur J 22(34):12002–12005

80. Nohra B, El Moll H, Rodriguez Albelo LM, Mialane P, Marrot J, Mellot-Draznieks C, O'Keeffe M, Ngo Biboum R, Lemaire J, Keita B, Nadjo L, Dolbecq A (2011) Polyoxometalate-based metal organic frameworks (POMOFs): structural trends, energetics, and high electrocatalytic efficiency for hydrogen evolution reaction. J Am Chem Soc 133 (34):13363–13374

81. Qin J-S, Du D-Y, Guan W, Bo X-J, Li Y-F, Guo L-P, Su Z-M, Wang Y-Y, Lan Y-Q, Zhou H-C (2015) Ultrastable polymolybdate-based metal-organic frameworks as highly active electrocatalysts for hydrogen generation from water. J Am Chem Soc 137 (22):7169–7177

82. Wu HB, Xia BY, Yu L, Yu X-Y, Lou XWD (2015) Porous molybdenum carbide nano-octahedrons synthesized via confined carburization in metal-organic frameworks for efficient hydrogen production. Nat Commun 6:6512

83. Li J-S, Tang Y-J, Liu C-H, Li S-L, Li R-H, Dong L-Z, Dai Z-H, Bao J-C, Lan Y-Q (2016) Polyoxometalate-based metal-organic framework-derived hybrid electrocatalysts for highly efficient hydrogen evolution reaction. J Mater Chem A 4(4):1202–1207

84. Tang Y-J, Gao M-R, Liu C-H, Li S-L, Jiang H-L, Lan Y-Q, Han M, Yu S-H (2015) Porous molybdenum-based hybrid catalysts for highly efficient hydrogen evolution. Angew Chem Int Ed 54(44):12928–12932

85. Li J-S, Li S-L, Tang Y-J, Han M, Dai Z-H, Bao J-C, Lan Y-Q (2015) Nitrogen-doped Fe/Fe$_3$C@graphitic layer/carbon nanotube hybrids derived from MOFs: efficient bifunctional electrocatalysts for ORR and OER. Chem Commun 51(13):2710–2713

86. Yang X, Feng X, Tan H, Zang H, Wang X, Wang Y, Wang E, Li Y (2016) N-doped graphene-coated molybdenum carbide nanoparticles as highly efficient electrocatalysts for the hydrogen evolution reaction. J Mater Chem A 4(10):3947–3954

87. Barsukova-Stuckart M, Izarova NV, Jameson GB, Ramachandran V, Wang Z, van Tol J, Dalal NS, Ngo Biboum R, Keita B, Nadjo L, Kortz U (2011) Synthesis and characterization of the dicopper(II)-containing 22-palladate(II)[Cu^{II2}Pd^{II22}P^{V12}O$_{60}$(OH)$_8$]$^{20-}$. Angew Chem Int Ed 50(11):2639–2642

88. Rousseau G, Zhang S, Oms O, Dolbecq A, Marrot J, Liu R, Shang X, Zhang G, Keita B, Mialane P (2015) Sequential synthesis of 3 d-3 d, 3 d-4 d, and 3 d-5 d hybrid polyoxometalates and application to the electrocatalytic oxygen reduction reaction. Chem Eur J 21(34):12153–12160

89. Liu G, Pan J, Yin L, Irvine JTS, Li F, Tan J, Wormald P, Cheng H-M (2012) Heteroatom-modulated switching of photocatalytic hydrogen and oxygen evolution preferences of anatase TiO$_2$ microspheres. Adv Funct Mater 22(15):3233–3238

90. Zhong X, Sun Y, Chen X, Zhuang G, Li X, Wang J-G (2016) Mo doping induced more active sites in urchin-like W$_{18}$O$_{49}$ nanostructure with remarkably enhanced performance for hydrogen evolution reaction. Adv Funct Mater 26(32):5778–5786

91. Xu W, Liu C, Xing W, Lu T (2007) A novel hybrid based on carbon nanotubes and heteropolyanions as effective catalyst for hydrogen evolution. Electrochem Commun 9 (1):180–184

92. Toma FM, Sartorel A, Iurlo M, Carraro M, Parisse P, Maccato C, Rapino S, Gonzalez BR, Amenitsch H, Da Ros T, Casalis L, Goldoni A, Marcaccio M, Scorrano G, Scoles G, Paolucci F, Prato M, Bonchio M (2010) Efficient water oxidation at carbon nanotube–polyoxometalate electrocatalytic interfaces. Nat Chem 2(10):826–831

93. Ma Y-Y, Wu C-X, Feng X-J, Tan H-Q, Yan L-K, Liu Y, Kang Z-H, Wang E-B, Li Y-G (2017) Highly efficient hydrogen evolution from seawater by a low-cost and stable CoMoP@C electrocatalyst superior to Pt/C. Energy Environ Sci 10(3):788–798

94. Wang H, Maiyalagan T, Wang X (2012) Review on recent progress in nitrogen-doped graphene: synthesis, characterization, and its potential applications. ACS Catal 2(5):781–794

95. Lin Z, Waller GH, Liu Y, Liu M, Wong C-P (2013) Simple preparation of nanoporous few-layer nitrogen-doped graphene for use as an efficient electrocatalyst for oxygen reduction and oxygen evolution reactions. Carbon 53:130–136

96. Liu R, Zhang G, Cao H, Zhang S, Xie Y, Haider A, Kortz U, Chen B, Dalal NS, Zhao Y, Zhi L, Wu C-X, Yan L-K, Su Z, Keita B (2016) Enhanced proton and electron reservoir abilities of polyoxometalate grafted on graphene for high-performance hydrogen evolution. Energy Environ Sci 9(3):1012–1023

97. Li J-S, Wang Y, Liu C-H, Li S-L, Wang Y-G, Dong L-Z, Dai Z-H, Li Y-F, Lan Y-Q (2016) Coupled molybdenum carbide and reduced graphene oxide electrocatalysts for efficient hydrogen evolution. Nat Commun 7:11204

98. Ma X, Meng H, Cai M, Shen PK (2012) Bimetallic carbide nanocomposite enhanced Pt catalyst with high activity and stability for the oxygen reduction reaction. J Am Chem Soc 134(4):1954–1957

99. Liu Y, Li G-D, Yuan L, Ge L, Ding H, Wang D, Zou X (2015) Carbon-protected bimetallic carbide nanoparticles for a highly efficient alkaline hydrogen evolution reaction. Nanoscale 7 (7):3130–3136

100. Xiao P, Ge X, Wang H, Liu Z, Fisher A, Wang X (2015) Novel molybdenum carbide–tungsten carbide composite nanowires and their electrochemical activation for efficient and stable hydrogen evolution. Adv Funct Mater 25(10):1520–1526

101. Liu C-H, Tang Y-J, Wang X-L, Huang W, Li S-L, Dong L-Z, Lan Y-Q (2016) Highly active Co-Mo-C/NRGO composite as efficient oxygen electrode for water-oxygen redox cycle. J Mater Chem A 4:18100–18106

102. Fan X, Zhou H, Guo X (2015) WC nanocrystals grown on vertically aligned carbon nanotubes: an efficient and stable electrocatalyst for hydrogen evolution reaction. ACS Nano 9(5):5125–5134

103. Hunt ST, Nimmanwudipong T, Román-Leshkov Y (2014) Engineering non-sintered, metal-terminated tungsten carbide nanoparticles for catalysis. Angew Chem Int Ed 53 (20):5131–5136

104. Zhao Y, Kamiya K, Hashimoto K, Nakanishi S (2013) Hydrogen evolution by tungsten carbonitride nanoelectrocatalysts synthesized by the formation of a tungsten acid/polymer hybrid in situ. Angew Chem Int Ed 52(51):13638–13641

105. Levy RB, Boudart M (1973) Platinum-like behavior of tungsten carbide in surface catalysis. Science 181(4099):547–549

106. Wang X-L, Tang Y-J, Huang W, Liu C-H, Dong L-Z, Li S-L, Lan Y-Q (2017) Efficient electrocatalyst for the hydrogen evolution reaction derived from polyoxotungstate/polypyrrole/graphene. ChemSusChem 10:2402–2407

107. Yan G, Wu C, Tan H, Feng X, Yan L, Zang H, Li Y (2016) N-Carbon coated P-W2C composite as efficient electrocatalyst for hydrogen evolution reactions over the whole pH range. J Mater Chem A 5:765–772

108. Tang Y-J, Wang Y, Wang X-L, Li S-L, Huang W, Dong L-Z, Liu C-H, Li Y-F, Lan Y-Q (2016) Molybdenum disulfide/nitrogen-doped reduced graphene oxide nanocomposite with enlarged interlayer spacing for electrocatalytic hydrogen evolution. Adv Energy Mater 6 (12):1600116

109. Morales-Guio CG, Hu X (2014) Amorphous molybdenum sulfides as hydrogen evolution catalysts. Acc Chem Res 47(8):2671–2681
110. Tan C, Zhang H (2015) Epitaxial growth of hetero-nanostructures based on ultrathin two-dimensional nanosheets. J Am Chem Soc 137(38):12162–12174
111. Jaramillo TF, Jørgensen KP, Bonde J, Nielsen JH, Horch S, Chorkendorff I (2007) Identification of active edge sites for electrochemical H_2 evolution from MoS_2 nanocatalysts. Science 317(5834):100–102
112. Voiry D, Salehi M, Silva R, Fujita T, Chen M, Asefa T, Shenoy VB, Eda G, Chhowalla M (2013) Conducting MoS_2 nanosheets as catalysts for hydrogen evolution reaction. Nano Lett 13(12):6222–6227
113. Liao L, Zhu J, Bian X, Zhu L, Scanlon MD, Girault HH, Liu B (2013) MoS_2 formed on mesoporous graphene as a highly active catalyst for hydrogen evolution. Adv Funct Mater 23 (42):5326–5333
114. Gao M-R, Chan MKY, Sun Y (2015) Edge-terminated molybdenum disulfide with a 9.4-Å interlayer spacing for electrochemical hydrogen production. Nat Commun 6:7493

Gel-Electrophoretic Chromatography of Polyoxometalate Clusters in Aqueous Solution

Ryo Tsunashima

Abstract In this chapter, how the electrophoresis works in polyoxometalate chemistry was summarized in detail. Since POM clusters are too small for showing traditional molecular sieving effect required for separation by electrophoresis, they show differences in electrophoretic mobility. The mobility is well understood by a correlation between the cluster mobility and structurally determined surface charge density. By observing these mobility differences in mixed POM solutions, each component can be separated. The electrophoretic chromatography for POMs is now discussed for a genuine analytical technique for investigation of cluster species in solution.

Keywords Gel electrophoresis • Polyoxometalate

Contents

R. Tsunashima (✉)
Graduate School of Science and Technology for Innovation, Yamaguchi University, Yamaguchi, Japan
e-mail: ryotsuna@yamaguchi-u.ac.jp

1 Introduction

The study of molecular metal oxides or polyoxometalates (POMs), which are polymeric clusters of oxo anions (MO_x where M = Mo, W, V, Nb and x = 4–7), is now extended to a huge area of scientific research for chemistry, physics, and bioscience. These are originated from the advantage of POMs and major contemporary interest due to the plethora of shapes, sizes, physical properties, and applications they have. Examples of such applications include photoinduced water splitting, electronics, catalysis, nanotechnology, and medicine [1–13].

The structural diversity in POMs is the one of important advantages of POMs but can present a problem when attempting to discover and characterize unknown clusters, either in the solid state or even more so in solution. This difficultly can be elegantly illustrated when one considers the discovery of "molybdenum blue," first mentioned in Carl Scheele's report from 1,783 but only structurally defined over two centuries later in 1995 when Achim Müller and coworkers were able to use single crystal XRD to solve the structure. The structure was revealed to be of a complicated Mo-oxide molecular wheel ca. 3.6 nm in diameter containing 154 molybdenum atoms and over 500 oxygen-based ligands.

This discovery opened the fields of nano-molecular and supramolecular chemistry based on these gigantic metal oxide clusters. The reasons for the delay between the initial observations and solving the structure of "molybdenum blue" were not only due to the inherent technical limitations of that time but also the difficulties involved in the crystallization of such large molecular nanostructures. For example, they are present as mixtures; even simple 1:1 mixtures are virtually impossible to crystallize. Simple and quick analytical techniques such as TLC and HPLC that allow us to identify and separate clusters from mixtures are clearly indispensable in organic synthesis and the development of similar techniques would be greatly beneficial for the study of POMs. These advances could potentially open up new synthetic approaches and provide greater synthetic detail, leading to increased understanding of reaction mechanisms, improvement of yields, and the discovery of new clusters and materials.

In the case of DNA, mobility is typically described as a function of its molecular weight, because the variations in charge and surface charge density of DNA are directly proportional to its size and mass. Optimal separation is therefore only expected under conditions where the molecule or particle sizes are comparable with the pore size of the gel, producing the molecular sieving effect. At the gel concentrations that we have used 1 wt%, the range of pore sizes are 100–200 nm and therefore the size is not comparable to the size of the clusters. In this case, mobility of the particle, here POM, will be correlated to charge and size of clusters.

At the solution phase of the ionic materials, ionic radius is more important rather than crystallographic radius. In general, ionic radius is concentration dependent and two models have been considered with Debye length. With crystallographic radius R and Debye length κ^{-1}, $R\kappa$ value gives important information when one considers ionic size in solution:

- $R\kappa < 1$; point charge model
- $R\kappa > 1$; rigid body model

    In the case that a Debye layer is thin as compared with crystallographic size, ions are no longer point charge. The ion is considered as particle where we can find a surface on the ion. This is the simplest view for why surface charge is correlated to the electrophoretic mobility [14]. This consideration strongly suggests that POMs in solution are now considered can be regarded to both cases.

    A study of electrophoretic techniques has been used to investigate POMs before [15–19]. However, the details of cluster's mobility and mechanism are poorly investigated; especially, the correlation of size and charge, in the form of surface charge densities, with mobility for a variety of POM clusters is indispensable to establish the electrophoretic chromatography as a genuine analytical technique for the investigation of the cluster species in solution.

2   Gel Electrophoresis for Polyoxometalate Chemistry

2.1   Separation of Gigantic Polyoxometalates of Mo-Brown Ball and Mo-Blue Wheel

Since the "Mo-brown ball" $\{Mo_{132}\}$ and "Mo-blue wheel" $\{Mo_{154/152}\}$ have very large sizes and charges, these clusters are ideal candidates for investigation by electrophoresis. Therefore, the clusters were applied (individually and as a 1:1 mixture) to an agarose gel buffered at pH 5 and a voltage of 100 V was applied for between 1 and 10 min. The condition would be usual and corresponded to that for DNA and/or proteins. Figure 1 shows pictures of the gel during electrophoresis taken at 0, 6, and 10 min. This shows that both POMs moved toward the anode with
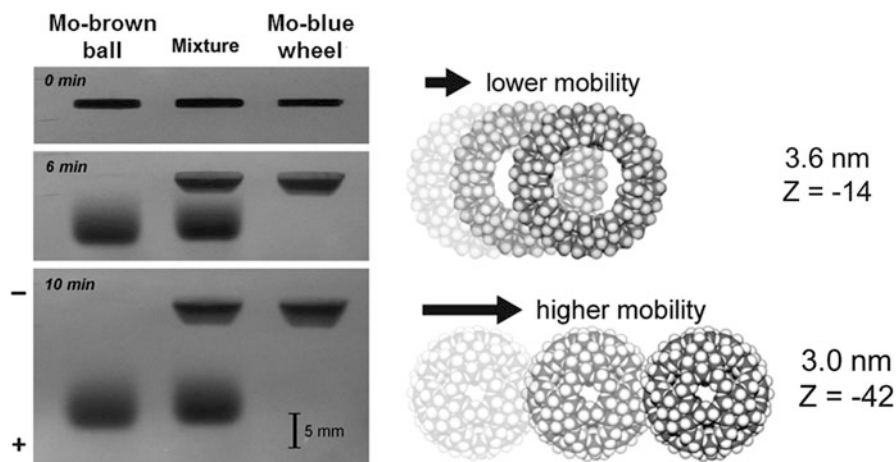
Fig. 1 Photographs of a gel for electrophoretic separation of molybdenum blue and molybdenum brown taken at 0, 6, and 10 min intervals during the run. Each column is: (*left*) $\{Mo_{132}\}$; (*middle*) 1:1 mixture of $\{Mo_{132}\}$ and $\{Mo_{154/152}\}$; and (*right*) $\{Mo_{154/152}\}$, all at 2.0 mM concentrations

different mobilities, each following a linear relationship between displacements of the band as a function of time but that the $\{Mo_{132}\}$ sphere moves faster than the $\{Mo_{154/152}\}$ wheel. The higher mobility of the $\{Mo_{132}\}$ ball can be rationalized when one considers its smaller size and higher charge than those of the $\{Mo_{154/152}\}$ wheel. The charge and crystallographic diameter of $\{Mo_{132}\}$ are -42 and 3.0 nm and those of $\{Mo_{154/152}\}$ are -14 and 3.6 nm. A mixed solution of the two clusters can therefore be separated into the distinct brown and blue bands, and their different mobility behavior can be attributed to their relative size and charge.

In different to other traditional POMs such as the stable Keggin clusters, larger gigantic POMs are rather sensitive to oxidation and high pH in aqueous solution. This was indicated by a slight fading of the intense blue and brown colors of $\{Mo_{154/152}\}$ and $\{Mo_{132}\}$ during extended (15–20 min) electrophoresis runs, indicating partial oxidation of the samples. This oxidative degradation is even more evident when the experiment is run in aqueous gels without buffer. However, we found that by using a buffer (pH 5) and limiting the time of the electrophoresis experiment to no more than 10 min then there is no noticeable color fading and oxidative decomposition.

2.2 Isolation and Analysis of Polyoxometalates after Electrophoretic Separation

To assess the stability of POMs during electrophoresis, clusters were first isolated from the gel matrix by following two methods (Fig. 2):

- Method A "extraction"; submersing cut segments of the gel into water, allowing the clusters to diffuse out from the gel matrix.
- Method B "collection slot"; used a second slot prepared at the anode side of the gel, where the POM can migrate toward and then be directly removed by pipette.

The solution obtained by method B was more concentrated than that of method A.

Fig. 2 Photographs of gels and schematic demonstration of extraction methods A and B, where $t2 > t1$
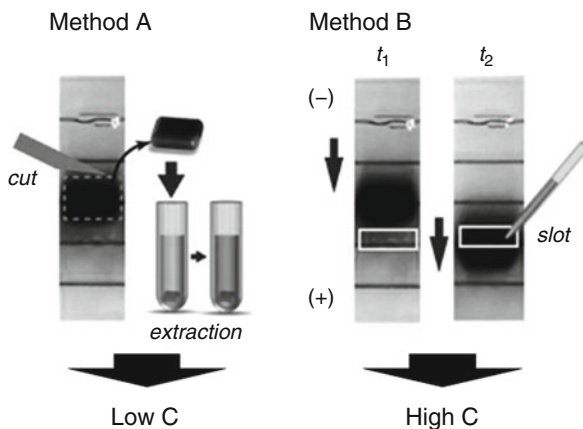
2.2.1   Method A

The extracted solutions were suitable for characterization by spectroscopy, namely UV-Vis and DLS. Decreasing the solubility of the POMs in the extracted solutions by addition of potassium salt, alkylammonium salt, and/or polar organic solvent led to formation of a precipitate, which could be filtered, dried, and further characterized by IR spectroscopy. The solutions of $\{Mo_{154/152}\}$ and $\{Mo_{132}\}$ prepared by method A showed similar UV-Vis spectra to those of dilute solutions of the preloaded pure samples. The DLS plots showed a slightly larger particle size and wider size distributions for the samples after electrophoresis. This is presumably because the POMs have associated with some of the sugar-based components of the gel matrix via hydrogen bonding and/or direct displacement of the metal oxo-ligands by the abundant alkoxy groups [20]. The IR spectrum of the $\{Mo_{132}\}$ precipitate prepared by extraction method A followed by addition of acetone gave a similar spectrum to that of the preloaded $\{Mo_{132}\}$ but with additional peaks corresponding to agarose, confirming the association of the agarose and POM.

2.2.2   Method B

Samples of $\{Mo_{154}\}$ and $\{Mo_{132}\}$ precipitated after electrophoresis were obtained by extraction method B followed by addition of dimethylstearylammonium bromide and acetone and KCl and acetone, respectively. Precipitates of Keggin and Dawson clusters were similarly prepared as tetrabutylammonium and tetraethanolammonium salts. The IR spectra for samples prepared after electrophoresis showed good correspondence with the spectra of those of the control samples prepared directly by cation exchange of the original loading solutions. The spectral data therefore support the hypothesis that the POM clusters are stable during electrophoresis experiments when the pH is buffered to pH 5 and the experiment duration is limited to 10 min.

2.3   *Dyeing Polyoxometalates in Gel*

To further explore the potential of gel electrophoresis in POM separation and to characterize mobility as a function of charge and size, a range of related clusters were selected. These were the Dawson and Keggin clusters of general formulae $\{P_2W_{18}\}$ $([P_2W_{18}O_{62}]^{6-})$, $\{P_2W_{17}Co\}$ $([P_2W_{17}O_{61}(CoOH_2)]^{8-})$, $\{P_2W_{17}Mn\}$ $([P_2W_{17}O_{61}(MnOH_2)]^{7-})$, $\{S_2Mo_{18}\}$ $([(SO_3)_2Mo^V{}_2Mo^{VI}{}_{16}O_{54}]^{6-})$, $\{BW_{12}\}$ $([BW_{12}O_{40}]^{5-})$, $\{SiW_{12}\}([SiW_{12}O_{40}]^{4-})$, and $\{CoW_{12}\}$ $([CoW_{12}O_{40}]^{6-})$ [21–25]. Since most of these POMs are colorless, or very light colored in contrast to the partially reduced Mo-brown and Mo-blue clusters presented previously, a method for visualizing the fully oxidized POMs was developed by dyeing of the post-electrophoresis gels with a reducing agent. Dyeing is performed by casting an

Fig. 3 Photographs of gel after electrophoresis and then after the dyeing process by casting of reducing agent. All polyoxometalates (POMs) were loaded in 5 mL portions at 20 mM and show a visible band after dyeing. POMs are $\{P_2W_{18}\}$, $\{P_2W_{17}Co\}$, $\{P_2W_{17}Mn\}$, $\{S_2Mo_{18}\}$, and $\{SiW_{12}\}$, from *left* to *right*
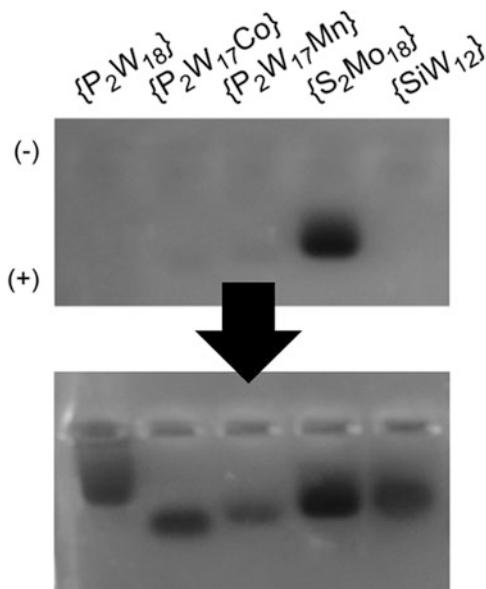
$Na_2S_2O_4$ solution (1 wt%) with a few drops of HCl (6 M) onto the gel; the reduced POMs are highly colored and can be easily identified on the gel plates as shown in Fig. 3. The $\{S_2Mo_{18}\}$ contains two reduced Mo centers in its native state and is therefore colored even before the dyeing process.

2.4 Counterion of Polyoxometalates

A water soluble Ni salt of the $\{SiW_{12}\}$, $[Ni(H_2O)_6]_2[SiW_{12}O_{40}]$, was prepared, which enabled us to follow where the counter cations were throughout the electrophoresis. After electrophoresis of $[Ni(H_2O)_6]_2[SiW_{12}O_{40}]$ and reduction for dyeing (Fig. 4), a brown band had migrated toward the cathode. A similar band was observed for the nickel nitrate control; the original Ni counter cations of the POM had therefore separated and migrated toward the cathode. Since buffer solution contains Na^+, counter cation of POM is replaced from the original Ni cations.

2.5 Electrophoretic Mobility and Charge of Cluster

According to the conventional theory of electrophoresis, mobility depends upon a large number of parameters; these include structural properties of the molecules (size, shape, charge, and mass), applied voltage, gel concentration, pH, and reagent concentrations. Here, several different POMs are characterized in terms of their mobility at fixed conditions below:

Fig. 4 Photograph of gels after electrophoresis and dyeing process. Samples are: (*left*) $Na_4[SiW_{12}O_{40}]$; (*middle*) [Ni $(H_2O)_6]_2[SiW_{12}]$; and (*right*) $Ni(NO_3)_2 \cdot 6H_2O$. The anionic POM migrated toward the anode while Ni cations migrated toward the cathode

$[Ni(H_2O)_6]_2[SiW_{12}O_{40}]$

(+)

SiW_{12}

Ni(II)

(−)

$Na_4[SiW_{12}O_{40}]$ $Ni[NO_3)_2 \cdot 6H_2O$
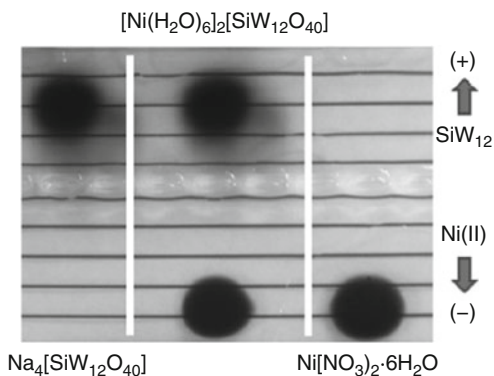
- 20 mM loading concentration
- pH 5 controlled by HOAc/NaOAc buffer
- Electric field strength of 7.69 V cm^{-1}
- Applied for 10 min.

Agarose gels were prepared at 1 wt% in buffer solution and mobilities were estimated by digital analysis of high resolution photographs of the gels using a CCD camera. Analysis of cluster mobilities shows a general trend according to both the charge and size of the clusters. The charges of the $\{P_2W_{18}\}$, $\{P_2W_{17}Mn\}$, $\{P_2W_{17}Co\}$, and $\{S_2Mo_{18}\}$ clusters are −6, −7, −8, and −6, respectively, and their mobilities vary proportionally with the cluster charges (Fig. 5). A similar relationship between cluster charge and anion mobility is also observed for the Keggin clusters $\{SiW_{12}\}$, $\{BW_{12}\}$, and $\{CoW_{12}\}$, where the charges are −4, −5, and −6, respectively. When comparing only Keggin clusters, or only Dawson clusters, the mobility varies linearly with charge as the approximate size and surface area of the clusters remain constant for each family. However, when making comparisons across the two families, the difference in cluster size must also be accounted for: the $\{P_2W_{18}\}$ and $\{CoW_{12}\}$ clusters, compared in Fig. 5, both have a −6 charge but have different mobilities. Thus, they were able to be separated from a mixture. The reason for the difference is due to the smaller size of the $\{CoW_{12}\}$ compared to the $\{P_2W_{18}\}$, resulting in the higher mobility of $\{CoW_{12}\}$. The diameters of the Keggin and Dawson clusters are estimated (from crystallographic data) to be 1.0 and 1.2 nm, respectively.

2.6   Correlation Between Mobility and Polyoxometalate Structure

2.6.1   Mobility and Crystallographic Radius of Polyoxometalate

In conventional gel electrophoresis, smaller particles should show a higher migration than larger particles of similar charge; however, this is normally only possible
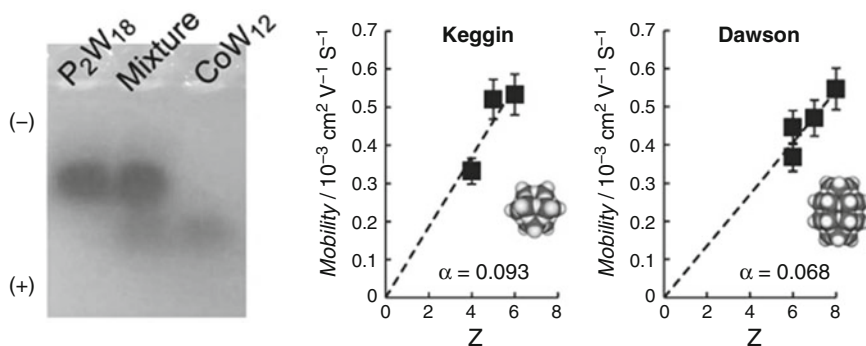
Fig. 5 Photograph of a gel after the electrophoresis and dyeing process. Each column is: {P2W18}; 1:1 mixture of {P2W18} and {CoW12}; and {CoW12}. Plots of mobility for Keggin clusters {SiW12}, {BW12}, and {CoW12} with charge (Z) as well as mobility for Dawson clusters {P2W18}, {P2W17Mn}, {P2W17Co}, and {S2Mo18}. Sample loading concentrations are 20 mM. Error bars represent the standard deviations observed over multiple runs. The α represents its slope
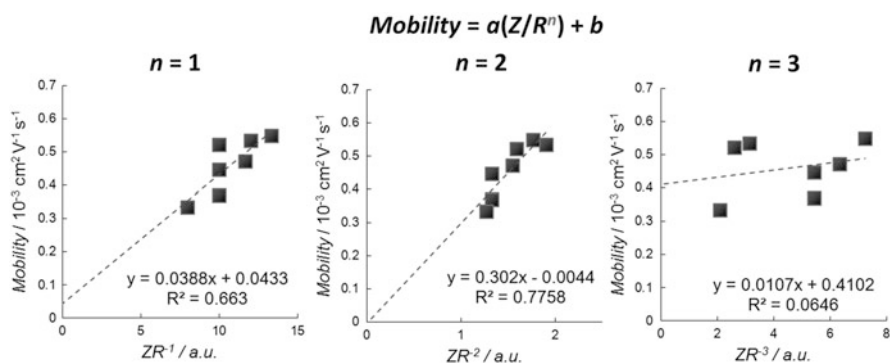
Fig. 6 Plot of mobilities against ZR^{-n} with $n = 1, 2,$ and 3

for very large (>100 nm) species due to the molecular sieving effect of the porous gel matrix. Despite this potential limitation, it was still possible to correlate the mobility of a range of POMs with their charge and size. This was accomplished by applying the standard practice in electrophoresis, which employs surface charge density as the fundamental parameter that governs mobility if the particles fall within the Debye–Hückel limit, as shown below:

$$\mu = \sigma/4\pi\eta\kappa \tag{1}$$

where μ, σ, η, and κ, are mobility, surface charge density, solvent viscosity, and inverse Debye length, respectively [14]. Since both the Keggin and Dawson clusters do not fit the same linear relationship when mobilities are plotted against charge (each cluster group forms a separate linear relationship, see Fig. 5), mobilities were plotted against ZR^{-n} with $n = 1, 2,$ and 3 (Fig. 6) where R values were estimated

from crystallographic data. It was clear that $n = 2$ gave good correlation with experimental values of mobilities, namely surface charge density. This correlation is particularly important as it links the cluster mobilities to their charge and size across the different families of POM clusters.

In the case of DNA, mobility is typically described as a function of its molecular weight, because the variations in charge and surface charge density of DNA are directly proportional to its size and mass. Optimal separation is therefore only expected under conditions where the molecule or particle sizes are comparable with the pore size of the gel, producing the molecular sieving effect. At the gel concentrations used here (1 wt%), the range of pore sizes are 100–200 nm and are therefore not comparable to the size of the clusters [14, 26, 27]; however, the clusters can still be separated with relatively high resolution as shown previously. The correlation between the cluster surface charge density and mobility must therefore be caused by another type of interaction between the POMs and the gel. These attractive interactions could be attributed to hydrogen bonding between the oxo-ligands of the POM and the hydroxyl groups of the agarose; such interactions between sugar-based polymer matrices and POMs have been previously reported [20].

2.6.2 Mobility and Ionic Radius in Solution

As mentioned in the introduction part, ionic radius is concentration dependent and two models have been considered with Debye length. With crystallographic radius R and Debye length κ^{-1}, $R\kappa$ value gives important information when one considers ionic size in solution:

- $R\kappa < 1$; point charge model
- $R\kappa > 1$; rigid body model

In the case that a Debye layer is thin as compared with crystallographic size, ions are no longer point charge. The ion is considered as particle where we can find a surface on the ion. This is the simplest view for why surface charge is correlated to the electrophoretic mobility [14]. This consideration strongly suggests that POMs in solution are now considered with the latter model, namely POMs are not simple point charge model due to their relatively large molecular sizes. Since Debye length is a function of ionic strength, concentration dependence on mobility was investigated (Fig. 7). With decrease in mobility, namely decreases in surface charge density of the cluster, mobility seems to show concentration dependence. Further investigation onto concentration dependence would clarify not only the mobility of the POMs but also structural model of the POM in the solution.

Fig. 7 Concentration dependence on mobilities for several types of POM clusters (pH 5 controlled by HOAc/NaOAc buffer, electric field strength of 7.69 V cm^{-1}, applied for 10 min)
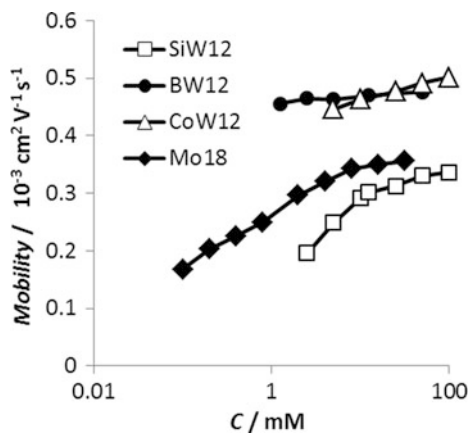
3 Chromatographic Analysis of the Reaction for {Mo$_{154/152}$}

One of the most important applications of chromatographic techniques is reaction monitoring and conventional quick chromatography techniques, such as TLC, are indispensable for optimizing organic reaction conditions (Fig. 8). A major goal of our work was therefore to demonstrate the use of gel electrophoresis in the reaction monitoring of POM syntheses. Especially, structural diversity of POMs is strongly correlated to mobility for fine separation of POMs from solution. These become useful tools for analyzing reaction mixture, where a series of reaction conditions for the formation of the gigantic "molybdenum blue" cluster {Mo$_{154/152}$} were characterized by gel electrophoresis.

3.1 Reaction to {Mo$_{154/152}$}

Solutions of Molybdenum-blues (MBs), first mentioned by Scheele in 1783, comprise a family of nanostructured POM clusters where their deep-blue color originates from the partial reduction of Mo^{VI} centers to Mo^{V} giving a delocalized mixed valence state [7, 28–32]. Their preparation is achieved by the partial reduction of solutions of acidified molybdate(VI). Crystallization of the solutions leads to isolation of particular species, the nature of which is precisely defined by the pH of the reaction mixture. Specifically, acidification of Na$_2$MoO$_4$ aqueous solution (12.7 mM, 25 mL) with hydrochloric acid (32%, 2.7 mL, results in solution pH $\approx$ 1) and consecutive reduction by Na$_2$S$_2$O$_4$ (0.15 g, 0.86 mmol) leads to the formation
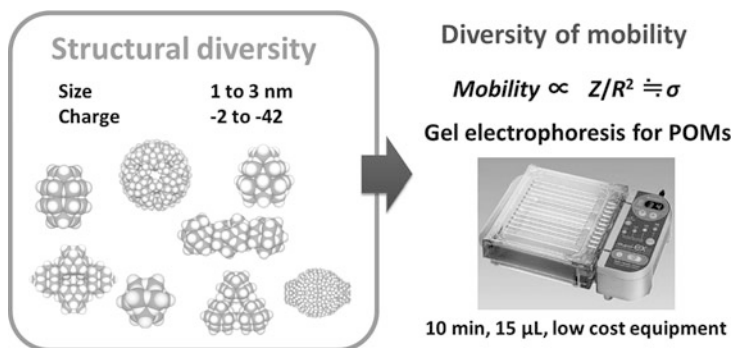
Fig. 8 Schematic summary of gel electrophoresis for POM chemistry

of a nanostructured, wheel shaped, Mo-oxide cluster composed of 154 (152) Mo atoms bridged by O atoms after 1–2 days.

$$153MoO_4^{2-} + 14S_2O_4^{2-} + 263H^+ \rightleftharpoons \{Mo_{154/152}\} + 28SO_3^{2-} + 55.5H_2O \quad (2)$$
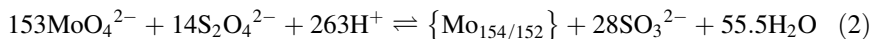
In general, isolation of POM clusters has been achieved by crystallization, which requires precise control of both reaction and crystallization conditions, as well as appropriate selection of cations and solvents. Occasionally, the inability to isolate single crystals from a reaction mixture leads to ambiguity with respect to the structure of the compound(s) isolated. This is due to the inherent difficulty of analyzing such complex mixtures. For example, the majority of the MB species have similar solubility and absorption in UV-Vis-NIR region, making the direct probing of the speciation of the reaction mixture practically impossible.

3.2 Diagram of Mo-Blue and Mo-Brown in Solution

We have investigated such MB reaction mixture as a function of pH and reagents ratio (R) and mapped the reaction coordinates that define and control the system.

3.2.1 Mo-Blue and Mo-Brown

A series of reaction mixtures under different experimental conditions of pH (1–4) and R (0.07, 0.14, 0.23, 0.56, and 0.9) were characterized by UV-Vis-NIR spectroscopy. The MB species have typical absorption bands around at 600–1,100 nm which are attributed to the inter-valence charge transfer (IVCT). Similar bands were observed for all the combinations of experimental conditions (pH, R) except from the sets (3, 0.90) and (4, 0.56–0.90). Under these experimental conditions, the
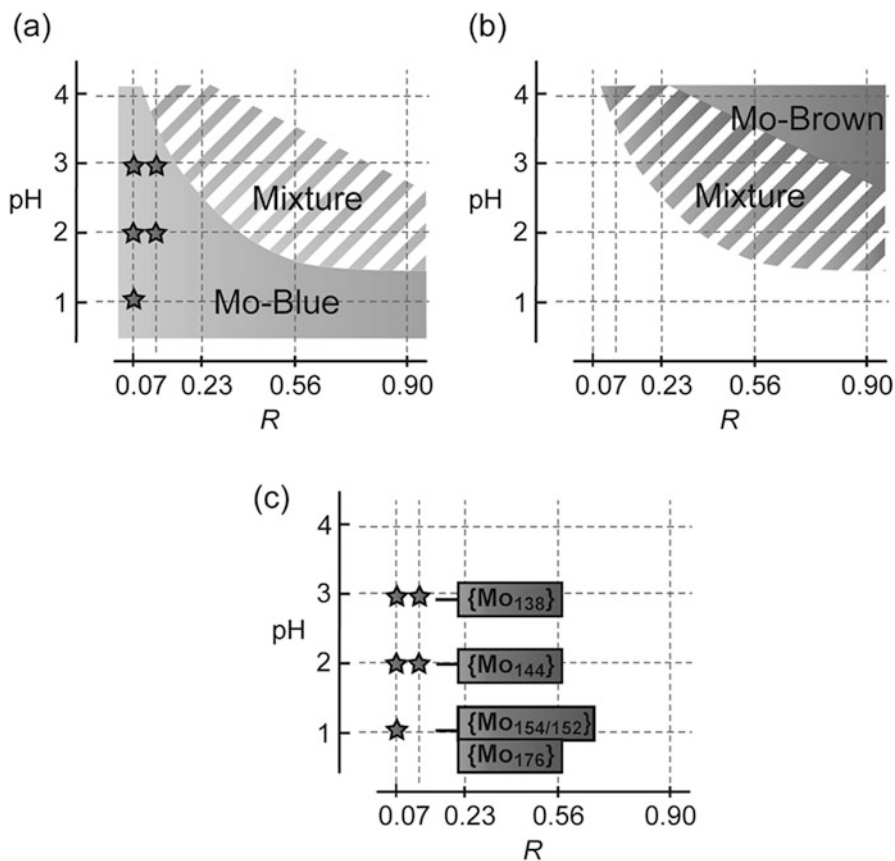
Fig. 9 Diagram of (a) Mo-blue, (b) Mo-brown, and (c) MB-wheel obtained by single crystal

reaction mixtures appeared to be brown instead of blue due to the higher amount of reducing agent, which lead to the formation of Mo-Brown species [28, 30–32]. The UV-Vis-NIR data allowed us to identify the areas of the parameter space that lead to the formation of MB and the areas of Mo-brown species [(3, 0.90) and (4, 0.56–0.90)] (Fig. 9). The area of the parameter space which favors the formation of Mo-brown species was partially contaminated with MB species as confirmed by chromatographic gel electrophoresis (see below for further details).

3.2.2 Crystallization from the Reactions

After leaving the reaction mixtures to stand at room temperature for 3 days, single crystals were obtained from the (1, 0.07) and (2, 0.07–0.14) reaction sets. Single crystal X-ray diffraction (XRD) analysis revealed two cluster types within the

reaction mixture at (1, 0.07); $Na_{15}\{Mo_{154/152}\}\cdot ca.400H_2O$ and $Na_{16}[Mo_{176}O_{528}H_{16}$ $(H_2O)_{80}]\cdot ca.450H_2O$ ($[Mo_{176}O_{528}H_{16}(H_2O)_{80}]^{16-}$ = $\{Mo_{176}\}$) [33]. From the reaction set (2, 0.07–0.14), single crystals of $Na_{24}\{[Mo_{144}O_{437}H_{14}(H_2O)_{56}]_{0.5}[Mo_{144}O_{437}H_{14}(H_2O)_{60}]_{0.5}\}\cdot 350H_2O$ (= $\{Mo_{144}\}$) [34] were obtained. Finally, the reaction sets (3, 0.07–0.14) gave single crystals after 24 h when treated with ammonium chloride. The cluster was crystallographically identified as $[Mo_{138}O_{410}(OH)_{20}(H_2O)_{46}]^{40-}$ (= $\{Mo_{138}\}$) [35].

3.3 Chromatographic Gel Electrophoresis of Reaction Solutions

Although reaction sets (1–3, 0.07) and (2–3, 0.14) gave single crystals, it was possible to identify the species in solution in the other collected batches using gel electrophoresis. Figure 10 shows the photograph of gels taken after the electrophoresis of the reaction mixtures after 1 day of reaction. The reaction set (1, 0.07) gave a single blue band, implying that there is only a single product attributable to an MB species. The reaction conditions used are consistent with the synthesis of the $\{Mo_{154/152}\}$ anions. (The MB-wheel, $\{Mo_{154/152}\}$, was synthesized from an Na_2MoO_4 aqueous solution in the presence of $Na_2S_2O_4$ reducing agent at $pH \approx 1$, yielding blue crystals after 2 days).

On the other hand, solutions from the reaction mixtures that did not crystallize were separated into several bands corresponding to species with different electrophoretic mobility and colors (blue, green, and brown). As such, we revealed that Mo-brown was a contaminant in reactions (4, 0.14), (3–4, 0.23), (2–4, 0.56), and (2–4, 0.90).

3.3.1 Diagram of MB-Wheels

Isolation of MB-material was achieved by the reaction with TEAH chloride. Upon treatment by TEAH chloride, a blue precipitate was immediately observed from reactions (1–3, 0.07–0.23) and (1–2, 0.56–0.9). The IR spectra of these blue powders showed an Mo-O-Mo vibration at around 900–500 cm^{-1} and they were similar to $\{Mo_{154/152}\}$ anion. Figure 10b shows a photograph of gel after the electrophoresis of filtrates after separating the TEAH salts. All the blue bands that had the slowest mobility in the initial filtrates seen in reactions (1–3, 0.07–0.23) and (1–2, 0.56–0.9) had disappeared, showing isolation of MB-wheels as TEAH salts. By comparison of the mobility data and IR spectra, it can be suggested that the MB-wheels are formed in reactions (1–3, 0.07–0.23) and (1–2, 0.56–0.9) as shown in Fig. 11. In addition, Ozeki reported that reaction pH effects to control the x value of $\{Mo_{154-x}\}$ ($x = 0$–16). Depending on reaction pH, lacunary gigantic MB-wheels were formed, where pH increase tends to cause increases in x [35]. As mentioned before, we also
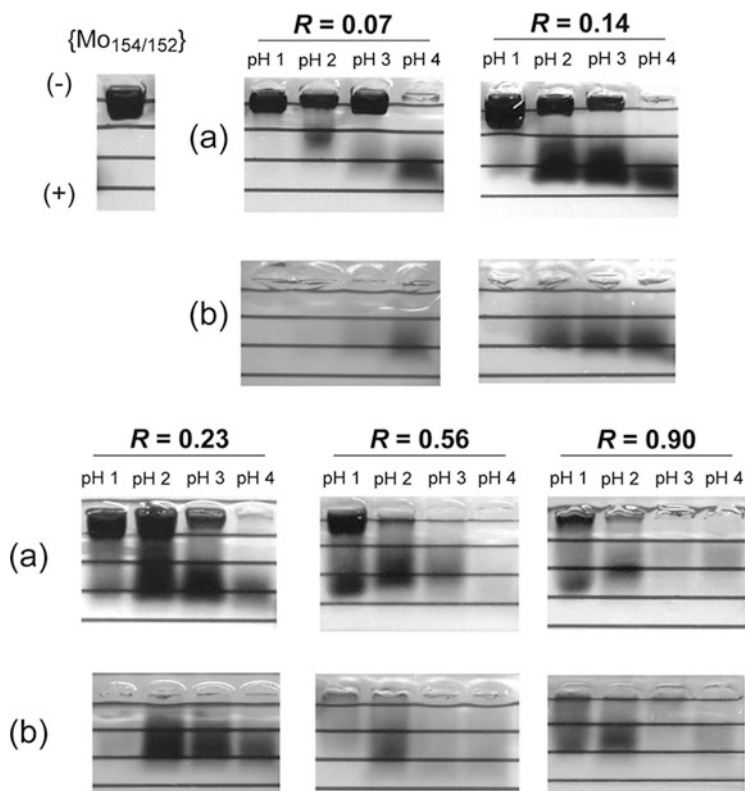
Fig. 10 Photograph of gels after electrophoresis of (**a**) filtrates after reactions and (**b**) filtrates after treatment of TEAH (taken at 10 min of the run). In the gels shown in (**b**), blue bands that have the slowest mobility were diminished if compared with initial solution shown figure (**a**). Comparable mobility of the blue band with $\{Mo_{154/152}\}$ and IR spectra of TEAH salt indicate separation of MB-wheels.

isolated $\{Mo_{144}\}$ and $\{Mo_{138}\}$ anions from reactions at pH 2 and 3 ($R = 0.07$–0.14), respectively, showing a similar tendency with changing pH.

3.3.2   Other MB Clusters in the Solution System

By focusing on the isolation of other POMs detected by gel-electrophoretic analysis, several sets of reaction yielded blue precipitates after treatment with TBA (reactions except for (3, 0.90) and (4, 0.56–0.90)). Recrystallization from acetonitrile yielded single crystals which were identified as the TBA salt of $[Mo^V_2Mo^{VI}_{16}O_{54}(SO_3)_2]^{6-}$ ($\{S_2Mo_{18}\}$) [11] by single crystal XRD analysis. This Dawson-like cluster has been reported earlier in agreement with the employed reaction conditions (4, 0.07) (while the concentration of MoO_4^{2-} differs). A diagram in which $\{S_2Mo_{18}\}$ was obtained was shown in Fig. 4a. Further, an increase of the pH and R parameters yielded orange

Fig. 11 Diagram of
MB-wheels
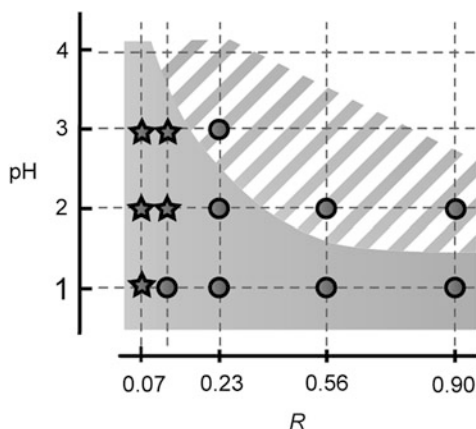
crystals of the $[(\mu_6\text{-}SO_3)Mo^V_6O_{15}(\mu_2\text{-}SO_3)_3]^{8-}$ ($\{S_4Mo_6\}$) anion after 2 weeks [36].
The parameter space scanned for the isolation of the hexameric cluster is shown in
Fig. 4b. The synthesis was reported using hydrazine and $(NH_4)_2SO_3^{2-}$ as a reductant
and template source, respectively. Reaction condition (pH, $[SO_3^{2-}]/[Mo]$) is agreed
with (5.5, 5.3). Large content of SO_3^{2-} was required for reaction.

Interestingly, both $\{S_2Mo_{18}\}$ and $\{S_4Mo_6\}$ clusters were not identified by mass
spectra that we have characterized using reaction solution, indicating self-assembly
triggered by the addition of TBA and/or acetonitrile after which the sulfite anion
acted as template. The insight must be highlighted when formation mechanisms of
such hetero-POM will be discussed.

4   Summary

In this chapter, the separation of a diverse range of polyoxometalate clusters using
gel electrophoresis has been fully demonstrated. Basic understandings of electro-
phoretic mobility revealed good correlation between the cluster migration and
surface charge density. These studies revealed that gel electrophoresis of POM
compounds help us for:

- Isolation from mixture
- Characterization of purity
- Monitoring a reaction

Then, several examples were shown to demonstrate this usefulness by gel
electrophoresis. These are appeared in:

- Isolation of nanoscale molecules of $\{Mo_{132}\}$ and $\{Mo_{154}\}$ from mixtures

- Extraction of POMs from gel
- Obtaining structural information by relationship between cluster structure (surface charge density) and mobility
- Guiding reaction phase diagram for Mo-blue reaction system by using gel electrophoresis

The gel-electrophoretic technique could therefore play a key role in elucidating the composition of new or unknown cluster systems.

References

1. Müller A, Peters F, Pope MT, Gatteschi D (1998) Chem Rev 98(1):239–272
2. Hill CL (1998) Chem Rev 98(1):1–2
3. Hasenknopf BF (2005) Front Biosci 10:275
4. Liu T (2010) Langmuir 26(12):9202–9213
5. Long D-L, Burkholder E, Cronin L (2007) Chem Soc Rev 36(1):105–121
6. Kortz U, Müller A, Slageren J, Schnack J, Dalal NS, Dressel M (2009) Coord Chem Rev 253(19–20):2315–2327
7. Long D-L, Tsunashima R, Cronin L (2010) Angew Chem Int Ed Engl 49(10):1736–1758
8. Miras HN, Cooper GJT, Long D-L, Bögge H, Müller A, Streb C, Cronin L (2010) Science 327(5961):72–74
9. Ziv A, Grego A, Kopilevich S, Zeiri L, Miro P, Bo C, Müller A, Weinstock IA (2009) J Am Chem Soc 131(18):6380–6382
10. Noro S-I, Tsunashima R, Kamiya Y, Uemura K, Kita H, Cronin L, Akutagawa T, Nakamura T (2009) Angew Chem Int Ed Engl 48(46):8703–8706
11. Long D-L, Kögerler P, Cronin L (2004) Angew Chem Int Ed Engl 43(14):1817–1820
12. Müller A, Krickemeyer E, Meyer J, Bögge H, Peters F, Plass W, Diemann E, Dillinger S, Nonnenbruch F, Randerath M, Menke C (1995) Angew Chem Int Ed Engl 34(19):2122–2124
13. Long D-L, Cronin L (2006) Chem Eur J 12(14):3698–3706
14. Viovy J-L (2000) Rev Mod Phys 72(3):813–872
15. Hettiarachchi K, Ha Y, Tran T, Cheung A (1995) J Pharm Biomed Anal 13(4–5):515–523
16. Ito T, Yamase T (2009) Eur J Inorg Chem 5205
17. Rusu M (2000) J Radioanal Nucl Chem 245(2):353–356
18. Himeno S, Kitano E, Chasen N (2007) Electrophoresis 28(10):1525–1529
19. Peng J, Ma H-Y, Han Z-G, Dong B-X, Li W-Z, Lu J, Wang E-B (2003) Dalton Trans 3850
20. Ruuttunen K, Vuorinen T (2004) Carbohydr Polym 58(4):443–448
21. Lyon DK, Miller WK, Novet T, Domaille PJ, Eric Evitt E, Johnson DC, Finke RGJ (1991) J Am Chem Soc 113(19):7209–7221
22. Claude R-D, Michel F, Raymonde F, Rene T (1983) Inorg Chem 22:207
23. Müller A, Krickemeyer E, Bögge H, Schmidtmann M, Peters F (1998) Angew Chem Int Ed Engl 37:3360
24. Müller A, Das SK, Fedin VP, Krickemeyer E, Beugholt C, Bögge H, Schmidtmann M, Hauptfleisch BJ (1999) Z Anorg Allg Chem 625(7):1187–1192
25. Uchida S, Mizuno N (2004) J Am Chem Soc 126(6):1602–1603

26. Chrambach A, Dunn MJ, Radola BJ (1992) Advances in electrophoresis, vol 5. VCH, Weinheim, p 4
27. Rodbard D, Chrambach A (1970) Proc Natl Acad Sci U S A 65(4):970–977
28. Müller A, Meyer J, Krickemeyer E, Diemann E (1996) Angew Chem Int Ed Engl 35(11): 1206–1208
29. Song Y-F, Tsunashima R (2012) Chem Soc Rev 41(22):7384–7402
30. Müller A, Roy S (2003) Coord Chem Rev 245(1–2):153–166
31. Müller A, Serain C (2000) Acc Chem Res 33(1):2–10
32. Baker LCW, Glick DC (1998) Chem Rev 98(1):3–50
33. Müller A, Merca A, Al-Karawi AJM, Garai S, Bögge H, Hou G, Wu L, Haupt ETK, Rehder D, Haso F, Liu T (2012) Chem Eur J 18(51):16310–16318
34. Müller A, Krickemeyer E, Bögge H, Schmidtmann M, Beugholt C, Das SK, Peters F (1999) Chem Eur J 5(5):1496–1502
35. Shishido S, Ozeki T (2008) J Am Chem Soc 130(32):10588–10595
36. Manos MJ, Woollins JD, Slawin AMZ, Kabanos TA (2002) Angew Chem Int Ed Engl 41(15): 2801–2805

Alkoxido-Derivatised Lindqvist- and Keggin-Type Polyoxometalates

R. John Errington, Balamurugan Kandasamy, Daniel Lebbie, and Thompson Izuagie

Abstract The targeted application of polyoxometalates (POMs) in catalysis, materials science and biology requires an in-depth understanding of how their properties might be tuned through compositional and structural molecular engineering. In practice, this requires chemical methodologies that enable reliable, systematic manipulation of families of related POMs in conjunction with detailed experimental and theoretical studies. Lindqvist-type hexametalates $[LM'M_5O_{18}]^{n-}$ provide a convenient platform for systematic studies in which M, M′ and L may be varied, and this chapter gives an overview of the development of versatile synthetic methods and the results of detailed reactivity studies based on alkoxido-derivatised anions $[(RO)M'M_5O_{18}]^{n-}$. Solid-state structures and NMR studies of solution reactivities are providing an insight into the effects on bonding and electronic properties of metal and ligand substitution in this family of POMs, and comparisons with the related Keggin-type POMs $[(RO)M'PW_{11}O_{39}]^{n-}$ enable an assessment of the effect of the supporting POM structure on the reactivity of the heterometal site. The chapter begins with recent investigations of aggregation in nonaqueous synthesis of POMs from metal alkoxides and the introduction of heterometal sites into the hexametalate framework. Subsequent sections discuss how protonolysis of M′OR bonds can be used in the synthesis of ligand-exchanged anions and also for the generation of highly reactive $\{M'M_5\}$ species in solution.

Keywords Hydrolysis • Keggin • Lindqvist • Metal alkoxides • Polyoxometalates • Protonation

R.J. Errington (✉), B. Kandasamy, D. Lebbie, and T. Izuagie
School of Chemistry, Newcastle University, Newcastle upon Tyne NE1 7RU, UK
e-mail: John.Errington@newcastle.ac.uk

Contents

1 Introduction

1.1 *Convergence of Polyoxometalate and Metal Alkoxide Chemistry*

The technological importance of metal oxides continues to grow with the increasing demand for improved materials in, e.g. electronics, energy conversion/storage and catalysis [1–4]. Consequently, there is a need to develop precursor chemistry for the atomic-scale manipulation of metal oxides for new versatile processing methods that provide precise control over properties.

One of the main reasons for the interest in and expansion of polyoxometalate (POM) chemistry over recent years is that POMs provide a platform for the systematic variation of composition within a variety of molecular metal oxide structural families. The selection and incorporation of specific well-defined POMs into functional materials provide, in principle, a precise method for tuning the properties of the system and represents an important approach to design and control in metal oxide molecular nanoscience.

Metal alkoxides $M_x(OR)_y$ are a related class of molecular compounds that may be regarded as alkylated metal oxides [5, 6]. Their solubility in organic solvents and sensitivity towards hydrolysis have led to their extensive use as precursors for the controlled growth of targeted solid oxide phases and ceramics via the 'sol-gel' process [7, 8]. The hydrolytic conversion of metal alkoxide solutions to solid oxide materials is now well established in materials chemistry and provided the basis for 'chimie douce' approaches to oxide materials [9]. Efforts to elucidate mechanistic details of metal alkoxide hydrolysis and the associated solution aggregation processes have resulted in the isolation and structural characterisation of a significant number of polyoxoalkoxides (POAs) $M_xO_y(OR)_z$ as putative intermediates or as oxide precursors in their own right [5, 6, 10–18].

Anionic polyoxoalkoxidometalates (POAMs) $[M_xO_y(OR)_z]^{n-}$ represent a direct link between metal alkoxides and POMs and can be regarded as alkylated POMs.

The range of such species has greatly expanded since Knoth's initial work [19], and those with multidentate alkoxido ligands have received attention as versatile POM-organic hybrids [20–22].

A full understanding and mastery of the complex solution processes underlying molecular metal oxide aggregation and structural interconversion still represents the 'holy grail' of POM chemistry, and progress towards this goal is important if the full potential of these versatile species is to be realised. The protonation-condensation reactions involved in the synthesis of POMs by acidification of monomeric oxometalates such as MoO_4^{2-} and WO_4^{2-} and the hydrolysis-condensation processes involved in formation of POAs from metal alkoxides share fundamental aspects of solution chemistry, and, although detailed mechanisms are still largely unknown, it is evident that MOH groups play an important role in both cases.

This chapter provides an overview of some of our approaches to rational, nonaqueous synthesis of heterometallic POMs possessing MOR groups and their protonolysis reactivity [23–27]. Examples are described to illustrate the systematic synthesis of related families of POM hybrids and the study of effects arising from substitution of different $\{M'(OR)\}^{x+}$ units into $\{(RO)M'M_5\}$ Lindqvist- and $\{PW_{11}\}$ Keggin-type POMs. Such studies are providing an insight into the subtle reactivity differences arising from incorporation of $\{M'(OR)\}^{x+}$ into the different metal oxide frameworks. Our methods enable POMs to be efficiently enriched in ^{17}O which, as ^{17}O is an expensive isotope, greatly facilitates ^{17}O NMR solution reactivity studies that are otherwise problematic due to the low natural abundance of ^{17}O (0.037%). Consequently, detailed ^{17}O NMR studies are now revealing important features of the remarkable assembly processes involved in the formation of these heterometalates, and this insight is informing new synthesis design.

1.2 Lindqvist-Type Hexametalates

As one of the smallest and most symmetrical of the POM structural types, the hexametalates $[M_6O_{19}]^{n-}$ (Fig. 1) and their derivatives are attractive from the viewpoint of solution reactivity studies. The highly charged anions $[M_6O_{19}]^{8-}$ of group 5 metals Nb and Ta are obtained from strongly alkaline solutions derived from M_2O_5, and $[Nb_6O_{19}]^{8-}$ was the first of this family to be structurally characterised by Lindqvist in 1953 [28]. These niobates and tantalates are usually studied in aqueous solution as alkali metal salts, although tetraalkylammonium salts will dissolve in organic solvents [29, 30]. Recently, the chemistry of these niobates and tantalates has expanded, aided by milder and more convenient synthetic routes [31]. The hexavanadate $[V_6O_{19}]^{8-}$ has not been isolated, but a series of alkoxido derivatives $[V_6O_{19-x}(OR)_x]^{n-}$, including partially reduced species, have been characterised [32].

The most commonly studied members of the Lindqvist hexametalate family are those of the group 6 metals Mo and W, which may be obtained by acidification of $[MO_4]^{2-}$ in organic solvents [33–37] and by alkaline hydrolysis of $MO(OR)_4$ in organic solvents [38–40]. In terms of reactivity, the hexatungstate is rather inert,

Fig. 1 Representation of
the Lindqvist hexametalate
structure
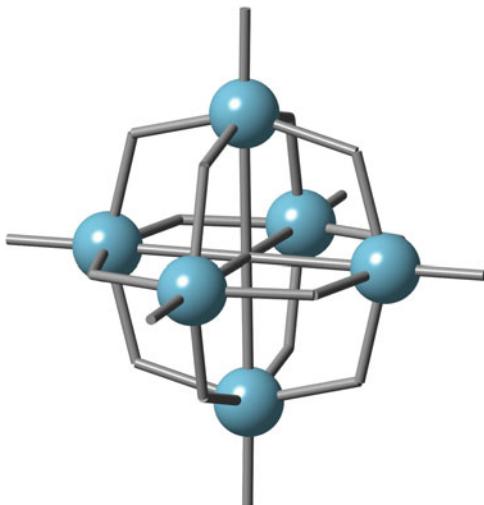
whereas the hexamolybdate can be derivatised by replacing one or more of the oxido ligands by Mo–N multiple-bonded nitrogenous ligands [23, 41–47]. The incorporation of a heterometal and associated ligands $\{M'L\}^{z+}$ to give substituted anions $[(LM')_xM_{6-x}O_{19-x}]^{n-}$ provides an alternative means of introducing reactive sites into these Lindqvist hexametalates, and we have therefore devoted significant effort to the development of efficient synthetic routes to such heterometallic species [48–54]. Our conceptual approach and studies of fundamental assembly processes are described in Sect. 2.1, while targeted synthesis of $\{MW_5\}$ and $\{MMo_5\}$ species is summarised in Sects. 2.2 and 2.3, respectively.

2 Polyoxometalates from Metal Alkoxides

2.1 *Isopolytungstates [W_xO_y]$^{n-}$ from WO(OR)$_4$*

The tungsten oxoalkoxides WO(OR)$_4$ dissolve in organic solvents and provide a nonaqueous source of WO$_3$. The W(VI) in these compounds is Lewis acidic, and, for less bulky R groups, dimerisation occurs through the formation of OR bridges, showing that the oxygens of the alkoxido ligands are more basic than the terminal oxido ligands. Variable-temperature and EXSY ^{1}H NMR studies revealed the dynamic nature of these dimeric structures, which involves stepwise cleavage of W–(μ-OMe) bonds and rearrangement of ligands around resulting five-coordinate W centres [55]. The addition of even small amounts of water to toluene solutions of these oxoalkoxides produced ill-defined insoluble solids, and we have not been able

to isolate and characterise any POAs from these reactions. However, this situation changes markedly in the presence of base.

$$6WO(OR)_4 + 2OH^- + 12H_2O \rightarrow [W_6O_{19}]^{2-} + 24ROH \quad (1)$$

$$WO_4^{2-} + 5WO(OMe)_4 + 10H_2O \rightarrow [W_6O_{19}]^{2-} + 20MeOH \quad (2)$$
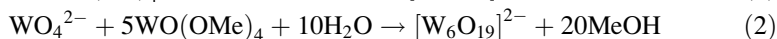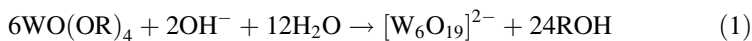
The conversion of an alkoxide precursor $MO_m(OR)_n$ to an isopolyoxometalate $[M_xO_y]^{z-}$ requires a source of negative charge in addition to the water for hydrolysis of the alkoxido groups. Jahr and coworkers were the first to show that tetraalkylammonium Lindqvist hexatungstates $(R_4N)_2[W_6O_{19}]$ may be obtained from $WO(OMe)_4$ by hydrolysis in the presence of R_4NOH according to Eq. (1) [38–40]. We adopted a slightly different approach and used the tetrabutylammonium (TBA) salt of monotungstate $(TBA)_2WO_4$ to provide the necessary anionic charge in acetonitrile, as in Eq. (2). By adding stoichiometric amounts of ^{17}O-enriched water, we were able to show by ^{17}O NMR spectroscopy that this reaction is essentially quantitative, which is testament to the stability of the Lindqvist hexametalate structure [48]. Recently, our more detailed ^{17}O NMR studies have shown that, after an initial period, a comparatively long-lived intermediate is observable (Fig. 2) and efforts are now underway to identify this species.

A theoretical analysis of the protonation-condensation processes responsible for the aqueous formation of $[W_6O_{19}]^{2-}$ from $[WO_4]^{2-}$ proposed two aggregation
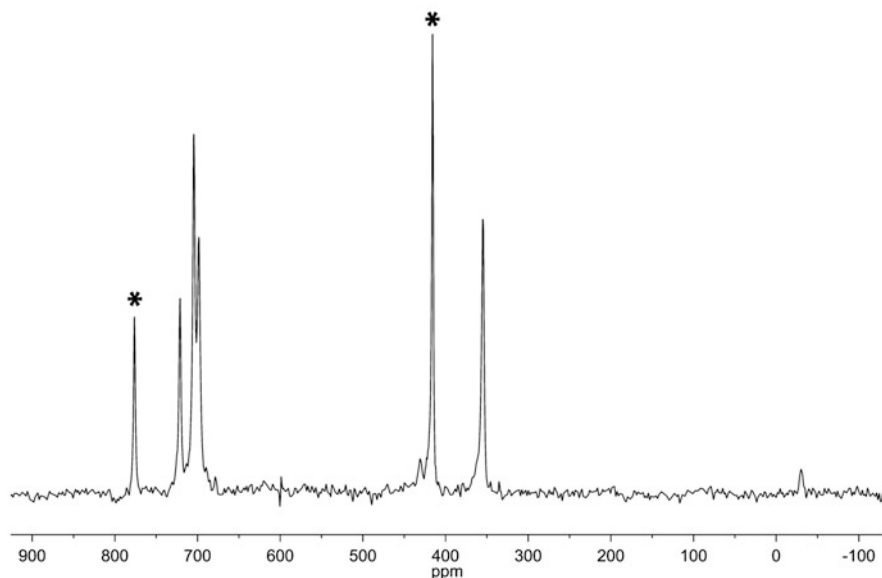
Fig. 2 ^{17}O NMR spectrum of the hydrolysis of a 1:5 mixture of $(TBA)_2[WO_4]$ and $WO(OMe)_4$ after heating at 60°C and removal of crystalline $(TBA)_2[W_6O_{19}]$. Peaks with an asterisk are due to $[W_6O_{19}]^{2-}$, and remaining peaks are due to an apparent intermediate species

mechanisms based on fragments observed in CID–ESIMS spectra of acetonitrile solutions of $(TBA)_2[W_6O_{19}]$, and minimum energy structures were calculated for $\{W_n\}$ intermediates for $n = 2$–5 [56, 57]. In a follow-up paper, further theoretical investigation of these intermediates in aqueous solution under different pH conditions highlighted the importance of interactions between solvent water and electrophilic tungsten centres, which increase the coordination number of the metal and become more favourable at lower pH. An independent reinvestigation of the same mechanisms and intermediates reached broadly similar conclusions [58]. While these theoretical analyses provide valuable insight into the energetics of possible interconversion processes, they do not reflect the experimental observation that aqueous acidification of WO_4^{2-} produces $[H_2W_{12}O_{42}]^{10-}$ and $[W_7O_{24}]^{6-}$ as the dominant species rather than $[W_6O_{19}]^{2-}$ [59, 60]. This discrepancy is most likely because calculations were based on the fragment ions in the ESI mass spectra from acetonitrile solutions of $(TBA)_2[W_6O_{19}]$, and effects of counter-cation and solvent variation on speciation were neglected.

$$WO_4^{2-} + WO(OMe)_4 \rightarrow \left[W_2O_5(OMe)_4\right]^{2-} \tag{3}$$

$$\left[W_2O_5(OMe)_4\right]^{2-} + 2\,H_2O \rightarrow [W_2O_7]^{2-} + 4\,MeOH \tag{4}$$
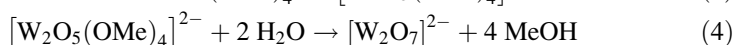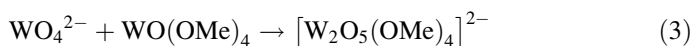
In our nonaqueous studies, monotungstate WO_4^{2-} was expected to be sufficiently nucleophilic to bind to the electrophilic W atoms in $[\{WO(OMe)_4\}_2]$ with formation of a WOW linkage and concomitant cleavage of the (μ-OMe) bridges. This was borne out by the formation of $[W_2O_4(\mu\text{-}O)(\mu\text{-}OMe)_2(OMe)_2]^{2-}$ in the 1:1 reaction between WO_4^{2-} and $WO(OMe)_4$ in MeCN shown in Eq. (3). This anion was structurally characterised as its $[Me_3NCH_2Ph]^+$ salt (Fig. 3) and indicates that
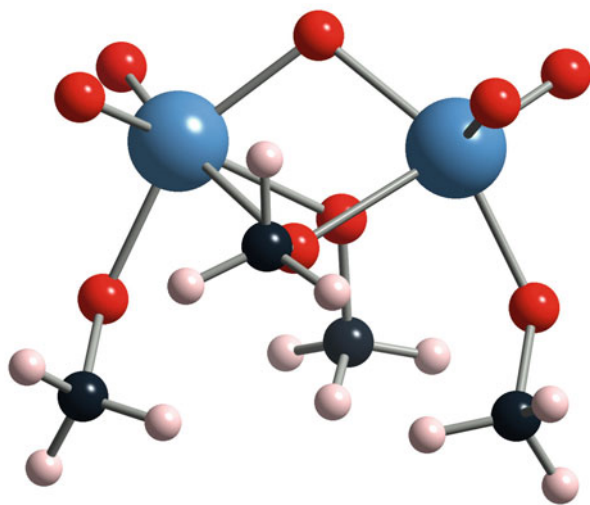
Fig. 3 Structure of the anion in $[PhCH_2NMe_3]_2[W_2O_5(OMe)_4]$. Blue, W; red, O; black, C; white, H

the initial nucleophilic attack by WO_4^{2-} was followed by a rapid ligand redistribution to give the symmetrical product (Scheme 1) [61].

Equation (4) demonstrates that the dinuclear anion $[W_2O_5(OMe)_4]^{2-}$ is potentially a precursor to $[W_2O_7]^{2-}$ which, although proposed as a possible dinuclear intermediate in the aqueous formation of $[W_6O_{19}]^{2-}$ [56, 57], has not been isolated and characterised from solution. Interestingly, the product from stoichiometric hydrolysis of $(TBA)_2[W_2O_5(OMe)_4]$ showed five resonances in its ^{183}W NMR spectrum rather than the expected single peak [62]. The chemical shifts (relative intensities) of 44 (1), 40 (2), 29 (1), -70 (1) and -85 (2) ppm imply the formation of a polynuclear $\{W_7\}_n$ species in contrast to the dinuclear structure of (TBA)$_2$[Mo$_2$O$_7$], which can be prepared in acetonitrile. The greater degree of aggregation in the case of tungsten probably reflects the basicity of the hydrolysis products in this system combined with a greater preference for higher tungsten coordination numbers through the formation of bridging W–O σ-bonds at the expense of less energetically favourable terminal W=O π-bonds. In this regard, it is worth noting that this uncharacterised polytungstate readily forms tetranuclear species such as $[W_4O_{12}(O_2CH_2)(OH)]^{3-}$ (Fig. 4) and is converted to $[W_6O_{19}]^{2-}$ in methanol, while $[Mo_2O_7]^{2-}$ has been reported to form the unstable pentamolybdate $[Mo_5O_{17}H]^{3-}$ in the presence of water [63]. These observations serve to emphasise the labile and reactive nature of POAMs generated under these conditions and indicate that, as
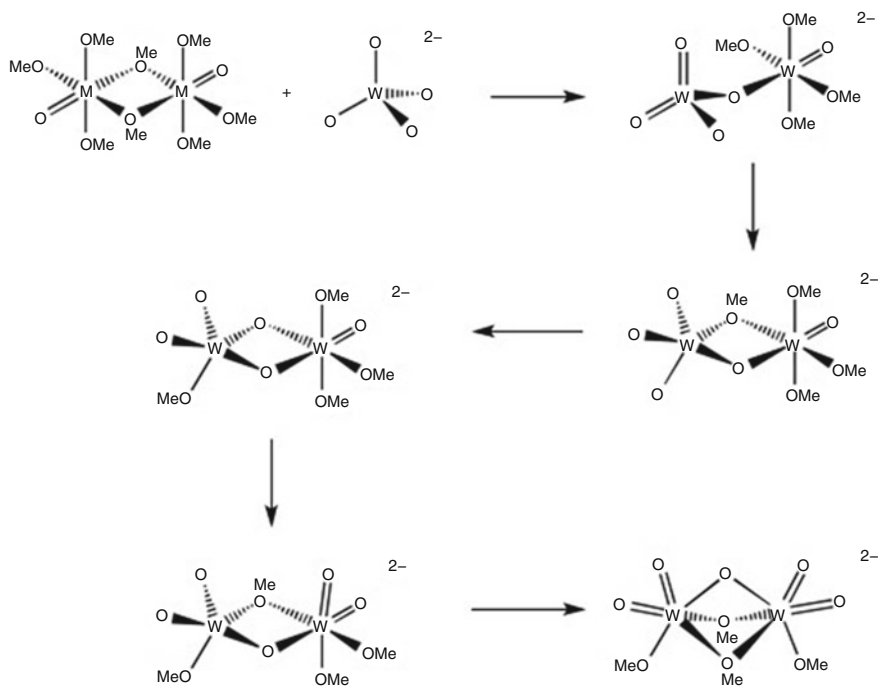
Scheme 1 A possible ligand redistribution mechanism for formation of the symmetrical anion $[W_2O_5(OMe)_4]^{2-}$ from $[\{WO(OMe)_4\}_2]$ and WO_4^{2-}

Fig. 4 Structure of the anion $[W_4O_{12}(O_2CH_2)(\mu_4\text{-}OH)]^{3-}$. Blue, W; red, O; black, C; white, H
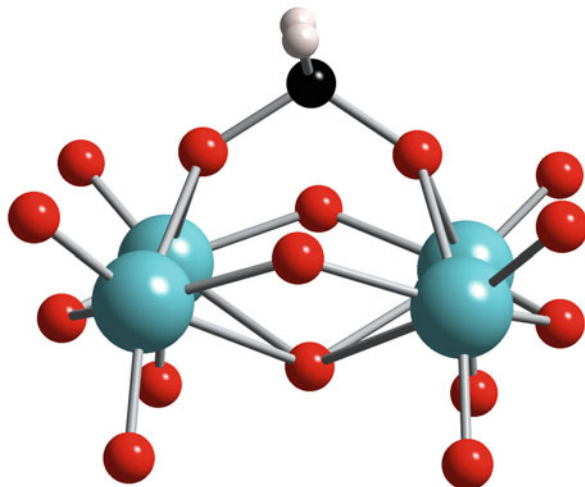
well as proton transfer, intramolecular ligand exchange between metal centres is a facile process.

2.2 Heterometallic Tungstates $[(RO)MW_5O_{18}]^{n-}$

The most significant aspect of this hydrolytic approach to POM synthesis from mixtures of the constituent metal alkoxides in the presence of an organic-soluble oxoanion is the access it provides to heterometallic $\{M'M_5\}$ Lindqvist species containing reactive M'–OR bonds [48–54]. What is remarkable about these reactions is that they proceed to give good to high yields of the target anions, whereas hydrolysis of the individual metal alkoxides, with their different structures and solution dynamics, occurs at different rates to give complex mixtures of POAs, and this complexity is exacerbated when the alkoxides are mixed prior to hydrolysis. The introduction of the oxoanion therefore has a profound influence on these hydrolysis reactions, most likely by cleaving bridging interactions in aggregated alkoxide precursors and inducing oxido-alkoxido ligand redistribution, as was observed in the reaction between WO_4^{2-} and $[\{WO(OMe)_4\}_2]$ described in Sect. 2.1. In addition, the anionic hydrolysis products are likely to be more soluble in polar organic solvents than the neutral products of metal alkoxide hydrolysis.

2.2.1 M(IV)-Substituted Tungstates $[(RO)MW_5O_{18}]^{3-}$

The general hydrolytic reaction in Eq. (5) has provided access to the $\{M^{IV}(OR)\}^{3+}$ substituted POMs $(TBA)_3[(RO)MW_5O_{18}]$ (M=Ti, Zr, Hf, Sn) from alkoxides M$(OR)_4$ and their adducts [48–54]. In considering this approach, it is important to

bear in mind the nature of the alkoxido groups, as they affect the degree of association of the alkoxide precursors and hence the dynamics of the reaction. Typical heterometal alkoxide precursors used include [{Ti(OMe)$_4$}$_4$], [{Zr(O^{i}Pr)$_3$(μ-O^{n}Pr)(HO^{i}Pr)}$_2$] [64] and [Sn(O^{t}Bu)$_4$] [65] and, in an attempt to dissociate the oligomeric structures, generate MOW bonds and initiate ligand redistribution; these were first heated in solution with (TBA)$_2$[WO$_4$] before the addition of [{WO(OMe)$_4$}$_2$] followed by further heating and subsequent hydrolysis.

$$3\ WO_4^{2-} + 7\ WO(OR)_4 + 2\ M(OR)_4 + 17\ H_2O$$

$$\rightarrow 2\ [(RO)MW_5O_{18}]^{3-} + 34\ ROH \tag{5}$$
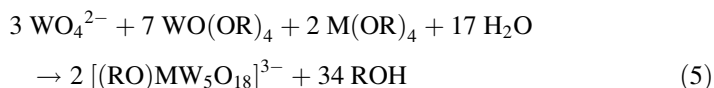
The monomeric anions [(MeO)TiW$_5$O$_{18}$]$^{3-}$ and [(MeO)SnW$_5$O$_{18}$]$^{3-}$ contain six-coordinate heterometals and terminal methoxido ligands, but incorporation of the larger zirconium heterometal gives the dimeric [{(μ-MeO)ZrW$_5$O$_{18}$}$_2$]$^{6-}$ with seven-coordinate Zr(IV) (Fig. 5). ^{17}O NMR spectra are characteristic of {MW$_5$O$_{18}$} frameworks, with two W=O peaks (the most intense for W$_{eq}$=O and the other for W$_{ax}$=O), one peak for MOW, two peaks for WOW and one peak for the central μ_6-O (Table 1). The chemical shifts of MOW and μ_6-O peaks are most sensitive to the nature of the heterometal M (Table 1), while in the ^{1}H NMR spectra, the methoxido resonances reflect bonding differences for the alkoxido groups, and upfield shifts are consistent with the bridging nature of OMe in the {ZrW$_5$} anion and a more ionic Sn-OMe bond in the {SnW$_5$} anion. The electronic effect of replacing Ti(IV) or Zr(IV) by Sn(IV) appears to be transmitted through the POM via the central μ_6-O to the *trans*-position occupied by W$_{ax}$=O, as indicated by the ^{17}O chemical shifts for μ_6-O and W$_{ax}$=O and the large upfield shift of the
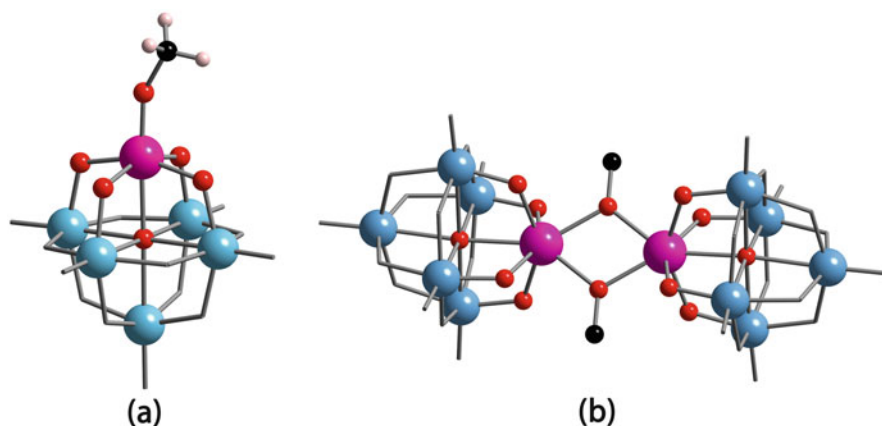
Fig. 5 Representations of the structures of (**a**) the monomeric anions [(MeO)MW$_5$O$_{18}$]$^{3-}$ (M=Ti, Sn) and (**b**) dimeric [{(μ-MeO)ZrW$_5$O$_{18}$}$_2$]$^{6-}$. Blue, W; magenta, M or Zr; red, O bonded to M or Zr; black, C; white, H

Table 1 NMR data for $\{(MeO)MW_5\}$ Lindqvist anions (M=Ti, Zr, Sn)

Anion[a]	[17]O chemical shift/ppm				[1]H chemical shift/ppm
	W=O	MOW	WOW	μ_6-O	MOMe
$[(MeO)TiW_5O_{18}]^{3-}$	721 (eq), 713 (ax)	525	390, 380	−58	4.08
$[\{(\mu\text{-}MeO)ZrW_5O_{18}\}_2]^{6-}$	711 (eq), 691 (ax)	484	385, 377	−58	3.74
$[(MeO)SnW_5O_{18}]^{3-}$	720 (eq), 684 (ax)	395	383, 364	17	3.64[b]

[a]As $^n Bu_4 N^+$ salts
[b]$^3 J(^1 H^{119} Sn) = 77$ Hz

W_{ax} resonance in ^{183}W NMR spectra from 64.5 ppm for $[(MeO)TiW_5O_{18}]^{3-}$ to −128.1 ppm for $[(MeO)SnW_5O_{18}]^{3-}$ [54].

The heterometalate $(TBA)_3[(MeO)TiW_5O_{18}]$ has also been synthesised by an alternative method involving initial degradation of the plenary $(TBA)_2[W_6O_{19}]$ with $(TBA)OH$ and subsequent addition of $Ti(OMe)_4$ according to Eq. (6). After addition of $(TBA)OH$ in acetonitrile to ^{17}O-enriched $(TBA)_2[W_6O_{19}]$, the ^{17}O NMR spectrum after stirring at room temperature was quite complex and showed no peaks due to remaining $[W_6O_{19}]^{2-}$. Several terminal W=O peaks in the range 660–725 ppm are significantly upfield from the W=O resonance for $[W_6O_{19}]^{2-}$ at 774 ppm, which is consistent with the presence of more highly charged anions. Upon addition of $Ti(OMe)_4$, the spectrum was greatly simplified, even at room temperature and without addition of the water required for the stoichiometric reaction shown in Eq. (6). After warming to ensure dissolution of all solids, the spectrum contained major peaks due to $[(MeO)TiW_5O_{18}]^{3-}$ in addition to significant extra peaks at 698 and 657 ppm (Fig. 6). The spectrum did not change much upon further heating, and $(TBA)_3[(MeO)TiW_5O_{18}]$ was obtained in about 75% yield from the reaction solution by crystallisation. These NMR results show that the dynamics of $[W_6O_{19}]^{2-}$ base degradation and subsequent ligand redistribution in this reaction are relatively fast, and this approach presents new opportunities for the synthesis of reactive Lindqvist derivatives under mild conditions, especially as ^{17}O-enriched $(TBA)_2[W_6O_{19}]$ may be prepared efficiently as described in Sect. 2.1.

$$5[W_6O_{19}]^{2-} + 8OH^- + 6Ti(OMe)_4 + 5H_2O$$
$$\rightarrow 6[(MeO)TiW_5O_{18}]^{3-} + 18MeOH \tag{6}$$
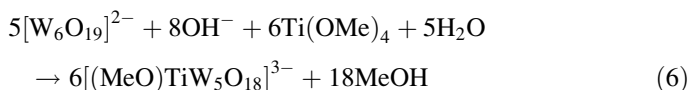
2.2.2 M(V)-Substituted Tungstates $[(RO)MW_5O_{18}]^{2-}$

The vanadium-substituted $(TBA)_3[VW_5O_{19}]$ can be synthesised by aqueous routes [66, 67], and ^{17}O-enriched samples are readily accessible from $VO(OR)_3$ using our nonaqueous hydrolytic approach, but we were unable to synthesise $[(MeO)VW_5O_{18}]^{2-}$ containing terminal V(OMe) [48], presumably due to the stronger π-bonding in terminal V=O compared to group 4 metals [68]. The niobium
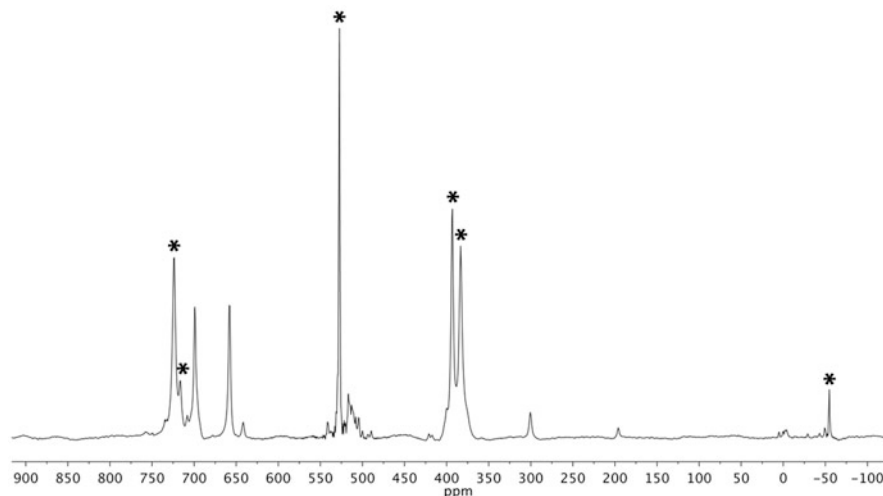
Fig. 6 ^{17}O NMR spectrum of the reaction indicated by Eq. (6) without addition of water, after warming to dissolve solids. Peaks marked with an asterisk are due to $[(MeO)TiW_5O_{18}]^{3-}$

analogue $(TBA)_2[(MeO)NbW_5O_{18}]$ was, however, obtained according to Eq. (7) and, although attempts to obtain single crystals for X-ray crystallography resulted in hydrolysis to $(TBA)_4[(\mu-O)(NbW_5O_{18})_2]$, the presence of terminal Nb-OMe was deduced from ^1H, ^{17}O and ^{183}W NMR spectra which were consistent with an effective C_{4v} symmetry for the anion in solution.

$$WO_4^{2-} + 4WO(OMe)_4 + Nb(OMe)_5 + 10H_2O$$
$$\rightarrow [(MeO)NbW_5O_{18}]^{2-} + 20MeOH \qquad (7)$$
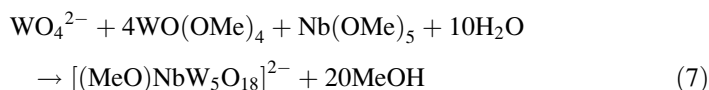
2.3 Heterometallic Molybdates $[(RO)TiMo_5O_{18}]^{n-}$

Substituted titanomolybdates $(TBA)_3[(RO)TiMo_5O_{18}]$ may be obtained using the same hydrolytic protocol as the tungstates described above. However, as the preparation of molybdenum oxoalkoxide $MoO(OMe)_4$ is less straightforward than its tungsten analogue [69], the modified approach illustrated by Eq. (8) is more convenient, where the negative charge is derived from a mixture of the molybdates $[Mo_2O_7]^{2-}$ and $[Mo_8O_{26}]^{4-}$ [52]. The isopropoxide product must be separated from unreacted $[Mo_8O_{26}]^{4-}$, suggesting that some of the $Ti(O^iPr)_4$ is hydrolysed to POA by-products at a comparative rate to the heterometalate formation. Notably, this reaction does not proceed with $[\{Ti(OMe)_4\}_4]$ presumably because of the tetrameric nature of the methoxide.

$$[\text{Mo}_2\text{O}_7]^{2-} + [\text{Mo}_8\text{O}_{26}]^{4-} + 2\text{Ti}\left(\text{O}^i\text{Pr}\right)_4 + 3\text{H}_2\text{O}$$

$$\rightarrow 2\left[\left(^i\text{PrO}\right)\text{TiMo}_5\text{O}_{18}\right]^{3-} + 6^i\text{PrOH} \tag{8}$$

$$5[\text{Mo}_6\text{O}_{19}]^{2-} + 8\text{OH}^- + 6\text{Ti}\left(\text{O}^i\text{Pr}\right)_4 + 5\text{H}_2\text{O}$$

$$\rightarrow 6\left[\left(^i\text{PrO}\right)\text{TiMo}_5\text{O}_{18}\right]^{3-} + 18^i\text{PrOH} \tag{9}$$
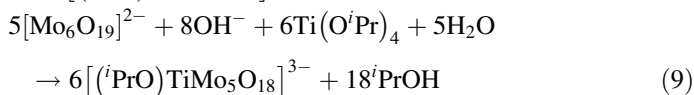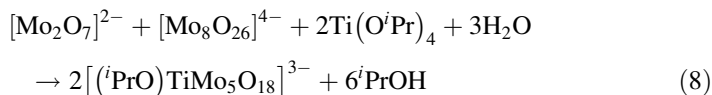
By analogy with the synthesis of $(\text{TBA})_3[(\text{MeO})\text{TiW}_5\text{O}_{18}]$ from a reactive mixture generated by base degradation of $(\text{TBA})_2[\text{W}_6\text{O}_{19}]$ as described in Sect. 2.2.1, $(\text{TBA})_3[(^i\text{PrO})\text{TiMo}_5\text{O}_{18}]$ was successfully synthesised from $(\text{TBA})_2[\text{Mo}_6\text{O}_{19}]$ and $\text{Ti}(\text{O}^i\text{Pr})_4$ according to Eq. (9). This alternative method is now preferred over our original procedure as it gives a higher yield and eliminates the problems associated with the removal of $(\text{TBA})_4[\text{Mo}_8\text{O}_{26}]$ from the product.

3 Protonolysis Reactions of $[(\text{RO})\text{M}'\text{M}_5\text{O}_{18}]^{n-}$

Access to a range of alkoxido derivatives $(\text{TBA})_n[(\text{RO})\text{M}'\text{M}_5\text{O}_{18}]$ has enabled us to explore the effects of (1) different heterometals M' and (2) variation of metals M in the lacunary $\{\text{M}_5\text{O}_{18}\}^{6-}$ 'ligand' on the reactivity of the single M(OR) site. Applications of metal alkoxides generally involve interactions with protic reagents HX and liberation of alcohol. While this type of reaction may at first seem trivial, details of metal alkoxide reactions are often ambiguous, and mechanisms are rarely fully elucidated, so these $\{(\text{RO})\text{M}'\text{M}_5\}$ systems provide an opportunity to probe the reactivity of a single, isolated site within a metal oxide matrix. The significantly ionic nature of M'–OR bonds leads to Lewis acidic metal and basic oxygen atoms [5, 6], while other factors that are likely to affect the detailed course of the reactions include the Brønsted acidity of HX, the ability of X^- to act as a ligand and the ease with which the heteroatom M' can increase its coordination number. In the case of $[(\text{RO})\text{M}'\text{M}_5\text{O}_{18}]^{n-}$ POMs, the oxygen atoms in the $\{\text{M}_5\text{O}_{18}\}^{6-}$ framework must also be considered as they may provide alternative binding sites for protons and, in this regard, their basicity will be affected by the nature of $\{\text{M}'(\text{OR})\}^{x+}$.

3.1 Ligand Metathesis
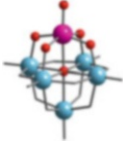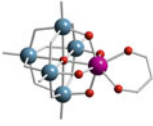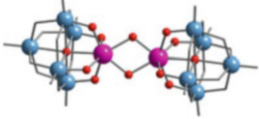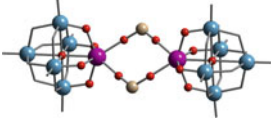
In reactions with protic species HX where the anion X^- can act as a ligand towards the heterometal M', straightforward access to derivatives $[\text{XM}'\text{M}_5\text{O}_{18}]^{n-}$ is afforded by treatment of $[(\text{RO})\text{M}'\text{M}_5\text{O}_{18}]^{n-}$ with an excess of HX, and the resulting families of POMs provide insight into bonding variations. As a general rule, the ease with which alkoxido ligands are exchanged in alcoholysis reactions increases with steric bulk of the alkoxido group bonded to the metal, which generally disfavours methoxido ligand exchange. In this case, however, treatment of the

{(MeO)M′M$_5$} POMs with an excess of primary, secondary or tertiary alcohols gave the desired ligand-exchanged product after prolonged heating and removal of the more volatile methanol. Reactions involving the more acidic phenols proceeded more readily to give aryloxido derivatives (TBA)$_3$[(ArO)M′M$_5$O$_{18}$]. The range of ligands introduced via these metathesis reactions is shown in Table 2.

In terms of qualitative reaction rates, the tin-substituted anions [(RO)SnW$_5$O$_{18}$]$^{3-}$ were most reactive, while reactions with titanomolybdates [(RO)TiMo$_5$O$_{18}$]$^{3-}$ were generally faster than those of their tungstate analogues. With potentially bidentate X$^-$ ligands, chelates were obtained with the larger Zr heterometal. Hence, in the [(2-CHOC$_6$H$_4$O)M′M$_5$O$_{18}$]$^{3-}$ products from reactions with salicylaldehyde, monodentate binding modes were observed in {TiM$_5$} and {SnW$_5$} anions with the carbonyl group orientated away from the six-coordinate heterometal, but the {ZrW$_5$} anion contained seven-coordinate Zr and a chelating salicylaldehydate ligand. Chelate bonding modes were also observed for the ligands in [(acac)ZrW$_5$O$_{18}$]$^{3-}$ and [(CH$_3$CO$_2$)ZrW$_5$O$_{18}$]$^{3-}$ derivatives [49].

X-ray crystal structures of this family of POMs revealed some interesting bonding trends. MOC bond angles and M-O bond distances have been proposed as indicators of the amount of π-bonding in MOR and MOAr bonds, which is

Table 2 {LM′M$_5$} Lindqvist anions obtained by protonolysis of {(RO)M′M$_5$} species

Structure type	{M′M$_5$}	L
	{TiW$_5$}	OH, OMe, OEt, O^{i}Pr, O^{t}Bu
		OPh, OC$_6$H$_4$Me-4, OC$_6$H$_4$^{t}Bu-4, OC$_6$H$_4$OH-4
		OC$_6$H$_4$OH-3, OC$_6$H$_3$(OH)$_2$-3,5, OC$_6$H$_4$CHO-2
	{ZrW$_5$}	OPh, OC$_6$H$_4$Me-4, OC$_6$H$_4$CHO-2
	{SnW$_5$}	OH, OMe, OEt, O^{i}Pr, O^{t}Bu
		OPh, OC$_6$H$_4$Me-4, OC$_6$H$_4$^{t}Bu-4, OC$_6$H$_4$OH-4
		OC$_6$H$_4$OH-3, OC$_6$H$_4$CHO-2
	{TiMo$_5$}	OMe, O^{i}Pr, O^{i}Bu, O^{t}Bu
		OC$_6$H$_4$Me-4, OC$_6$H$_4$CHO-2
	{ZrW$_5$}	OAc, acac, OC$_6$H$_4$CHO-2
	{ZrW$_5$}	OH, OMe
	{ZrW$_5$}	O$_2$PPh$_2$

expected to be more prevalent in alkoxides than in aryloxides [5, 6], and data for
$\{(RO)M'M_5\}$ and $\{(ArO)M'M_5\}$ POMs are shown in Table 3. In $\{TiM_5\}$ anions,
the average Ti-OR bond, 1.77 Å for $\{TiW_5\}$ and 1.78 Å for $\{TiMo_5\}$, was shorter
than the average Ti-OAr bond, 1.83 Å for $\{TiW_5\}$ and 1.88 Å for $\{TiMo_5\}$, which is
consistent with a greater degree of π-bonding in the alkoxides. The average TiOC
angle in $\{(RO)TiM_5\}$ anions was 153° for tungstates and 150° for molybdates,
while for the $\{(ArO)TiM_5\}$ anions, the average angle for both tungstates and
molybdates was 149°.

While previous studies have suggested that the MOC angle is not a reliable
indicator of the π contribution to terminal M–OR or M–OAr bonds [6, 70], the
average SnOC angles in $\{SnW_5\}$ alkoxides and aryloxides (131 and 130°, respec-
tively) are significantly smaller than in their transition metal counterparts. Together
with the longer average Sn–O bonds (1.97 Å for both SnOR and SnOAr) [71], this
appears to be consistent with greater ionic contributions to the Sn–O bonds, which
would result in a greater electron density at the SnOC oxygen and, consequently,

Table 3 M'–O bond lengths and M'OC angles for monomeric $[(RO)M'M_5O_{18}]^{3-}$ anions with
terminal OR ligands

Anion[a]	R	M'–O/Å	M'OC/°
$[(RO)TiW_5O_{18}]^{3-\,b}$	Me[b]	1.758(10)	148.6(12)
	^iPr	1.768(15)	160(3)
	$^tBu^c$	1.771(12)	155.0(14)
	Ph	1.852(6)	139.5(6)
	$4\text{-}MeC_6H_4$	1.845(8)	141.7(8)
	$4\text{-}^tBuC_6H_4{}^b$	1.80(2)	161(3)
	$2\text{-}(CHO)C_6H_4$	1.869(7)	138.6(7)
$[(RO)TiMo_5O_{18}]^{3-\,d}$	Me[b]	1.753(6)	144.5(8)
	^iPr	1.794(8)	155.7(12)
	$^tBu^b$	1.789(3)	152.2(4)
	$4\text{-}MeC_6H_4$	1.861(7)	141.7(7)
	$2\text{-}(CHO)C_6H_4$	1.890(8)	143.5(9)
$[(RO)SnW_5O_{18}]^{3-\,e}$	$^iPr^b$	1.947(16)	123.9(16)
	$^tBu^b$	1.983(11)	136.8(12)
	Ph	1.916(4)	128.4(4)
	$4\text{-}MeC_6H_4$	1.954(5)	129.2(6)
	$4\text{-}^tBuC_6H_4$	1.995(6)	127.4(6)
	$2\text{-}(CHO)C_6H_4$	1.98(2)	127(2)
$[(RO)ZrW_5O_{18}]^{3-\,f}$	Ph	1.866(6)	175.0(8)
	$4\text{-}MeC_6H_4$	2.03(3)	142(3)

[a] As $^nBu_4N^+$ salts
[b] Clegg et al. [48] and Errington et al. [50]
[c] Average values of independent anions in the crystal structure
[d] Errington et al. [52] and Coyle et al. [53]
[e] Kandasamy [70]
[f] Errington et al. [49]

alkoxido or aryloxido ligands that are more basic than those in the transition metal analogues. The structurally characterised $\{(ArO)ZrW_5\}$ species with monodentate aryloxido ligands (Ar=Ph and 4-MeC_6H_4) were monomeric, indicating that aryloxido ligands in these $\{ZrW_5\}$ Lindqvist anions prefer to be terminal, in contrast to the methoxido analogue which dimerises through OMe bridges. This is presumably due to steric interactions between the aryl *ortho*-positions and the M′OZr bridging oxygens, which become greater as the ZrOC angle decreases. The ZrOC angle at bridging OMe in $[\{(\mu\text{-MeO})ZrW_5O_{18}\}_2]^{6-}$ is 124°, whereas this angle is 142 and 175° in the structurally characterised monomeric $\{(ArO)ZrW_5\}$ derivatives.

These results have demonstrated the versatility of this approach for the rational and systematic preparation of a variety of $\{LM'M_5\}$ Lindqvist anions, which should now enable theoretical predictions of ligand- and heterometal-dependent properties to be tested experimentally. For example, the molecular static first hyper-polarisability of $[(2\text{-CHOC}_6H_4O)ZrW_5O_{18}]^{3-}$ with bidentate salicylaldehyde has been calculated to be much larger than that for $\{LZrW_5\}$ anions with monodentate aryloxido ligands [72], so after DFT calculations to determine ligands that will optimise electronic properties, it should be straightforward to synthesise samples for measurements.

3.2 Hydrolysis and Condensation

As expected from the trends in bonding parameters discussed in Sect. 3.1, the hydrolytic susceptibility of the M′–OR bond in $\{(MeO)M'M_5\}$ alkoxido POMs varied significantly with M′. A two-step process was envisaged in which an initial hydroxido product might then undergo subsequent reaction with $\{(MeO)M'M_5\}$ or condensation to produce a M′OM′-bridged aggregate. These steps are shown in Eqs. (10)–(12) for anions with octahedral M^{IV} heterometals.

$$[(MeO)M'M_5O_{18}]^{3-} + H_2O \leftrightarrows [(HO)M'M_5O_{18}]^{3-} + MeOH \qquad (10)$$

$$[(HO)M'M_5O_{18}]^{3-} + [(MeO)M'M_5O_{18}]^{3-}$$
$$\leftrightarrows [(\mu\text{-O})(M'M_5O_{18})_2]^{6-} + MeOH \qquad (11)$$

$$2\,[(HO)M'M_5O_{18}]^{3-} \leftrightarrows [(\mu\text{-O})(M'M_5O_{18})_2]^{6-} + H_2O \qquad (12)$$
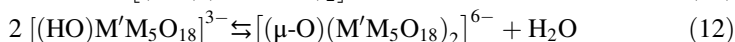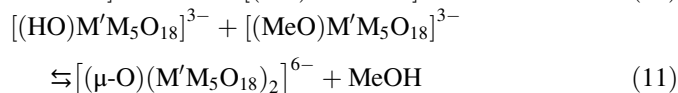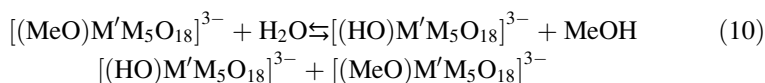
$[(MeO)SnW_5O_{18}]^{3-}$ hydrolysis in MeCN proceeded rapidly to completion and produced the hydroxido species $[(HO)SnW_5O_{18}]^{3-}$ which showed an FTIR peak at $3,648\ \text{cm}^{-1}$ for $\nu(OH)$ and a ^1H NMR singlet at 3.42 ppm in d_6-dmso. The resonance in the ^{119}Sn spectrum measured without proton decoupling showed $^2J(^1H^{119}Sn)$ coupling of 47.7 Hz, which was removed by proton decoupling. The ^{119}Sn NMR spectrum of this hydroxide species also showed that condensation to give $[(\mu\text{-O}) (SnW_5O_{18})_2]^{6-}$ is slow at room temperature (Fig. 7) and can be prevented by using

Fig. 7 ^{119}Sn NMR spectra of a solution of (TBA)$_3$[(HO)SnW$_5$O$_{18}$] in MeCN at room temperature (**a**) and after heating at 85–90°C for 2 h (**b**)
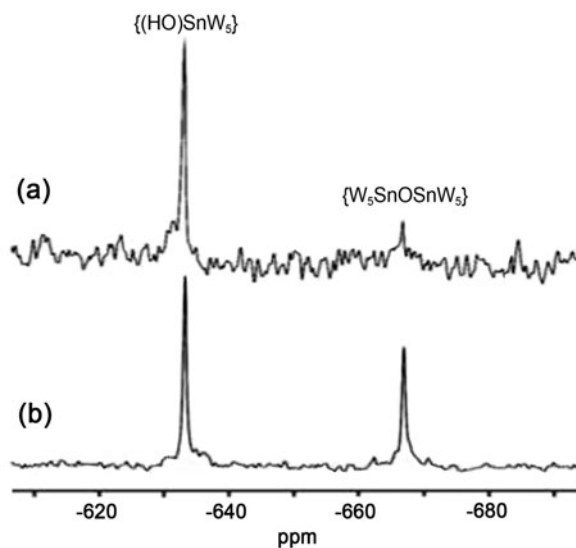
better donor solvents such as PhCN or dmso [71] (Lebbie D, Errington RJ, unpublished results 2017). In contrast, ^{1}H and ^{17}O NMR studies showed that hydrolysis of monomeric [(MeO)TiM$_5$O$_{18}$]$^{3-}$ anions (M=W, Mo) in MeCN is significantly slower than for the {SnW$_5$} anion, but the oxo-bridged species [(μ-O)(TiM$_5$O$_{18}$)$_2$]$^{6-}$ are formed more readily. Attempts to force the hydrolysis of the {M$_5$} anions to completion by carrying out reactions at higher temperatures therefore resulted in isolation of the oxo-bridged POMs [50, 53]. However, we found that hydrolysis of (TBA)$_3$[(MeO)TiW$_5$O$_{18}$] occurs significantly more rapidly in dmso, which may be due to a lower pKa for water in dmso than in MeCN. In addition, the better donor capability of dmso inhibits the condensation process. These effects together enabled us to isolate and characterise (TBA)$_3$[(HO)TiW$_5$O$_{18}$], as confirmed by an FTIR peak due to ν(OH) at 3,672 cm^{-1}, the absence of ν_{as}(TiO) for (TiOTi) and a ^{1}H NMR peak at 9.57 ppm for TiOH in d_6-dmso. The crystal structure of (TBA)$_3$[(HO)TiW$_5$O$_{18}$] demonstrated the monomeric nature of the anion but, unsurprisingly, the terminal {TiOH} groups were disordered over all six metal positions (Lebbie D, Errington RJ, unpublished results 2017).

In the case of dimeric [{(μ-MeO)ZrW$_5$O$_{18}$}$_2$]$^{6-}$, our ^{17}O NMR studies of hydrolysis in MeCN provided evidence for the formation of an asymmetric intermediate [(μ-HO)(μ-MeO)(ZrW$_5$O$_{18}$)$_2$]$^{6-}$ en route to the symmetrically bridged product [{(μ-HO)ZrW$_5$O$_{18}$}$_2$]$^{6-}$. This reaction did not proceed further to the oxo-bridged species [(μ-O)(ZrW$_5$O$_{18}$)$_2$]$^{6-}$ [49]. It is worth noting that, in aqueous media, other workers have prepared monomeric [(H$_2$O)$_3$ZrW$_5$O$_{18}$]$^{2-}$ as the [Me$_4$N]$^+$ salt and the ligand-exchanged anions [(H$_2$O)$_{3-n}$(dmso)$_n$ZrW$_5$O$_{18}$]$^{2-}$ were obtained by recrystallisation from water-dmso ($n = 1$) or dmso ($n = 2$). Treatment of these monomeric anions with (TBA)OH was shown to give (TBA)$_6$[{(μ-HO)ZrW$_5$O$_{18}$}$_2$] [73].

3.3 Protonation with Acids of Weakly Coordinating Anions

Weakly coordinating anions play an important role in the generation of reactive, electrophilic metal centres in homogeneous organometallic or metalorganic catalysts [74], and the mechanistic understanding gained from such studies is now being applied in the 'surface organometallic chemistry' approach to heterogeneous catalysis [75, 76]. A key feature of this approach is the production of oxide-supported reactive metal centres that are analogous to those of molecular species that have been studied in solution. The analogy between POMs and bulk metal oxides raises the question of whether it is possible to manipulate reactive sites in POMs to provide similar insights into reactivity and enable comparisons with oxide surfaces.

In reactions between $\{(RO)M'M_5\}$ and HX where X^- is a weakly coordinating ligand, protonation of M'OR will decrease the anion charge and produce labile ROH, dissociation of which will provide access to the heterometal site. Subsequently, any molecules in solution that are better ligands than X^- or ROH would be expected to bind to the 'exposed' electrophilic heterometal and, in weak donor solvents such as MeCN, this may be the POM itself. We have therefore explored reactions between $HBF_4 \cdot OEt_2$ and $[(RO)M'W_5O_{18}]^{3-}$ (M'=Ti, Sn) in order to establish whether new, reactive $[M'W_5O_{18}]^{2-}$ species might be generated in solution. NMR studies were carried out in order to ascertain whether the site of protonation for the anions $[(RO)M'W_5O_{18}]^{3-}$ was M'OR or the oxygens of the $W_5O_{18}{}^{6-}$ oxometalate ligand, of which the bridging M'OW oxygens are expected to be the most basic. ^{17}O NMR is useful for monitoring protonation of POMs because of (1) a general downfield shift of peaks, particularly for terminal W=O, when the POM becomes less negatively charged and (2) an upfield shift of specific oxygen sites upon protonation [77]. Gradual addition of $HBF_4 \cdot OEt_2$ to ^{17}O-enriched $[(MeO)TiW_5O_{18}]^{3-}$ resulted in downfield shifts for W=O, TiOW and WOW peaks, indicating a decrease in the anion charge. Addition of >1 mol-equivalent of acid caused an upfield shift of the TiOW peak, and the spectrum became more complex (Lebbie D, Errington RJ, unpublished results 2016). These changes are consistent with initial protonation at TiOMe (which is not ^{17}O enriched and does not appear in the spectrum), which can therefore be designated as the most basic site in the anion. After addition of >1 mol-equivalent of HBF_4, the TiOW sites appear to be protonated to give more complex species derived from $[TiW_5O_{18}H_x]^{(2-x)-}$ units, which are as yet uncharacterised.

An ^{17}O NMR study of 1:1 protonation of $(TBA)_3[(MeO)SnW_5O_{18}]$ with $HBF_4 \cdot OEt_2$ again showed no significant upfield shift of the SnOW peak, suggesting that the reaction had proceeded with protonation at SnOMe, which is consistent with a comparatively high basicity for this oxygen as indicated by X-ray structural data as well as the ease of hydrolysis. The ^{119}Sn NMR spectrum, however, showed a mixture of species, including a characteristic doublet pattern that we assigned to $[FSnW_5O_{18}]^{3-}$ with a large $^1J(^{19}F^{119}Sn)$ coupling of 2,613 Hz [27] (Lebbie D, Errington RJ, unpublished results 2016). This implies that, after removal of the methoxido ligand, the Sn(IV) centre is sufficiently Lewis acidic to abstract fluoride

from BF_4^- and again confirms that protonation enhances the reactivity of the heterometal site in the absence of strongly coordinating ligands.

From the reaction between Ph_2PO_2H and $(TBA)_6[\{(\mu\text{-MeO})ZrW_5O_{18}\}_2]$, we were able to isolate and characterise $(TBA)_6[\{(\mu\text{-}Ph_2PO_2)ZrW_5O_{18}\}_2]$ in which the phosphinate ligands adopt a bridging rather than a chelating mode (Fig. 8). In addition, the phosphinate ligands appeared to be labile, as the aggregated anion $[(\mu_3\text{-HO})_2\{ZrW_5O_{18}\}_3H]^{7-}$ (Fig. 9) was obtained upon prolonged recrystallisation
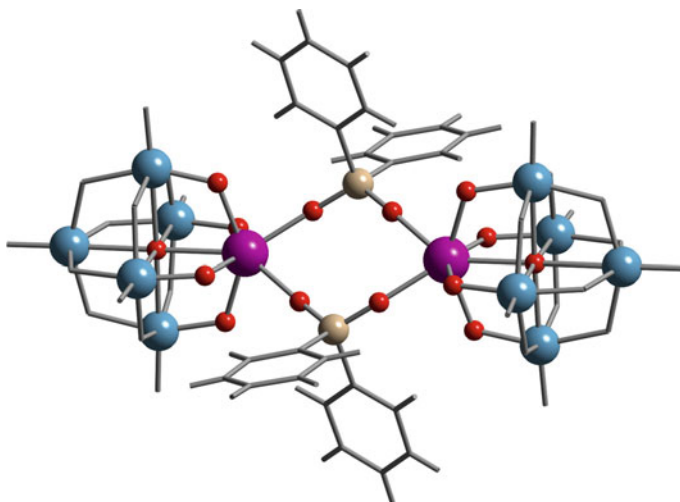
Fig. 8 Structure of the anion $[\{(\mu\text{-}Ph_2PO_2)ZrW_5O_{18}\}_2]^{6-}$. Blue, W; magenta, Zr; red, O bonded to Zr; grey, P
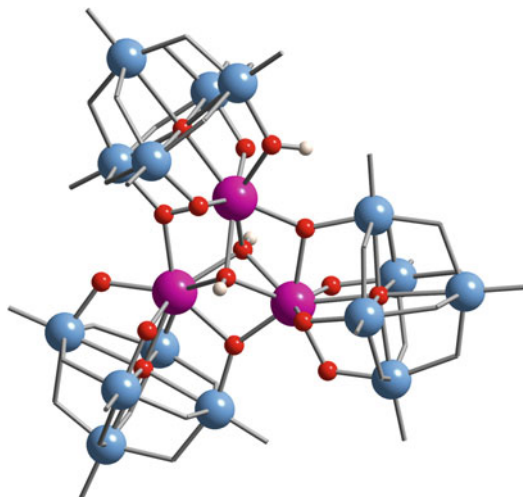
Fig. 9 Structure of the anion $[(\mu_3\text{-HO})_2(ZrW_5O_{18})_3H]^{7-}$. Blue, W; magenta, Zr; red, O bonded to M or Zr; white, H

Fig. 10 Structure of the
anion $[(TiW_5O_{18})_2]^{4-}$.
Blue, W; magenta, Ti; red,
O bonded to Ti
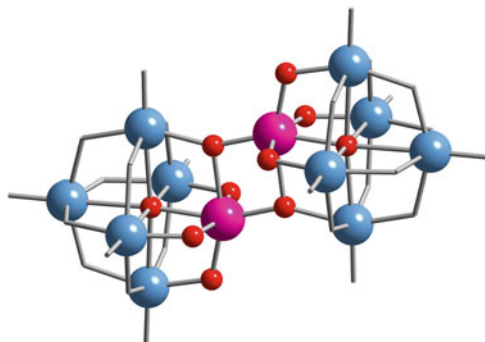
[49]. This appears to be consistent with the formation of bifunctional $[ZrW_5O_{18}]^{2-}$ units containing Lewis acidic Zr and basic ZrOW sites, which then assemble in the presence of trace amounts of water. Similar chemistry appears to occur in the $\{TiW_5\}$ system, where the aggregated $[\{TiW_5O_{18}\}_2]^{4-}$ (Fig. 10) was obtained by Cl^- abstraction from $[ClTiW_5O_{18}]^{3-}$ with Ag^+. Prolonged recrystallisation of this dimer in the presence of adventitious water resulted in isolation of the protonated $[(\mu\text{-}O)(TiW_5O_{18}H)_2]^{4-}$, which can also be more directly synthesised by protonation of $[(\mu\text{-}O)(TiW_5O_{18})_2]^{6-}$ with $HBF_4 \cdot OEt_2$ [27] (Lebbie D, Errington RJ, unpublished results 2016).

From these observations, it is clear that removal of alkoxido ligands from $[(RO)M'M_5O_{18}]^{n-}$ Lindqvist anions by protonation with acids of weakly coordinating anions does indeed generate reactive species that are bifunctional by virtue of Lewis acidic M' and basic M'OM sites, and these may self-assemble to form aggregates and/or interact with substrates such as H_2O. Given that halide abstraction provides another route to such species, these systems would appear to provide a solution-based approach to molecular metal oxide reactivity that should complement heterogeneous studies of oxide-supported reactive metal sites by surface organometallic chemistry.

4 Comparisons with $[(RO)MPW_{11}O_{39}]^{n-}$ Anions

The most extensively studied POMs are those of the Keggin family $[EM_{12}O_{40}]^{n-}$ and their derivatives, where E is a central heteroatom. We found that the organic-soluble 'lacunary' derivative $(TBA)_6[NaPW_{11}O_{39}]$ is a useful precursor for the nonaqueous synthesis of $\{M'PW_{11}\}$ Keggin-type POMs [23–27, 78] and we were interested to compare the reactivity of substituted Keggin-type alkoxido derivatives $[(RO)MPW_{11}O_{39}]^{n-}$ with that of the Lindqvist hexametalates. This $\{PW_{11}O_{39}\}$ precursor may be enriched in ^{17}O by simple treatment with ^{17}O-enriched H_2O, which provided efficient access to a range of ^{17}O-enriched substituted anions for ^{17}O NMR

studies [27, 79]. Halides $(TBA)_4[ClMPW_{11}O_{39}]$ were obtained by reacting $(TBA)_6[NaPW_{11}O_{39}]$ with MCl_4 in CH_2Cl_2 (Ti) or MeCN (Sn) and then converted to the methoxides $(TBA)_4[(MeO)TiPW_{11}O_{39}]$ and $(TBA)_4[(MeO)SnPW_{11}O_{39}]$ by treatment with NaOMe in a similar fashion to that originally reported by Knoth [80]. Reactions were monitored in solution by ^{31}P, ^{17}O and ^{119}Sn NMR as appropriate. Kholdeeva and coworkers have previously studied related $\{PTiW_{11}\}$ systems in relation to activity in catalytic alkene epoxidation, and our nonaqueous results complement these studies [81–84].

As in the case of the Lindqvist anions discussed above, the Sn(IV)-substituted Keggin anion $[(MeO)SnPW_{11}O_{39}]^{4-}$ underwent hydrolysis much more rapidly than its Ti(IV) congener to give $[(HO)SnPW_{11}O_{39}]^{4-}$, even in the presence of traces of H_2O. Consequently, rigorously dry conditions are essential in order to obtain pure $(TBA)_4[(MeO)SnPW_{11}O_{39}]$, which may explain why this POM has not been reported previously. By contrast, hydrolysis of $[(MeO)TiPW_{11}O_{39}]^{4-}$ in MeCN was slow, with 60% of the methoxide remaining after 1 h. Kholdeeva and coworkers previously reported that a mixture of $[(HO)TiPW_{11}O_{39}]^{4-}$ and $[[(\mu\text{-}O)(TiPW_{11}O_{39})_2]^{8-}$ was produced in this reaction, but, as in the case of the $\{(MeO)TiW_5\}$ Lindqvist anion, we were able to exploit the faster hydrolysis rate and inhibition of condensation in dmso to isolate pure $(TBA)_4[(HO)TiPW_{11}O_{39}]$. The formation of oxo-bridged $[[(\mu\text{-}O)(MPW_{11}O_{39})_2]^{8-}$ from hydroxide anions $[(HO)MPW_{11}O_{39}]^{4-}$ was slower in both cases (M=Ti and Sn) than their Lindqvist counterparts, possibly due to a combination of increased charge and steric interactions in the Keggin systems.

The protonation of $[(RO)MPW_{11}O_{39}]^{4-}$ anions with $HBF_4 \cdot Et_2O$ has also been studied in detail by ^{17}O and ^{31}P NMR, and results suggest that, in contrast to the Lindqvist anion $[(MeO)TiW_5O_{18}]^{3-}$, initial protonation occurs at TiOW rather than TiOMe in $[(MeO)TiPW_{11}O_{39}]^{4-}$, whereas in $[(HO)SnPW_{11}O_{39}]^{4-}$, SnOH is still sufficiently basic to be protonated before SnOW [79]. This implies that the introduction of $\{MOR\}^{3+}$ has a greater polarising effect on the oxometalate framework in the $\{MPW_{11}\}$ Keggin anions than in the $\{MW_5\}$ Lindqvist anions, as was suggested by previous theoretical investigations [85].

5   Conclusions

The targeted synthesis of alkoxido-derivatised Lindqvist-type POMs $[(RO)M'M_5O_{18}]^{n-}$ has been achieved via controlled nonaqueous reactions, and ^{17}O NMR studies of different strategies indicate that the generation of tungstate or molybdate precursors by degradation of $[M_6O_{19}]^{2-}$ may offer kinetic advantages and milder reaction conditions. The protolytic manipulation of organic ligands in hybrid POMs adds an extra dimension to systematic POM chemistry and facilitates overlap with metalorganic and organometallic chemistry. While it has yet to be fully exploited, this capability will be valuable for tuning the properties of hybrid POMs. The effects on protonolysis reactions of heterometal substitution and of

changing the supporting oxometalate structural framework from Lindqvist to Keggin are being revealed by NMR studies. These show, for example, that $[(MeO)SnW_5O_{18}]^{3-}$ is more reactive than $[(MeO)TiW_5O_{18}]^{3-}$ by virtue of the greater iconicity of the Sn–OMe bond and that reactions involving the formation of M′OM bridging bonds between heterometal atoms from terminal MOH are inhibited in donor solvents and are also less favourable for Keggin anions. ^{17}O NMR studies confirm that initial protonation with HX occurs at M′OR to give, in the absence of strongly bonding X⁻, reactive $\{M'M_5O_{18}\}$ species that contain Lewis acidic M′ and basic M′OM sites. These studies are providing an experimental basis for theoretical calculations aimed at a deeper understanding of mechanistic aspects of POM reactivity [86], details of which will be published elsewhere.

References

1. Yu X, Marks TJ, Facchetti A (2016) Metal oxides for optoelectronic applications. Nat Mater 15:383–396
2. Yuan C, Wu HB, Xie Y, Lou XW (2014) Mixed transition-metal oxides: design, synthesis, and energy-related applications. Angew Chem Int Ed 53:1488–1504
3. Kung HH (1989) Transition metal oxides: surface chemistry and catalysis, studies in surface science and catalysis, vol 45. Elsevier, Amsterdam
4. Meyer J, Hamwi S, Kröger M, Kowalsky W, Riedl T, Kahn A (2012) Transition metal oxides for organic electronics: energetics, device physics and applications. Adv Mater 24:5408–5427
5. Bradley DC, Mehrotra RC, Gaur DP (1978) Metal alkoxides. Academic, London
6. Bradley DC, Mehrotra RC, Rothwell IP, Singh A (2001) Alkoxo and aryloxo derivatives of metals. Academic, London
7. Hench LL, West JK (1990) The sol-gel process. Chem Rev 90:33–72
8. Brinker CJ, Scherer GW (1990) Sol-gel science. Academic, San Diego
9. Sanchez C, Rozes L, Ribot F, Laberty-Robert C, Grosso D, Sassoye C, Boissiere C, Nicole L (2010) "Chimie douce": a land of opportunities for the designed construction of functional inorganic and hybrid organic-inorganic nanomaterials. C R Chim 13:3–39
10. Watenpaugh K, Caughlan CN (1967) The crystal and molecular structure of the first hydrolysis product ($Ti_7O_{24}Et_{19}$) of titanium tetraethoxide. J Chem Soc Chem Commun 2:76–77
11. Schmidt R, Mosset A, Galy J (1991) New compounds in the chemistry of group 4 transition-metal alkoxides. Part 4. Synthesis and molecular structures of two polymorphs of $[Ti_{16}O_{16}(OEt)_{32}]$ and refinement of the structure of $[Ti_7O_4(OEt)_{20}]$. J Chem Soc Dalton Trans 8:1999–2005
12. Day VW, Eberspacher TA, Klemperer WG, Park CW, Rosenberg FS (1991) Solution structure elucidation of early transition-metal polyoxoalkoxides using ^{17}O nuclear magnetic resonance spectroscopy. J Am Chem Soc 113:8190–8192
13. Mosset A, Galy J (1988) Synthèse et etude structural de l'édifice $Ti_{16}O_{16}(OC_2H_5)_{32}$: un example de maclage intramoléculaire. C R Acad Sci Paris Ser II 307:1747–1750
14. Day VW, Eberspacher TA, Klemperer WG, Park CW (1993) Dodecatitanates: a new family of stable polyoxotitanates. J Am Chem Soc 115:8469–8470

15. Chen YW, Klemperer WG, Park CW (1992) Polynuclear titanium oxoalkoxides: molecular building blocks for new materials? MRS Online Proc Libr 271:57–63

16. Day VW, Eberspacher TA, Chen Y, Hao J, Klemperer WG (1995) Low-nuclearity titanium oxoalkoxides: the trititanates $[Ti_3O](OPr^i)_{10}$ and $[Ti_3O](OPr^i)_9(OMe)$. Inorg Chim Acta 229:391–405

17. Rozes L, Sanchez C (2011) Titanium oxo-clusters: precursors for a Lego-like construction of nanostructured hybrid materials. Chem Soc Rev 40:1006–1030

18. Rozes L, Steunou N, Fornasieri G, Sanchez C (2006) Titanium-oxo clusters, versatile nanobuilding blocks for the design of advanced hybrid materials. Monatsh Chem 137:501–528

19. Knoth W, Harlow RL (1981) Derivatives of heteropolyanions. 3. O-alkylation of $Mo_{12}PO_{40}{}^{3-}$ and $W_{12}PO_{40}{}^{3-}$. J Am Chem Soc 103:4265–4266

20. Chen Q, Zubieta J (1992) Coordination chemistry of soluble metal oxides of molybdenum and vanadium. Coord Chem Rev 114:107–167

21. Khan MI, Chen Q, Goshorn DP, Zubieta J (1993) Polyoxoalkoxide clusters of vanadium: structural characterisation of the decavanadate core in the "fully reduced" vanadium (IV) species $[V_{10}O_{16}\{(OCH_2)_3CCH_2CH_3\}_4]^{2-}$ (R = $-CH_2CH_3$, $-CH_3$). Inorg Chem 32:672–680

22. Hu X, Xiao Z, Huang B, Hu X, Cheng M, Lin X, Wu P, Wei Y (2017) Syntheses and post-functionalization of tri-substituted polyalkoxohexavanadates containing tris(alkoxo) ligands. Dalton Trans 46:8505–8513

23. Errington RJ, Richards DG, Clegg W, Fraser KA (1994) New aspects of non-aqueous polyoxometalate chemistry. In: Müller A, Pope MT (eds) Polyoxometalates: from platonic solids to anti-retroviral activity. Topics in molecular organization, vol 10. Kluwer, Dordrecht, pp 105–114

24. Errington RJ (2001) Rational approaches to polyoxometalate synthesis. In: Pope MT, Müller A (eds) Polyoxometalate chemistry: from topology via self-assembly to applications. Kluwer, Dordrecht, pp 1–22

25. Errington RJ (2003) General strategies for non-aqueous polyoxometalate synthesis. In: Borrás-Almenar JJ, Coronado E, Müller A, Pope MT (eds) Polyoxometalate molecular science. Kluwer, Dordrecht, pp 55–77

26. Errington RJ (2003) Structure of oxo metallic clusters. In: McCleverty JA, Meyer TJ (eds) Comprehensive coordination chemistry II, vol 2. Elsevier, Oxford, pp 759–773

27. Errington RJ (2017) Nonaqueous polyoxometalate synthesis for systematic studies of hydrolysis, protonation and reduction. In: van Eldik R, Cronin L (eds) Polyoxometalate chemistry, Adv Inorg Chem, vol 69. Elsevier, Cambridge, pp 287–336

28. Lindqvist I (1953) The structure of the hexaniobate ion in 7 Na_2O 6 Nb_2O_5 32 H_2O. Arkiv Kemi 5:247–250

29. Marek KA (2001) PhD thesis, University of Illinois at Urbana-Champaign, Champaign

30. Klemperer WG, Marek KA (2013) An ^{17}O NMR study of hydrolyzed Nb^V in weakly acidic and basic aqueous solutions. Eur J Inorg Chem 10–11:1762–1771

31. Nyman M (2011) Polyoxoniobate chemistry in the 21st century. Dalton Trans 40:8049–8058

32. Daniel C, Hartl H (2009) A mixed-valence V^{IV}/V^V alkoxo-polyoxovanadium cluster series $[V_6O_8(OCH_3)_{11}]^{n+/-}$: exploring the influence of a μ-oxo ligand in a spin frustrated structure. J Am Chem Soc 131:5101–5114

33. Tytko KH, Schoenfeld B (1975) Concerning solid isopolymolybdates and their relation to isopolymolybdate ions in aqueous solution. Z Naturforsch Teil B 30:471–484

34. Boyer M, Le Meur B (1979) Nouvelle préparation et propriétés de l'ion hexatungstique $W_6O_{19}{}^{2-}$. C R Acad Sci Ser IIC 281:59–62

35. Che M, Fournier M, Launay JP (1979) The analog of surface molybdenyl ion in Mo/SiO_2 supported catalysts: the isopolyanion $Mo_6O_{19}{}^{3-}$ studied by EPR and UV-visible spectroscopy. Comparison with other molybdenyl compounds. J Chem Phys 71:1954–1960

36. Sanchez C, Livage J, Launay JP, Fournier M (1983) Electron delocalization in mixed-valence tungsten polyanions. J Am Chem Soc 105:6817–6823

37. Klemperer WG (1990) Inorg Synth 27:74–78 and 80–81
38. Jahr KF, Fuchs J, Witte P, Flindt EP (1965) Hydrolysis of amphoteric metal alkoxides. V. Saponification of tetraethyl tungstate(VI) in the presence of various bases. Chem Ber 98:3588–3599
39. Jahr KF, Fuchs J, Oberhauser R (1968) Hydrolysis of amphoteric metal alkoxides. IX. Saponification of tetramethyl tungstate(VI) in the presence of tetraalkylammonium bases. Chem Ber 101:477–481
40. Fuchs J, Jahr KF (1968) Über neue Polywolframate und –molybdate. Z Naturforsch Teil B 23:1380
41. Hsieh T-C, Zubieta J (1986) Synthesis and characterization of oxomolybdate clusters containing coordinatively bound organo-diazenido units: the crystal and molecular structure of the hexanuclear diazenido-oxomolybdate, $(NBu^n_4)_3[Mo_6O_{18}(N_2C_6H_5)]$. Polyhedron 5:1655–1657
42. Kang H, Zubieta J (1988) Co-ordination complexes of polyoxomolybdates with a hexanuclear core: synthesis and structural characterization of $(NBu^n_4)_2[Mo_6O_{18}(NNMePh)]$. J Chem Soc Chem Commun 17:1192–1193
43. Du Y, Rheingold AL, Maatta EA (1992) A polyoxometalate incorporating an organoimido ligand: preparation and structure of $[Mo_5O_{18}(MoNC_6H_4CH_3)]^{2-}$. J Am Chem Soc 114:345–346
44. Proust A, Thouvenot R, Chaussade M, Robert F, Gouzerh P (1994) Phenylimido derivatives of $[Mo_6O_{19}]^{2-}$: synthesis, X-ray structures, vibrational, electrochemical, ^{95}Mo and ^{15}N NMR studies. Inorg Chim Acta 224:81–95
45. Clegg W, Errington RJ, Fraser KA, Holmes SA, Schäfer A (1995) Functionalisation of $[Mo_6O_{19}]^{2-}$ with aromatic amines: synthesis and structure of a hexamolybdate building block with linear difunctionality. J Chem Soc Chem Commun 4:455–456
46. Strong JB, Yap GPA, Ostrander R, Liable-Sands LM, Rheingold AL, Thouvenot R, Gouzerh P, Maatta EA (2000) A new class of functionalized polyoxometalates: synthetic, structural, spectroscopic, and electrochemical studies of organoimido derivatives of $[Mo_6O_{19}]^{2-}$. J Am Chem Soc 122:639–649
47. Zhang J, Xiao F, Hao J, Wei Y (2012) The chemistry of organoimido derivatives of polyoxometalates. Dalton Trans 41:3599–3615
48. Clegg W, Elsegood MRJ, Errington RJ, Havelock J (1996) Alkoxide hydrolysis as a route to early transition-metal polyoxometalates: synthesis and crystal structures of heteronuclear hexametalate derivatives. J Chem Soc Dalton Trans 5:681–690
49. Errington RJ, Petkar SS, Middleton PS, McFarlane W, Clegg W, Coxall RA, Harrington RW (2007) Synthesis and reactivity of the methoxozirconium pentatungstate $(^nBu_4N)_6[\{(\mu\text{-}MeO)ZrW_5O_{18}\}_2]$: insights into proton transfer reactions, solution dynamics and assembly of $\{ZrW_5O_{18}\}^{2-}$ building blocks. J Am Chem Soc 129:12181–12196
50. Errington RJ, Petkar SS, Middleton PS, McFarlane W, Clegg W, Harrington RW (2007) Non-aqueous synthetic methodology for TiW5 polyoxometalates: protonolysis of $[(MeO)TiW_5O_{18}]^{3-}$ with alcohols, water and phenols. Dalton Trans 44:5211–5222
51. Errington RJ, Harle G, Clegg W, Harrington RW (2009) Extending the Lindqvist family to late 3d transition metals: a rational entry to CoW5 hexametalate chemistry. Eur J Inorg Chem 34:5240–5246
52. Errington RJ, Coyle L, Middleton PS, Murphy CJ, Clegg W, Harrington RW (2010) Synthesis and structure of the alkoxido-titanium pentamolybdate $(^nBu_4N)_3[(^iPrO)TiMo_5O_{18}]$: an entry into systematic TiMo5 reactivity. J Clust Sci 21:503–514
53. Coyle L, Middleton PS, Murphy CJ, Clegg W, Harrington RW, Errington RJ (2012) Protonolysis of $[(^iPrO)TiMo_5O_{18}]^{3-}$: access to a family of TiMo5 Lindqvist type polyoxometalates. Dalton Trans 41:971–981
54. Kandasamy B, Wills C, McFarlane W, Clegg W, Harrington RW, Rodríguez-Fortea A, Poblet JM, Bruce PG, John Errington R (2012) An alkoxido-tin substituted polyoxometalate $[(MeO)SnW_5O_{18}]^{3-}$: the first member of a new family of reactive $\{SnW_5\}$ Lindqvist-type anions. Chem Eur J 18:59–62

55. Clegg W, Errington RJ, Kraxner P, Redshaw C (1992) Solid-state and solution studies of tungsten(VI) oxotetraalkoxides. J Chem Soc Dalton Trans 8:1431–1438

56. Vilà-Nadal L, Rodríguez-Fortea A, Yan L-K, Wilson EF, Cronin L, Poblet JM (2009) Nucleation mechanisms of molecular oxides: a study of the assembly–disassembly of $[W_6O_{19}]^{2-}$ by theory and mass spectrometry. Angew Chem Int Ed 48:5452–5456

57. Vilà-Nadal L, Rodríguez-Fortea A, Poblet JM (2009) Theoretical analysis of the possible intermediates in the formation of $[W_6O_{19}]^{2-}$. Eur J Inorg Chem 34:5125–5133

58. Lang Z-L, Guan W, Yan L-K, Wen S-Z, Su Z-M, Hao L-Z (2012) The self-assembly mechanism of the Lindqvist anion $[W_6O_{19}]^{2-}$ in aqueous solution: a density functional theory study. Dalton Trans 41:11361–11368

59. Maksimovskaya RI, Burtseva KG (1985) ^{17}O and ^{183}W NMR studies of the paratungstate anions in aqueous solutions. Polyhedron 4:1559–1562

60. Hastings J, Howarth OW (1992) A ^{183}W, ^1H and ^{17}O nuclear magnetic resonance study of aqueous isoplytungstates. J Chem Soc Dalton Trans 2:209–215

61. Clegg W, Errington RJ, Fraser KA, Richards DG (1993) Evidence for rapid ligand redistribution in non-aqueous tungstate chemistry: rational synthesis of the binuclear tungsten oxoalkoxide $[W_2O_5(OMe)_5]^{2-}$. J Chem Soc Chem Commun 13:1105

62. Errington RJ, Kerlogue MD, Richards DG (1993) Non-aqueous routes to a new polyoxotungstate. J Chem Soc Chem Commun 7:649

63. Filowitz M, Klemperer WG, Shum W (1978) Synthesis and characterization of the pentamolybdate ion $Mo_5O_{17}H^{3-}$. J Am Chem Soc 100:2580–2581

64. Seisenbaeva GA, Gohil S, Kessler VG (2004) Influence of heteroligands on the composition, structures and properties of homo- and heterometallic zirconium alkoxides. Decisive role of thermodynamic factors in their self-assembly. J Mater Chem 14:3177–3190

65. Caruso J, Alam TM, Hampden-Smith MJ, Rheingold AL, Yap GAP (1996) Alcohol-alkoxide exchange between $Sn(OBu^t)_4$ and $HOBu^t$ in co-ordinating and non-co-ordinating solvents. J Chem Soc Dalton Trans 13:2659–2664

66. Flynn CM, Pope MT (1971) Tungstovanadate heteropoly complexes. I. Vanadium(V) complexes with the constitution $M_6O_{19}^{n-}$ and V:W $\geq$ 1:2. Inorg Chem 10:2524–2529

67. Domaille P (1984) 1- and 2-dimensional tungsten-183 and vanadium-51 NMR characterization of isopolymetalates and heteropolymetalates. J Am Chem Soc 106:7677–7687

68. Nugent WA, Mayer JM (1988) Metal-ligand multiple bonds. Wiley, New York

69. Kessler VG, Mironov AV, Turova NY, Yanovsky AI, Struchkov YT (1993) The synthesis and X-ray crystal structure of molybdenum oxomethoxide $[Mo(OMe)_4]_2$. Polyhedron 12:1573–1576

70. Smith GD, Fanwick PE, Rothwell IP (1990) Synthesis, structure, and spectroscopic properties of germanium and tin compounds containing aryloxide ligation: comparison of aryloxide bonding to group 4 and group 14 metal centers. Inorg Chem 29:322–3226

71. Kandasamy B (2011) PhD thesis, University of St. Andrews, St. Andrews

72. Zhuang J, Yan L, Liu C, Su Z (2009) A quantum chemical study of the structure, bonding characteristics and nonlinear optical properties of aryloxido and salicylaldehydo derivatives of $[XW_5O_{10}]^{3-}$ (X = Zr or Ti). Eur J Inorg Chem 17:2529–2535

73. Carabineiro H, Villanneau R, Carrier X, Herson P, Lemos F, Ribeiro FR, Proust A, Che M (2006) Zirconium-substituted isopolytungstates: structural models for zirconia-supported tungsten catalysts. Inorg Chem 45:1915–1923

74. Strauss SH (1993) The search for larger and more weakly coordinating anions. Chem Rev 93:927–942

75. Scott SL, Basset J-M, Niccolai GP, Santini CC, Candy J-P, Lecuyer C, Quignard F, Choplin A (1994) Surface organometallic chemistry: a molecular approach to surface catalysis. New J Chem 18:115–122

76. Copéret C, Comas-Vives A, Conley MP, Estes DP, Fedorov A, Mougel V, Nagae H, Núnez-Zarur F, Zhizhko PA (2016) Surface organometallic and coordination chemistry toward single-

site heterogeneous catalysts: strategies, methods, structures, and activities. Chem Rev 116:323–421

77. Pascual-Borras M, López X, Rodriguez-Fortea A, Errington RJ, Poblet JM (2014) ^{17}O NMR chemical shifts in oxometalates: from the simplest monometallic species to mixed-metal polyoxometalates. Chem Sci 5:2031–2042

78. Wingad RL (1999) PhD thesis, Newcastle University, Newcastle upon Tyne

79. Izuagie T (2017) PhD thesis, Newcastle University, Newcastle upon Tyne

80. Knoth WH, Domaille PJ, Roe DC (1983) Halometal derivatives of $W_{12}PO_{40}^-$ and related [183]W NMR studies. Inorg Chem 22:198–201

81. Kholdeeva OA, Maksimov GM, Maksimovskaya RI, Kovaleva LA, Fedotov MA, Grigoriev VA, Hill CL (2000) A dimeric titanium-containing polyoxometalate. Synthesis, characterization, and catalysis of H_2O_2-based thioether oxidation. Inorg Chem 39:3828–3837

82. Kholdeeva OA, Trubitsina TA, Maksimov GM, Golovin AV, Maksimovskaya RI (2005) Synthesis, characterization, and reactivity of Ti(IV)-monosubstituted keggin polyoxometalates. Inorg Chem 44:1635–1642

83. Maksimov GM, Maksimovskaya RI, Kholdeeva OA, Fedotov MA, Zaikovskii VI, Vasil'ev VG, Arzumanov SS (2009) Structure and properties of $H_8(PW_{11}TiO_{39})_2O$ heteropolyacid. J Struct Chem 50:618–627

84. Jiménez-Lozano P, Skobelev IY, Kholdeeva OA, Poblet JM, Carbó JJ (2016) Alkene epoxidation catalyzed by Ti-containing polyoxometalates: unprecedented β–oxygen transfer mechanism. Inorg Chem 55:6080–6084

85. Fernández JA, López X, Poblet JM (2007) A DFT study on the effect of metal, anion charge, heteroatom and structure upon the relative basicities of polyoxoanions. J Mol Catal A Chem 262:236–242

86. Pascual-Borras M (2017) PhD thesis, Universitat Rovira I Virgili, Tarragona

Index